

FINAL REPORT

Metric Identification and Protocol Development for Characterizing DNAPL Source Zone Architecture and Associated Plume Response

SERDP Project ER-1612

October 2013

Linda Abriola
Eric Miller
Kurt Pennell
Andrew Ramsburg
John Christ
Tufts University

Distribution Statement A

This document has been cleared for public release



This report was prepared under contract to the Department of Defense Strategic Environmental Research and Development Program (SERDP). The publication of this report does not indicate endorsement by the Department of Defense, nor should the contents be construed as reflecting the official policy or position of the Department of Defense. Reference herein to any specific commercial product, process, or service by trade name, trademark, manufacturer, or otherwise, does not necessarily constitute or imply its endorsement, recommendation, or favoring by the Department of Defense.

REPORT DOCUMENTATION PAGE				Form Approved OMB No. 0704-0188	
Public reporting burden for this collection of information is estimated to average 1 hour per response, including the time for reviewing instructions, searching existing data sources, gathering and maintaining the data needed, and completing and reviewing this collection of information. Send comments regarding this burden estimate or any other aspect of this collection of information, including suggestions for reducing this burden to Department of Defense, Washington Headquarters Services, Directorate for Information Operations and Reports (0704-0188), 1215 Jefferson Davis Highway, Suite 1204, Arlington, VA 22202-4302. Respondents should be aware that notwithstanding any other provision of law, no person shall be subject to any penalty for failing to comply with a collection of information if it does not display a currently valid OMB control number. PLEASE DO NOT RETURN YOUR FORM TO THE ABOVE ADDRESS.					
1. REPORT DATE (DD-MM-YYYY)		2. REPORT TYPE Final		3. DATES COVERED (From - To) Sept 2008-Sept 2013	
4. TITLE AND SUBTITLE Metric Identification and Protocol Development for Characterizing DNAPL Source Zone Architecture and Associated Plume Response				5a. CONTRACT NUMBER W912HQ-08-C-0003	
				5b. GRANT NUMBER n.a.	
				5c. PROGRAM ELEMENT NUMBER ER-1612	
6. AUTHOR(S) Linda M. Abriola, Eric L. Miller, Kurt D. Pennell, Andrew Ramsburg, John A. Christ				5d. PROJECT NUMBER W74RDV73090621	
				5e. TASK NUMBER 1-4	
				5f. WORK UNIT NUMBER P00008	
7. PERFORMING ORGANIZATION NAME(S) AND ADDRESS(ES) Tufts University Research Administration 20 Professors Row Medford, MA 02155				8. PERFORMING ORGANIZATION REPORT NUMBER	
9. SPONSORING / MONITORING AGENCY NAME(S) AND ADDRESS(ES) Dr. Andrea Leeson SERDP/ESTCP Program Office 4800 Mark Center Drive, Suite 17D08 Alexandria, VA 22350-3600				10. SPONSOR/MONITOR'S ACRONYM(S) SERDP	
				11. SPONSOR/MONITOR'S REPORT NUMBER(S)	
12. DISTRIBUTION / AVAILABILITY STATEMENT					
13. SUPPLEMENTARY NOTES					
14. ABSTRACT The overarching goal of this research is to develop and demonstrate a comprehensive approach for field characterization of DNAPL source zones which quantifies the key features that control plume response. Here the intent is to integrate targeted (local-scale) <i>in situ</i> tests with transect-based observations of downstream contaminant flux or concentration and information on subsurface geologic variability. To address its primary goal, the research encompasses the following specific objectives: (1) identification of the most information rich metrics for linking NAPL architecture to plume response; (2) development and refinement of <i>in situ</i> test methods and modeling tools that can be used to quantify identified metrics in targeted regions of the source zone; (3) integration of these metrics and tools with current machine learning characterization methods for an overall source zone assessment protocol; and (4) development of simplified models for prediction of plume response. The research approach integrates batch, column and aquifer cell experiments with mathematical modeling and data processing tools to identify and quantify features of the DNAPL architecture controlling down gradient plume response.					
15. SUBJECT TERMS Field characterization; Metric identification; DNAPL;					
16. SECURITY CLASSIFICATION OF: No classified information			17. LIMITATION OF ABSTRACT SAR	18. NUMBER OF PAGES	19a. NAME OF RESPONSIBLE PERSON Dr Linda Abriola
a. REPORT	b. ABSTRACT	c. THIS PAGE			19b. TELEPHONE NUMBER (include area code) 617-627-3237

Table of Contents

List of Figures	iv
List of Tables	xii
List of Acronyms	xiv
Acknowledgements	xv
Abstract	xvi
Objective	xviii
I. Background.....	1
II. Materials and Methods	3
II.1. Data Generation for Metric Identification and Protocol Evaluation.....	3
II.1.1. Introduction	3
II.1.2. Batch and Aquifer Cell Experiments	3
II.1.2.1. Introduction to Dissolution and Micellar Solubilization of Mixed NAPLs	3
II.1.2.2. Batch Experiments.....	4
II.1.2.3. Aquifer Cell Experiments	7
II.1.3. Field-Scale Numerical Simulations.....	14
II.2. Refinement of In-Source Push-Pull Tests.....	19
II.2.1. Introduction	19
II.2.2. Batch, Column, and Aquifer Cell Experiments.....	20
II.2.2.1. Materials and Analytical Methods	20
II.2.2.2. Experimental Set Up.....	22
II.2.3. Push-Pull Tracer Test Model Development	24
II.2.3.1. Partitioning Tracer Model.....	24
II.2.3.2. Fine-Scale 3D Simulator.....	29
II.2.3.3. Tracer Push-Pull Sensitivity and Inverse Modeling.....	30
II.3. Processing Methods for Identification of Source Zone Features.....	37
II.3.1. Introduction	37
II.3.2. Standard Manifold Regression	40
II.3.2.1. Overview	40
II.3.2.2. Morphological Feature Extraction	43
II.3.2.3. Manifold Dimension Reduction using Laplacian Eigenmaps.....	46
II.3.2.4. Spectral Regression Method for Embedding Function Learning.....	48
II.3.2.5. Linear Bayesian Regression Method and Confidence Interval Estimation.....	49
II.3.3. Integrated Manifold Regression	50
II.3.4. Multi-task Manifold Regression.....	52

II.3.5. Sparse Data Manifold Regression	54
II.4. Development of Simplified Modeling Tools	56
II.4.1. Introduction	56
II.4.2. Upscaled Models for Mass Depletion	57
II.4.3. Upscaled Models for Push-Pull Tracer Tests	58
II.4.3.1. Generation of Heterogeneous Source-Zone Realizations	58
II.4.3.2. Source-Zone Metrics	59
II.4.3.3. Model Development	60
III. Results and Discussion	64
III.1 Data Generation for Metric Identification and Protocol Development	64
III.1.1. Batch and Aquifer Cell Experiments	64
III.1.1.1. Batch Experiments	64
III.1.1.2. Aquifer Cell Experiments.....	69
III.1.2. Numerical Simulations.....	99
III.1.2.1. Field-scale Numerical Simulations.....	99
III.2. Refinement of In-Source Push-Pull Tests.....	113
III.2.1. Batch, Column, and Aquifer Cell Experiments	113
III.2.1.1. Liquid-Liquid Equilibrium Studies	113
III.2.1.2. Non-equilibrium Tracer Transport	119
III.2.1.3. Push-Pull Test Design	130
III.2.1.4. Interpreting Asymmetric Recovery Curves in Push Pull Tracer Tests	140
III.2.2. Push-Pull Tracer Test Model Development.....	150
III.2.2.1. Fine-Scale 3D Simulator	150
III.2.2.2. Tracer Push-Pull Sensitivity and Inverse Modeling	150
III.3. Processing Methods for Identification of Source Zone Features.....	163
III.3.1. Machine Learning Results	163
III.3.2. Machine Learning Conclusions	174
III.4. Development of Simplified Modeling Tools	175
III.4.1. Upscaled Model for Mass Depletion	175
III.4.1.1. Model Refinement and Validation	175
III.4.2. Upscaled Models for Push-Pull Tracer Tests.....	178
III.4.2.1. Model Development	178
III.4.2.2. Model Verification	185
III.4.2.3. Conclusions for Upscaled PPTT Model Development.....	190
III.4.2.4. Assessment of Source Zone Features, using Push-Pull Data.....	190
IV. Conclusions and Implications for Future Research / Implementation.....	202
IV.1. Data Generation for Metric Identification and Protocol Evaluation.....	203

IV.2. Refinement of In-Source Push-Pull Tests	205
IV.3. Processing Methods for Identification of Source Zone Features	206
IV.4. Development of Simplified Modeling Tools	206
V. Literature Cited	208
VI. Appendices	222
VI.1. A. Supporting Data	222
VI.2. B. List of Scientific/Technical Publications	222
VI.2.1. B.1. Articles in peer-reviewed journals	222
VI.2.2. B.2. Technical reports	222
VI.2.3. B.3. Conference or symposium proceedings scientifically recognized and referenced	223
VI.2.4. B.4. Conference or symposium abstracts	223
VI.2.5. B.5. Text books or book chapters	225

List of Figures

Figure M.1.1: Picture of aquifer cell 4 (AC 4) prior to TCE-DNAPL injection.	10
Figure M.1.2: Schematic diagram of aquifer cell (AC 5) permeability distribution.	11
Figure M.1.3 Field Reconstruction—Conceptualization for Obtaining the 2-D Permeability Field.	17
Figure M.2.1. Spatial variation of concentration at NAPL-aqueous interface for (a) local equilibrium assumption, (b) linear driving force model based on a film boundary layer (c) dual diffusion model, and (d) dual diffusion plus surface partitioning model; figure adapted and modified from Abriola and Bradford (1998).	26
Figure M.3.1: The source zone plotted in 3D is modeled as being comprised of two parts: “pools” for which the saturation exceeds 0.15 and “ganglia” for which the saturation is lower than 0.15. Flow through the source zone gives the down-gradient concentration data in 2D.	38
Figure M.3.2: The framework of our regression-based machine learning approach. The morphological feature extraction is shared by both training and test stage, because it is an image processing method which is to be applied to both the training and test data.	39
Figure M.3.3. The identifiability issue of regression function. Due to the difference of initial spill, the metrics corresponding to the similar concentration image is quite different, for example, the concentration data in (a) and (b) look most similar, but the metrics, mass in pool, are quite different.	42
Figure M.3.4: The observation of concentration image according to their pool fraction value. ..	44
Figure M.3.5. Morphological feature vectors corresponding to concentration data from Figure M.3.4.	45
Figure M.3.6: Two dimensional embedding of concentration image data and associated pool fraction (left) and mass in pools (right). The color of each dot indicates the pool fraction or pool mass respectively. The manifolds we find demonstrate that the data with similar metrics are located nearby one another. The unit of mass in pool is kilogram.	48
Figure M.3.7: The framework of manifold regression for sparse concentration data. The morphological feature extraction is used for the full training data which gives the manifold coordinate. The embedding function is learned from sparse data which is sampled from the full concentration data according to the location of wells.	55
Figure M.4.1. Two-dimensional domains cropped out of three-dimensional numerically generated realizations; (a) 3D PCE-NAPL realizations generated by UTCHEM; (b) 2D vertical plane selected at the center of SZ, the marked rectangular region at the center marks the location and dimensions of the selected 2D regions for developing the upscaled model; (c) NAPL saturation in the selected region at four different time snapshots during the dissolution.	63
Figure R.1.1. Equilibrium aqueous solubility of TCE and PCE as a function of mole fraction.	64

Figure R.1.2. Equilibrium solubility of TCE and PCE in 4% Tween 80 from binary DNAPL mixtures. Raoult's law predictions of ideal solubilization behavior are shown as dashed lines. .65	65
Figure R.1.3. Equilibrium solubility of decane and dodecane in 4% Tween 80 from a binary multicomponent organic liquid at various mole fractions.67	67
Figure R.1.4. Measured decane solubilities from a pure decane liquid and an a NAPL consisting of 1:1 (molar) PCE:decane at five concentrations of Tween 80.67	67
Figure R.1.5. Temporal evolution in DNAPL source zone and corresponding down-gradient dissolved phase mass flux for AC1 initial ganglia dominated source zone containing 1:1 (m/m) TCE:PCE-DNAPL source zone) prior to and following surfactant floods. Source zone DNAPL saturations are in volumetric fractions; downgradient TCE and PCE aqueous concentrations are mg/L.71	71
Figure R.1.6. TCE and PCE flux-averaged effluent concentrations and normalized mass removed as a function of pore volume for AC1. Flux averaged effluent concentrations during surfactant flood 1 (23 PV) and 2 (35 PV) are shown by the grey boxes.73	73
Figure R.1.7. Temporal evolution in DNAPL source zone (column 1) and corresponding down-gradient dissolved phase TCE (column2) and PCE (column 3) mass flux for AC3 (initial ganglia dominated source zone containing 1:1 (m/m) TCE:PCE-DNAPL source zone) prior to and following surfactant floods. Source zone DNAPL saturations are in volumetric fractions; downgradient TCE and PCE aqueous concentrations are mg/L.74	74
Figure R.1.8. TCE and PCE flux-averaged effluent concentrations (left axis) and fractional mass recovered (right axis) as a function of pore volume flushed through the aquifer cell for AC3. Flux averaged effluent concentrations during surfactant floods 1 (15.5 PV) and surfactant flood 2 (45 PV) are shown by the grey boxes.75	75
Figure R.1.9. TCE and PCE flux-averaged effluent concentrations (left axis) and source zone averaged DNAPL mole fraction (right axis) as a function of pore volumes flushed through AC3. Note that elevated effluent concentrations due to surfactant flooding were omitted (represented by gray boxes).....76	76
Figure R.1.10. Relative reduction in mass discharge for TCE and PCE in AC3 as a function of the relative mass removed for each component. A relative reduction <0 indicates an increase in mass discharge, while a relative reduction > 0 indicates a decrease in mass discharge.77	77
Figure R.1.11. Temporal evolution in source zone architecture (column 1), down gradient dissolved phase TCE (column 2) and PCE (column 3) mass flux from the pooled source zone consisting of 1:1 (m/m) TCE:PCE-DNAPL source zone in AC2. Source zone DNAPL saturations are in volumetric fractions; downgradient TCE and PCE aqueous concentrations are mg/L.79	79
Figure R.1.12. TCE and PCE flux-averaged effluent concentrations (left axis) and fractional mass removed (right axis) from the pool dominated aquifer cell experiment (AC2). Flux	

averaged effluent concentrations during surfactant flood 1 (11 PV) and surfactant flood 2 (25 PV) are marked by the grey boxes.	81
Figure R.1.13. TCE and PCE flux-averaged effluent concentrations during aqueous flushing alone and source zone averaged mole fraction as a function of pore volume for AC2. Flux averaged effluent concentrations during surfactant floods 1 and 2 were removed and are represented by grey boxes.....	82
Figure R.1.14 Temporal evolution in source zone architecture and downgradient, dissolved phase TCE plume development in the neat TCE aquifer cell experiment (AC4). Source zone DNAPL saturations are in volumetric fractions; downgradient TCE aqueous concentrations are mg/L. ...	83
Figure R.1.15. Temporal changes in source zone PF as a function of TCE-DNAPL fractional mass removed.....	84
Figure R.1.16. TCE flux-averaged effluent concentration as a function of mass removed from the source zone for AC4.	85
Figure R.1.17. Source zone morphology and PF at 10, 100 and 250 times the median sand grain size (d_{50}) for the initial SZA in AC4.	86
Figure R.1.18. Experimental flux averaged effluent concentrations and prediction based on the Christ 2010 upscaled model using a per-pixel averaging window, DBA and CBA.....	87
Figure R.1.19. Simulated (top) and actual (bottom) permeability distribution of aquifer cell 5 (AC5).	89
Figure R.1.20. Conservative tracer dye (sodium fluorescein) movement through AC5 (illuminated with 450 nm Kino-Flo Blue bulbs) at 0.5 PVs.	90
Figure R.1.21. Bromide tracer breakthrough (left axis) and fractional bromide mass recovered (right axis) during a 1/3 pulse conservative tracer test in AC5.....	91
Figure R.1.22. Bromide and PFBA tracer breakthrough during the extended conservative tracer test in AC5.	92
Figure R.1.23. Temporal evolution in SZA and down-gradient plume concentrations for AC5. The side-port concentration measurements were obtained from the first and second transect, while ports A4 and B3 were located within the low permeability zones and therefore were not sampled.	94
Figure R.1.24. TCE flux-averaged effluent concentrations as a function of pore volume from AC5. Flux averaged effluent concentrations during surfactant flooding (at 22 PV) are indicated by the grey box.....	95
Figure R.1.25. Simulated and experimental effluent breakthrough concentration of the conservative tracer; (a) entire test duration; (b) and (c) magnified around the flow interruption periods at approximate pore volumes 2.0 and 4.7, respectively.	97

Figure R.1.26. Simulated distribution of normalized tracer concentration in the aquifer cell before (left) and after (right) a flow interruption during injection phase of a conservative tracer test.	98
Figure R.1.27. Simulated distribution of normalized tracer concentration before (left) and after (right) a flow interruption during the flushing of the tracer out of the aquifer cell.	98
Figure R.1.28. Schematic representation of cases included in the database of 3-D simulations of DNAPL source zone architecture-plume response in a relatively homogeneous glacial outwash deposit.	100
Figure R.1.29. Three examples of the DNAPL SZA for the cases where the permeability field was modified in a relatively homogeneous glacial outwash deposit.	101
Figure R.1.30. Range of SZA metrics obtained from the database of 3D simulations in a relatively homogeneous glacial outwash deposit.	102
Figure R.1.31. Representative PCE saturation distributions in a highly heterogeneous glaciofluvial deposit – 2D simulations case 1 to case 4.	104
Figure R.1.32 Representative PCE saturation distributions for different spill rates in a highly heterogeneous glaciofluvial deposit - simulation case 1, case 2, case 5, case 6, case 9 and case 10.	106
Figure R.1.33. Representative PCE saturation distributions for simulation in a highly heterogeneous glaciofluvial deposit -case 1, case 2, case7, and case 8.	108
Figure R.1.34. 2-D simulation results extracted from 3-D simulation.	111
Figure R.1.35. 2-D and 3-D PCE saturation distribution with Leverett scaling.	111
Figure R.1.36. 2-D and 3-D PCE saturation distribution with HP Method.	112
Figure R.2.1. Ternary phase diagrams at $22.0 \pm 0.1^\circ\text{C}$ for 1-pentanol (a), 1-hexanol (b), and 2-octanol (c) developed from liquid-liquid equilibrium batch experiments. Experimental data are shown as tie lines. UNIFAC predictions of the binodal curves defining each two phase region are shown as dotted lines. The binodal curve defining the aqueous phase is not visible but exists in the lower right corner of each phase diagram.	114
Figure R.2.2. The distribution of 1-pentanol (a), 1-hexanol (b), and 2-octanol (c) between the NAPL and aqueous phase at $22.0 \pm 0.1^\circ\text{C}$ as established by liquid-liquid equilibrium data (circles) and UNIFAC predictions (dashed line). Note that data span the range of possible aqueous concentrations but that differences in solubility necessitate change in the horizontal range for each panel. Insets show dilute range with the regressed, linear partitioning model (solid line).	115
Figure R.2.3. Breakthrough curves for bromide (a), 1-pentanol (b), 1-hexanol (c), and 2-octanol (d) tracer tests conducted at $22 \pm 2^\circ\text{C}$. Dispersivity was fit (dash-dot) to bromide data. Predictive simulations using measured values for the partition coefficients are also shown using equilibrium (dotted), linear driving force (solid), and dual diffusion (dashed) models. Values of the partition coefficient employed in these simulations were 4.20, 17.4, and 149 $L_{\text{aq}}/L_{\text{NAPL}}$ for 1-pentanol, 1-	

hexanol, and 2-octanol, respectively, at $22.0 \pm 0.1^\circ\text{C}$. Note that linear driving force and dual diffusion models produce nearly identical results, the pore volume scale changes for each panel, and the normalized concentration scale changes for panel d.120

Figure R.2.4. Limitation of the local equilibrium assumption for partitioning alcohols in zones of uniformly entrapped DNAPL. The hydraulic residence time within the zone is $\frac{L}{nS_{aq}v}$, and the

partitioning index is defined to be $S_n K_p^{C_i}$. The line is shown as a visual guide for the simulation results shown as open circles.123

Figure R.2.5. Packing structure used to create the pooled source zone.124

Figure R.2.6. 2-D aquifer cell used to examine partitioning tracer transport in a pooled TCE-DNAPL source zone. The photograph (a) sampling port labels (columns 1- 4 and rows A-F). Light transmission results are shown as a pixel by pixel saturation estimation (b), discrete averaging saturation estimation (c), and continuum averaging saturation estimation (d).126

Figure R.2.7. Effluent data and model simulations for the aquifer cell experiment containing the isolated pool. Bromide (circles and solid line), pentanol (diamonds and dashed line), hexanol (squares and dash-dot line) and 2-octanol (triangles and dotted line) are included. The model was fit to the bromide data by adjusting dispersivity. All partitioning tracer breakthrough curves were subsequently predicted using this fitted dispersivity.127

Figure R.2.8. Comparison of tracer concentrations in the sampling ports (columns 1 and 2) to those predicted by the model. 1-pentanol (diamonds, dashed line), 1-hexanol (squares, dash-dot line) and 2-octanol (triangles, dotted line) are included. Panel labels correspond to specific ports show in Figure R.2.6.129

Figure R.2.9. Initial TCE-DNAPL saturation distributions in the 2D aquifer cell for the low, mid and high PF experiments. Shown on the left are photographs of each aquifer cell (100 cm in length, 44 cm in packed height and 1.5 cm in thickness). Shown on the right are light transmission images of saturation distribution. All color bars range from no saturation (blue) to a saturation of 0.4 (red).132

Figure R.2.10. Representative experiment (Mid PF, Fast-Fast Flow) for which the analytical solution has relatively good performance. Shown here are data (symbols) for each tracer and two simulations, a fit of the analytical solution to the data by adjusting only TCE-DNAPL saturation, and a prediction using the actual TCE-DNAPL saturation determined via light transmission (0.8%).135

Figure R.2.11. 2-octanol recovery curve for the high PF, fast-fast flow experiment used here to illustrate the influence of the major simplifying assumptions associated with the analytical solution.139

Figure R.2.12. Representations of the forty highly simplified source zones employed in the development of the empirical approach to interpreting asymmetric recovery curves in push-push partitioning tracer tests.142

Figure R.2.13. 2-octanol recovery curves resulting from push-pull tests conducted in realizations 24 (solid), 29 (short dash), 30 (dot dash), 31 (short dash) and 32 (dotted). Also included are the diagrams of the corresponding source zones.	143
Figure R.2.14. 2-octanol recovery curves resulting from push-pull tests conducted in realizations 7 (dashed), 8 (dotted), and 21 (solid). Also included are the diagrams of the corresponding source zones.	145
Figure R.2.15. Example of inflections in asymmetric recovery curves.....	146
Figure R.2.16. Interpretation of an asymmetric recovery curve using the empirical approach developed in this research. The data shown here are those from the 2-octanol recovery curve produced from the mid PF, fast-fast experiment.	148
Figure R.2.17. Light transmission image of DNAPL architecture in the mid PF, fast-fast experiment used to illustrate the empirical approach to interpreting asymmetric recovery curves obtained during push-pull partitioning tracer tests. The boxed regions correspond to those used in Equation R.2.8.	149
Figure R.2.18. Skeleton diagram of study area.....	152
Figure R.2.19. DNAPL saturation distribution.....	152
Figure R.2.20 Sensitivity of tracer concentration in aqueous phase with respect to DNAPL saturation at the end of pull phase. The left figure is obtained using the adjoint sensitivity method, the right figure is obtained by running the forward model many times.....	154
Figure R.2.21. Sensitivity of tracer concentration in aqueous phase to DNAPL saturation at different time steps during the pull phase.	154
Figure R.2.22. DNAPL saturation distribution.....	155
Figure R.2.23. Sensitivity of tracer concentration to DNAPL saturation at four time steps during the pull phase. Left four figures are the sensitivity matrices of Hexanol, and the right four figures are the sensitivity matrices of Octanol.....	156
Figure R.2.24 Sensitivity of tracer concentration to DNAPL saturation at four time steps during the pull phase. Left four figures are the sensitivity matrices of Hexanol, and the right four figures are the sensitivity matrices of Octanol.....	157
Figure R.2.25. Sensitivity of tracer concentration to DNAPL saturation with different tracer injection concentrations at 4h of the pull phase.....	158
Figure R.2.26. Sensitivity of tracer concentration to DNAPL saturation with different injection and extraction flow rates at 4h of the pull phase.	159
Figure R.2.27. “Real” DNAPL saturation distributions for first example.....	160
Figure R.2.28. estimated DNAPL saturation distributions for first example.	161
Figure R.2.29. “Real” DNAPL saturation distributions for second example.....	161

Figure R.2.30. estimated DNAPL saturation distributions for second example.....	162
Figure R.3.1: The interpretation of sand box and the location of wells. The size of sand box is 45.5 cm x 102.5 cm. The concentration data is 91 x 41 pixels. According to the measurement in this plot, we can determine the coordinates of each wells in the concentration data, for example, well A1 is (11,21), thus we use the pixel value of (11,21) in concentration data as the sparse sample data.....	165
Figure R.3.2. The absolute error vs relative error scatter plots of M_p and M_s from SGS data set-4 using multi-task manifold regression.....	172
Figure R.3.3. The absolute error vs relative error scatter plots of M_p and M_s from TP/MC data set using multi- task manifold regression.	173
Figure R.4.1 Prediction of dissolution behavior using Christ et al. (2006) model for low GTP SZAs generated by changing the correlation length of the original permeability fields.	176
Figure R.4.2. Two-domain upscaled model comparison to numerical simulation results for (a) 200-, 400-, and 600-day spill simulations with no emplaced NAPL, (b) – (e) 400-day simulations with various volumes of NAPL emplaced at pools (See Christ et al., 2010 for a full description), and (f) comparison to 2-D aquifer cell experiment results of Suchomel and Pennell (2006). Equation 8 refers to equation R.4.1.....	177
Figure R.4.3. Mean squared errors between the fit and observed breakthrough curves; (a) Distribution of mean squared errors between breakthrough curves for all simulations; and (b) demonstration of breakthrough curves for 4 samples representative of different MSE value ranges; solid lines show prediction and dashed lines represent observation data.....	179
Figure R.4.4. Selecting the best model based on the statistics of the regression models; (a) standard error of the models; (b) adjusted R-squared value; (c) prediction error sum of squares: PRESS; The graphs on the top row present the absolute value of the statistics. The graphs on the bottom show the gained improvement by adding one more predictor parameter at a time to the model. The horizontal lines on the lower row figures mark the one-percent improvement criterion.	183
Figure R.4.5. Predicted versus observed effective mass transfer coefficients for the best model (model 4).....	184
Figure R.4.6. Predicted versus observed effective mass transfer coefficients for the test dataset.....	186
Figure R.4.7. First two-dimensional aquifer cell test used to verify developed model, Ervin (2012).....	189
Figure R.4.8. Breakthrough curves for the partitioning tracer test conducted by Ervin (2012); (a) 1-hexanol tracer; (b) 2-octanol tracer; circles show the measured effluent concentration, solid lines are BTCs predicted by the developed upscaled model. The smaller figures on the upper right corner show the same BTCs on a logarithmic scale.....	189

Figure R.4.9. Forward simulation of a PPTT in a heterogeneous source zone (Example 4); (a) 3D heterogeneous NAPL realization and location of the test well, horizontal planes mark the interrogation zone; (b) a horizontal cross section at the middle of the interrogation zone; (c) and (d) concentration breakthrough curves of the pull phase at the well location, in linear and logarithmic scales, respectively. MSE values are reported in Table R.4.4.....	193
Figure R.4.10. Forward simulation of a PPTT in a heterogeneous source zone (Example 5); (a) 3D heterogeneous NAPL realization and location of the test well, horizontal planes mark the interrogation zone; (b) a horizontal cross section at the middle of the interrogation zone; (c) and (d) concentration breakthrough curves of the pull phase at the well location, in linear and logarithmic scales, respectively. MSE values are reported in Table R.4.4.....	194
Figure R.4.11. Equilibrium and rate-limited prediction of a PPTT in a heterogeneous region; dashed line shows observed BTC for 2-octanol; solid lines show the upscaled and equilibrium predictions (Example 5). MSEs are reported in Table R.4.4.	195
Figure R.4.12. Comparison of estimated and actual values for: (a) vertical spreading, (b) pool fraction, and (c) NAPL saturation. Blue circles show values of parameters obtained for 2D simulations; red triangles and green squares show values of parameters for 3D simulations, in Examples 4 and 5, respectively. The middle 45-degree-line represents the perfect estimation and the other two lines mark root-mean-square deviation below and above perfect estimation. Vertical spreading of Example 4 is an outlier and is not shown on plot (a); see Table R.4.5 for its values.	198
Figure C.1.1. Flow chart outlining the suggested Protocol.	203

List of Tables

Table M.1.1. Range of organic liquid phase compositions and surfactant concentrations used to evaluate the applicability of Raoult's law to describe micellar solubilization of multicomponent NAPLs.....	5
Table M.1.2. Summary of aquifer cells and experimental conditions.	8
Table M.1.3. Porous media characteristics of aquifer cell 5 (AC5).....	11
Table M.1.4. Simulations with different spill scenarios	15
Table M.1.5. Simulations with different permeability realizations	16
Table M.2.1. Physical properties of alcohol tracers and TCE	21
Table M.2.2. UNIFAC group interaction parameters (α_{ij})	24
Table M.3.1 The distance between the data corresponding to Figure M.3.2.1 in image space, morphological feature space and manifold space, bold figures indicate pairings with smallest distances when measured using pixels, raw features, and manifold coordinates	43
Table M.4.1 Characteristics of the realizations and input parameters in numerical simulations. Additional and changed input compared to Table M.1.4 is presented here.....	59
Table R.1.1. Measured changes in micelle size following NAPL solubilization in 1.0 % (wt.) Tween 80 solutions	68
Table R.1.2. Summary of ensemble statistics for PCE distribution metrics for highly heterogeneous glaciofluvial deposit.....	103
Table R.1.3. K-S Test Statistic for Cases 1 to 4 (Critical Value = 0.441, $\alpha = 0.05$). Values higher than the critical value at the given confidence level are highlighted.....	105
Table R.1.4. K-S Test Statistic for Cases 1, 2, 5, 6, 9, and 10 (Critical Value = 0.435, $\alpha = 0.05$).....	106
Table R.1.5. K-S Test Statistic for Cases 1, 2, 7, and 8 (Critical Value = 0.435, $\alpha = 0.05$).....	108
Table R.1.6. Dimensionless mean source zone metrics for highly and mildly heterogeneous aquifers.....	109
Table R.2.1. Reported partition coefficients for 1-pentanol, 1-hexanol and 2-octanol	116
Table R.2.2. Isotherm parameters for tracers at a TCE-DNAPL-water interface.....	118
Table R.2.3. Parameters related to column experiments and simulations	121
Table R.2.4. Relevant 2-D box parameters	125
Table R.2.5. Tracer test flow rates for mixed source zone experiments.....	130
Table R.2.6. Ratios of saturation estimates obtained with the analytical solution to those measured via light transmission. Bold values represent the experiment shown in Figure R.2.10	136

Table R.2.7. Comparison of saturation values obtained by fitting different sections of the recovery curves shown in Figure R.2.10	137
Table R.2.8. Important input parameters for modeling.....	151
Table R.2.9. Three different scenarios for injection and extraction flow rates.....	159
Table R.3.1. Conditions of the 3 different data sets generated for the machine algorithm implementation	164
Table R.3.2 (a). The hyper-parameters setting of standard procedure and integrated algorithm for data set-1	166
Table R.3.2 (b). The hyper-parameters setting of standard procedure and integrated algorithm for TP\MC model.....	166
Table R.3.3 (a): The Statistical Result of standard procedure, integrated algorithm and multi-task learning using data set-1	168
Table R.3.3 (b): The Statistical Result of standard procedure, integrated algorithm and multi-task learning using data set-2.....	168
Table R.3.3 (c): The Statistical Result of standard procedure, integrated algorithm and multi-task learning using data set-3.....	168
Table R.3.3 (d): The Statistical Result of standard procedure, integrated algorithm and multi-task learning using data set-4.....	168
Table R.3.3 (e): The Statistical Result of the standard procedure, integrated algorithm and multi-task learning using sparse data generated by the TP\MC model	168
Table R.3.4. The statistical result of multi-task manifold regression using SGS data set-4 and TP/MC sparse data.....	170
Table R.4.1. Coefficients and standard errors of the developed regression models	182
Table R.4.2. Parameters of the first aquifer cell experiment used for model verification	188
Table R.4.3. Parameters of the upscaled model used for simulation of PPTTs in heterogeneous domains	192
Table R.4.4. Mean squared errors for upscaled simulations	192
Table R.4.5. Estimated source zone parameters with PPTTS conducted in heterogeneous source zones; parameters are estimated using the upscaled model developed in this research and the local equilibrium model	199
Table R.4.6. Margin of error for the estimated parameters with rate-limited analysis	199

List of Acronyms

BTC	BreakThrough Curve
DNAPL	Dense Non-Aqueous Phase Liquid
FID	Flame Ionizaiton Detector
GC	Gas Chromatography
GTP	Ganglia-To-Pool
LLE	Liquid Liquid Equilibrium
MODFLOW	Modular three-dimensional finite-difference groundwater model
PCE	Tetrachloroethene
PF	Pool Fraction
PITT	Partitioning Interwell Tracer Tests
PPTT	Push-Pull Tracer Test
PV	Pore Volumes
SGS	Sequential Gaussian Simulation
SZA	Source Zone Architecture
TCE	Trichloroethene
TP/MC	Transition Probability- Markov Chain
UTCHEM 9.0	University of Texas Chemical Flooding Simulator
VALOR	Vertical and Lateral Organic Redistribution Simulator
3-D	Three dimensional
2-D	Two dimensional

Acknowledgements

Over the course of this research project, many faculty, staff, and students have contributed their time, energy and thought. This work was truly a collaborative endeavor and could not have been completed without the contributions of the following individuals: Dr Linda Abriola (Tufts U), Dr Kurt Pennell (Tufts U), Dr Andrew Ramsburg (Tufts U), Dr John Christ (US Air Force Academy), Dr Eric Miller (Tufts U), Dr Natalie Cápiro (Tufts U), Dr Rhiannon Ervin (Tufts U, now Geosyntec Consultants), Dr Ali Boroumand (Tufts U), Mr Tyler Marcet (Tufts U), Ms Tian Tang (Tufts U), Mr Richard Wheeler (US Air Force Academy), Mr David Pool (US Air Force Academy) and Ms Kate Wallace (US Air Force Academy).

Our sincere thanks is extended to the members of the SERDP Scientific Advisory Board for their knowledge, insights and energy that helped keep our outcome focused and made this work stronger. This project also benefited from interactions with investigators from another SERDP project that focused on source zone characterization: ER-1611 Practical Cost-Optimization of Characterization and Remediation Decisions at DNAPL Sites with Consideration of Prediction Uncertainty (Dr. Jack Parker, PI). The SERDP staff has supported us in countless ways, always responding in a professional and cheerful manner. Our very special thanks are extended to Andrea Leeson, Jeff Marqusee and the HGL support staff, without whose vision and support this work would never have taken place.

Abstract

a. Objectives: The overarching goal of this research is to develop and demonstrate a comprehensive approach for field characterization of DNAPL source zones which quantifies the key features that control plume response. Here the intent is to integrate targeted (local-scale) *in situ* tests with transect-based observations of downstream contaminant flux or concentration and information on subsurface geologic variability. To address its primary goal, the research encompasses the following specific objectives: (1) identification of the most information rich metrics for linking NAPL architecture to plume response; (2) development and refinement of *in situ* test methods and modeling tools that can be used to quantify identified metrics in targeted regions of the source zone; (3) integration of these metrics and tools with current machine learning characterization methods for an overall source zone assessment protocol; and (4) development of simplified models for prediction of plume response.

b. Technical approach: The research approach integrates batch, column and aquifer cell experiments with mathematical modeling and data processing tools to identify and quantify features of the DNAPL architecture controlling down gradient plume response.

c. Results: A comprehensive set of experiments and numerical simulations was undertaken to quantify important source zone metrics that control down gradient plume response and to create observation data for subsequent characterization modeling tool development. A large library of three dimensional (3D) field-scale DNAPL source zone scenarios was created to encompass a realistic range of release conditions and permeability distributions. Stochastic permeability fields were generated using two distinct models: sequential Gaussian simulation and Markov-chain transitional probability. Simulations confirmed the strong influence of source zone architecture (SZA) (e.g., pool fraction) on long-term dissolution behavior. Modeling results indicated that the DNAPL release rate, capillary pressure parameters, and the distribution of persistent low permeability layers were the most significant factors influencing DNAPL source zone metrics and down-gradient plume response. For highly heterogeneous permeability fields, results suggest that analyses must be conducted in 3D to provide reliable predictions. Heterogeneous source zone aquifer cell experiments confirmed the mathematical model results, demonstrating the strong influence of SZA on dissolution behavior. Experiments with discrete lenses, as well as with more realistic stochastic permeability fields modeled using Markov-Chain transitional probability theory, were observed to give rise to two-stage mass flux behavior, attributed to persistent pools. Comparisons between mathematical model predictions and laboratory measurements revealed the importance of considering measurement scale in defining local saturations and average source zone metrics. A consistent methodology was recommended and demonstrated to determine saturation distributions from aquifer cell light transmission data.

The second task of the project dealt with the estimation of local saturation and SZA metrics using partitioning tracer tests. This task was completed through the coupling of mathematical modeling with batch, column and aquifer cell experiments. Analytical models for push-pull tracer tests analysis typically assume linear equilibrium partitioning, a uniform NAPL saturation,

and a homogenous medium. The reasonableness of each of these assumptions was investigated. Application of equilibrium partitioning behavior failed to reproduce column experimental observations. A linear driving force model, however, was shown to provide excellent predictions. Diffusion limitations within the NAPL and surface accumulation at the NAPL interface were found negligible for realistic source zone conditions. Tracer test interpretation was also shown to be highly sensitive to the tracer water/NAPL partitioning coefficient, with application of common group contribution methods for partitioning coefficient estimation potentially leading to underestimation of NAPL saturations. Batch measurements for representative tracers demonstrated that partitioning behavior is nonlinear but may be approximated with a linear function below specified concentrations. Application of kinetic partitioning with the assumption of a uniform NAPL saturation was shown to provide a reasonable match to recovery curves obtained in heterogeneous 2-D aquifer cell experiments. An empirical approach was developed to interpret recovery curves, offering potential for identifying the distance to and the fraction of the vertical domain occupied by NAPL. Development and application of a coupled adjoint sensitivity method to the transport equations suggests the promise of this method for estimation of total DNAPL mass, average saturation, and distance of DNAPL from the push-pull well from concentration breakthrough observations.

In the third project task, machine learning methods were developed and used to successfully estimate SZA metrics (mass of pools, mass of ganglia, and pool fraction) from observations of plume concentrations in a down gradient transect. The library of source zone realizations created in task I was used to train and test the models. A fundamentally new machine learning processing method was developed employing ideas from manifold learning and embedding for estimating each metric individually. This approach was also extended using ideas from multi-task learning to determine the three metrics jointly based on enforcing a physical relationship among the three. Strong performance can be obtained both with densely sampled data as well as when a more limited sampling of transect concentration data are available, as is the case with typical laboratory experimental field applications.

In task four, an improved upscaled model was developed to predict flux averaged concentration evolution down gradient of DNAPL source zones. Inputs to the model include the initial pool fraction; the initial flux-averaged concentration; and the initial fraction of that flux eluting from pool zones. This enhanced model improved on the upscaled model developed under previous SERDP sponsorship by enabling the prediction of two-stage mass recovery behavior that may be observed in the field, especially at “aged” sites. An upscaled model was also developed and validated for application for the interpretation of two-well and push pull partitioning tracer tests. The model incorporates rate-limited partitioning through an effective mass transfer coefficient correlation that depends on four SZA parameters: the vertical spread of the DNAPL; the injection/extraction rate; pool fraction; and average DNAPL saturation. The application of the upscaled model was demonstrated for simulations of interwell and push pull tracer tests, producing accurate estimates of average NAPL saturation (DNAPL mass).

d. Benefits: The research described herein provides an improved understanding of the coupling of down gradient plume response to DNAPL architecture and highlights the importance of measurement scale and mass transfer limitations to source zone characterization. The suite of data processing techniques and upscaled models developed in this research offers site managers specific tools that can be employed for source zone characterization and remedy screening. These tools include methods for the design and evaluation of localized push pull partitioning tracer tests; machine learning techniques for the estimation of DNAPL source zone metrics from plume transect concentration observations; and simplified screening models that incorporate these metrics to predict plume evolution and persistence.

Objective

The overarching goal of this research is to develop and demonstrate a comprehensive approach for field characterization of DNAPL source zones which quantifies the key features that control plume response. Here the intent is to integrate targeted (local-scale) *in situ* tests with transect-based observations of downstream contaminant flux or concentration and information on subsurface geologic variability. To address its primary goal, the research encompasses the following specific objectives: (1) identification of the most information rich metrics for linking NAPL architecture to plume response; (2) development and refinement of *in situ* test methods and modeling tools that can be used to quantify identified metrics in targeted regions of the source zone; (3) integration of these metrics and tools with current machine learning characterization methods for an overall source zone assessment protocol; and (4) development of simplified models for prediction of plume response.

I. Background

Widespread use of chlorinated ethenes, such as trichloroethene (TCE) and tetrachloroethene (PCE), in dry cleaning and degreasing operations has led to groundwater contamination at thousands of industrial facilities and governmental installations. The majority of contaminant plumes at such sites emanate from aquifer regions containing dense nonaqueous phase liquid (DNAPL). DNAPL source zones, comprised of immobile ganglia and/or pools of free-product, can persist in the subsurface for decades or centuries, due to a combination of low aqueous-phase solubility and rate-limited dissolution. Although significant effort has been directed toward improving methods for recovering DNAPL from the subsurface, it is now generally accepted that no single technology will result in complete mass removal. Thus, recent research has focused on quantifying the benefits and limitations of partial mass removal.

Further advancement in the management of DNAPL source zones will require a fundamental and comprehensive understanding of the relationship between source zone mass distribution, mass depletion, and dissolved-phase plume response. A number of source zone features are thought to play an important role in the efficacy of source zone remediation and long-term plume behavior. In a recent National Research Council (NRC) study, these features were classified into four broad categories: (i) composition and presence of the NAPL, (ii) hydrogeology, (iii) source zone geometry and dissolution, and (iv) source zone biogeochemistry (NRC 2005). Multi-component NAPLs are common at field sites and can lead to preferential dissolution, resulting in both temporal and spatial changes of the dissolved-phase concentration signals evaluated during source zone characterization and assessment. Physical-chemical properties of the NAPL and subsurface heterogeneity have been shown to strongly impact the infiltration and final distribution of NAPLs within the subsurface (Mayer and Hassanizadeh 2005; Rathfelder et al. 2003; Totten et al. 2007). Experimental (e.g., Suchomel and Pennell (2006)) and numerical modeling studies have confirmed that even minor changes in subsurface characteristics (e.g., hydraulic conductivity distribution) can result in substantial changes to commonly employed metrics, such as the maximum organic saturation or the organic saturation spatial moments. Thus, NAPL properties, release characteristics and subsurface hydrogeology largely govern the resulting SZA (i.e., local scale DNAPL distribution) observed at field sites (Lemke et al. 2004a; Lemke et al. 2004b).

Previous studies have revealed that there is a strong link between SZA and down gradient plume response to partial mass removal. In a prior SERDP project (Abriola et al. 2008), we developed the ganglia-to-pool (GTP) ratio to describe the NAPL distribution within the source zone (Christ et al. 2005; Lemke and Abriola 2006), and later linked the GTP ratio to plume responses using upscaling methods (Christ et al. 2006). Experimental studies conducted in laboratory-scale aquifer cells containing a PCE-NAPL source zone demonstrated the strong relationship between reductions in mass discharge and the initial GTP ratio (Suchomel and Pennell 2006). For example, in ganglia-dominated source zones (GTP ratio > 1) greater than 70% NAPL mass

removal was required before reductions in plume concentrations were observed, while in pool-dominated systems (GTP ratio <1) the correlation between mass removal and mass discharge reduction approached a 1:1 relationship. While this metric has been demonstrated useful in the assessment and prediction of system behavior in simulated and laboratory experiments, no general guidance exists for its quantification in practice, nor is it clear that the GTP ratio is the most appropriate parameter for prediction of long term plume response to mass removal in the field. Thus, there is a clear need for systematic development and assessment of alternative metrics to quantify DNAPL architecture based upon field-observable parameters.

While a number of source zone characterization technologies are currently available, most require extensive sampling and produce data that are meaningful only on the scale of the measurement. For example, partitioning interwell tracer tests (PITTs) provide estimates of NAPL saturations which are average values over the flow path. Thus, a high spatial sampling density (both horizontal and vertical) is required to delineate the distribution of DNAPL within a source zone. Previous PITT studies have explored stochastic-based (James et al., 1997, 2000; Zhang and Graham, 2001) and streamline-based (Datta-Gupta et al., 2002, Jawitz et al., 2003) inverse modeling techniques to infer the SZA. However, applicability of these methods may ultimately be limited by the high cost of conducting high-resolution PITTs over the entire source zone. Furthermore, it is not clear that a distribution of volume averaged NAPL saturations will be meaningful in predicting long term plume response. Thus, the most critical knowledge gap that currently limits the advancement of source zone characterization is the need to develop detailed knowledge of DNAPL architecture.

Over the course of previous SERDP research (Project ER-1293), it became clear that features of a DNAPL distribution, such as GTP ratio, may be of greater importance for source zone remedy selection and analysis of technical feasibility and more easily estimated in practice than the precise spatial distribution of the DNAPL saturations. Thus, this research was designed to develop a comprehensive approach to field characterization of the key features of DNAPL source zones that control plume response. The research undertaken was designed to identify the most information rich metrics for characterizing DNAPL architecture and to develop test methods for metric quantification. The developed characterization protocol will integrate targeted (local-scale) *in situ* tests with transect-based observations of downstream contaminant flux or concentration and information on subsurface geologic variability. The research approach couples a matrix of batch, column, and aquifer cell experiments with mathematical modeling and processing tools to develop and quantify key architectural metrics. Results of the proposed research are also intended to advance understanding of plume response to SZA and alterations to architecture resulting from mass depletion.

II. Materials and Methods

The research plan is organized around four tasks: (I) Data generation for metric identification and protocol evaluation; (II) Refinement of in-source push-pull tests; (III) Processing methods for identification of source zone features; and (IV) Development of simplified modeling tools; Methods and materials employed for each task are described below.

II.1. Data Generation for Metric Identification and Protocol Evaluation

II.1.1. Introduction

While the ganglia-to-pool ratio (GTP) has been shown to be useful for estimating plume responses to source zone mass removal, it is not necessarily the most appropriate metric for source zone characterization. Therefore, one goal of this task was to develop additional quantifiable metrics, and to evaluate their utility and limitations through a combination of experimental and mathematical modeling studies. Research activities focused on the first three categories of source zone features described in the NRC (2005) study; (a) *NAPL composition*, (b) *subsurface lithology* (heterogeneity), and (c) *source zone geometry and dissolution*. Laboratory-scale aquifer cell experiments were coupled with multi-dimensional, multi-phase numerical modeling to identify and evaluate source zone attributes and corresponding metrics that govern down-gradient plume evolution. Also as part of this work, aquifer cell studies were conducted to develop a data base of realizations to demonstrate the effects of DNAPL SZA, specifically saturation distribution and NAPL composition, on down-gradient plume concentrations as a function of source depletion. Mass depletion was achieved through NAPL dissolution under natural gradient conditions and active source zone treatment using surfactant flushing, in which surfactants were selected to minimize changes in the source zone DNAPL architecture. Single-component (TCE or PCE) and mixed DNAPLs (TCE+PCE) were utilized in batch and aquifer cell experiments. The experimental data obtained from the aquifer cell studies were used to validate and refine numerical simulators, and results obtained from the aquifer cell studies and model simulations were used to provide data for the identification and evaluation of existing (e.g., GTP ratio) and other source zone metrics and modeling tools in Tasks III and IV.

II.1.2. Batch and Aquifer Cell Experiments

II.1.2.1. Introduction to Dissolution and Micellar Solubilization of Mixed NAPLs

When utilizing enhanced dissolution to achieve aquifer remediation, either as a standalone treatment technique or as a part of a treatment train, an understanding of the relationship between NAPL composition and dissolution is required to maximize the efficiency of remediation efforts. While most research related to surfactant enhanced source zone remediation has focused on the solubilization behavior of pure organic liquids (Diallo et al. 1994, Jafvert et al. 1994, Dwarakanath et al. 1999, Taylor et al. 2001), the NAPL present at contaminated sites often consists of a number of different components, including grease, stabilizing agents, fuels and various different solvents (Jackson and Dwarakanath 1999, McCray et al. 2000, Moran et al. 2007). Therefore, a detailed understanding of the contribution of each component in these

mixtures to solubilization behavior is required to accurately predict mass removal and plume response. Traditionally, estimates of mass removal resulting from enhanced solubility have assumed that micellar solubilization behaves in a manner similar to aqueous NAPL dissolution, where structurally similar compounds follow a Raoult's Law convention. This ideal behavior is based on the assumption that the equilibrium solubility ($C_{w,sol}$) of a NAPL constituent in water is equal to the product of mole fraction (x_i) of the constituent in the organic phase and the aqueous solubility ($C_{w,aq. sol}$) of the pure NAPL constituent; which can be written as $C_{w,sol} = C_{w,aq. sol} \times x_i$.

Although Raoult's law convention has been successfully used to describe the solubility of hydrophobic organic compounds in solutions of cyclic oligosaccharides, cyclodextrin (Carroll and Brusseau 2009), this may not be the case in micellar solutions. For example, Nagarajan et al. (1984) examined the solubility of benzene in aqueous solutions of sodium dodecyl sulfate (SDS) and cetyltrimethylammonium chloride (CTAC) in mixtures of benzene and hexane. The authors observed a synergistic effect on the solubility of hexane, where the molar solubilization ratio of hexane initially increased when small amounts of benzene were present in the organic phase. These results were verified by Chaiko et al. (1984), who measured the solubilization from mixtures of various aliphatic and aromatic hydrocarbons in a number of different surfactants. The selective solubilization behavior observed in both studies was attributed to the different locus of solubilization of the two components. The more polar benzene was hypothesized to partition within both the inner core and outer palisade layer of the micelle, increasing the hydrophobic region within the micelle, subsequently creating a larger microenvironment for the more non-polar compound, in this case the aliphatic hydrocarbons. Only a limited number of studies have investigated the micellar enhanced solubility of organic compounds relevant from an environmental restoration perspective, and these have mainly been limited to polyaromatic hydrocarbons, including naphthalene, phenanthrene, fluoranthene and pyrene (Prak and Pritchard 2002, Bernardez and Ghoshal 2004). The results from these studies were not as conclusive as those previously mentioned, and the solubilization behavior was found to be linear for certain combinations of PAHs, and not for others. More recent studies using ^1H nuclear magnetic resonance (NMR) spectroscopy suggest that the locus of solubilization is not restricted to the core of the micelle alone (Bernardez 2008). To investigate the solubility enhancement from mixtures of aromatic compounds, McCray et al. (2001) measured the micellar solubilization of toluene, ethylbenzene and butylbenzene in a biosurfactant (dirhamnolipid). The authors found that the more hydrophobic compounds were solubilized to a greater extent than predicted using a Raoult's Law convention, while the solubilities of more polar compounds were under-predicted. These results suggest that the more hydrophobic compounds have a greater affinity for uptake in the micelle core.

II.1.2.2. Batch Experiments

Due to the prevalence of multicomponent DNAPLs at contaminated sites, the objective of this study was to determine the solubilization behavior of TCE/PCE and decane/dodecane mixtures in surfactants that are commonly used for subsurface remediation. A series of batch experiments was completed to evaluate both the equilibrium aqueous dissolution and micellar solubilization

of mixed NAPLs over a range of mole fractions. The purpose of these experiments was to determine if micellar solubilization followed the Raoult's Law convention, where the solubility of individual NAPL constituents is equal to the mole fraction each constituent in the NAPL times the aqueous solubility of the pure constituent (Schwarzenbach et al. 2003). A summary of the organic liquid mixtures and surfactants evaluated in these experiments is provided in Table M.1.1.

Table M.1.1. Range of organic liquid phase compositions and surfactant concentrations used to evaluate the applicability of Raoult's law to describe micellar solubilization of multicomponent NAPLs

NAPL	Mole Fraction Range	Tween 80 Conc. (% wt.)	Aerosol MA [®] -80I Formulation
TCE + PCE	0-1.0	0-5	3% AMA-80I + 8% (wt.) 2-propanol + 6% (wt.) NaCl
Decane + Dodecane	0-1.0	0.5-5	NA
Decane + PCE	0.5	0-5	NA

All organic solvents and reagents (minimum ACS grade) were used as received. Trichloroethene (TCE), 2-propanol, decane, dodecane, calcium chloride (CaCl₂) dehydrate and sodium chloride (NaCl) were obtained from Fisher Scientific (Fairlawn, NJ). Tetrachloroethene (PCE) was purchased from Sigma Aldrich (St. Louis, MO). Polyoxyethylene (POE) (20) sorbitan monooleate (Tween 80) was purchased from Uniqema (Paterson NJ; Lot # 2398A). Tween 80 has an average molecular weight, critical micelle concentration (CMC) and hydrophile-lipophile balance (HLB) of 1310 g/mol, 35 mg/L and 15.0, respectively (Shiau et al. 1994). Sodium dihexyl sulfosuccinate (Aerosol MA-80I), which has an average molecular weight of 388 g/mol and a CMC 1200 mg/L (Dwarakanath et al. 1999), was used as received from Ctyec Inc. (Woodland Park, NJ; Lot # SU3121103). All aqueous solutions were prepared in deionized water purified via a Milli-Q Gradient A10, (Millipore Billerica, MA) with a resistivity of 18.0 MΩ·cm at 25°C.

Multi-component organic liquid mixtures were prepared gravimetrically at room temperature, and then used immediately to minimize changes in the organic phase mole fraction due to losses from volatilization. Aqueous solutions of Tween 80, containing 500 mg/L CaCl₂ as a background electrolyte, were prepared gravimetrically and mixed vigorously with a magnetic stir bar and plate until all surfactant was completely dissolved. An Aerosol MA[®]80I (AMA-80) solution

containing 6% (wt.) NaCl, 2.7% (wt.) AMA-80I and 8% (wt.) 2-propanol was prepared gravimetrically by combining 3.0 g AMA-80, 6 g NaCl and 8 g 2-propanol, after which the mixture was diluted to 1 L with DI water. The solution was then mixed vigorously until the surfactant was completely dissolved. All surfactant solutions were prepared immediately prior to use.

The specific methods used to prepare the batch reactors varied depending on whether the NAPL was more or less dense than water. For organic phases that were more dense than water (TCE+PCE, PCE+decane), batch reactors consisted of 35 mL borosilicate glass vials. To each vial, 20 mL of aqueous surfactant solution or 500 mg/L CaCl_2 solution was added, followed by 4 mL of either single- or multi-component organic liquid using a gas-tight syringe. The vials were then capped immediately and shaken gently on an oscillating shaker tray (Labquake Shaker; Barnstead Thermolyne, Dubuque, IA) for 48-72 hours in a constant temperature chamber maintained at $22 \pm 1^\circ\text{C}$. After equilibration, the contents of each batch reactor were separated into two distinct phases by centrifugation at $760 \times g$ for 30 minutes. To determine the dissolved concentration of the organic solutes, which included the amount dissolved in the aqueous solution plus the amount contained in micelles, triplicate aqueous phase samples (0.35 mL) were removed from each reactor and transferred to a 2-mL glass vial containing 1.45 mL of 2-propanol. The resulting solution was homogenous and could be directly analyzed using gas chromatographic (GC) methods (Pennell et al. 1997). For organic liquid phases that were less dense than the aqueous phase (i.e., decane, dodecane and their respective mixtures), batch reactors were prepared in 8 mL glass vials that were sealed with open top screw caps equipped with Teflon[®]-backed septa. To maintain the same organic liquid to aqueous solution ratio as the denser than water batch experiments, 1 mL of organic liquid and 4 mL of surfactant solution or DI water containing 500 mg/L CaCl_2 were added to each reactor vial. The vials were then mixed gently via end-over-end oscillation for a period of 72 hours on a Labquake shaker. The vials were then inverted for 24-48 hours to separate the organic liquid and aqueous phases. Triplicate aqueous phase samples (0.35 mL) were removed from the inverted vials using a gas-tight syringe and transferred to 2 mL glass vials containing 1.45 mL of 2-propanol. Additional aqueous phase samples (1 mL) were obtained from the batch reactors for subsequent quantification of micelle size.

Organic solute concentrations in both aqueous and micellar solutions were measured using a gas chromatograph equipped with an autosampler and flame ionization detector (GC-FID; Agilent 7890A, Santa Clara, CA). Sample aliquots (1 μL) were injected at an inlet split ratio of 20:1 and a temperature of 210°C . Chromatographic separation was accomplished using a DB-5 capillary column (30 m length \times $0.25\mu\text{m}$ film thickness \times $250\mu\text{m}$ inside diameter; Agilent Technologies, Santa Barbara, CA) that was maintained at a constant pressure of 14.5 psi with helium as the carrier gas. In order to avoid fouling of the column from the non-volatile surfactant components, a packed inlet trap was utilized, which consisted of 80-100 mesh Poropak Type P (Supelco; Bellefonte, PA). Analysis of the chlorinated hydrocarbons was completed isothermally at an oven temperature of 35°C . For the batch experiments measuring the solubility of hydrocarbon

mixtures and decane/PCE mixtures, separation was accomplished using the following oven temperature sequence; 55 °C for 4 min, increased to 210 °C at 20 °C/min, held for 1 min, and finally increased to 275°C at 50°C/min, resulting in a total run time of 15.0 min. Method detection limits, determined using the EPA Method (USEPA 2003), were 1.25, 0.9, 0.84 and 0.72 mg/L for PCE, TCE, decane and dodecane, respectively.

Further characterization of micellar solubilization was accomplished by measuring changes in surfactant micelle size before and after uptake of organic species in 10 g/L Tween 80 solutions. Micelle size was determined by dynamic light scattering (DLS) using a ZetaSizer Nano ZS analyzer (Malvern Instruments Ltd., Southborough, MA). The DLS was operated in non-invasive back scattering (NIBS®) mode at an angle of 173°. Prior to use, the DLS instrument was calibrated using a monodisperse suspension of polystyrene spheres (Nanosphere Size Standards, Duke Scientific, Palo Alto, CA) with a mean diameter of 97 ± 3 nm. Aqueous surfactant solutions were first contacted with the appropriate organic liquid for 48 hours, at which time a 1 mL aliquot was removed for DLS analysis at a wavelength of 532 nm and temperature of 22°C. Micelle size distribution measurements were also completed following equilibration with the multicomponent organic liquids. Prior to and after the equilibration period, triplicate samples (1 mL) obtained from each aqueous surfactant solution were analyzed by DLS.

II.1.2.3. Aquifer Cell Experiments

Previous studies of source zone mass removal and mass discharge behavior have focused on single component DNAPLs, even though a majority of contaminated field sites contain chlorinated solvent mixtures, additives and residual components from cleaning operations. In order to interpret plume response following subsurface remediation at mixed-DNAPL contaminated sites, it is necessary to understand the relationship between changes in aqueous phase contaminant discharge with transitioning SZA and NAPL composition. The first three aquifer cells (AC 1, 2, and 3) completed under this subtask aimed to examine the downgradient plume response from binary TCE- and PCE-DNAPL source zones as a function of NAPL composition, SZA and mass removal.

To address knowledge gaps related to the development of upscaled models and further explore the effects subsurface heterogeneity, the fourth (AC4) and fifth (AC5) aquifer cells completed under this subtask investigated mass removal and plume response from single component DNAPL (TCE) source zones. The main goal of these two aquifer cell studies was to provide more realistic heterogeneous DNAPL source zones which incorporated more complex permeability distributions, which improved model verification and calibration efforts.

Aquifer cell media were selected to create a range of source zone NAPL saturation distributions, which were expressed as ganglia-to-pool ratios (GTPs) and pool fractions (PFs):

Definitions:

- Ganglia is the presence of NAPL below or at the porous media specific residual saturation,
- Pools are the presence of NAPL in excess of the porous media specific residual saturation,
- Ganglia-to-pool ratio, GTP is the ratio of the source zone ganglia volume to pool volume,
- Pool-fraction, PF, is the ratio of pool volume to total DNAPL volume in the source zone.

These definitions will be used throughout this report.

Results of the aquifer cell experiments provided dissolution data that were used to (a) verify the machine learning algorithms developed under Task III and (b) evaluate the effect of scale and the predictive ability of simplified screening models to estimate the evolution of mass discharge from DNAPL source zones. A summary of the aquifer cell (AC) studies and the corresponding experimental conditions is provided in Table M.1.2.

Table M.1.2. Summary of aquifer cells and experimental conditions.

Experiment	Source Zone DNAPL	Flushing Scheme	Permeability Field	Initial SZA
AC1	1:1 TCE/PCE (mol/mol)	500 mg/L CaCl ₂ + two 1 PV surfactant	40/50 with F-70 lenses	Low PF
AC2	1:1 TCE/PCE (mol/mol)	500 mg/L CaCl ₂ + two 1 PV surfactant	20/30 with F-70 lenses	High PF
AC3	1:1 TCE/PCE (mol/mol)	500 mg/L CaCl ₂ + two 1 PV surfactant	40/50 with F-70 lenses	Low PF
AC4	neat TCE	500 mg/L CaCl ₂	40/50 with F-70 lenses	Low PF
AC5	neat TCE	500 mg/L CaCl ₂ + one 1 PV surfactant	Markov-Chain 12/20, 20/30, 40/50, F-95	High PF

All organic solvents and reagents used in the aquifer cell experiments were ACS grade or better, and were used as received. TCE, 2-propanol, sodium bromide and calcium chloride dehydrate were obtained from Fisher Scientific (Fairlawn, NJ). PCE, pentafluorobenzoic acid (PFBA) and sodium fluorescein were obtained from Sigma Aldrich (St. Louis, MO). Oil Red-O dye and erioglaucine were obtained from Alfa Aesar (Ward Hill, MA). Polyoxyethylene (POE) (20) sorbitan monooleate (Tween 80) was purchased from Uniqema (Paterson NJ; Lot # 2398A). All aqueous solutions were prepared in deionized water purified using a Milli-Q Gradient A10 (EMD Millipore Corp.; Billerica, MA) with a resistivity of 18.0 M Ω ·cm at 25°C. The water was degassed under constant vacuum pressure for a minimum of 12 hours to minimize the entrapment of air in the porous media. Multicomponent DNAPL solutions and surfactant solutions were prepared as described in Section II.1.2.2.

Aquifer cells 1 and 2 (AC1, AC2) were packed with two size fractions of Accusand (20-30 and 40-50 mesh) obtained from the Unimin Corp. (New Canaan, CT). These Accusands were selected as the background porous media for the aquifer cells based on their well characterized properties (Schroth et al. 1996), translucence, and demonstrated effectiveness in prior light transmission studies (Suchomel and Pennell, 2006; Bob et al. 2008). F-70 Ottawa sand (40-270 mesh) obtained from U.S. Silica Co. (Berkeley Springs, WV) was emplaced as low-permeability lenses throughout the higher permeability background matrix within the aquifer flow cells. The intrinsic permeability of F-70 Ottawa sand is approximately $8.2 \times 10^{-12} \text{ m}^2$, while 20-30 mesh Accusand and 40-50 mesh Accusand have intrinsic permeabilities of approximately $2.5 \times 10^{-10} \text{ m}^2$ and $7.3 \times 10^{-11} \text{ m}^2$, respectively (Schroth et al. 1996). AC 3- 5 were packed with Ottawa sands obtained from U.S. Silica as described in detail below (Table M.1.3).

Controlled release of DNAPL was performed in aquifer cells that were similar in design to those originally developed by Dr. Pennell's research group as part of SERDP project ER-1293. Briefly, the aquifer cells consisted of two one-half inch thick glass panels held in place by an aluminum frame with overall dimensions of 1.0 m length by 48 cm height with a 1.4 cm internal thickness (Figure M.1.1), and fully screened influent and effluent end chambers. Each aquifer cell was configured to contain a source zone region that was approximately 50 cm in length and a down-gradient plume region that was approximately 50 cm in length. The plume region contained twenty-five low volume glass sampling ports that were located within the front glass panel to monitor dissolved-phase plume concentrations over the course of each experiment. Following assembly, the aquifer cells were packed under water-saturated conditions in 3 cm lifts with moderate agitation and mixing to minimize stratification. In each aquifer cell a 3-cm thick layer of F-70 Ottawa sand was emplaced along the bottom of the aquifer to prevent DNAPL migration between the aluminum frame and glass. In addition, a layer of F-70 sand was placed above the needle injection point (12 cm long \times 6 cm height) to minimize backflow of the DNAPL during injection.

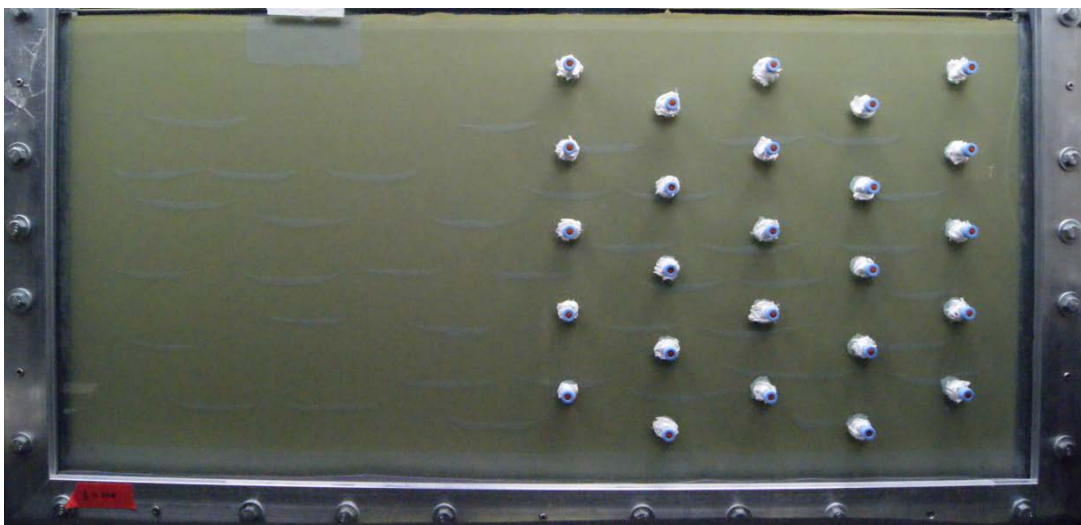


Figure M.1.1: Picture of aquifer cell 4 (AC 4) prior to TCE-DNAPL injection.

Aquifer cells 1-4 were packed with 40-50 mesh Ottawa sand as the background medium, with randomly located low-permeability lenses (F70 Ottawa sand) placed throughout the aquifer cell. The position and size of F-70 lens were determined using a stochastic based model that generated permeability distributions with 35 to 40 lenses, occupying approximately 6.5 % of the total aquifer cell volume (Figure M.1.1).

To evaluate the effects of subsurface heterogeneity on aqueous phase mass discharge, a fifth aquifer cell (AC 5) was packed based on a random permeability field generated by a transitional probability-Markov chain code using statistical parameters from the Tübingen Site (Maji 2005). This permeability distribution was intended to more closely mimic subsurface conditions at a well-characterized field site, and was also utilized to evaluate the efficacy of the machine learning algorithms to predict down-gradient mass discharge from SZA metrics (Task 4). Four different size fractions of silica sand (12-20; 20-30; 40-50 and 40-270 mesh) were utilized to create a two order-of-magnitude range in permeability (10^{-10} to 10^{-12} m²) throughout the source zone and down-gradient plume regions. Properties of the sands utilized in the aquifer cells are summarized in Table M.1.3. The permeability field for AC5 was generated using TPROGS (Carle 1999) using a grid spacing of 0.5 cm (H) by 2.5 cm (L), and selected based on the locations of the low permeability zones which are shown in Figure M.1.2. Due to clogging of the influent and effluent wells by the fines present in the F-95 sand, a 1-cm wide vertical layer of 40-50 mesh Ottawa sand was packed adjacent to both fully-screened influent and effluent well chambers.

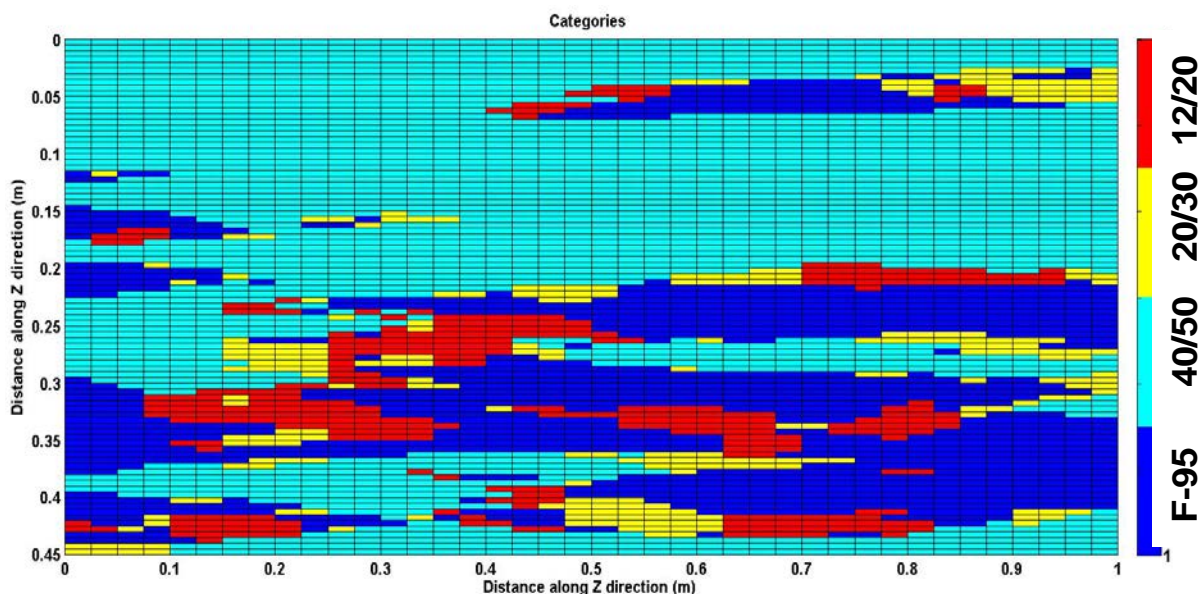


Figure M.1.2: Schematic diagram of aquifer cell (AC 5) permeability distribution.

Table M.1.3. Porous media characteristics of aquifer cell 5 (AC5)

Sand	Size Fraction	Permeability (m ²)
Filpro Silica Sand	12/20	5.1e-10
Ottawa Sand	20/30	2.5e-10
Ottawa Sand	40/50	7.3e-11
Ottawa Sand	F95	3e-12

Following the construction and packing of each aquifer cell, a constant head flow system was utilized to establish a hydraulic gradient of less than 2 cm across the length of the aquifer cell. Teflon tubing was used to deliver the background influent solution (500 mg/L CaCl₂ prepared in de-aired Milli-Q water) from a 5 or 12 L mariotte bottle equipped with an aspirator to the influent end chamber located on the left hand side of the cell. The insertion of 0.635 cm outside diameter glass tubing in the upper opening of the reservoir through a tight fitting rubber stopper provided a constant hydraulic head independent of the water volume in the vessel. The aqueous flow rate was controlled by adjusting the heights of the constant head influent reservoir and the effluent tubing discharge point. This experimental set-up allowed for the establishment of

constant flow rates of approximately 1 to 4 mL per minute for the duration of the aquifer cell experiment. In this configuration, the upper boundary of the aquifer cell was unconfined and the water table could rise and lower based on the height of water in the influent and effluent chambers.

After establishing steady flow in the aquifer cell, a non-reactive tracer test was completed by injecting a one-third pore volume (PV) pulse of 13.5 mM NaBr and 5 mg/L of a fluorescent dye (sodium fluorescein) through the fully screened influent chamber at a seepage velocity of either 0.6 (AC 4, to mimic natural gradient conditions) or 2.4 m/day (AC 1-3 and 5, to mimic surfactant flooding conditions). Flux-averaged effluent concentrations, localized port concentration measurements and digital images of the fluorescent dye illuminated with 450 nm Kino-Flo Blue bulbs were taken approximately every 30 minutes to quantify non-reactive tracer breakthrough and to visualize migration of the tracer front through the aquifer cell. Due to the high degree of heterogeneity present in AC5, additional tracer tests were completed to evaluate the influence of mobile and immobile zones of water on non-reactive tracer transport behavior. For these experiments, a suite of non-reactive tracers were employed, including a fluorescent dye (fluorescein), bromide and pentafluorobenzoic acid (PFBA). This enabled the evaluation of the overall flow properties of the aquifer cell and the influence of low permeability lenses on the storage and release of non-reactive solutes. The three tracers were selected to investigate the effects of (a) molecular size on diffusive mass transport within the lower permeability zones and (b) mass transfer between zones of mobile and immobile water (physical non-equilibrium) on solute transport behavior. Due to differences in molecular weight and structure, the aqueous diffusion coefficients for Br⁻, PFBA and fluorescein are 0.075, 0.03 and 0.02 cm²/hr, respectively (Nelson et al. 2003). Previous studies have shown that Br⁻, PFBA and fluorescein act conservatively at or above neutral pH and in the presence of low organic carbon silica sands (Hu and Brusseau 1995, Nelson et al. 2003). A separate set of one dimensional (1-D) column experiments was completed to confirm conservative behavior of the three tracers. Prior to addition of the tracer solution, the influent solution pH was monitored and adjusted to ca. 7.2 with 0.1 M NaOH. The tracer test was then completed by injecting 2.3 pore volumes (PV) of the mixed tracer solution, which contained ca. 550 mg/L Br, 100 mg/L PFBA and 5 mg/L fluorescein. A vertical transect of side-ports (63 cm from the injection well) was sampled to obtain local tracer concentrations in conjunction with visualization of the dye front and flux averaged effluent concentrations. Flow interruptions of 22 hours and 17.6 hours were conducted at 2.1 PV (i.e., during the tracer pulse injection) and 4.96 PV (i.e., during elution flushing), respectively, to investigate the influence of rate limited mass transfer of the tracers between the low permeability zones and more transmissive regions of AC5.

Following completion of flow characterization experiments, DNAPL was injected into each aquifer cell to simulate a subsurface spill. The DNAPL, which was dyed red with Oil-Red-O (4×10^{-4} M), was released into the source zone region through a 16 cm long, 18 gauge needle packed to a depth of approximately 10 cm below the sand surface. Approximately 40 mL of DNAPL was injected into each cell at a constant flow rate of 0.5 mL/min to 2.0 mL/min using a

Harvard Apparatus model 22 syringe pump to create both ganglia- and pool-dominated source zones, respectively. Following DNAPL injection, flow within the cell was interrupted and the DNAPL was allowed to redistribute for a 24 hour period before restarting flow. The initial DNAPL saturation distributions within the source zone region of the cells were quantified using a light transmission system (see below).

Following DNAPL release and characterization, a 500 mg/L CaCl_2 background solution was flushed continuously through the aquifer cell at a rate of 1 mL/minute, which yielded a residence time of approximately 1.5 days. To quantify spatial and temporal changes in flux-averaged and local dissolved-phase TCE concentrations, effluent and side-port were collected every 0.67 PVs (1 PV = 2200 mL). Light transmission analysis was performed every 5 PVs to monitor changes in SZA. These data were then utilized to evaluate the upscaled models developed in Task IV and the machine learning algorithms from Task III.

Following DNAPL release and an initial water flushing period, the aquifer cells were flushed with 1 to 1.5 PVs of an aqueous solution containing 4% Tween 80 to accelerate mass removal. Surfactant solutions were introduced at a seepage velocity of 2.4 m/day into the aquifer cells after steady-state concentrations were measured in the effluent. Flushing intervals varied in each aquifer cells as follows: after approximately 24 and 35 PVs in AC-1, after approximately 5 and 25 PV in AC-2, after approximately 15 and 45 PV in AC-3 and following 20 PV in AC-5. AC-4 did not utilize any micellar enhanced dissolution, and thus, mass removal was due to aqueous dissolution alone. Light transmission analysis was performed before and after each surfactant flush to evaluate the effect of aggressive mass removal on SZA, while effluent samples were collected continuously during the surfactant floods to determine total mass removed due to micellar enhanced solubilization. Following the introduction of the surfactant pulse, flow through the box was interrupted for 12 hours to maximize solubilization since dissolution during surfactant flooding has been observed to be a rate limited process (Pennell et al. 1994, Taylor et al. 2001). Side-port samples were also collected to evaluate plume development during the surfactant flushing. This surfactant flood was followed by an additional water flooding period, and then a final surfactant flood.

Aqueous TCE and PCE concentrations were analyzed by GC-FID as described in Section II.1.2.2 above. Bromide, chloride and PFBA were analyzed via ion chromatography on a Dionex ICS-2100 (Waltham, MA). Analyte separation was accomplished on an AS18 fast hydroxide ion selective column, with a mobile phase ionic strength of 23 mM. Due to the high organic content of the effluent samples during the surfactant pulses, bromide breakthrough in the aquifer cells was measured using a bromide ion-selective probe (Cole Parmer, Vernon Hills, IL) connected to an Accumet Model 50 pH/ion/conductivity meter (Fisher Scientific). To measure the spatial saturation of the DNAPL source zone, a light transmission system developed by Dr. Pennell's Lab for SERDP project ER-1293 was employed. The light transmission (LT) system was based on the original design of by Tidwell and Glass (1994), as adapted by Suchomel and Pennell (2006). A Sony α 550 digital camera was used to image the aquifer cell, which was illuminated with a Flathead 80 light bank (Kino Flo Inc., Burbank, CA). Local DNAPL saturations were

estimated by comparison of the digital image to previously generated hue-NAPL saturation calibration curves, which were developed using the experimental method of Darnault et al. (2001). Thickness-averaged saturation distributions were calculated on a per pixel basis ($\sim 0.3 \text{ mm} \times 0.3 \text{ mm}$) using MATLAB 2009B software (MathWorks, Inc. Waltham, MA), and summed over the entire source zone region to estimate the total volume of DNAPL present in the source zone. The DNAPL volumes obtained by LT analysis were within 5 % of values calculated from the DNAPL injection flow rate and duration. DNAPL saturations of less than or equal to 0.18 (40-50 mesh) or 0.11 (20-30 and 12-20 mesh) were considered to represent discrete ganglia, while DNAPL saturations that were greater than these value represented “pools”. Residual saturation values were obtained from Pennell et al. (1996) for the same size fractions of Ottawa sand, and confirmed using the intrinsic permeability-residual DNAPL saturation correlation developed by Powers et al. (1992) for various sand size fractions. The resulting DNAPL saturation distributions were expressed in terms of GTP ratio or PF.

II.1.3. Field-Scale Numerical Simulations

In addition to the experimental work, this task focused on the development of a 3-D field-scale simulation library. This library was designed to provide a variety of SZAs resulting from various spill and permeability scenarios and was used to identify source zone features controlling plume evolution evaluated in Task III. PCE-NAPL infiltration and entrapment was simulated with UTCHEM 9.0 using 16 realizations of a baseline permeability field representative of a relatively homogeneous glacial outwash deposit. Permeability field realizations were developed using Sequential Gaussian Simulation geostatistical methods (Lemke et al. 2004) conditioned to the Bachman, Michigan site (Abriola et al. 2005). Three spill scenarios were examined in each permeability realization (Table M.1.4), namely: a release consistent with a slow, persistent leak (400 day release); a release corresponding to a catastrophic release (4 day release); and a spill configuration with a 400-day release at two separate locations in the domain (see Christ et al. 2010). To explore the influence of hydraulic property heterogeneity, additional 400-day release scenarios were simulated using modified realizations of the baseline permeability field. Modifications to the permeability field included a smaller correlation length and higher variance (Table M.1.5). Taken together, these simulations provide a large library comprised of scenarios with different spill release history, spill configuration and heterogeneity of hydraulic properties.

Table M.1.4. Simulations with different spill scenarios

Parameter					
Fluid Properties		Water	PCE		
Density ρ_α (g/cm ³) ^a		0.999	1.625		
Dynamic Viscosity (cP) ^a		1.121	0.89		
Compressibility (Pa ⁻¹) ^a		4.4 x 10 ⁻¹⁰	0.0		
Aqueous Diffusivity (cm ² /s) ^b		-	8.6 x 10 ⁻⁶		
Aqueous Solubility (g/L) ^c		-	0.150		
Initial Saturation		1.0	0.0		
P_c-s_α-$k_{r\alpha}$ Model Parameters^a					
(Ref) Air Entry Pressure (kPa)		2.809			
Pore Size Index		2.0773			
Interfacial Tension					
Air/Water (dyn/cm)		72.75			
PCE/Water (dyn/cm)		47.8			
Irreducible Water Saturation		0.080			
Max Residual Organic Saturation (s_{nr}^{max})		0.151			
Reference Permeability (μm ²)		19.7			
Matrix Properties^a					
Variogram Parameters		Horizontal	Vertical		
Nugget		0.333	0.333		
Range (m)		7.0	1.07		
Integral Scale (m)		2.33	0.36		
Lognormal Transformed \overline{K} variance ($\sigma^2 \ln(K)$) ^a		0.29			
Mean Hydraulic Conductivity, \overline{K} (m/d) ^a		16.8			
Anisotropy Ratio k_v/k_h		0.5			
Applied Hydraulic Gradient, (m/m)		0.01			
Longitudinal Dispersivity, ω_m (m) ^a		0.30			
Horizontal Transverse Dispersivity, ω_p (m) ^d		0.10			
Vertical Transverse Dispersivity, ω_p (m) ^d		0.0075			
Median Grain Size, d_{50} (μm) ^a		295			
Uniformity Index, U_i ^a		1.86			
Uniform Porosity, ϕ ^a		0.36			
Δx (m) ($N_x = 26$)		0.3048			
Δy (m) ($N_y = 26$)		0.3048			
Δz (m) ($N_z = 128$)		0.0726			
Different Spill Scenarios		Case 1	Case 2	Case 3	Case 4
Spill Volume (L)		128	128	128	192
Spill Duration (d)		400	400	4	600
Release Rate (L/m ² -d)		0.32	0.32	32	0.32
Spill Location		Block center	2 blocks off-center	Block center	Block center

^a Lemke et al. [2004]; ^b Dekker and Abriola [2000b]; ^c Horvath [1982]; ^d EPA (1986)

Table M.1.5. Simulations with different permeability realizations

Parameter					
Fluid Properties		Water		PCE	
Density ρ_α (g/cm ³) ^a		0.999		1.625	
Dynamic Viscosity (cP) ^a		1.121		0.89	
Compressibility (Pa ⁻¹) ^a		4.4 x 10 ⁻¹⁰		0.0	
Aqueous Diffusivity (cm ² /s) ^b		-		8.6 x 10 ⁻⁶	
Aqueous Solubility (g/L) ^c		-		0.150	
Initial Saturation		1.0		0.0	
P_c-s_α-$k_{r\alpha}$ Model Parameters^a					
(Ref) Air Entry Pressure (kPa)		2.809			
Pore Size Index		2.0773			
Interfacial Tension					
Air/Water (dyn/cm)		72.75			
PCE/Water (dyn/cm)		47.8			
Irreducible Water Saturation		0.080			
Max Residual Organic Saturation (s_{nr}^{max})		0.151			
Reference Permeability (μm ²)		19.7			
Different Matrix Properties^a		Case 5		Case 6	
Variogram Parameters		Horizontal	Vertical	Horizontal	Vertical
Nugget		0.333	0.333	0.333	0.333
Range (m)		4.66	0.72	4.66	0.72
Integral Scale (m)		1.55	0.24	1.55	0.24
Lognormal Transformed \overline{K} variance ($\sigma^2 \ln(K)$) ^a		1.0		1.5	
Mean Hydraulic Conductivity, \overline{K} (m/d) ^a		16.8			
Anisotropy Ratio k_v/k_h		0.5			
Applied Hydraulic Gradient, (m/m)		0.01			
Longitudinal Dispersivity, ω_m (m) ^a		0.30			
Horizontal Transverse Dispersivity, ω_p (m) ^d		0.10			
Vertical Transverse Dispersivity, ω_p (m) ^d		0.0075			
Median Grain Size, d_{50} (μm) ^a		295			
Uniformity Index, U_i ^a		1.86			
Uniform Porosity, ϕ^a		0.36			
Δx (m) ($N_x = 26$)		0.3048			
Δy (m) ($N_y = 26$)		0.3048			
Δz (m) ($N_z = 128$)		0.0726			
Spill Scenario					
Spill Volume (L)		128			
Spill Duration (d)		400			
Release Rate (L/m ² -d)		0.32			
Spill Location		Block center			

^a Lemke et al. [2004]; ^b Dekker and Abriola [2000b]; ^c Horvath [1982]; ^d EPA (1986)

For each infiltration and entrapment simulation, DNAPL depletion (dissolution) and plume development was simulated using the modular three-dimensional transport simulator (MT3DMS) modified to simulate NAPL dissolution. In each simulation the concentration profile at down-gradient transects (middle or end section of the domain) was recorded at every 5 or 20 simulation time steps. Thus each dissolution simulation produced from 100 to 1000 time-dependent SZA-plume response signals for examination and interpretation in Task III.

In addition to the 6 cases outlined in tables M.1.4 and M.1.5, simulations with permeability fields based upon a highly heterogeneous glaciofluvial deposit (Herten site; Maji 2005) were performed to investigate the influence of: (i) the capillary pressure-saturation parameters; (ii) residual organic saturation; (iii) spill rate; (iv) hypothetical field structure; and (v) dimensionality on the DNAPL migration and entrapment architecture. Three-dimensional (3-D) permeability realizations were generated using a transition-probability-based Markov chain (TP/MC) approach. The glaciofluvial deposit permeability realizations were characterized by four dominant lithofacies with a high degree of continuity in the horizontal versus the vertical direction (Figure M.1.3). Further details on the permeability realizations can be found in Wang (2013).

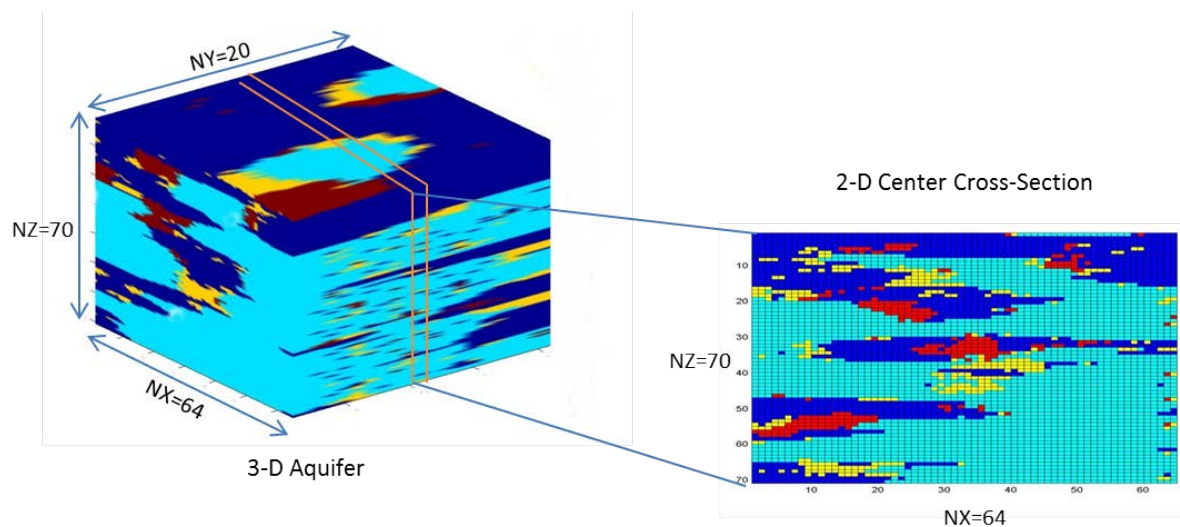


Figure M.1.3 Field Reconstruction—Conceptualization for Obtaining the 2-D Permeability Field.

Hypothetical tetrachloroethylene (PCE) spills were simulated in these scenarios using the Michigan-Vertical and Lateral Organic Redistribution (M-VALOR) simulator (see Table M.1.4 for numerical simulation input parameters) in two-dimensional (2-D) profiles extracted from the 3-D realizations (Figure M.1.3). Ten ensembles of different simulation cases were generated

based on variations of the base case (Table M.1.4), namely: two different sets of capillary pressure-saturation parameters, two sets of residual organic saturations, two hypothetical field structures, and three different spill rates. Each ensemble contained 20 permeability field realizations for a total of 200 SZA scenarios. The capillary pressure-saturation (Pc-sat) simulations investigated scenarios where Pc-sat parameters were assumed independent of (Haverkamp and Parlange (1986) Method) and dependent on soil permeability (Leverett (1941) scaling Method). In the first method, the entry pressure is assigned as a categorical variable based on the permeability, while in the later method the entry pressure scales with the permeability following the method of Leverett (1941). Organic residual saturations were assumed to be either uncorrelated or correlated to permeability values. Three different hypothetical spill scenarios were simulated for the ensembles, namely fast, medium, and slow DNAPL release rates. All simulations were quantified using commonly employed DNAPL distribution metrics (center of mass and spread along vertical and lateral directions; GTP and PF; and maximum organic saturation).

To investigate the influence of dimensionality on DNAPL migration, selected scenarios were simulated in 2D and 3D using UTCHEM 9.0. SZA metrics for the two scenarios (2D v. 3D) were compared to quantify the influence of dimensionality in these medium- and high heterogeneity scenarios. Further details on the simulation input parameters can be found in Wang (2013).

Finally, the experimental aquifer cell data were complemented by numerical simulations of these aquifer cell experiments. In these scenarios, M-VALOR was used to simulate the infiltration, entrapment, and dissolution of TCE in two-dimensional aquifer cells. Capillary pressure-saturation (Pc-sat) properties were obtained from Schroth et al. (1996). In both the experimental and simulated scenarios, the soil matrix properties were generated according to the transition probability-based Markov Chain permeability distribution, representative of highly heterogeneous glaciofluvial deposits (see previous description). To generate an ensemble of permeability field realizations for these numerical simulations, the base case permeability field (aquifer cell) was discretized into 41x91 grid nodes with grid dimensions of 0.025x0.005m. This unconditional categorical simulation was then sampled using a set of 22 randomly located points. These points, representing ~0.5% of the discretized area, were then sampled to generate new realizations. This level of categorical sampling has previously been shown to be sufficient for successful aquifer reconstruction (Maji 2005). Simulated TCE saturation distributions were compared visually to the experimentally obtained saturation distribution and quantified using the upscaling approaches developed by Christ et al. (2012) as part of this research.

To evaluate factors controlling plume evolution of DNAPL source zones in the statistically homogeneous, heterogeneous, and highly heterogeneous permeability fields, numerical simulation results were quantified using traditional statistics (NAPL saturation mean and variance), spatial architecture metrics (first and second moment in x , y -, and z -directions), and novel SZA metrics (GTP ratio and PF). Statistical analyses were performed to obtain the mean and variance of various source zone configuration metrics for each simulation ensemble in the

library. These ensemble statistics were then used for application and refinement of the machine learning algorithms in Task III.

II.2. Refinement of In-Source Push-Pull Tests

II.2.1. Introduction

Although soil coring and direct push sampling techniques are the most common methods for DNAPL mass delineation (Costanza and Davis, 2000; Guilbeault et al., 2005; Kram et al., 2001; Meinardus et al., 2002; NRC, 2005), partitioning tracer tests offer an alternative approach to characterization. Partitioning interwell tracer tests (PITT) can be employed to characterize large volumes of the subsurface by estimating spatially averaged saturations (Annable et al., 1998a,b; Brooks et al., 2002; Jin et al., 1995). The spatial resolution of a DNAPL saturation estimate from a PITT is directly related to the distance (i.e., the volume swept) between the two observation points. Such overall NAPL saturations are essentially estimates of total NAPL mass, and do not quantify NAPL architecture. To employ the PITT technology to estimate the spatial distribution of NAPL saturation would require acquisition of high-density temporal tracer concentration data at numerous locations within the source zone (James et al., 1997). The combination of additional wells and chemical analyses may make PITTs cost prohibitive at many sites. The single well or Push-Pull Tracer Test (PPTT) is an alternative to the Interwell test. This test is conducted in a much smaller domain and so provides averaged data over a local zone around the test well (Huang et al., 2010; Istok et al., 2002). Tomoch et al. (1973) used PPTTs in the oil industry to estimate the residual oil saturation in the field. Since then PPTTs have been used in environmental engineering to estimate a variety of different properties including: longitudinal dispersivity (Gelhar and Collins, 1971), effective porosity (Hall et al., 1991), solute sorption (e.g., Cassiani et al., 2005), the rate of solute degradation (e.g., Haggerty et al. 2004, Schroth and Istok, 2006), NAPL saturation (e.g., Davis et al., 2005; Istok et al., 2002), and the rate of mass transfer into zones of immobile water (Haggerty et al., 2001).

PITT data analysis typically relies upon the assumption of linear equilibrium partitioning of the solutes serving as the tracer, despite evidence suggesting the partitioning may be nonlinear (Wise 1999, Wise et al. 1999) and kinetic (Willson et al., 2000; Imhoff and Pirestani, 2004; Moreno-Barbero and Illangasekare, 2006). Jawitz et al. (2003) suggest that problems relating to nonlinearity may be overcome by careful selection of solutes and solute concentrations, since in the dilute range, many tracers display near linear partitioning behavior (Rao et al., 2000). Although such selection can justify the use of particular solutes, the partition coefficients employed in the analysis of PITT breakthrough curves are frequently based upon insufficient data, i.e. on measurements at a single aqueous phase concentration or on estimation routines (Dwarakanath and Pope, 1998). Rigorous determination of the partitioning behavior over a range of dilute concentrations are few; a fact which may help explain discrepancies between PITT estimates and actual NAPL saturations in the SERDP-sponsored, blind test conducted at the Dover National Test Site (Brooks et al., 2002).

Mass transfer limitations, due to diffusion controlled partitioning with high NAPL saturation zones (Willson et al., 2000), may also help explain the discrepancies in the blind PTTT test conducted by Brooks et al. (2002). PITT interpretation approaches commonly assume local equilibrium and complete hydraulic accessibility of the DNAPL (Annable et al., 1998a; Willson et al., 2000). It is recognized, however, that spatial variability of aquifer properties or DNAPL distributions, will promote non-uniform flow fields that can lead to nonequilibrium conditions (see, for example, Brooks et al., 2002; Imhoff and Pirestani, 2004; Jalbert et al., 2003; Meinardus et al., 2002; Moreno-Barbero and Illangasekare, 2005; Willson et al., 2000). Flow field heterogeneity can also result in hydraulic isolation of DNAPL and underestimation of contaminant mass during tracer tests (Moreno-Barbero and Illangasekare, 2006; Rao et al., 2000). In addition, diffusive transport (within immobile aqueous phase and DNAPL zones) and adsorption at the DNAPL–aqueous interface could influence tracer transport, and consequently decrease the accuracy of DNAPL saturation estimates (e.g., Zhu et al., 2009).

The above discussion points to the need for a comprehensive investigation of mass transfer processes at both the local and upscaled levels. It is the hypothesis of this research that an improved understanding of mass transfer limitations may be employed to develop improved models for the design and interpretation of PITTs. Thus, the objective of this task is to develop a PPTT that yields quantitative information about NAPL saturation and architecture at discrete depth intervals. While the information gained from these PPTTs is localized, we anticipate that a limited number of these tests will provide sufficient data to refine the SZA metric estimates derived from transect data processing methods (see Task III).

The research plan for this task consists of a series of batch and column experiments and coupled modeling investigations designed to assess the equilibrium phase behavior and mass transfer characteristics of a suite of candidate tracers. Subsequent aquifer cell experiments are then used to develop a modified PPTT methodology and to evaluate its performance for the characterization of features of nonuniform distributions of DNAPL.

II.2.2. Batch, Column, and Aquifer Cell Experiments

II.2.2.1. Materials and Analytical Methods

Three representative alcohol tracers, 1-pentanol (99%), 1-hexanol (98%), and 2-octanol (97%), were selected based upon use in previous tracer tests (e.g. Brooks et al., 2002; Hartog et al., 2010; Jalbert et al., 2003; Jin et al., 1997; Moreno-Barbero et al., 2007; Ramsburg et al., 2005; Willson et al., 2000). Trichloroethene (TCE) (ACS grade) was employed as a representative DNAPL, and 2-propanol (IPA) (HPLC grade), which is miscible with water, was used as a solvent in preparing samples for analysis. All chemicals were obtained from Sigma Aldrich and used as received. Relevant properties of 1-pentanol, 1-hexanol, 2-octanol and TCE are presented in Table M.2.1. All aqueous solutions were made using water purified to have resistivity > 18.1 MΩ*cm and TOC < 10 ppb using a MilliQ A-10 system (Millipore).

Table M.2.1. Physical properties of alcohol tracers and TCE

Alcohol	$K_p^{C_i}$ ($L_{aq}/L_{TCE-DNAPL}$)	Density (g/mL)	Solubility, in aq. (mg/L)	Solubility, aq. in (mg/L)	Purity %
1-pentanol	3.8 ^{a,f}	0.815 ^{b,d}	2.19%w ^{b,d}	7.46%w ^{b,d}	99
1-hexanol	18.6 ^{a,f}	0.820 ^{a,d}	0.706%w ^{a,d}	7.42%w ^{a,d}	98
2-octanol	317 ^{a,f}	0.82 ^{a,d}	0.127 ^{a,d}	3.40%w ^{a,d}	97
trichloroethene	-	1.45 ^{b,c}	0.098 ^{a,e}	0.032 ^{b,d}	ACS grade

^a20 °C; ^b25 °C; ^ctemperature was not reported; ^dRiddick and Bunger (1970); ^eHorvath et al. (1999); ^fDwarakanath and Pope, 1998

For transport experiments (1-D column and 2-D box), TCE-DNAPL was dyed with 10^{-4} M Oil-Red-O (Alfa Aesar) for the purpose of visualization. Previous research has shown that the addition of Oil-Red-O at this concentration does not significantly affect the relevant physical properties of the DNAPL (Taylor et al., 2001), nor the partitioning behavior of the tracers (Willson et al., 2000).

Federal Fine Ottawa sand (30-140 mesh) was obtained from U.S. Silica and used as the background packing media for all column and aquifer cell experiments. Federal fine is quartz sand comprised of 99.7% Silicon Dioxide (U.S. Silica) and has an intrinsic permeability of $4.2 \times 10^{-11} \text{ m}^2$ (Suchomel et al., 2007). Federal Fine Ottawa sand was either used as received or sieved to obtain specific size fractions (e.g., 40-50, 45-50). F-70 sand (intrinsic permeability of $8.2 \times 10^{-12} \text{ m}^2$, Suchomel et al., 2007) was obtained from U.S.Silica and used as the low permeability material in aquifer cell experiments.

Alcohol and TCE concentrations were quantified using a Hewlett-Packard 6890 Gas Chromatograph (GC) equipped with a DB-5 (0.32 mm diameter, 30 m long) column and flame ionization detector. A five-point calibration curve was obtained each day of use and checked using a calibration standard every 20 samples. The detection limit for each 1-pentanol, 1-hexanol, and 2-octanol is 1 mg/L. The detection limit for TCE is 5 mg/L. Bromide and chloride concentrations were quantified using a Dionex ICS-2000 Ion Chromatograph (IC) equipped with an AS-18 column (4 x 250 mm) and operated isocratically at 23.0 mM potassium hydroxide. Water contents were quantified using a Mettler Toledo DL38 Karl Fischer Titrator. Prior to each day of use the titrator was calibrated with an AquaStar 1% water standard. Calibration was checked with the water standard every ten samples. Phase densities were quantified using 2 mL glass pycnometers calibrated with water prior to each day of use. Equilibrium interfacial tensions (IFT)

between the aqueous and organic phases were quantified via drop shape analysis (IT Concept Tracker).

II.2.2.2. Experimental Set Up

Liquid-liquid equilibrium (LLE) experiments permit accurate quantification of the partitioning over all possible alcohol concentrations while also allowing assessment of interfacial tension between the aqueous phase and the DNAPL. Initial overall compositions (comprising various amounts of water, tracer and TCE) were created in triplicate within 35 mL borosilicated glass centrifuge tubes (Corning, part number: 8422-35) with PFTE lined screw-cap closures (Kimble Chase part number 45066C). Tubes were subsequently equilibrated for 72 hr on oscillating shakers (LabQuake, model T415110) located within a controlled temperature room (Harris Environmental) operating at $22.0 \pm 0.1^\circ\text{C}$. Previous experiments suggest 72 hr is sufficient for these types of systems to reach equilibrium (Gossett, 1987; Ramsburg and Pennell, 2002). After equilibration, the tubes were centrifuged at 1500 rpm and 22°C for 10 min (Beckman Coulter Avanti J-25) prior to careful separation and sampling (see analytical methods below) of the aqueous phase and DNAPL.

1-D transport experiments were conducted in Kontes borosilicate glass columns (4.8 cm i.d.) following methods described in Ervin et al. (2011). The 45-50 mesh Ottawa Sand (see Section II.2.2.1) was selected to generate TCE-DNAPL ganglia (dyed with Oil-Red-O) that exist primarily as singlets (Schnaar and Brusseau, 2005; Ramsburg et al., 2011). Conservative, nonreactive tracer tests were conducted pre and post TCE-DNAPL emplacement to estimate dispersivity and confirm the uniformity of the emplaced DNAPL distribution (Ervin et al. 2011). Partitioning tracer tests were conducted using 2 PV pulses introduced at the same flow rate. For non-equilibrium column studies, a fast flow rate (2.2 mL/min) and a packed length (5.0 cm) were selected to promote the observation of non-equilibrium conditions so that partitioning kinetics could be quantified. In columns where multiple tracer pulses were introduced to the system, they were conducted successively, ensuring that no concentration from the previous pulse was detected in the effluent before the next pulse began. Effluent samples were collected over short intervals through the peak of the BTC and over increasingly longer intervals as the test continued using a fraction collector (Retriever II, ISCO). Dissolution of the TCE-DNAPL was prevented by using Milli-Q water saturated with TCE for all aqueous solutions introduced to the column. This experimental procedure ensured that each BTC was associated with the same saturation of TCE-DNAPL.

2-D transport experiments were performed employing two sizes of aquifer cells (60 cm length x 40 height x 1.5 cm thickness & 100 cm length x 50 cm height x 1.5 cm thickness). Sampling ports were installed in the front to permit measurement of local tracer concentrations. Different experiments employed different arrays of these port sampling locations (see Section III.2). Both ends of the aquifer cell have fully screened end chambers through which flow was established. Ottawa Federal Fine (30-140 mesh) sand is used as the background porous media and F-70 is used to create all low permeability layers. Aquifer cells were packed and TCE-DNAPL released, as described in Suchomel et al. (2007). The DNAPL saturation distribution in each box was

assessed using a light transmission (LT) system based upon the methods described in Suchomel and Pennell (2006). Quantification of DNAPL saturation is based upon image hues that are correlated to saturation with calibration curves developed using the method of Darnault et al. (1998). This method produces a pixel-by-pixel estimation of thickness-averaged saturation. Saturation, however, is an REV based property of the phase. Recent work by Christ et al. (2012) has demonstrated that the pixel-by-pixel estimates of saturation must be upscaled to better represent the physical definition of saturation. Following the guidance of Christ et al. (2012) thickness averaged saturation distributions were estimated over a 0.98 cm x 0.98 cm averaging window using Matlab 10.0 (Mathworks, Inc.). (This is compared to a pixel size of 0.02 cm x 0.02 cm). Two types of averaging were applied: i) discrete block averaging, which uses averaging windows that do not overlap; ii) continuous averaging, which uses overlapping averaging windows. For these experiments, a unit volume of porous media was defined as pooled if the TCE-DNAPL saturation is greater than 17%, which was selected based upon residual saturations observed in our column experiments.

The phase behavior of each alcohol in the water-alcohol-TCE ternary was predicted using an isothermal flash calculation performed in Matlab version R2009b. UNIFAC (Fredenslund et al., 1975) was employed to estimate activity coefficients using available structural parameters (Hansen et al., 1991). Greater detail on this model can be found in Ervin et al. (2011). Interaction parameters used for each group are shown in Table M.2.2. Iteration convergence was established when successive changes to molar phase fractions and component mole fractions were less than 1×10^{-10} .

Table M.2.2. UNIFAC group interaction parameters (α_{ij})

α_{ij}	group 1 C-C	group 2 C=C	group 5 -OH	group 7 H ₂ O	group 37 Cl-C=C
group 1 C-C	0 ^a	74.54 ^b	644.6 ^b	1300 ^b	-0.505 ^c
group 2 C=C	292.3 ^b	0 ^a	724.4 ^b	785.6 ^d	237.3 ^c
group 5 -OH	328.2 ^b	470.7 ^b	0 ^a	353.5 ^c	253.9 ^c
group 7 H ₂ O	342.4 ^b	-26.52 ^d	-229.1 ^c	0 ^a	651.9 ^d
group 37 Cl-C=C	41.90 ^c	-3.167 ^c	640.9 ^c	1100 ^d	0 ^a

^a by definition; ^b Magnussen et al. (1981); ^c Gmehling et al. (1982); ^d Cooling et al. (1992)

II.2.3. Push-Pull Tracer Test Model Development

II.2.3.1. Partitioning Tracer Model

A number of conceptual approaches for interphase partitioning behavior, including equilibrium, linear driving force, dual diffusion and surface resistance, were implemented in a numerical simulator to explore the mechanisms controlling tracer transport in systems of entrapped ganglia (i.e., in our column experiments). All of these models assume that transport occurs only in the aqueous phase, with an immobile TCE-DNAPL, distributed uniformly as spherical singlets. This assumption is supported by visualization of DNAPL distributions within similar size fractions of sandy media (e.g., Schnaar and Brusseau, 2005). Within the model, TCE-DNAPL dissolution is assumed negligible and the flow is uniform, consistent with the experimental methods employed. Based upon the above assumptions, flow and mass balance equations for the two fluid phases (aqueous and DNAPL) need not be explicitly written.

The governing equation for 1-D tracer mass transport is a simplified version of the multiphase advective-dispersive-reactive transport equation, where tracer interaction occurs only with the DNAPL:

$$nS_n \frac{\partial C_n}{\partial t} + nS_{aq} \frac{\partial C_{aq}}{\partial t} = nS_{aq} (\alpha|v| + D_{aq}) \frac{\partial^2 C_{aq}}{\partial x^2} - nS_{aq} v \frac{\partial C_{aq}}{\partial x} \quad (\text{M.2.1})$$

Here C_{aq} is the bulk phase aqueous concentration [$\text{M}\cdot\text{L}^{-3}$], C_n is average concentration of the tracer contained within the DNAPL [$\text{M}\cdot\text{L}^{-3}$], and v is the pore water velocity [$\text{L}\cdot\text{T}^{-1}$]. α , D_{aq} , S_{aq} , S_n , and n are the dispersivity [L], solute diffusivity in the aqueous phase [$\text{L}^2\cdot\text{T}^{-1}$], aqueous saturation [-], DNAPL saturation [-], and porosity [-], respectively, which are assumed to be temporally and spatially invariant.

The alternative conceptual modeling approaches employed here for tracer partitioning vary in the way the source/sink term $nS_n \frac{\partial C_n}{\partial t}$ is represented. These models differ in their assumptions pertaining to transport within the DNAPL (completely mixed versus diffusive transport) and descriptions of solute exchange between the DNAPL and aqueous phase (equilibrium, linear driving force kinetics, and surface resistance). Detailed presentations of these models are available elsewhere (e.g., Brusseau and Rao, 1989; Liggieri et al., 1997). What follows below are brief descriptions of how each approach was implemented for one dimensional alcohol transport in a medium containing entrapped TCE-DNAPL. Irrespective of the alternative approaches adopted to represent the sink/source term, all models employed third and second type boundary conditions for the column inlet and outlet, respectively. Equations were discretized using a Crank-Nicholson finite difference approach and solved numerically.

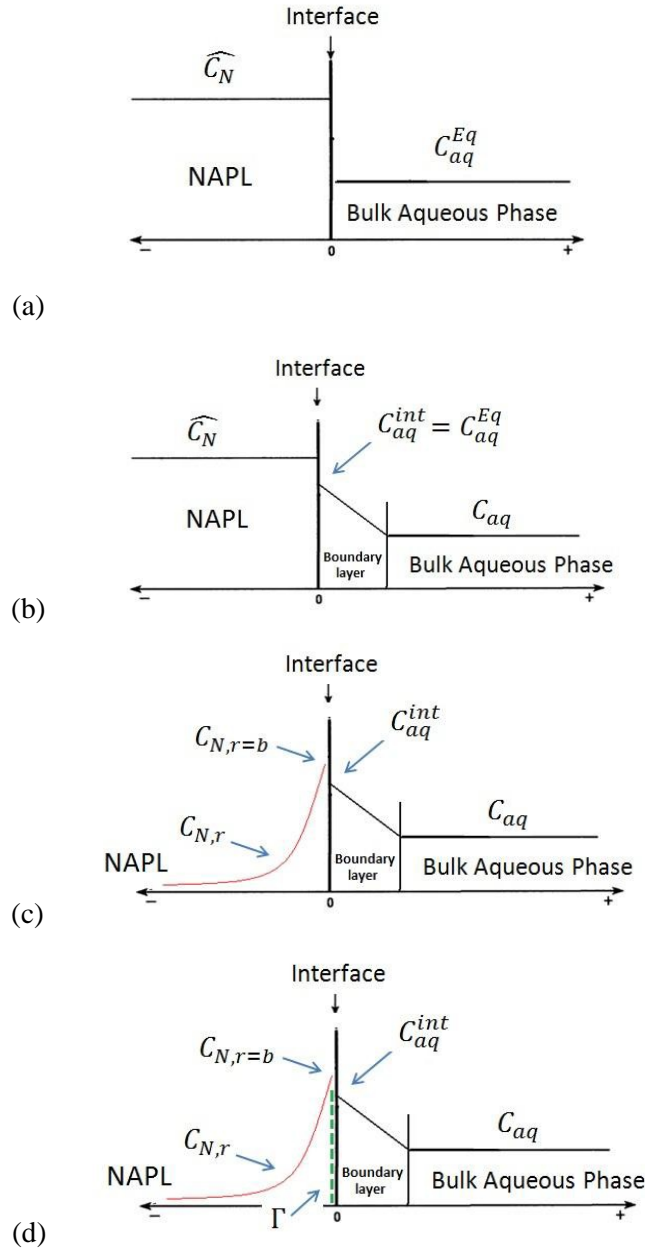


Figure M.2.1. Spatial variation of concentration at NAPL-aqueous interface for (a) local equilibrium assumption, (b) linear driving force model based on a film boundary layer (c) dual diffusion model, and (d) dual diffusion plus surface partitioning model; figure adapted and modified from Abriola and Bradford (1998).

Equilibrium

Here it is assumed that the flow rate is sufficiently slow such that the DNAPL and aqueous concentrations reach equilibrium at the grid resolution scale of the model. Defining $K_p^{C_i}$ as the concentration-based equilibrium partitioning coefficient (Ramsburg et al., 2010) of the tracer between the DNAPL and aqueous phases, yields:

$$nS_n \frac{\partial C_n}{\partial t} = nS_n K_p^{C_i} \frac{\partial C_{aq}}{\partial t} \quad (\text{M.2.2})$$

Linear Driving Force

The linear driving force approach assumes that diffusion across an immobile aqueous phase boundary layer can be represented by a first order mass transfer expression. Intra-DNAPL diffusional resistance is ignored, and distribution of components inside the DNAPL is assumed uniform. Component concentrations at the interface of the boundary layer and the DNAPL are assumed to be in equilibrium, while a linear concentration gradient exists within the stagnant aqueous film surrounding each DNAPL droplet. The source/sink term becomes:

$$nS_n \frac{\partial C_n}{\partial t} = \hat{k} \left(C_{aq} - \frac{C_n}{K_p^{C_i}} \right) \quad (\text{M.2.3})$$

Here \hat{k} is a lumped mass transfer coefficient [T^{-1}]. For the model results presented herein, the lumped mass transfer coefficient was evaluated using an empirical correlation developed for NAPL dissolution (Powers et al., 1992). Ramsburg et al. (2011) have recently shown that the Powers et al. (1992) and Imhoff et al. (1994) correlations are capable of, and offer similar performance when, describing the mass transfer of chlorinated solvent degradation products within columns containing uniform saturations of DNAPL.

Dual Diffusion

In this approach, as with the linear driving force model, interphase mass transfer occurs through an immobile aqueous boundary layer surrounding DNAPL ganglia. Thus, Equation 3.3 remains valid for the source/sink term. The assumption that the DNAPL is well mixed is, however, relaxed. Diffusion within the NAPL is assumed to be Fickian and the radial distribution of tracer concentration within the NAPL droplets satisfies (Rasmuson and Neretnieks, 1980):

$$\frac{\partial C_{n,r}}{\partial t} = D_n \left(\frac{\partial^2 C_{n,r}}{\partial r^2} + \frac{2}{r} \frac{\partial C_{n,r}}{\partial r} \right) \quad (\text{M.2.4})$$

subject to the following boundary conditions:

$$D_n \frac{\partial C_{n,r=b}}{\partial r} = k_f \left(C_{aq} - \frac{C_{n,r=b}}{K_p^{C_i}} \right) \quad (\text{M.2.5})$$

$$\frac{\partial C_{n,r=0}}{\partial r} = 0 \quad (\text{M.2.6})$$

Here $C_{n,r}$ is the component concentration within the DNAPL [$\text{M}\cdot\text{L}^{-3}$] at radial position, r [L], D_n is solute diffusion coefficient in the DNAPL [$\text{L}^2\cdot\text{T}^{-1}$], b is radius of the DNAPL droplet [L], and k_f is the mass transfer coefficient [$\text{L}\cdot\text{T}^{-1}$]. Equation M.2.5 (continuity of fluxes) assumes no surface accumulation at the DNAPL-aqueous interface.

Previous studies have measured the average singlet radius of entrapped NAPL for various sand fractions (Powers et al., 1992; Schnaar and Brusseau, 2005). Schnaar and Brusseau (2005) and Ramsburg et al. (2011) developed regressions that relate an effective DNAPL drop radius to the saturation and textural characteristics of the granular medium. The correlation of Ramsburg et al. (2011) is employed herein to estimate ganglia size. To convert from k_f to \hat{k} , the model assumes that all of the DNAPL surface area is accessible to the tracer, and that this surface area can be calculated assuming a uniform distribution of spherical droplets:

$$\hat{k} = k_f \left(\frac{3nS_{aq}}{b} \right) \quad (\text{M.2.7})$$

An existing numerical model (Mendoza-Sanchez and Cunningham, 2007) was adapted to simultaneously solve the system of Equations. Equation M.2.5 serves to couple the aqueous phase and DNAPL transport equations at the interface. The solution was validated against an existing semi-analytical solution (Rasmuson and Neretnieks, 1980). Accuracy of the dual diffusion algorithm was verified through comparisons with linear driving force solutions for an extreme (high) DNAPL diffusion coefficient.

Dual Diffusion and Surface Partitioning

A key assumption in both the linear driving force and dual diffusion conceptual models is that mass fluxes toward and away from the DNAPL/aqueous interface are equal, such that no surface accumulation occurs. In a surface partitioning model, tracer accumulation at the interface is permitted, adding a third resistance to tracer mass transport. The approach employed herein is based largely on the work of Liggieri et al. (1997), who studied adsorption kinetics of

alkylphosphines oxides at a water/hexane interface. A mass balance equation within the interface is expressed as:

$$\frac{\partial \Gamma}{\partial t} = k_f (C_{aq} - C_{int}) - D_n \frac{\partial C_{n,r=b}}{\partial r} \quad (\text{M.2.8})$$

where Γ is the accumulation of mass at the interface [$\text{M} \cdot \text{L}^{-2}$]. In this formulation, Equation M.2.8 replaces Equation M.2.5. The left hand side of Equation M.2.8 is rewritten as $\frac{\partial \Gamma}{\partial C_{int}} \frac{\partial C_{int}}{\partial t}$ and a local equilibrium assumption is invoked at the interface, with Γ represented by a Langmuir isotherm expression. Using this approach, the maximum capacity at the interface between the aqueous phase and DNAPL is not reached until C_n becomes equal to the effective solubility of tracer in the DNAPL ($K_p^{C_i} C_{aq}$). The system of equations is solved iteratively. At the start of each time step, the known isotherm parameters and the C_{int} from the previous time step are used to estimate the accumulation term coefficient $\left(\frac{\partial \Gamma}{\partial C_{int}} \right)$. The system of equations is then solved for new interface concentrations, which are compared with the original values (Ervin et al., 2011). Iterations are performed until the convergence criterion (0.001 mg/m^2) is reached and all equations are satisfied.

II.2.3.2. Fine-Scale 3D Simulator

Based upon the partitioning tracer formulation presented above, a three dimensional, fine-scale simulator was developed to model PPTTs at in heterogeneous media. The simulator was used for 2D and 3D simulations for the interpretation of laboratory experiments and for the development of an upscaled field model (see task IV).

The simulator consists of two modules for solving flow and mass transport equations, respectively. The flow module is a slightly modified version of MODFLOW (Harbaugh 2005), which solves the equation:

$$\frac{\partial}{\partial x} \left(K_x \frac{\partial \varphi}{\partial x} \right) + \frac{\partial}{\partial y} \left(K_y \frac{\partial \varphi}{\partial y} \right) + \frac{\partial}{\partial z} \left(K_z \frac{\partial \varphi}{\partial z} \right) = S_s \frac{\partial \varphi}{\partial t} - G \quad (\text{M.2.9})$$

where φ [L] is the hydraulic head, K_x, K_y , and K_z [$L \cdot T^{-1}$] are the hydraulic conductivities in the three principal coordinate directions, S_s is the specific storage of the aquifer, and G [T^{-1}] is the injection/extraction term. During a PPTT, the tracer solution is injected after the flow reaches a steady state condition. Therefore the flow is transient only for a short period of time between the push and pull phases. Given that this transient period is short in comparison to the duration of the other test phases, in the model applications a steady flow condition was assumed for each phase.

A relative permeability function k_{rw} (Kaluarachchi and Parker, 1992) was incorporated in the model to account for the reduction in permeability due to the presence of the organic phase:

$$K_{x_i} = \frac{k_{rw} k_{x_i} \rho}{\mu} \quad (\text{M.2.10})$$

where

$$k_{rw} = S_{aq}^{0.5} \left(1 - (1 - S_{aq}^{1/m})^m \right)^2 \quad (\text{M.2.11})$$

and

$$m = 1 - \frac{1}{n_{vg}} \quad (\text{M.2.12})$$

Here S_{aq} is the aqueous phase saturation, n_{vg} is the Van Genuchten parameter that represents the uniformity of the pore size distribution, and k_{x_i} is the intrinsic permeability in x_i direction.

The permeability and NAPL saturation distributions used in the simulations of the PPTTs were adopted from the NAPL realizations produced under Task I. These permeability fields are heterogeneous and anisotropic.

Tracer transport was simulated with the linear driving force model formulation presented in Section II.2.3.1. The complete 3D discretization of governing equations and the developed finite-difference solution may be found in Bouromand (2013).

II.2.3.3. Tracer Push-Pull Sensitivity and Inverse Modeling

Using the three dimensional, fine-scale simulator as a foundation, additional modeling work was undertaken to explore the sensitivity of PPTT observations to SZA. To this end a numerical algorithm was developed which implements a coupled adjoint sensitivity method to explore the sensitivity of well observations of tracer concentration breakthrough to perturbations of the DNAPL saturation within the interrogated zone. The developed adjoint method introduces a vector of adjoint variables to formulate the coupled adjoint state equations for tracer concentrations in both the aqueous and DNAPL phases. This approach differs from previous studies in the environmental literature that have primarily focused on one control equation for flow or transport in saturated regimes (e.g. Michalak and Kitanidis, 2004). The results of this investigation have utility for local source zone characterization and can provide a quantitative understanding of the sensitivity of tracer concentration to the spatial variation in saturation. The developed adjoint state method also facilitates the analysis of sensitivity to other system states and parameters. After obtaining the sensitivity matrix of tracer concentrations to DNAPL saturation, coupled with the observed tracer concentrations at different time steps during the pull

phase, we can back estimate the characteristics of DNAPL saturation. In this estimation process, three specific metrics were considered: distance of DNAPL from the well, estimated total mass of DNAPL, and estimated average DNAPL saturation.

For the PPTT, the general control equations for contaminant transport are given as:

$$nS_{aq} \frac{\partial C_{aq}}{\partial t} + \hat{k}(C_{aq} - \frac{C_n}{K_{eq}}) = \nabla \cdot [nS_{aq}(D_{hij} \nabla C_{aq})] - \nabla \cdot (nS_{aq} v C_{aq}) + q_s C_l \quad (M.2.13)$$

$$\frac{\partial C_n}{\partial t} = \frac{\hat{k}}{nS_n} (C_{aq} - \frac{C_n}{K_{eq}}) \quad (M.2.14)$$

$$\text{Subject to boundary: } [-nS_{aq}(D_{hij} \nabla C_{aq})] \cdot \vec{n} = 0 \quad (M.2.15)$$

$$\text{and initial conditions: } C_{aq}(x, y, z, 0) = 0 \quad C_n(x, y, z, 0) = 0 \quad (M.2.16)$$

The first equation accounts for mass transport in the aqueous phase, and the second equation describes the mass balance in the DNAPL phase, assuming a linear driving force mass transfer model. Here we adopt a second type boundary condition, which indicates that there is no diffusive flux at the boundaries.

The goal of the adjoint sensitivity methodology is to investigate the sensitivity of a performance measure to the local perturbations in the DNAPL saturation. Here the performance measure P is defined as:

$$P = \iint_{V,t} h(S_{aq}, C_{aq}) dV dt \quad (M.2.17)$$

where $h(S_{aq}, C_{aq})$ is a functional of the state of the system, V is the spatial domain, and the integration is over the entire time and space domain. The marginal sensitivity of this performance measure with respect to the parameter S_{aq} is obtained by differentiating equation (M.2.17):

$$\frac{dP}{dS_{aq}} = \iint_{V,t} (\frac{\partial h}{\partial S_{aq}} + \frac{\partial h}{\partial C_{aq}} \frac{\partial C_{aq}}{\partial S_{aq}}) dV dt = \iint_{V,t} (\frac{\partial h}{\partial S_{aq}} + \frac{\partial h}{\partial C_{aq}} \Phi_1) dV dt \quad (M.2.18)$$

where dP/dS_{aq} is the marginal sensitivity of interest. Φ_1 is one of the two state sensitivities, $\Phi_1 = \partial C_{aq} / \partial S_{aq}$, it is a measure of the change in system state C_{aq} due to a small change in the parameter S_{aq} . We also define $\Phi_2 = \partial C_n / \partial S_{aq}$ as the other state sensitivity, which represents the change in system state C_n due to a small change in the parameter S_{aq} . Since these two state

sensitivities are unknown, adjoint theory can be used to eliminate them from the previous equation. Thus, the marginal sensitivity can be calculated in terms of the adjoint states.

Differentiating the governing equations for the PPTT (including initial and boundary conditions) with respect to the parameter S_{aq} (Neupauer and Wilson, 1999, 2001), we can obtain the governing equations in terms of the state sensitivities:

$$nS_{aq} \frac{\partial \Phi_1}{\partial t} + \frac{\partial \hat{k}}{\partial S_{aq}} (C_{aq} - \frac{C_n}{K_{eq}}) + \hat{k}(\Phi_1 - \frac{\Phi_2}{K_{eq}}) - \frac{\partial(q_s C_l)}{\partial S_{aq}} + n \frac{\partial C_{aq}}{\partial t} - \nabla \cdot (nD_{hij} \nabla C_{aq} + nS_{aq} D_{hij} \nabla \Phi_1) + \nabla \cdot (nvC_{aq} + nS_{aq} v\Phi_1) = 0 \quad (M.2.19)$$

$$-nS_n \frac{\partial \Phi_2}{\partial t} + n \frac{\partial C_n}{\partial t} + \frac{\partial \hat{k}}{\partial S_{aq}} (C_{aq} - \frac{C_n}{K_{eq}}) + \hat{k}(\Phi_1 - \frac{\Phi_2}{K_{eq}}) = 0 \quad (M.2.20)$$

$$[(nD_{hij}) \nabla C_{aq} + nS_{aq} D_{hij} \nabla \Phi_1] \cdot \vec{n} = 0 \quad (M.2.21)$$

$$\Phi_1(x, y, z, 0) = 0 \quad \Phi_2(x, y, z, 0) = 0 \quad (M.2.22)$$

To simplify the problem, here we assume that the dispersion tensor, seepage velocity, and source and sink flow rates do not depend on the aqueous phase saturation at the time of interest. We take the inner product of each term in equations (M.2.19) and (M.2.20) with the adjoint states Ψ_1 and Ψ_2 respectively, which, at this stage, are just arbitrary functions. Integrating over time and space, we then add these equations to the right-hand side of equation (M.2.18). Since the right-hand sides of (M.2.19) and (M.2.20) are equal to zero, the addition of their products to (M.2.18) does not change the value of it. The resulting equation is given by:

$$\begin{aligned} \frac{dP}{dS_{aq}} = & \iint_{V,t} \left[\frac{\partial h}{\partial S_{aq}} + \frac{\partial h}{\partial C_{aq}} \Phi_1 \right. \\ & + \Psi_1 (nS_{aq} + \rho_b K_d) \frac{\partial \Phi_1}{\partial t} + \Psi_1 n \frac{\partial C_{aq}}{\partial t} - \Psi_2 n S_n \frac{\partial \Phi_2}{\partial t} + \Psi_2 n \frac{\partial C_n}{\partial t} \\ & + \Psi_1 \hat{k}(\Phi_1 - \frac{\Phi_2}{K_{eq}}) + \Psi_1 \frac{\partial \hat{k}}{\partial S_{aq}} (C_{aq} - \frac{C_n}{K_{eq}}) + \Psi_2 \hat{k}(\Phi_1 - \frac{\Phi_2}{K_{eq}}) + \Psi_2 \frac{\partial \hat{k}}{\partial S_{aq}} (C_{aq} - \frac{C_n}{K_{eq}}) \\ & - \Psi_1 (nD_{hij} \nabla C_{aq} + nS_{aq} D_{hij} \nabla \Phi_1) \\ & \left. + \Psi_1 \nabla \cdot (nvC_{aq} + nS_{aq} v\Phi_1) \right] dVdt \end{aligned} \quad (M.2.23)$$

Because the adjoint states are not defined at this stage, we can prescribe their properties in a manner that achieves our goal of eliminating Φ_1 and Φ_2 from equation (M.2.23). We integrate equation (M.2.23) by parts twice, apply Gauss's divergence theorem to the spatial divergence

terms and temporal divergence over the time period, substitute the initial and boundary conditions on state sensitivities of Φ_1 and Φ_2 , and obtain the governing equations for the adjoint states as:

$$nS_{aq} \frac{\partial \Psi_1}{\partial \tau} + \hat{k}(\Psi_1 + \Psi_2) - \nabla \cdot (nS_{aq} D_{hij}^T \nabla \Psi_1) - (nS_{aq} v) \cdot \nabla \Psi_1 + \frac{\partial h}{\partial C_{aq}} = 0 \quad (M.2.24)$$

$$nS_n \frac{\partial \Psi_2}{\partial \tau} + \frac{\hat{k}}{K_{eq}}(\Psi_1 + \Psi_2) = 0 \quad (M.2.25)$$

$$[nS_{aq} D_{hij}^T \nabla \Psi_1 + nS_{aq} v \Psi_1] \cdot \vec{n} = 0 \quad (M.2.26)$$

$$\Psi_1(x, y, z, t_f) = 0 \quad \Psi_2(x, y, z, t_f) = 0 \quad (M.2.27)$$

Here $\tau = t_f - t$ is defined as backward time, and t_f is the final time of simulation. Comparison with the governing equations, reveals that the adjoint state equations have a similar form, but the signs of the first-derivative terms are reversed. In addition, the adjoints of the Dirichlet boundary condition remains unchanged; however, the Neumann boundary condition becomes a Cauchy boundary condition. After simplification, the marginal sensitivity of the performance measure becomes:

$$\begin{aligned} \frac{dP}{dS_{aq}} = \iiint_{V,t} [n\Psi_1 \frac{\partial C_{aq}}{\partial t} + n\Psi_2 \frac{\partial C_n}{\partial t} + \frac{\partial \hat{k}}{\partial S_{aq}}(\Psi_1 + \Psi_2)(C_{aq} - \frac{C_n}{K_{eq}}) \\ + \nabla \Psi_1 \cdot (nD_{hij} \nabla C_{aq}) + \Psi_1 \nabla \cdot (nvC_{aq})] dV dt \end{aligned} \quad (M.2.28)$$

In this problem scenario, the performance measure is the aqueous phase tracer concentration at observed at a particular time in the push-pull well:

$$h(S_{aq}, C_{aq}) = C(\mathbf{x}, \tau) \delta(\mathbf{x} - \mathbf{x}') \delta(\tau - \tau') \quad (M.2.29)$$

where $\delta(\cdot)$ denotes the Dirac delta function, \mathbf{x} is defined in three spatial directions, \mathbf{x}' is the location of push-pull well, and τ' is the certain time of interest.

The application of the adjoint method was then explored using three-dimensional hypothetical source zones containing heterogeneous DNAPL distributions. Two-dimensional uniform planar flow was assumed within a horizontal layer around the well, and non-equilibrium interphase mass transfer was described by an empirical correlation (Nambi and Powers, 2003) within each grid block, based upon its broader range of validity for organic phase saturations:

$$\text{Sh}^* = \frac{\hat{k} d_{50}^2}{D_a} = 37.2 \text{Re}'^{0.61} S_n^{1.24} \quad (\text{M.2.30})$$

Here Re' is the modified Reynolds number; in which the mean grain size, d_{50} , describes the length scale and the seepage velocity, v , represents the velocity component.

We first calculated tracer concentrations in the push-pull well at different time steps using the previous developed three-dimensional fine scale push-pull model. After that, the derived control equations of adjoint states were solved corresponding to the time steps. Coupled with the tracer concentrations and adjoint states, the marginal sensitivity can be solved using equation M.2.28 to obtain sensitivity matrix of tracer concentration with respect to perturbation of DNAPL saturation.

2.7.2.2 Geostatistical Inverse Method

Model calibration involves adjustment of the model structure and model parameters of a simulation model so as to make the input-output relation of the model fit any observed excitation-response relation of the real system. In contrast to the forward problem, the inverse problem seeks to find the unknown parameters when continuous or discrete observations are given. After obtaining the sensitivity matrix of tracer concentration to DNAPL saturation, coupled with the observed tracer concentrations at different time steps during the pull phase, we can back estimate the characteristics of DNAPL saturation. In this project, three specific metrics are considered: distance of DNAPL from the well location, estimated total mass of DNAPL, and estimated average DNAPL saturation.

Consider a physical system, with the corresponding observation system, the true system state will be smeared by observation error. When the physical system is simulated by a model M , model error or model structure error is introduced. Furthermore, if a model parameter is parameterized by a finite-dimensional parameter vector, a parameterization error is generated. Therefore, there is always a total error of the observed system state based on the real physical system.

In our case, the goal of the inverse problem is to estimate the DNAPL saturation from observations of tracer concentrations in the push-pull well at different time steps. The best estimation of the unknown parameters is the solution of the optimization problem, which is to find a local minimizer to minimize the L_2 norm of the total error, in other words, to minimize the least squares cost function:

$$F(x) = \frac{1}{2} \sum_{i=1}^m (f_i(x))^2 = \frac{1}{2} \sum_{i=1}^m (C_{aqi}(\mathbf{x}') - C_{aqi}^{obs}(\mathbf{x}'))^2 \quad (\text{M.2.31})$$

where $C_{aqi}^{obs}(\mathbf{x}')$ denotes the observations of tracer aqueous phase concentration in the push-pull well, and $C_{aqi}(\mathbf{x}')$ is implicitly a function of C_{aq} through equations (M.2.13) to (M.2.16),

$f = C_{aqi}(\mathbf{x}') - C_{aqi}^{obs}(\mathbf{x}')$, which represents the difference between the observed tracer concentration and the calculated tracer concentration through the push-pull model. This optimization problem is also called the generalized output least squares problems.

Least squares problems can be solved by various numerical methods. Methods based on gradient information, such as the steepest descent method, requires the functional derivative of the cost function with respect to the parameter S_{aq} . For non-linear least squares problems, the Gauss-Newton method and Levenberg-Marquardt method are two efficient methods, which are based on implemented first derivatives of the components of the vector function. We focused on these two approaches for solving non-linear least squares problems, and subsequently, we indicate how the adjoint sensitivity method can be used, coupled with the least squares methods, to obtain sensitivity information and then back estimate the DNAPL saturation.

In the case of DNAPL saturation estimation, the numerical method of optimization generally consists of three steps:

- (1) Choose an initial guess of DNAPL saturation distribution;
- (2) Design a way to generate a search sequence: $S_{aq_1}, S_{aq_2}, \dots, S_{aq_n}, \dots$ such that $F(S_{aq_{n+1}}) < F(S_{aq_n})$ for all n .
- (3) Stipulate a convergence criterion. If it is satisfied, then end the search procedure, and a local minimum is approximately achieved. Such sequence has the following general form:

$$S_{aq_{n+1}} = S_{aq_n} + \lambda_n d_n \quad (\text{M.2.32})$$

where vector d_n is called displacement direction, λ_n is a step size along this direction.

Stopping Criteria

There are several stopping criteria used to test the convergence of an iteration sequence.

- (1) The norm of displacement becomes very small after n iterations:

$$\|S_{aq_n} - S_{aq_{n-1}}\| < \varepsilon_1 \quad (\text{M.2.33})$$

- (2) The norm of gradient $\nabla F(S_{aq_n})$ becomes very small after n iterations:

$$\|\nabla F(S_{aq_n})\| < \varepsilon_2 \quad (\text{M.2.34})$$

- (3) The value of the objective function $F(S_{aq_n})$ has no significant change after n iterations:

$$|F(S_{aq_n}) - F(S_{aq_{n-1}})| < \varepsilon_3 \quad (\text{M.2.35})$$

- (4) As in all iterative processes, we need a safeguard against an infinite loop: $n \geq n_{\max}$.

Here, $\|\cdot\|$ is the L_2 norm defined in the observation space, and $\varepsilon_1, \varepsilon_2$ and ε_3 are given small positive numbers. Once one of the stopping criteria is met, the iteration progress will be ended.

Gauss-Newton Method

The Gauss-Newton method is based on a linear approximation to the components of function f in the neighborhood of parameter x . In the case of the push-pull tracer test, with small perturbation of aqueous phase saturation, we have:

$$C_{aq}(S_{aq} + h) = C_{aq}(S_{aq}) + J(S_{aq})h \quad J(S_{aq}) \in \mathbb{R}^{1 \times n} \quad (M.2.36)$$

where $(J(S_{aq}))_{ij} = (\partial(C_{aqi}(x') - C_{aqi}^{obs}(x')) / \partial S_{aqj})$ is the *Jacobian*.

We also define $J(S_{aq}) = WH(S_{aq})$, where W is a diagonal matrix with elements of weighting coefficients. In theory, the optimal weighting coefficients are related to the standard deviations of errors. In addition,

$$(H(S_{aq}))_{ij} = \frac{\partial C_{aqi}(x')}{\partial S_{aqj}} \quad (M.2.37)$$

The matrix of H is called the sensitivity matrix, which represents the sensitivity of model output of tracer aqueous phase concentration with respect model parameters of aqueous phase saturation. Considering the first order derivative and second order derivative of $F(x)$ with respect to aqueous phase concentration, we can get the Gauss-Newton direction:

$$\Delta S_{aq_n} = -(J_n^T J_n)^{-1} J_n^T f \quad (M.2.38)$$

Then the estimated aqueous phase saturation can be iterated by the Gauss-Newton step:

$$S_{aq_{n+1}} = S_{aq_n} - (J_n^T J_n)^{-1} J_n^T f \quad (M.2.39)$$

The iteration sequence generated is also known as the Gauss-Newton sequence.

Levenberg-Marquardt Method

Levenberg and Marquardt suggested a damped Gauss-Newton method. In this case, the Gauss-Newton direction is replaced by:

$$\Delta S_{aq_n} = -(J_n^T J_n + \lambda I)^{-1} J_n^T f \quad (M.2.40)$$

$$S_{aq_{n+1}} = S_{aq_n} - (J_n^T J_n + \lambda I)^{-1} J_n^T f \quad (M.2.41)$$

where I is the unit matrix, and λ is a coefficient called damping parameter. When $\lambda=0$, ΔS_{aq_n} reduces to the Gauss-Newton direction. On the other hand, when λ tends to infinity, ΔS_{aq_n} turns

to the steepest descent direction and the size of ΔS_{aq_n} tends to zero. Therefore, $F(S_{aq_{n+1}}) < F(S_{aq_n})$ can always be expected by increasing the value of λ . Thus, the damping parameter influences both the direction and the size of the step, and this leads us to make a method without a specific line search.

II.3. Processing Methods for Identification of Source Zone Features

II.3.1. Introduction

The problem of concern for Task III is the determination of a number of source zone DNAPL mass distribution metrics from observations of down-gradient DNAPL concentration data. In this project, we have focused on three specific metrics:

1. Pool fraction (f_p), defined as the fraction of source zone mass incorporated in pools.

Previously we have demonstrated the utility of ganglia to pool ratio (GTP) as a metric for predicting plume behavior in up-scaled model. Unfortunately, because GTP can assume values from zero to infinity, we have found it difficult to stably estimate from down-gradient concentration data. Pool fraction on the other hand is bounded between zero and one and has proven easier to estimate. Moreover, f_p is easily related to GTP as

$$f_p = (1 + GTP)^{-1}.$$

2. The mass of DNAPL in the source zone occupied by pools (M_p), and
3. The mass of DNAPL in the source zone occupied by ganglia (M_g).

Determination of these metrics is complicated by the fact that our uncertainty regarding the subsurface encompasses more than merely the distribution of contaminant. Most notably, the hydraulic conductivity is also typically not known with high precision. In practice, one possesses only soft information concerning the statistics of this important quantity. Given the availability of high quality computational models for flow and transport in the subsurface pioneered by our team, we are motivated to consider the use of machine learning methods for metric determination (Mitchell, 1997, Ma et al., 2010). In more detail, given a statistical model of the conductivity along with numerical models for both DNAPL entrapment and subsequent flow and transport, the idea here is to simulate a large number of conductivity fields, spill scenarios, and observations of down-gradient concentration from which one can then infer (or “learn”) a mapping from concentration to the metrics of interest. At this point it is important to make a distinction between the data that are used to learn this mapping, also known as *training data*, and *test data* that not associated with the learning process but are used to determine the accuracy of the algorithm. In our work, both the training and test data are drawn from simulations. In practice, however, the test data would come from observations taken in the field. Additionally,

we note that while the training process can be quite computationally intensive, it is performed entirely off-line. The test procedure, that is, the processing of real data, is quite efficient (Bishop 2006).

As illustrated in Figure M.3.1, the work is based on the use of observations of contaminant concentration collected down-gradient from the source zone at a single point in time. While in practice, such transects are constructed from a small number of wells, we initially assume here that a dense collection of data are acquired resulting in the availability of a concentration “image” for processing. Though admittedly an idealization, this assumption allows us to more readily develop and demonstrate the utility of an initial set of machine learning tools to address the rather challenging problem of source zone characterization from a single temporal snapshot of data. In Section II.3.5 of this report, we present an extension of our initial work designed to process sparse concentration data sampled at wells.

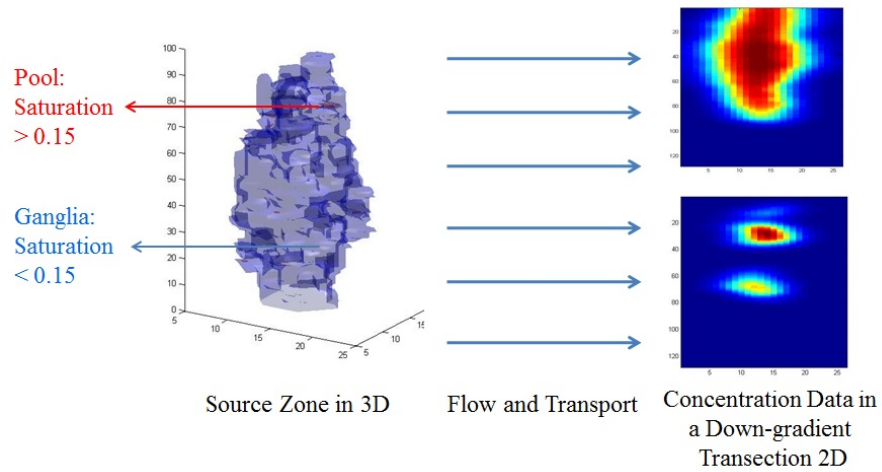


Figure M.3.1: The source zone plotted in 3D is modeled as being comprised of two parts: “pools” for which the saturation exceeds 0.15 and “ganglia” for which the saturation is lower than 0.15. Flow through the source zone gives the down-gradient concentration data in 2D.

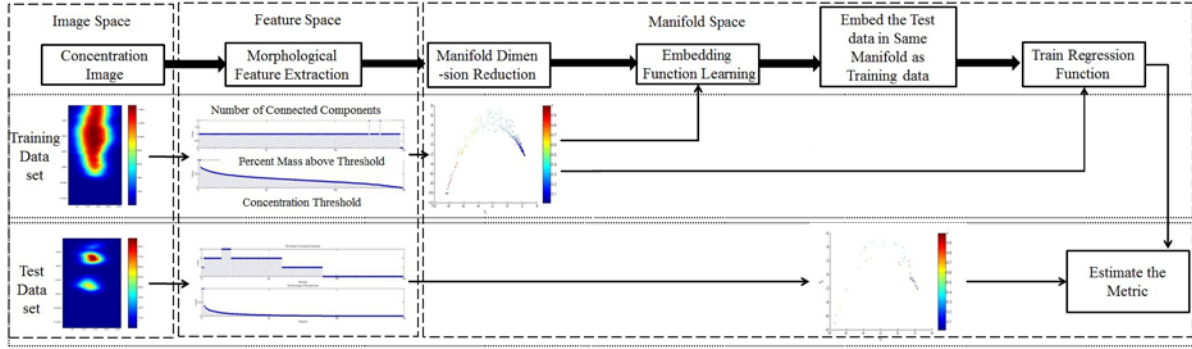


Figure M.3.2: The framework of our regression-based machine learning approach. The morphological feature extraction is shared by both training and test stage, because it is an image processing method which is to be applied to both the training and test data.

Motivated by the ideas in (Guo, 2008), our work in this task has focused on the use of state-of-the-art ideas in machine learning to construct a *regression function* for estimating one or all of the metrics from the down-gradient observations. This process is comprised of a number of component steps that are illustrated in Figure M.3.2 and described in detail in the following pages. While the computational models of entrapment and dissolution are certainly of use in generating data for building this regression function, it is still the case that the computational burden of running these models limits the size of the data sets available to us for this task. More precisely, rather than having millions of data sets as is the case in typical “big data” problems (e.g., the Netflix prize competition) as we discuss below, here we have hundreds of examples. As one typically requires at least an order of magnitude more training data than observations per data (Bishop, 2006), we must first reduce the dimensionality of the data after which a suitable regression function can be constructed. Within the machine learning literature, it is common practice to extract from data a reduced set of features. In Section II.3.2.2 we describe a new set of features based on morphological image processing operations (Gonzalez, 2010) applied to the down-gradient concentration transect data, the structure of which is driven by the underlying physics of the problem. As the dimension of the resulting feature vectors N_f is still well over 100, we employ manifold learning methods to obtain a low dimensional manifold coordinate vector (the dimension will be four) for training a regression function under a Bayesian approach. For testing, after we learn the embedding function (a mapping from morphological feature space to manifold space) using training data, we embed the test data in the same space and estimate the desired metrics and confidence intervals.

It is important to note that the use of manifold methods is motivated by more than just computational considerations. These techniques are required to address the identifiability problem in the data. As we discuss in greater depth in Section II.3.2.1, it is the case here that

“similar” pairs of both raw concentration data and even morphological feature vectors can correspond to very different source zone metrics, and likewise similar metrics may give rise to data and feature vectors that are “different” in an appropriate mathematics sense, thereby severely reducing the utility of any type of straightforward regression approach. The use of manifold techniques is required to obtain a representation of the data that addresses this limitation, thereby allowing for the metrics to be inferred with good accuracy from the observations.

II.3.2. Standard Manifold Regression

II.3.2.1. Overview

Given a collection of data (in our case down-gradient concentration information) and metrics describing a system we seek to estimate (in this case f_p , M_p or M_g), machine-learning algorithms determine a mapping from data to metric such that when new data are made available we are able to estimate the associated metric. The procedure of machine learning can be separated into two stages, *training* and *test*, which are illustrated in Figure M.3.2. In the training stage, we use known data/metric pairs to construct this mapping, while in the test stage we use data independent from training data set (in practice data from a field site) to evaluate the accuracy of the approach.

As shown in Figure M.3.2, the training and testing processes require a number of steps which we outline here before moving on to provide the details for each stage. The inputs to the training phase are observations of downstream concentration data $\mathbf{c}_i(x, y)$ and an associated metric t_i , for the known source zone associated with these concentration signals with $i = 1, 2, \dots, N$. The variables x and y represent the coordinates in a down-gradient transect where the concentration data are collected. Thus we may regard $\mathbf{c}_i(x, y)$ as an image where x and y index the coordinates of the pixels. It is also convenient to think of these data as a vector, \mathbf{c}_i , obtained by lexicographically ordering the pixels in the image. Thus N_c , the dimensionality of \mathbf{c}_i is equal to the product of the number of rows and columns in $\mathbf{c}_i(x, y)$. As explained in Section II.1 these training data are generated via Monte Carlo simulation where a number of hydraulic conductivity fields are generated using a statistical model. DNAPL infiltration is then simulated along with dissolution to generate the concentration data.

Referring again to Figure M.3.2, from the concentration data, the first three steps in training are feature extraction, manifold dimensionality reduction and embedding function learning. As we discuss shortly, these processing stages are employed to obtain quantities derived from the concentration observations that are, in some sense, more predictive of the metrics than the raw data. As mentioned previously, learning a good regression function requires that the size of the training set, N , be at least an order of magnitude larger than the dimensionality of the variables we use for estimation (Bishop, 2006). For our problem, N is about 500 while the dimensionality

of c_i is over 3000. To ameliorate this situation we first consider a collection of features derived directly from the data. In general, the features used for machine learning are application dependent. In many cases, one looks at statistics of the data such as mean, variance, and entropy of the data histogram (Hanchuan et al., 2005). Additionally, domain-specific intuition can be used to develop new features which can be more helpful for estimation. For our problem, we discuss in Section II.3.2.2 a set of quantities that are of use for estimating metrics from concentration signals. This is based on morphological signal processing methods.

Ultimately, the number of features we compute is still on the order of a few hundred. Dimensionality reduction is used to further extract from the data those degrees of freedom that are most relevant for solving the regression problem. More precisely, we seek to transform the feature vectors into a space such that the distance between vectors in this new space is reflective of the distance between the corresponding source zone metrics we seek to determine. If this condition is satisfied, then when the feature vector from a test data set is transformed into this space, the use of regression for the metric based on the training data points close to the test data point in manifold space is expected to be accurate. As this closeness requirement involves a highly nonlinear mapping of the feature vectors (Lui, 2012), standard linear dimensionality reduction methods such as Principal Component Analysis (PCA) (Bishop, 2006), are not appropriate. In our work, we employ a nonlinear dimension reduction method, specifically Laplacian Eigenmaps (LE), (Mikhail Belki, 2003) to construct a low dimensional manifold space such that the data with similar metrics are located near to one another.

To develop a sense for the difficulty of the problem, it is important to note that the closeness condition discussed in the last paragraph (known more formally as a *locality preserving* property) does not hold when the embedding manifold is taken to be the N_c dimensional Euclidean space of the raw concentration image data or even the N_f dimensional Euclidean space of the morphological feature vectors the details of which are developed in Section II.3.2.2. As an example, consider the three data and corresponding pool mass metrics illustrated in Figure M.3.3. In Table M.3.1, the squared Euclidean distances¹ between all three pairs of concentration image data and feature vectors are provided along with the distances computed using the manifold ideas developed in Section II.3.2.3. While cases (a) and (c) have the most similar pool masses (differing only by 0.7 kg), the raw concentration images and the raw feature vectors would predict that (a) and (b) were most similar. Indeed, in manifold space are (a) and (c) placed closest together. Moreover, pairs (a)/(b) and (b)/(c) which have about the same mass difference are also places about the same distance apart in manifold space.

Now, a known shortcoming of these manifold methods is that lack of an explicit embedding function for the processing of test data where the source zone metric is *not* known (Vincent 2003). Indeed, manifold techniques were initially designed for constructing low dimensional

¹ Given a pair of column vectors \mathbf{v} and \mathbf{w} , each of dimension d this distance is nothing more than $(\mathbf{v} - \mathbf{w})^T(\mathbf{v} - \mathbf{w})$ with T indicating the vector (or matrix) transpose operation.

representation of known data and not for regression. Thus, to embed the test data (which obviously will not include the associated metric value) in the same space as the training data, we need to learn an embedding function; that is, a mapping from morphological feature space to the manifold space, shown in Figure M.3.2. Here we apply spectral regression (SR) method (Deng Cai 2007) to learn this embedding function, after which we can embed the test data in the manifold where regression can then be performed.

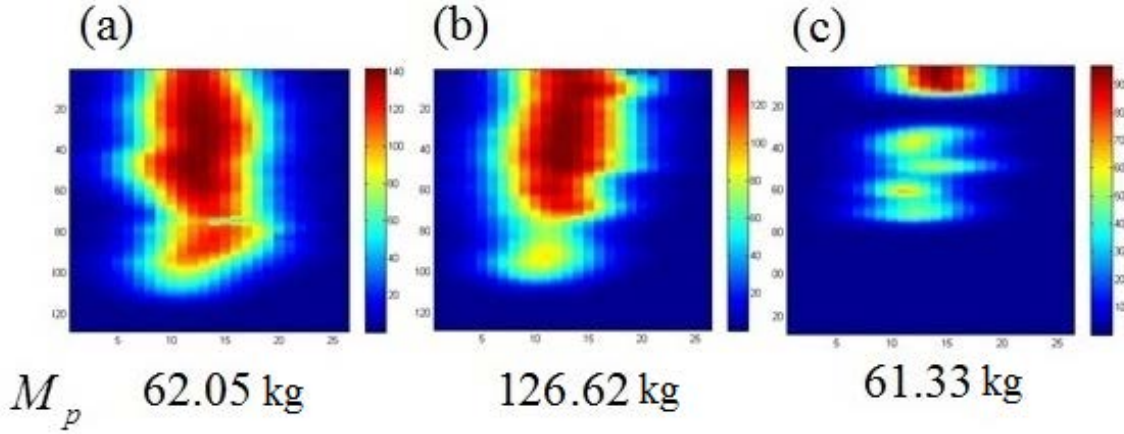


Figure M.3.3. The identifiability issue of regression function. Due to the difference of initial spill, the metrics corresponding to the similar concentration image is quite different, for example, the concentration data in (a) and (b) look most similar, but the metrics, mass in pool, are quite different.

The final step of training process is Bayesian regression (Bishop, 2006) for estimating the metrics from the manifold coordinates of the test data. Of most relevance here is that a Bayesian approach provides not only an estimate of the metric but also a confidence interval, allowing for the quantification of the uncertainty in this estimate.

In summary, the four-step training process just outlined results in (a) a collection of morphological feature vectors $\mathbf{x}_i \in R^d$, $i=1,2,\dots,N$, (b) an associated set of manifold coordinate vectors $\mathbf{r}_i \in R^m$ with $m \ll d$, (c) an embedding mapping for transforming concentration data, $\mathbf{c}(x, y)$, into a manifold coordinate vector, \mathbf{r} and (d) a Bayesian regression function that converts a manifold coordinate vector into an estimate of the source zone metric and an associated confidence measure.

Table M.3.1 The distance between the data corresponding to Figure M.3.2.1 in image space, morphological feature space and manifold space, bold figures indicate pairings with smallest distances when measured using pixels, raw features, and manifold coordinates

	Magnitude of Mass Difference (kg)	Pixel-Distance	Raw Feature Vector Distance	Manifold Distance
Comparing (a) to (c)	0.7	2900	20.1	1.2
Comparing (a) to (b)	64.5	918	7.3	30.9
Comparing (b) to (c)	65.2	2552	19.8	30.8

II.3.2.2. Morphological Feature Extraction

As discussed in the Section II.3.1, here we consider a reasonably common scenario in which we are provided observations of contaminant concentrations within a transect located away from the source zone and oriented orthogonally to the nominal direction of groundwater flow. The feature vector we develop is motivated by our intuition concerning how the *morphology*, defined below, of the observed concentration data is related to that of the unknown DNAPL saturation in the source zone. As an example, consider the concentration data and associated pool fractions, f_p shown in Figure M.3.4. Roughly speaking we observe that as the pool fraction increases, the geometry of the concentration data changes accordingly. Specifically, the number of “blobs” in the images increases and their sizes decrease. Motivated by this observation, here we seek features that capture the size and number of blobs in the concentration data believing that they are related to the metrics in a way that can be learned given sufficient examples. Note that the behavior just described is observed not only for these three cases but more generally for the many different data sets considered in the experiments in Section III.3. Additionally, similar intuition can also be established for the other two metrics considered in our work, the mass of DNAPL in pool regions, and the mass of DNAPL in ganglia.

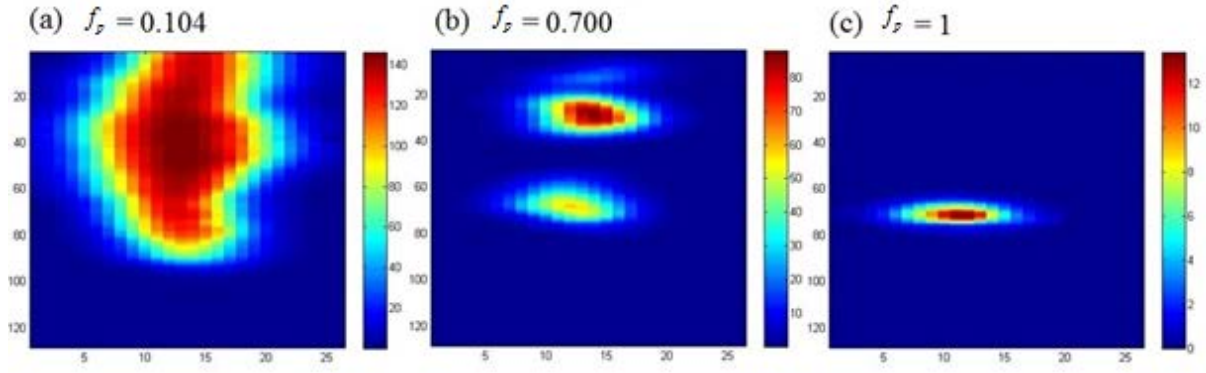


Figure M.3.4: The observation of concentration image according to their pool fraction value.

Within the image processing literature, the study of quantities such as the number and sizes of blobs in an image is known as *mathematical morphology* (Refael C. Gonzalez 2010). To motivate the mathematical definitions for the feature vector we develop, in Figure M.3.5 we display samples of the concentration data as height maps along with the corresponding morphological feature vectors for the same data displayed as images in Figure M.3.3.

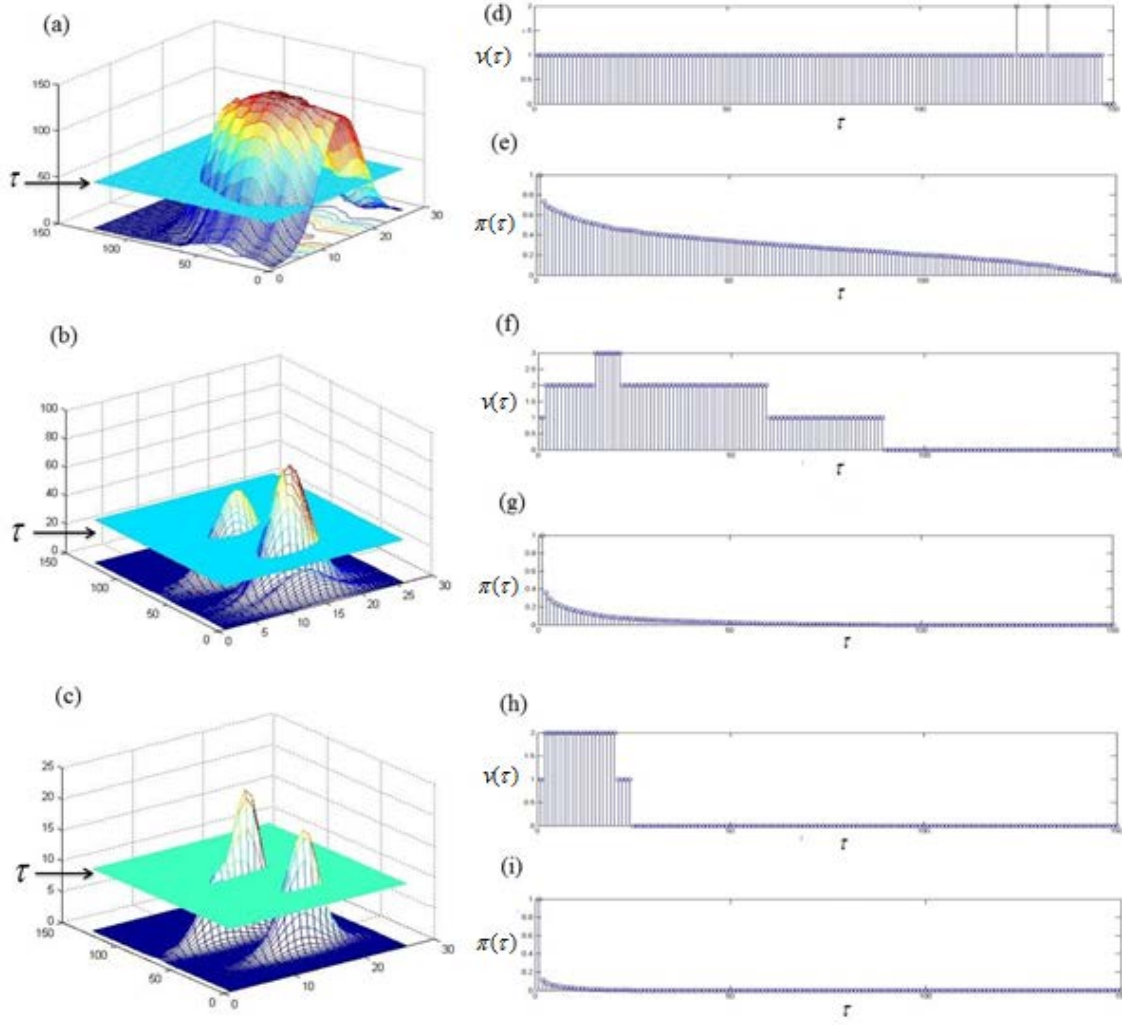


Figure M.3.5. Morphological feature vectors corresponding to concentration data from Figure M.3.4.

Mathematically, the key issues here are quantifying the notion of a “blob” and determining what characteristics of these blobs are useful. The first issue is addressed by a simple thresholding operation in which we specify the blobs at some level τ to be those pixels in the image whose concentrations exceed τ :

$$b(x, y; \tau) = \begin{cases} 1, & \mathbf{c}(x, y) > \tau \\ 0, & \text{else} \end{cases} \quad (\text{M.3.1})$$

From $b(x, y; \tau)$ we have found it useful to compute two quantities: the fraction of the area in $\mathbf{c}(x, y)$ for which $b(x, y; \tau) = 1$ denoted as $\pi(\tau)$, and the number of connected components at that level, $\nu(\tau)$. The fraction of area is computed via:

$$\pi(\tau) = \frac{\sum_{x,y} b(x, y; \tau)}{\sum_{x,y} b(x, y; 0)} \quad (\text{M.3.2})$$

where the denominator is nothing more than the number of pixels in the concentration image that are nonzero. A connected component is a group of pixels in the image such that one can move from any pixel in the set to any other through a series of North, South, East, and West moves (Gonzalez, 2010). Referring to the data in Figure M.3.4 again, for subfigure (a) with $\tau = 20$, the number of connected components is one. For (b) at $\tau = 10$ there are two connected components while in (c) with $\tau = 5$ there is only a single connected component.

The morphological feature vector we create, denoted as \mathbf{x} , is comprised of $\pi(\tau)$ and $\nu(\tau)$ for $\tau = 0, 1, 2, \dots, \tau_{\max}$ where τ_{\max} is the largest value of concentration in the training data set. We define $\mathbf{X} = [\mathbf{x}_1, \mathbf{x}_2, \dots, \mathbf{x}_N] \in \mathbb{R}^{d \times N}$ as the morphological feature matrix constructed using all data in our training set. In Figure M.3.5 (d)-(i), we plot $\nu(\tau)$ and $\pi(\tau)$ corresponding to concentration data in Figure M.3.4 (a)-(c). We see that for each of the different values of pool fraction, the behavior of these quantities as a function of threshold is quite distinct. The number of connected component is almost always one in Figure M.3.5 (d) for the low pool fraction case, indicating that there is only one large diffuse area in concentration image.² In Figure M.3.5 (f), the pattern is more variable, reflecting that the structures in the concentration image are themselves more complex. Finally, in Figure M.3.5 (h) the number of connected components drops to zero quite quickly reflecting the presence of only a single blob in the concentration data due to the high pool fraction (i.e., a lack of diffuse ganglia in the saturation profile). Similarly, the decay of $\pi(\tau)$ as a function of τ illustrated in Figures M.3.5 (e), (g) and (i) show a strong dependence on the underlying pool fraction.

II.3.2.3. Manifold Dimension Reduction using Laplacian Eigenmaps

As explained in the discussion surrounding Figure M.3.3, our use of manifold method is motivated by a desire to embed the training data comprised of the morphological feature vectors along with the known metrics into a low dimensional space where regression can be performed accurately. Here we use the Laplacian Eigenmaps (LE) approach (Belkin et al., 2003) to construct a manifold with the locality preserving property we desire. Mathematically, for each length $d + 1$ vector, (\mathbf{x}_i, t_i) obtained by concatenating the metric value to the feature vector we

² Although there is some variability in the feature vector (e.g. the number of connected component is two for a couple of larger values of the threshold) such inconsistencies have little impact in the ultimate utility of these features.

seek a low dimensional embedding, $\mathbf{r}_i \in R^m$ with $m \ll d+1$. Here \mathbf{r}_i is best thought of as an m -dimensional set of coordinates for the i^{th} datum in the manifold. The LE manifold is constructed by choosing the embedding coordinates to minimize the following objective function,

$$\min_{\mathbf{r}_i \in R^m} \sum_{i,j=1}^N \left\| \mathbf{r}_i - \mathbf{r}_j \right\|^2 \omega_{ij}. \quad (\text{M.3.3})$$

The weight ω_{ij} is constructed as a measure of the similarity between (\mathbf{x}_i, t_i) and (\mathbf{x}_j, t_j) , and is chosen to be largest when these quantities are closest. Here we propose a variant of the Gaussian weight function for which ω_{ij} is

$$\omega_{ij} = \exp \left(-\frac{\left\| \mathbf{x}_i - \mathbf{x}_j \right\|^2}{\sigma_1} \right) \exp \left(-\frac{|t_i - t_j|}{\sigma_2} \right). \quad (\text{M.3.4})$$

Thus the objective function (M.3.3) will incur a heavy penalty in the event that (\mathbf{x}_i, t_i) and (\mathbf{x}_j, t_j) are similar (for which the corresponding weight will be close to one) but are embedded far from one another. Thus, by choosing the embedding coordinates to minimize (M.3.3) we guarantee that if (\mathbf{x}_i, t_i) and (\mathbf{x}_j, t_j) are close, the \mathbf{r}_i and \mathbf{r}_j are close as well. The quantities σ_1 and σ_2 are used to scale the size of the weight associated with the feature vector and the metrics values respectively. Their selection is discussed in Section III.3.

To illustrate these ideas, consider again the three cases illustrated in Figures M.3.3 and M.3.5. With $\sigma_1 = 30$ and $\sigma_2 = 1$ (the values used in our experiments discussed below), when constructing the weight for comparing (a) and (b), the morphological feature vectors for these data sets are clearly similar, so that the first factor in (M.3.4) will be large, but the difference between the metrics, 64.57 kg, is huge so that the second factor in (M.3.4) will be very small, resulting in $\omega_{ab} = 0.27$. When we calculate the weight for (a) and (c), the first factor measuring the similarity between morphological features will be small, but the second factor will be large, yielding the weight $\omega_{ac} = 0.51$. Thus, using this approach we see that (a) and (c) are, in a sense, almost twice as similar as (a) and (b) which is exactly what we desire given that pool masses for (a) and (c) are much closer than those of (a) and (b).

In Figure M.3.6 we display a two-dimensional pool fraction manifold constructed using this approach. Thus, each \mathbf{r} vector has two components, r_1 and r_2 . Each circle in this space corresponds to one data set used in the experiments in Section III.3 with the color of the circle indicating the pool fraction for that data set. We also plot a few of the corresponding concentration images. From Figure M.3.6, we see that the value of f_p changes monotonically from zero to one when moving along the manifold. Thus, data sets whose metric values are similar will in fact be

mapped close to one another in \mathbf{r} space so that the locality preserving property discussed in Section II.3.1 is in fact evident at least with respect to the training data.

Two remarks are in order concerning the LE method. First, the process of solving the optimization problem in (M.3.3) is well known (Mikhail Belki, 2003). Second, full specification of the problem requires that the parameters σ_1 and σ_2 be provided. As described Section III.3, here we use a cross validation (Bishop, 2006) approach to determine these quantities adaptively from the data.

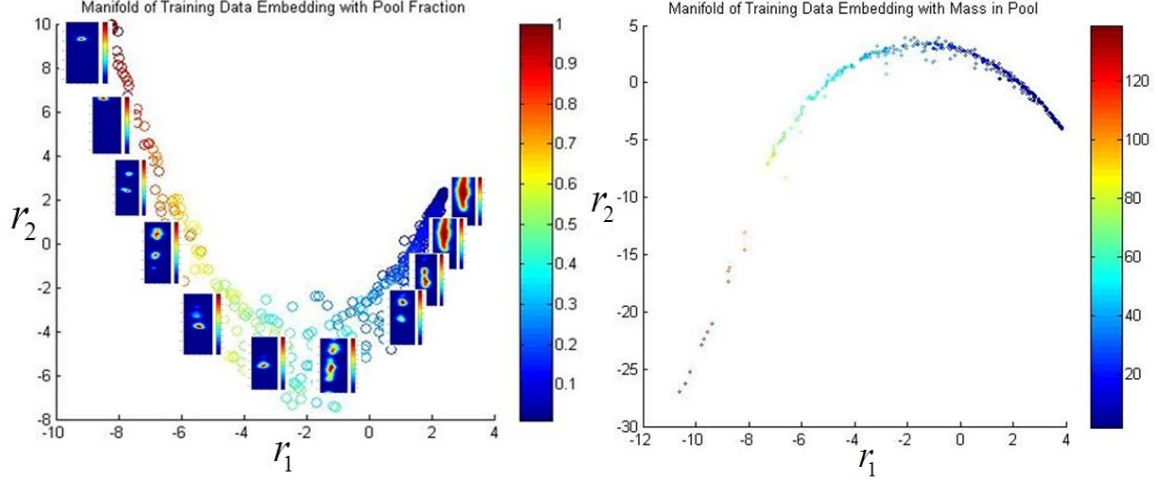


Figure M.3.6: Two dimensional embedding of concentration image data and associated pool fraction (left) and mass in pools (right). The color of each dot indicates the pool fraction or pool mass respectively. The manifolds we find demonstrate that the data with similar metrics are located nearby one another. The unit of mass in pool is kilogram.

II.3.2.4. Spectral Regression Method for Embedding Function Learning

As is evident from the discussion in Section II.3.2.3, LE requires that both the feature vector and the metric be known to determine the manifold coordinates. This is clearly a problem for regression where we do not possess the metric but rather would like to embed a test data set into the manifold and estimate its associated metric by looking at the metrics of the neighboring test data. Thus, to perform regression in manifold space it is necessary to extend the manifold embedding to test data comprised only of observed morphological feature vectors. We need then to learn the embedding function, which is a mapping from morphological feature space to manifold space. After LE embeds the training data in manifold space, the input of embedding function $\mathbf{x}_i, i=1,2,\dots,N$ and the output $\mathbf{r}_i, i=1,2,\dots,N$ are known. Using this vector pair, we

can learn the embedding function $\mathbf{r} = f(\mathbf{x})$, which can then be used to embed the morphological feature derived from test data into manifold space.

Spectral Regression (SR) casts embedding function learning into a regression framework. Since LE is a nonlinear dimension reduction method, the mapping function from feature space to manifold space should also be nonlinear. We assume that the nonlinear function lives in a Hilbert space specified by kernel $K(\cdot, \cdot)$ (Shawe-Taylor, 2004). The model of this nonlinear function is $f(\mathbf{x}) = \mathbf{A}^T \mathbf{k}(\mathbf{x})$, specified by the parameter matrix $\mathbf{A} \in R^{N \times m}$ and kernel function vector $\mathbf{k}(\mathbf{x}) = [k(\mathbf{x}, \mathbf{x}_1), k(\mathbf{x}, \mathbf{x}_2), \dots, k(\mathbf{x}, \mathbf{x}_N)]^T$. The optimization problem to learn \mathbf{A} is (Deng Cai 2007):

$$\mathbf{A}^* = \arg \min_{\mathbf{A}} \sum_{i=1}^N \left\| \mathbf{A}^T \mathbf{k}(\mathbf{x}_i) - \mathbf{r}_i \right\|^2 + \gamma \left\| \mathbf{A} \right\|_F^2 \quad (\text{M.3.5})$$

where γ is a regularization hyper-parameter and $\left\| \cdot \right\|_F^2$ is the Frobenius norm (sum of the squares of the elements of the matrix). The solution of problem (M.3.5) is $\mathbf{A}^* = \left((\mathbf{K} + \gamma \mathbf{I})^{-1} \mathbf{R}^T \right)^T$, where matrix \mathbf{K} is the $N \times N$ Gram matrix with $K_{ij} = k(\mathbf{x}_i, \mathbf{x}_j)$, and $\mathbf{R} = [\mathbf{r}_1, \mathbf{r}_2, \dots, \mathbf{r}_N]$. In the experiments in Section III.3, we use the Gaussian kernel (Cai, 2007),

$$k(\mathbf{x}, \mathbf{x}_i) = \exp \left(- \frac{\left\| \mathbf{x} - \mathbf{x}_i \right\|^2}{\sigma_{SR}} \right)$$

where the hyper-parameter σ_{SR} is determined by cross-validation.

II.3.2.5. Linear Bayesian Regression Method and Confidence Interval Estimation

The final step of our machine learning framework is training the regression function in manifold space to estimate the metric of test data. One of the advantages of Bayesian regression is that it can provide both the estimated metric itself along with a confidence interval allowing for the quantification of uncertainty in the estimate. The summary of standard linear Bayesian regression is provided with additional details in (Bishop, 2006). Here we discuss two implementation issues specific to our problem. As discussed in (Bishop, 2006), a linear regression function is used which takes the form $t(\mathbf{r}) = \mathbf{w}^T \mathbf{r} + b + \epsilon$, where the weight vector \mathbf{w} and the bias constant, b , are to be determined from the training data and ϵ is modeled as zero mean, additive Gaussian noise with variance β . The first issue is how to best choose β . Here, we employ an iterative approach which empirically appears to function well, but for which we do not yet have a theoretical justification. Specifically for all experiments, we initially set $\beta = 0.01$.

After determining \mathbf{w}^* and b^* , the optimal values for \mathbf{w} and b using the methods of (Bishop 2006), the random variable ϵ_i is estimated as $\hat{\epsilon}_i = t_i - \mathbf{w}^{*T} \mathbf{r}_i - b^*$, and β is updated as the sample variance of $\hat{\epsilon}_i$. With this new value of β , the regression function can again be computed and the process is repeated until convergence. The rate of convergence is quite fast; generally one iteration is enough.

For the fully Bayesian approach to regression construction discussed in (Bishop, 2006), we also require a prior probability distribution for the unknown metric being estimated for a given set of test data. Again a zero mean Gaussian model is used for which the variance needs to be determined. Unlike the specification of β , here we only possess one test data set so that sample variance methods cannot so easily be employed. To address this issue we assume that the embedding process is sufficiently accurate so that the training data in the neighborhood of the embedded test data will have associated metrics that are close to that of the test data. Under such an assumption, the variance of the metric for the test datum is taken as the sample variance of the metrics for these 10 neighboring training data.

II.3.3. Integrated Manifold Regression

In standard machine learning procedure, each of the processing methods discussed in Section II.3.2.3-II.3.2.5 is implemented in isolation of the other. Under such an approach, the manifold is constructed only with the goal of embedding the training data, and does not reflect the ultimate processing objective of estimating the metric from new test data. Thus, we are motivated to consider an integrated approach, which determines both the manifold embedding function and the regression function as the solution to a single, unified variational problem. Interestingly, the approach bypasses the need to explicitly construct the manifold coordinates of the training data, although given the embedding function, these quantities certainly could be computed to e.g. visualize the embedding. To the best of our knowledge, the idea of integrating manifold construction and spectral regression has not been considered even within the machine learning community and thus represents a unique contribution of our work beyond the specific application of environmental restoration.

Formally we integrate manifold dimension reduction, spectral regression and Bayesian regression using the following cost function,

$$\min_{\mathbf{A} \in \mathbb{R}^{d \times m}, \mathbf{w} \in \mathbb{R}^m} L(\mathbf{A}, \mathbf{w}, b) = \frac{1}{N^2} \sum_{i,j=1}^N \|f(\mathbf{x}_i) - f(\mathbf{x}_j)\|^2 \omega_{ij} + \gamma_1 \|\mathbf{A}\|_F^2 + \gamma_2 \frac{1}{N} \left\| \begin{pmatrix} \mathbf{w}^T, b \end{pmatrix} \begin{pmatrix} \mathbf{A}^T \mathbf{X} \\ \mathbf{1}^T \end{pmatrix} - \mathbf{t} \right\|^2 + \gamma_3 \left\| \begin{pmatrix} \mathbf{w}^T, b \end{pmatrix} \right\|^2 \quad (\text{M.3.6})$$

where $f(\mathbf{x}) = \mathbf{A}^T \mathbf{k}(\mathbf{x})$ is the embedding function for both the training and test data and $\mathbf{1}^T \in \mathbb{R}^{1 \times N}$ is the vector of all ones. The first term in (M.3.6) is motivated by the LE cost function and seeks an embedding of the training data that preserves locality. The second term $\|\mathbf{A}\|_F^2$ is the regularization term coming from SR, with the regularization hyper-parameter γ_1 playing the

same role as γ in (M.3.5). The third term in (M.3.6) arises from the mathematical details of the Bayesian regression problem provided in (Bishop, 2006). The hyper-parameter γ_2 is used to balance the desire for a good embedding with the needs of obtaining accurate regression results.

To find the optimal solution for problem (M.3.6), an alternating decent method is employed in which we use gradient descent to update \mathbf{A} with $\varpi = (\mathbf{w}^T, b)$ fixed and then update ϖ given \mathbf{A} . The update equations are derived as follows. Taking the derivative of (M.3.6) with respect to \mathbf{A} yields

$$\frac{\partial L}{\partial \mathbf{A}} = \frac{2}{N^2} \mathbf{A}^T \mathbf{X} \mathbf{L} \mathbf{X}^T + \gamma_1 \mathbf{A}^T + 2\gamma_2 \frac{1}{N} \mathbf{w} \mathbf{w}^T \mathbf{A}^T \mathbf{X} \mathbf{X}^T + 2\gamma_2 \frac{1}{N} \mathbf{w} \cdot (b \cdot \mathbf{1} - \mathbf{t})^T \mathbf{X}^T \quad (\text{M.3.7})$$

Using gradient descent algorithm we update the embedding matrix \mathbf{A} ,

$$\mathbf{A}^{(p)} = \mathbf{A}^{(p-1)} - \xi \frac{\partial L}{\partial \mathbf{A}^{(p-1)}} \quad (\text{M.3.8})$$

where ξ is the step size. Taking the derivative of (M.3.6) with respect to $\varpi = (\mathbf{w}^T, b)$,

$$\frac{\partial L}{\partial \varpi} = \frac{2\gamma_2}{N} \left(\begin{pmatrix} \mathbf{A}^T \mathbf{X} \\ \mathbf{1}^T \end{pmatrix} \left(\mathbf{A}^T \mathbf{X}, \mathbf{1} \right) + \frac{\gamma_3 N}{2\gamma_2} \mathbf{I} \right) \begin{pmatrix} \mathbf{w} \\ b \end{pmatrix} - \frac{2\gamma_2}{N} \begin{pmatrix} \mathbf{A}^T \mathbf{X} \\ \mathbf{1}^T \end{pmatrix} \mathbf{t}. \quad (\text{M.3.9})$$

Setting the partial derivative (M.3.8) to 0, we see that ϖ can be easily solved by

$$\begin{pmatrix} \mathbf{w} \\ b \end{pmatrix} = \left(\begin{pmatrix} \mathbf{A}^T \mathbf{X} \\ \mathbf{1}^T \end{pmatrix} \left(\mathbf{A}^T \mathbf{X}, \mathbf{1} \right) + \frac{\gamma_3 N}{2\gamma_2} \mathbf{I} \right)^{-1} \begin{pmatrix} \mathbf{A}^T \mathbf{X} \\ \mathbf{1}^T \end{pmatrix} \mathbf{t}. \quad (\text{M.3.10})$$

Now, (M.3.8) specifies the gradient of \mathbf{A}^T in terms of \mathbf{w} and the optimal solution of (\mathbf{w}, b) depends on \mathbf{A} in (M.3.10). This situation immediately suggests an alternative optimization approach. In this approach \mathbf{w} and \mathbf{A}^T are first initialized randomly, and then \mathbf{A}^T is updated via gradient descent using the current estimate of \mathbf{w} . We then use (M.3.10) to update \mathbf{w} . The algorithm is summarized in Algorithm-1. The convergence threshold is set to $\eta = 0.01$ and the maximum number of iterations is fixed at 50, the step size ξ is chosen by the diminishing rule (Bertsekas, 1999). Most of the experiments in Section III.3 end within 50 iterations.

Algorithm-1 : Integrated Manifold Regression Algorithm

Inputs: $(\mathbf{X}^T, \mathbf{t}) \sqsubseteq \{(\mathbf{x}_i, t_i)\}_{i=1}^N$, $\eta > 0$, $\sigma_1, \sigma_2, \sigma_{SR}, \gamma_1, \gamma_2, \gamma_3 > 0, \xi_1 > 0$

Outputs: Embedding function \mathbf{A} and weight vector of regression function (\mathbf{w}^T, b) .

Initialization: $\mathbf{A}^{(0)}$ and $(\mathbf{w}^T, b)^{(0)}$ random.

Repeat

- Gradient Descent Update $\mathbf{A}^{(p)}$ and $q = 1$

➤ Compute $\mathbf{A}_{q+1}^{(p+1)} = \mathbf{A}_q^{(p)} - \xi_q \frac{\partial L}{\partial \mathbf{A}_q^{(p)}}$.

➤ $q = q + 1$, $\xi_q = \xi_1 / q$.

➤ **Until** $\|\mathbf{A}_{q+1}^{(p+1)} - \mathbf{A}_q^{(p+1)}\|^2 < \eta$

- Compute $\varpi^{(p+1)} = (\mathbf{w}^T, b)^{(p+1)}$ using (M.3.9).

Until $\|(\mathbf{w}^T, b)^{(p+1)} - (\mathbf{w}^T, b)^{(p)}\|^2 < \eta$

II.3.4. Multi-task Manifold Regression

Thus far, we have considered the estimation of the three quantities f_p, M_p, M_g individually. That is, one “learner” is used to estimate pool fraction, another for the mass of DNAPL in pools and a third for the mass of DNAPL in ganglia. These three metrics however are not independent of one another. Thus, we hypothesize that an approach which incorporates the mathematical relationships among these quantities to determine all three at once should outperform the case where we ignore the coupling. More specifically, we exploit the fact that pool fraction is equivalent to the ratio of the mass in pools to the mass in pools plus the mass in ganglia.

The analytical method we have developed proceeds as follows. In order to simplify the computation, we first use LE to determine the manifold coordinates of the training data \mathbf{R} . To remove the need to compute the bias terms, i.e., the b_i in each of the regression functions, we *centralize* both \mathbf{R} and \mathbf{t} by removing the sample mean value from each. That is, we compute

$\bar{\mathbf{r}} = \frac{1}{N} \sum_{i=1}^N \mathbf{r}_i$, and then define a centralized \mathbf{R} as $[\mathbf{r}_1 - \bar{\mathbf{r}}, \mathbf{r}_2 - \bar{\mathbf{r}}, \dots, \mathbf{r}_N - \bar{\mathbf{r}}]$, and centralize \mathbf{t} as $[t_1 - \bar{t}, t_2 - \bar{t}, \dots, t_N - \bar{t}]$ where $\bar{t} = \frac{1}{N} \sum_{i=1}^N t_i$. In this way, the regression function for a given metric,

which was $t = \mathbf{w}^T \cdot \mathbf{r} + b$, becomes $t = \mathbf{w}^T (\mathbf{r} - \bar{\mathbf{r}}) + \bar{t}$ and we no longer need to determine the bias term b , thereby simplifying the mathematics a bit in the following.

Given these centralized manifold variables, we seek to simultaneously determine three regression functions, one each for the three metrics of interest, subject to the constraint that the estimated pool fraction is equal to the ratio of M_p to $M_p + M_g$. The optimization problem to solve then is

$$\begin{aligned} \min_{\substack{f_1, f_2, f_3, \\ \mathbf{w}_1, \mathbf{w}_2, \mathbf{w}_3}} L(\mathbf{A}_k, \mathbf{w}_k) &= \sum_{k=1}^3 \left\{ \frac{1}{N} \sum_{i=1}^N \|f_k(\mathbf{x}_i) - \mathbf{r}_{ki}\|^2 + \gamma_{k1} \|f_k\|_{H_K}^2 + \gamma_{k2} \frac{1}{N} \sum_{i=1}^N (\mathbf{w}_k^T f_k(\mathbf{x}_i) - t_{ki})^2 + \gamma_{k3} \|\mathbf{w}_k\|^2 \right\} \\ \text{subject to } & \frac{\mathbf{w}_2^T f_2(\mathbf{x}_i) + \bar{\mathbf{t}}_2}{\mathbf{w}_2^T f_2(\mathbf{x}_i) + \bar{\mathbf{t}}_2 + \mathbf{w}_3^T f_3(\mathbf{x}_i) + \bar{\mathbf{t}}_3} = \mathbf{w}_1^T f_1(\mathbf{x}_i) + \bar{\mathbf{t}}_1, \text{ for } i=1, \dots, N \end{aligned} \quad (\text{M.3.11})$$

where the estimation of pool fraction, mass of DNAPL in pool and ganglia are generated using the following linear regression functions.

$$\begin{aligned} f_p &= \mathbf{w}_1^T f_1(\mathbf{x}) + \bar{\mathbf{t}}_1 \\ M_p &= \mathbf{w}_2^T f_2(\mathbf{x}) + \bar{\mathbf{t}}_2 \\ M_g &= \mathbf{w}_3^T f_3(\mathbf{x}) + \bar{\mathbf{t}}_3 \end{aligned} \quad (\text{M.3.12})$$

In the objective function of (M.3.11), we sum the three objective functions (one for each metric) employed in our integrated approach to metric learning. The constraint in (M.3.11) enforces the physical relationship among the three quantities to be estimated. The hyper-parameters $\gamma_{k1} \sim \gamma_{k3}$ play the same roles as in (M.3.6). Using Lagrange multiplier, we can convert (M.3.11) into an unconstrained optimization problem as the following

$$\begin{aligned} \min_{\substack{f_1, f_2, f_3, \\ \mathbf{w}_1, \mathbf{w}_2, \mathbf{w}_3}} L &= \sum_{k=1}^3 \left\{ \frac{1}{N} \sum_{i=1}^N \|f_k(\mathbf{x}_i) - \mathbf{r}_{ki}\|^2 + \gamma_{k1} \|f_k\|_{H_K}^2 + \gamma_{k2} \frac{1}{N} \sum_{i=1}^N (\mathbf{w}_k^T f_k(\mathbf{x}_i) - t_{ki})^2 + \gamma_{k3} \|\mathbf{w}_k\|^2 \right\} \\ &+ \gamma_P \left(\frac{\mathbf{w}_2^T f_2(\mathbf{x}_i) + \bar{\mathbf{t}}_2}{\mathbf{w}_2^T f_2(\mathbf{x}_i) + \bar{\mathbf{t}}_2 + \mathbf{w}_3^T f_3(\mathbf{x}_i) + \bar{\mathbf{t}}_3} - \mathbf{w}_1^T f_1(\mathbf{x}_i) + \bar{\mathbf{t}}_1 \right)^2 \end{aligned} \quad (\text{M.3.13})$$

where $f_k(\mathbf{x}) = \mathbf{A}_k^T \mathbf{k}(\mathbf{x})$. While (M.3.13) provides for the joint determination of all three regression functions in a manner that reflects the physical relationship among the metrics, the approach comes at the cost of having to determine a rather large number of hyper-parameters; i.e., $\{\sigma_{k1}, \sigma_{k2}, \sigma_{kSR}, \gamma_{k1} \sim \gamma_{k3}, \gamma_P\}$. We use standard manifold regression to determine the hyper-parameters σ_{k1}, σ_{k2} and σ_{kSR} for manifold embedding, use integrated manifold learning algorithm to determine the regularization hyper-parameters $\gamma_{k1} \sim \gamma_{k3}$, and then use these hyper-parameters which have been selected for multi-task manifold regression. Finally 10 cross-validation is

employed to determine the last hyper-parameter γ_p . In order to solve problem (M.3.13), we use Algorithm-2 summarized below.

Algorithm-2 : Multi-task Manifold Regression Algorithm
<p>Inputs: $(\mathbf{R}_k, \mathbf{t}_k) \sqsubseteq \{(\mathbf{r}_{ki}, t_{ki})\}_{i=1}^N$, $\eta > 0$, $\sigma_{k1}, \sigma_{k2}, \sigma_{kSR}$, $\gamma_{k1} \sim \gamma_{k3}, \gamma_P > 0, \xi_1 > 0, k = 1, 2, 3$</p> <p>Outputs: Embedding function $\mathbf{A}_1, \mathbf{A}_2, \mathbf{A}_3$ and weight vector of regression function $\mathbf{w}_1, \mathbf{w}_2, \mathbf{w}_3$.</p> <p>Initialization: $\mathbf{A}_1^{(0)}, \mathbf{A}_2^{(0)}, \mathbf{A}_3^{(0)}$ and $\mathbf{w}_1^{(0)}, \mathbf{w}_2^{(0)}, \mathbf{w}_3^{(0)}$ random.</p> <p>Repeat</p> <ul style="list-style-type: none"> - Gradient Descent Update $\mathbf{A}_k^{(p)}$ and $q = 1, k = 1, 2, 3$ <ul style="list-style-type: none"> ➤ Compute $\mathbf{A}_{k,q+1}^{(p+1)} = \mathbf{A}_{k,q}^{(p)} - \xi_q \frac{\partial L}{\partial \mathbf{A}_{k,q}^{(p)}}$. ➤ $q = q + 1, \xi_q = \xi_1 / q$. ➤ Until $\ \mathbf{A}_{k,q+1}^{(p+1)} - \mathbf{A}_{k,q}^{(p+1)}\ ^2 < \eta$ - Gradient Descent Update $\mathbf{w}_k^{(p)}$ and $q = 1, k = 1, 2, 3$ <ul style="list-style-type: none"> ➤ Compute $\mathbf{w}_{k,q+1}^{(p+1)} = \mathbf{w}_{k,q}^{(p)} - \xi_q \frac{\partial L}{\partial \mathbf{w}_{k,q}^{(p)}}$. ➤ $q = q + 1, \xi_q = \xi_1 / q$. ➤ Until $\ \mathbf{w}_{k,q+1}^{(p+1)} - \mathbf{w}_{k,q}^{(p+1)}\ ^2 < \eta$ <p>Until $\ \mathbf{w}_k^{(p+1)} - \mathbf{w}_k^{(p)}\ ^2 < \eta, k = 1, 2, 3$</p>

II.3.5. Sparse Data Manifold Regression

In addition to the work described in Section II.1.3 we also consider the application of our methods to cases where down-gradient data may be sparse in the sense that a full image of the transect concentration is not available. This is intended to more closely mimic information available at field sites, where one is provided with contaminant plume concentrations from a number of discrete monitoring wells located throughout the contaminated area. To model this situation, we are initially considering a two-dimensional problem and modeling the experiments being performed under Task I. In more detail, we have developed a simulation library of roughly 7000 training data sets (down-gradient concentration measurements and associated DNAPL metrics) whose hydraulic permeability statistics and data acquisition geometries are the same as those used to determine the transition probability/Markov Chain (TP/MC) permeability field which was packed in the aquifer cell completed for Task I, and generated regression functions for pool fraction, pool mass, and ganglia mass. Unlike our previous approach which assumed data were collected over a complete, continuous transect, we have developed a new processing method for embedding sparsely collected data into the manifold. This approach bypasses the

need for interpolating the data and is capable of dealing with arbitrary sampling strategies. The framework is shown in Figure M.3.7.

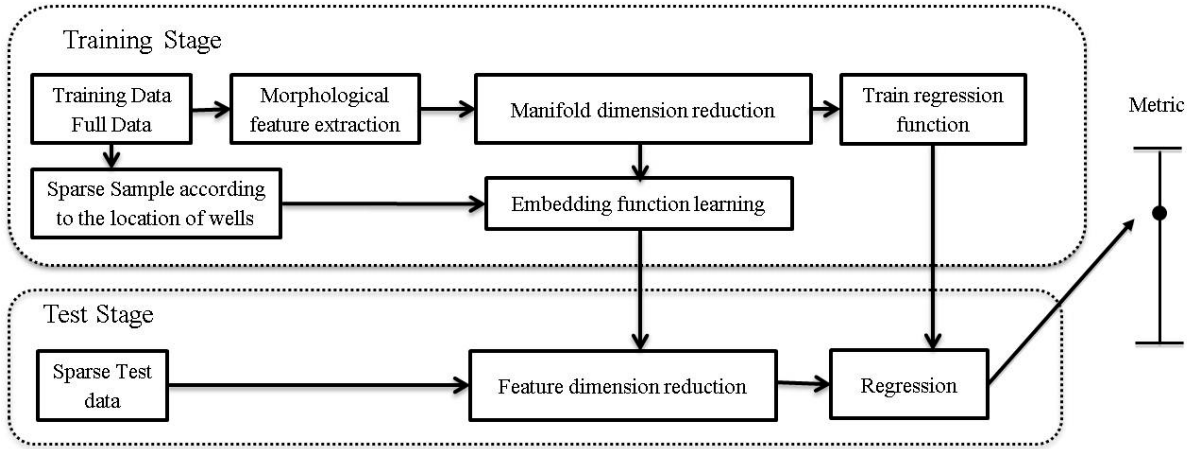


Figure M.3.7: The framework of manifold regression for sparse concentration data. The morphological feature extraction is used for the full training data which gives the manifold coordinate. The embedding function is learned from sparse data which is sampled from the full concentration data according to the location of wells.

Because we assume the availability of a full transect of training data, manifold construction proceeds in the same way as before via the extraction and processing of the morphological feature. Now however the test data set is comprised of only the sparse samples corresponding to the sampling ports used in the experiments. As these data do not naturally support the extraction of the morphological features, a new embedding method must be devised. With the manifold fixed and determined from the full set of training data, our approach is to learn an embedding function (that is an \mathbf{A} matrix) directly from the sparsely sampled training set without the intervening morphological feature calculation. That is, we use $f(\mathbf{x}_s) = \mathbf{A}^T \mathbf{k}(\mathbf{x}_s)$ in (M.3.5), where \mathbf{x}_s denotes the sparse concentration data to embed the sparse, test data into the manifold constructed using the fully observed downgradient concentration images. The training of the Bayesian regression function used to estimate the metrics from test data does not change from the approach discussed previously. For the integrated manifold regression, we use morphological features to calculate ω_{ij} and substitute \mathbf{x} with \mathbf{x}_s in (M.3.6). For multi-task learning, we use full concentration data to get the manifold coordinates \mathbf{R} . After centralizing it, we substitute \mathbf{x} with \mathbf{x}_s in (M.3.11).

II.4. Development of Simplified Modeling Tools

II.4.1. Introduction

In the field, the migration and entrapment of organic liquids in the subsurface is strongly influenced by fluid properties and release characteristics and by small and large scale heterogeneities in subsurface textural properties. In particular, spatial variations in permeability and capillary properties lead to the formation of complex and non-uniform distributions of DNAPL mass (Bradford et al., 2003; Dekker and Abriola, 2000; Essaid and Hess, 1993; Farthing et al., 2012; Kueper and Gerhard, 1995; Lemke et al., 2004). The application of local scale mass transfer coefficients for simulation of DNAPL dissolution or tracer partitioning in heterogeneous source zones is valid only when (a) heterogeneous properties are characterized at the same level (scale) as was used for development of the local scale model and (b) computational grid blocks are small enough to capture the spatial variability of the properties at this scale. Neither condition can feasibly be met in a field scale simulation. An alternative approach then for the simulation of multiphase transport behavior in heterogeneous systems is the use of simplified modeling tools. Such models are typically based upon average mass balance relationships or governing equations with reduced dimensionality and upscaled coefficients; they customarily incorporate spatially averaged parameters and SZA metrics to predict system response.

Several approaches have been used to link SZA metrics to mass discharge behavior. These approaches have involved application of Lagrangian modeling techniques (e.g., Jawitz et al., 2003, 2005; Enfield et al., 2005; Fure et al., 2006; Basu et al., 2008a); upscaled mass transfer relationships (e.g., Parker and Park, 2004; Park and Parker, 2005; Christ et al., 2006; Saenton and Illangasekare, 2007; Parker et al., 2008; Zhu and Sykes, 2004), and traditional analytical and numerical models (e.g., Kaye et al., 2008; Marble et al., 2008; Zhang et al., 2008). Motivated by the attractive simplicity of the GTP ratio, Christ et al. (2006), developed a simplified screening model based upon this metric that successfully captured the relationship between source zone mass removal and down-gradient contaminant flux reduction for a variety of field-scale numerical simulation scenarios. Although this and similar upscaled models may reproduce the general decline in flux-averaged concentrations with mass removal (e.g., Parker and Park, 2004; Christ et al., 2006; Fure et al., 2006; Zhang et al., 2008), they fail to capture the distinct ‘multi-stage’ concentration behavior observed as the SZA transforms from ganglia- to pool dominance (see, for example, Lemke et al., 2004b; Parker and Park, 2004; Brusseau et al., 2007, 2008; Suchomel and Pennell, 2006; Zhang et al., 2008).

The first goal of this task is to refine an existing upscaled mass transfer model to more accurately predict two-stage reductions in mass discharge as a function of mass removal and to investigate the relationship between SZA and mass recovery in pool-dominated source zones by employing the upscaled model. Pool-dominated source zones are anticipated at aged field sites that have been subject to dissolution under natural gradient conditions. Numerical simulations are employed in this research to investigate SZA characteristics that lead to two-stage mass

discharge and subsequently combined with experimental results to guide and test upscaled mass transfer model modifications.

When tracer partitioning in a source-zone region is explored, the large difference between partitioning and dissolution time scales greatly reduces the impact of mass removal on the partitioning rate. This difference renders most existing upscaled models, which were developed for upscaling mass transfer rate within a time domain, inappropriate for application to partitioning processes. Furthermore, experimental studies have shown that the effective mass transfer rates in a heterogeneous domain are significantly smaller than those estimated by local scale models when effective properties are used (Nambi, 1999; Parker and Park, 2004). Thus, the second goal of this task is to develop upscaled models to be used in the design and interpretation of partitioning tracer tests. Here local scale mass transfer coefficients are incorporated in a fine-grid two-dimensional model to simulate a series of partitioning tracer tests in heterogeneous DNAPL realizations. The output of these simulations is then adopted as observation data. For each test, a one-dimensional (upscaled) model is then fitted to the results of the 2D simulations and an effective mass transfer coefficient is estimated. A regression model is developed for the prediction of the effective mass transfer coefficient based on the characteristics of these realizations.

II.4.2. Upscaled Models for Mass Depletion

Under previous SERDP sponsorship, Christ et al. (2006) developed an upscaled model that uses two site specific parameters: initial average concentration (C_o) and GTP ratio, to quantify the approximate evolution of the contaminant plume as DNAPL dissolves. The DNAPL source zone simulations employed in their study were generated using the SGS-based simulations conditioned to the Bachman Road site (Lemke and Abriola, 2003; 2006; Lemke et al., 2004). The upscaled model was demonstrated to successfully predict single stage dissolution behavior commonly found in source zones that respond quickly in terms of mass removal per remediation effort (high GTP).

This simplified screening model build upon observations from Lemke and Abriola (2003, 2006) and Lemke et al. (2004) that GTP ratio metrics may be useful for distinguishing between DNAPL source zones with different dissolution signatures. High GTP signatures are dominated by ganglia zones that respond quickly to mass removal remediation efforts and generally exhibit single stage dissolution behavior. On the other hand, low GTP signatures are dominated by pools and yield “two-stage” dissolution behavior as DNAPL mass is removed.

For this task, the wide range of source zone architectures obtained from the simulations in Task I were supplemented by the generation of additional low GTP SZAs by changing the correlation length of the ensemble of the 16 3D permeability fields based.

To simulate these scenarios, the Christ et al. (2006) model was revisited to develop a new mass depletion parameter. The original model of Christ et al. (2006) takes the form:

$$\frac{\bar{C}(L)}{C^{eq}} = 1 - \left(1 - \frac{\bar{C}_0}{C^{eq}}\right) \left(\frac{M}{M_0}\right)^\beta \quad (\text{M.4.1})$$

where $\bar{C}(L)$ is the flux-weight aqueous phase concentration at the down gradient boundary, C^{eq} is the equilibrium aqueous solubility, \bar{C}_0 is the initial flux-weight concentration, M and M_0 is the DNAPL mass at the given time and at time $t=0$, respectively, and β is a mass depletion parameter obtained from the correlation between GTP and β . Christ et al. (2006) found $\beta = 1.5GTP^{-0.26}$ for the simulations used in Christ et al (2006), where $1.5 < GTP < 24$.

II.4.3. Upscaled Models for Push-Pull Tracer Tests

II.4.3.1. Generation of Heterogeneous Source-Zone Realizations

The first step in the development of the upscaled models for partitioning tracer test is to develop a suite of heterogeneous SZA realizations, spanning a realistic range of conditions. The simulations conducted under Task I were used as the basis for this effort. A total of 33 realizations were employed, encompassing both high and low $\ln K$ variance permeability fields. To maximize the number of realizations that could be handled, upscaled modeling was undertaken in two dimensional domains abstracted from these realizations. To obtain two-dimensional source zone realizations representative of a range of heterogeneity metrics, a vertical plane was passed through the DNAPL release point and one or two two-dimensional rectangular (40 cm high x 120 cm long) subsections were manually selected from each transect plane. The size of these 2D subsections was selected as representative of the scale of the zone interrogated in a PPTT (Davis et al. 2002, Istok et al. 2002, Davis et al. 2005, Pitterle et al. 2005).

Numerically generated dissolution mass removal data (Christ et al., 2010) were used to generate three or four DNAPL distribution scenarios from each 2D subsection. The selected location of the 2D domains was fixed in 3D space. Four snapshots at equal time intervals were taken from each domain and as independent realizations. The use of the same location at different mass removal stages provided variations of NAPL saturations and distribution architectures within the same permeability fields. In some cases, the third and fourth snapshots were not obtained because the entire mass within the marked 2D frame dissolved out during the first two stages. Using this technique, a total of 180 saturation realizations were generated from 65 two-dimensional permeability fields. This process was repeated for all 33 three-dimensional realizations. The process of fixing 2D frames within the 3D domains and selecting four temporal snapshots during the dissolution process is illustrated in Figure M.4.1.

Table M.4.1 Characteristics of the realizations and input parameters in numerical simulations. Additional and changed input compared to Table M.1.4 is presented here

Permeability Field	<u>Set 1</u>	<u>Set 2</u>	
Number of realizations	16	17	
$\overline{\ln(k)}$ (k in m/s)	26.0	26.0	
$\sigma_{\ln(k)}^2$	0.29	1.0	
Vertical correlation length: λ_z (m)	0.36	0.10	
Tracer Tests	<u>Tracer 1</u>	<u>Tracer 2</u>	<u>Tracer 3</u>
Tracer	Bromide	1-hexanol	2-octanol
Partition coefficient (L_{aq}/L_{NAPL})	-	17.4	149
Injection concentration (mg/L)	840	380	140
Molecular diffusivity in water, D_a (cm^2/s)	1.6 $\times 10^{-5}$	0.76×10^{-5}	0.65×10^{-5}

II.4.3.2. Source-Zone Metrics

In this research, the properties of source zones that may influence the effective mass transfer coefficient were explored to identify the factors controlling the upscaled mass transfer coefficient. The migration and entrapment of organic liquids in the subsurface is strongly influenced by both small and large scale heterogeneities in subsurface textural properties. The permeability fields are generally characterized by porosity, mean and variance of $\ln K$, and correlation lengths in the horizontal and vertical directions. The correlation lengths are obtained by constructing the semivariogram of the fields and fitting an exponential variogram model (Lemke et al. 2004).

The NAPL content in a domain is described by the overall mean saturation ($\overline{S_n}$). Apart from the total NAPL content, distribution of mass within the domain is a critical factor controlling the effective mass transfer coefficient. The shape of the distribution of the entrapped mass is another physical factor that could affect the effective mass transfer rate. The first and second spatial moments of the saturation matrix are used to quantify the NAPL distribution within the domain. The horizontal and vertical centers of mass are given by normalized first moments:

$$\bar{x} = \frac{M_{10}}{M_{00}} \quad \text{and} \quad \bar{z} = \frac{M_{01}}{M_{00}} \quad (\text{M.4.2})$$

The second spatial moment is a measure of mass spread about the center of mass, and is estimated in the horizontal and vertical directions by:

$$\sigma_{xx}^2 = \frac{M_{20}}{M_{00}} - \bar{x}^2 \quad \text{and} \quad \sigma_{zz}^2 = \frac{M_{02}}{M_{00}} - \bar{z}^2 \quad (\text{M.4.3})$$

Here:

$$M_{ij} = \int_{-\infty}^{\infty} \int_{-\infty}^{\infty} n \cdot \rho \cdot S_n(x, z) x^i z^j dx dz \quad (\text{M.4.4})$$

where ρ is the density of DNAPL, and x, z are horizontal and vertical distances of each node from the origin of the coordinate system.

II.4.3.3. Model Development

The two-dimensional simulator described in Section II.2.3.2 was implemented to model partitioning tracer tests in the generated heterogeneous fields. The effluent breakthrough curve obtained by the fine scale model was then taken as observation data for upscaled parameter fitting. For these simulations, a widely-used groundwater flow model, MODFLOW (Harbaugh, 2005), was coupled with the implementation of the linear driving force model (described in Section II.2.3.1) in a MATLAB (MATLAB 2008) script. Confined flow was simulated under constant flux boundary conditions. An empirical correlation (Nambi and Powers, 2003) was selected to estimate the local lumped mass transfer rate coefficient within each grid block, based upon its broader range of validity for organic phase saturations:

$$\text{Sh}^* = \frac{\hat{k} d_{50}^2}{D_a} = 37.2 \text{Re}'^{0.61} S_n^{1.24} \quad (\text{M.2.30-duplicate})$$

Here Re' is the modified Reynolds number; in which the mean grain size, d_{50} , describes the length scale and the seepage velocity, v , represents the velocity component.

Tracer test simulations were performed under conditions representative of field tracer tests. A pulse of a group of tracers, including one non-partitioning (conservative), i.e., bromide, and two partitioning alcohol tracers, i.e., 1-hexanol, and 2-octanol, was introduced to the domain. These selected tracers differ in their partitioning capacities, leading to chromatographic separation of tracers during the test. Tracers were uniformly injected across the left-hand boundary of each two dimensional sub-domain and a flux-averaged concentration at the right-hand boundary was quantified. One pore volume (1PV) of the tracer solution was injected, and followed by background solution flushing until either more than 99 percent of the injected mass was recovered or 40 PV of background solution was flushed through the domain. Tracer

characteristics and simulation conditions are according to Table M.1.4 with some modifications listed in Table 5.4.1. For each 2D domain (from a total of 180 domains) four tracer tests were simulated with flow rates ranging from 1 to 40 (mL/min).

All simulations were performed using a finely discretized ($5 \times 5mm$) two-dimensional grid. This level of discretization was chosen to permit resolution of the local flow field within the heterogeneous blocks at a scale consistent with the use of the local mass transfer coefficients. These simulations produced 480 sets of tracer breakthrough curves for further analysis (observation tracer data).

Following the development of the observation tracer data, a one-dimensional upscaled model was used to model the same tracer tests. The effective mass transfer coefficient in this upscaled model was fit to all 480 analyzed tracer tests. The non-partitioning tracer data were first used to fit the effective porosity and dispersivity. The fitted values for the dispersivity and effective porosity were then embedded in the model, and the upscaled model was fit to the breakthrough curves of 1-hexanol and 2-octanol tracers. A single effective mass transfer coefficient was used to simultaneously fit both tracer breakthrough curves. In this fitting, the 2-octanol data were weighted 5 times more than the 1-hexanol data in optimization algorithm. These weights were chosen based upon the higher potential of 2-octanol to partition (partition coefficient of 149 L_{aq}/L_{NAPL} for 2-octanol versus 17.4 L_{aq}/L_{NAPL} for 1-hexanol). The fit was performed using the lsqcurvefit function from MATLAB optimization tool. The mean squared error (MSE) between the observed and predicted breakthrough curves was calculated separately for all tests.

Once effective mass transfer rate coefficients were obtained for a wide range of source-zone configurations, a statistical analysis was performed to develop a constitutive equation descriptive of the mass transfer rate as a function of source-zone metrics. A multivariable power function was selected for the form of the constitutive model:

$$\frac{\overline{Sh}}{Sc} = \beta_0 \cdot x_1^{\beta_1} \cdot x_2^{\beta_2} \cdot \dots \cdot x_N^{\beta_N} \quad (M.4.5)$$

here $x_{1,2,\dots,N}$ are the predictor variables. Here the effective mass transfer coefficient ($\hat{k}, [T^{-1}]$) is expressed as the ratio of an upscaled Sherwood number ($\overline{Sh} = \hat{k}L^2/D_{aq}$) and the Schmidt number ($Sc = \nu/D_{aq}$). Multiple models were developed, sequentially incorporating increasing numbers of predictors. Models were evaluated based on three main statistics: adjusted r-squared; standard error of the model: S; and predicted residual sums of squares, PRESS (Helsel and Hirsch, 2002). The normal distribution of residuals, variance inflation factor (an index for the severity of multicollinearity between variables), and statistical significance of the coefficients were examined for all models.

Following the development of the upscaled mass transfer coefficient correlation, this expression can be incorporated into the upscaled model and used to estimate source zone metrics (selected predictor variables) and their associated confidence intervals.

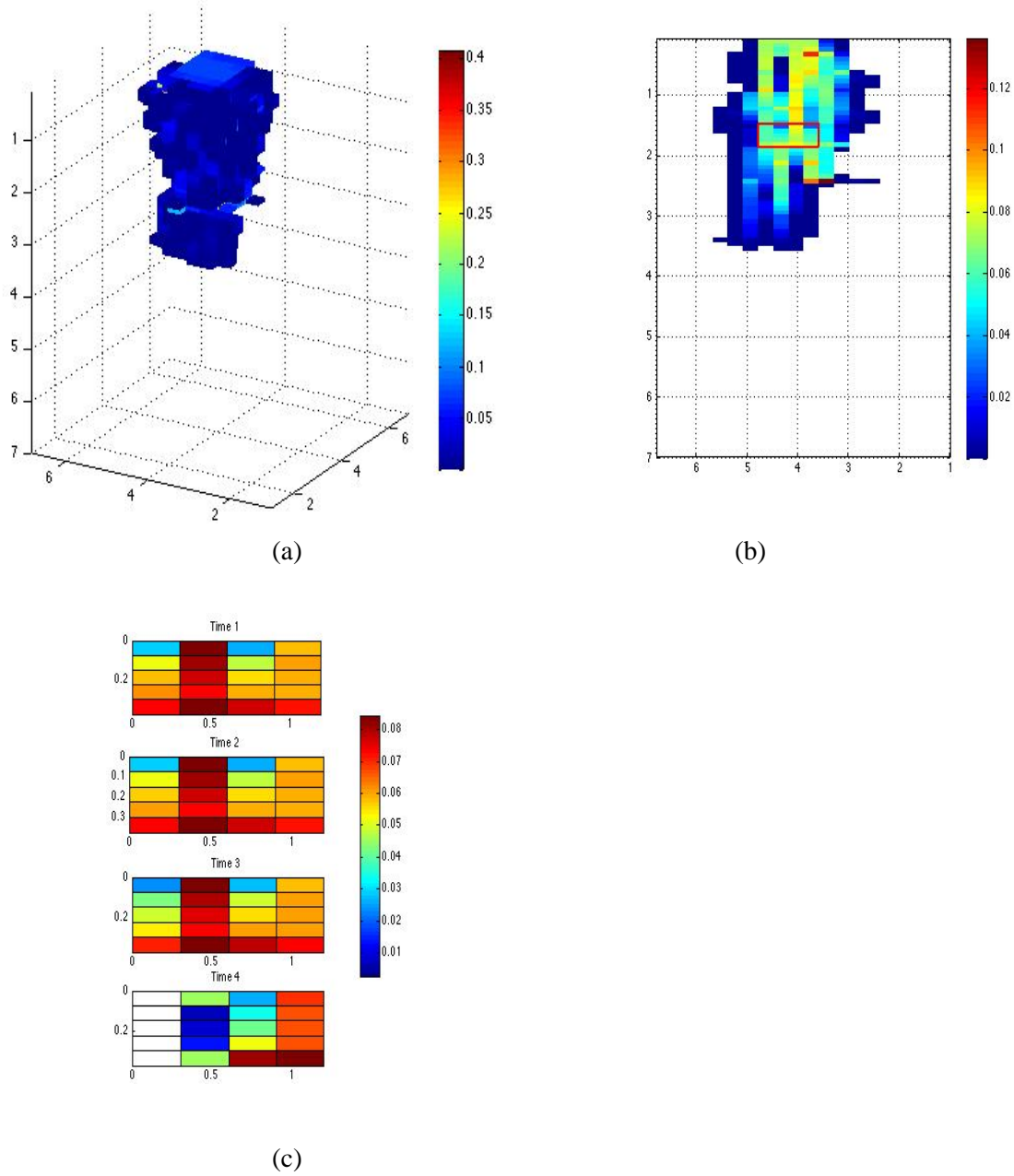


Figure M.4.1. Two-dimensional domains cropped out of three-dimensional numerically generated realizations; (a) 3D PCE-NAPL realizations generated by UTCHEM; (b) 2D vertical plane selected at the center of SZ, the marked rectangular region at the center marks the location and dimensions of the selected 2D regions for developing the upscaled model; (c) NAPL saturation in the selected region at four different time snapshots during the dissolution.

III. Results and Discussion

III.1 Data Generation for Metric Identification and Protocol Development

III.1.1. Batch and Aquifer Cell Experiments

III.1.1.1. Batch Experiments

A matrix of batch experiments was conducted to examine the equilibrium aqueous and micellar solubilization of PCE and TCE from DNAPL mixtures. Traditionally these systems have been described using a Raoult's law convention, where the aqueous solubility of the individual constituent (PCE or TCE) is multiplied by the mole fraction of each constituent in the NAPL. However, preliminary measurements performed during the initial stage of the project indicated that this assumption was not valid in the presence of certain surfactants. For these experiments, equilibrium aqueous solubilities were measured over a range of mole fractions to determine if deviations from Raoult's law convention were reproducible. The measured equilibrium aqueous solubilities of pure TCE and PCE were determined to be 1319 mg/L and 212 mg/L, respectively. The solubility of both TCE and PCE in water contacted with TCE/PCE NAPL mixtures over the mole fraction range of 0.2 to 1.0 was shown to follow the Raoult's law convention (Figure R.1.1), where the effective solubility was proportional to the solubility of the single component DNAPL and mole fraction of TCE or PCE in the mixed DNAPL. Therefore, the aqueous solubility of TCE or PCE from binary DNAPL mixtures is considered to be ideal under these experimental conditions.

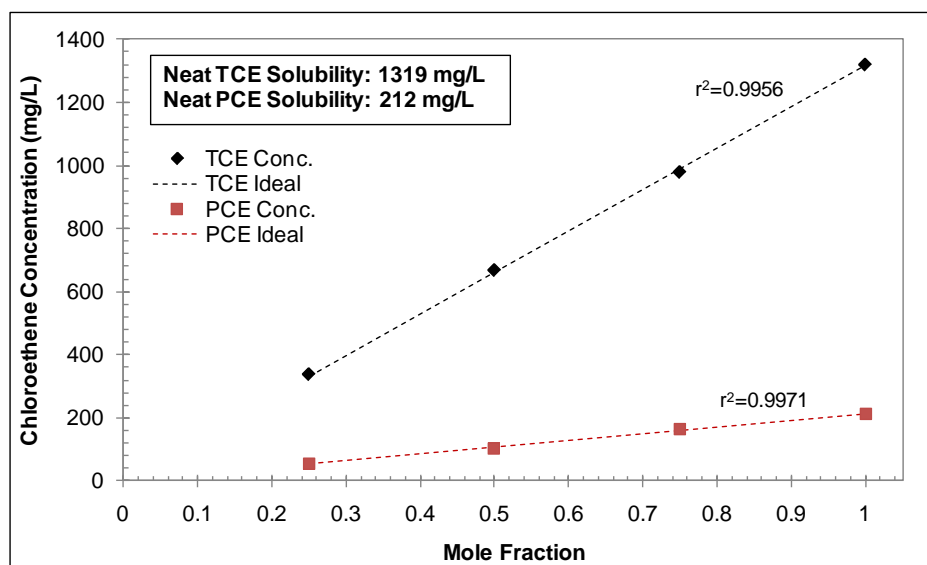


Figure R.1.1. Equilibrium aqueous solubility of TCE and PCE as a function of mole fraction.

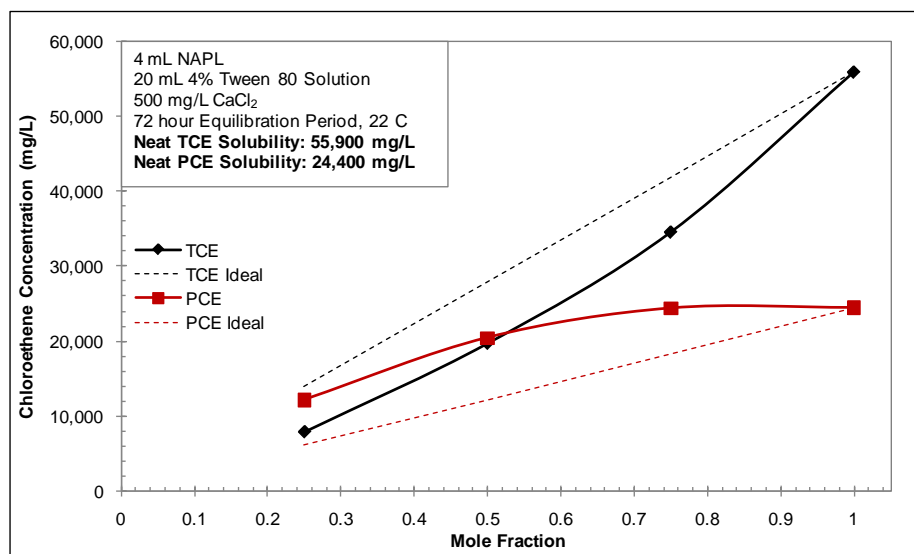


Figure R.1.2. Equilibrium solubility of TCE and PCE in 4% Tween 80 from binary DNAPL mixtures. Raoult's law predictions of ideal solubilization behavior are shown as dashed lines.

The equilibrium solubility of PCE and TCE was also measured in aqueous solutions of Tween[®] 80 (polyoxyethylene (20) sorbitan monooleate) to determine if the Raoult's law convention could be used to describe the micellar solubilization of each DNAPL constituent. Figure R.1.2 shows the measured equilibrium solubility of TCE and PCE versus the mole fraction of each constituent in binary DNAPL mixtures in a 4% (wt./wt.) Tween 80 solution. Based on the measured solubility of TCE and PCE in the Tween 80 solution, PCE was preferentially solubilized from the mixed NAPLs relative to TCE. Here, the measured solubility behavior of PCE could not be described using a Raoult's law convention, which under- and over- predicted the observed solubility of PCE and TCE, respectively. In a 4% Tween 80 solution, PCE solubilization was found to increase by 100, 67 and 32 percent at PCE mole fractions 0.25, 0.5 and 0.75, respectively. These data indicate that non-ideal behavior observed for PCE increased with decreasing PCE mole fraction in the NAPL. In contrast, TCE solubility was under-predicted by 43, 27 and 17.5 % at mole fractions of 0.25, 0.5 and 0.75 TCE, respectively. Similar behavior was observed for a range of Tween 80 solution concentrations (e.g., 1, 2, 3, and 5 % wt., data not shown). At all mole fractions and Tween 80 concentrations, preferential solubilization resulted in greater PCE solubility than would be predicted by the Raoult's law convention.

A second set of equilibrium solubility experiments was conducted with an anionic surfactant, Aerosol MA-80I to determine if the observed preferential solubilization of PCE was unique to Tween 80 or would occur with other surfactants. For a surfactant formulation consisting of 3.3% (wt.) Aerosol MA80I + 6g/L NaCl + 8% (wt.) 2-propanol, PCE solubility was 215, 102 and 41% greater than would be predicted based on Raoult's law convention at PCE mole fractions of 0.25,

0.5 and 0.75, respectively. The observed enhancements in PCE solubility resulted in a corresponding reductions in TCE solubility, which deviated from Raoult's law convention by 65, 55 and 36 percent for the 0.25, 0.5 and 0.75 mole fractions. These results clearly indicate that this behavior is not due to the surfactant formulation alone.

In order to determine if the observed deviations from Raoult's law were limited to chlorinated solvents such as PCE and TCE, a third set solubilization experiments was completed for two aliphatic hydrocarbons, decane and dodecane. It has been suggested that more polar compounds, including TCE and PCE, may be distributed in both the hydrophobic core and hydrophilic shell of surfactant micelles. In contrast, strongly hydrophobic compounds, such as decane and dodecane, are considered to partition primarily within the hydrophobic core of the micelles. Therefore, it was hypothesized that the solubility behavior of decane and dodecane would conform to the Raoult's law convention in micellar solutions of Tween 80.

The equilibrium solubility of decane and dodecane in 4 % (wt.) Tween 80 over the range of mole fractions tested is shown in Figure R.1.3. Although the solubility deviated slightly from predictions based on a Raoult's Law convention, the behavior was more predictable and decreased approximately linearly with the mole fraction in the NAPL phase. Since these hydrophobic compounds would predominantly solubilize into the hydrophobic core of the micelle, a number of other physiochemical properties pertaining to the NAPL mixture were used to evaluate other predictive models. Based on this analysis, it was found that the molar volume fraction of each component in the organic phase, which is similar to a Raoult's law convention, provided the best estimate of decane and dodecane solubility at a given surfactant concentration. This is similar to previous findings which suggested that solubility of hydrophobic compounds within the micelle core is inversely proportional to their molar volume (Nagarajan et al. 1985, Diallo et al. 1994).

To further evaluate the effect of DNAPL constituents on preferential dissolution, additional batch solubility experiments were completed with a 1:1 (molar) mixture of PCE and decane in micellar solutions of Tween 80 (Figure R.1.4). In all Tween 80 micellar solutions, decane was preferentially solubilized relative PCE, and the solubility of decane was under predicted based on a Raoult's law convention. PCE solubility was approximately 40% less than predicted assuming ideal behavior over the range of surfactant concentrations considered, whereas, decane solubilities were more than 100 percent greater than those predicted by the Raoult's law convention for all Tween 80 concentrations considered. These findings indicate that preferential solubilization is strongly influenced by the physiochemical properties of the NAPL constituents.

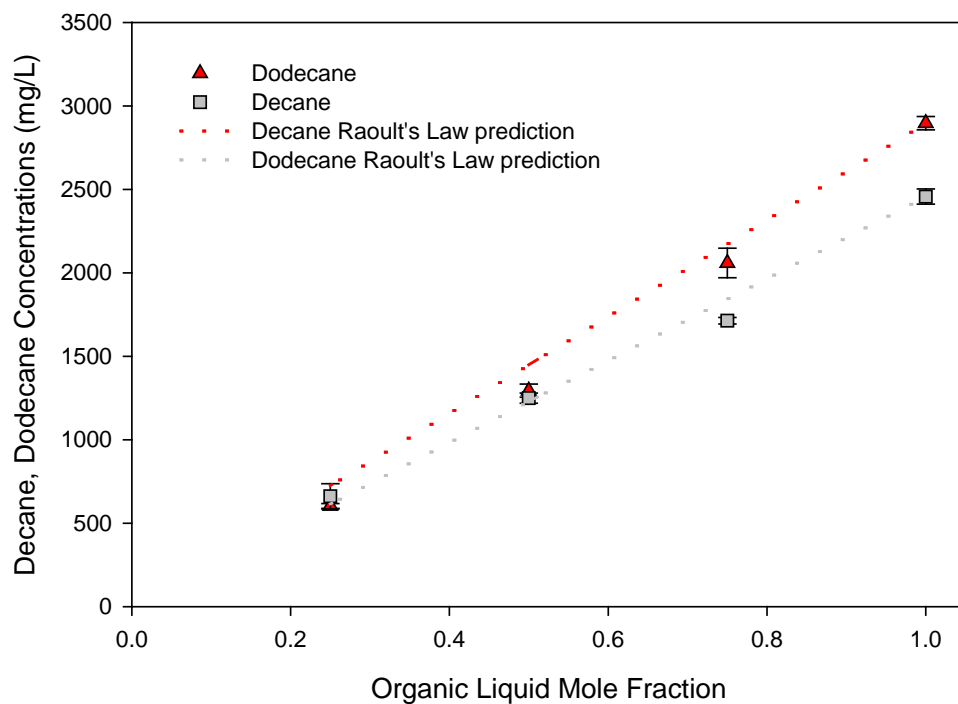


Figure R.1.3. Equilibrium solubility of decane and dodecane in 4% Tween 80 from a binary multicomponent organic liquid at various mole fractions.

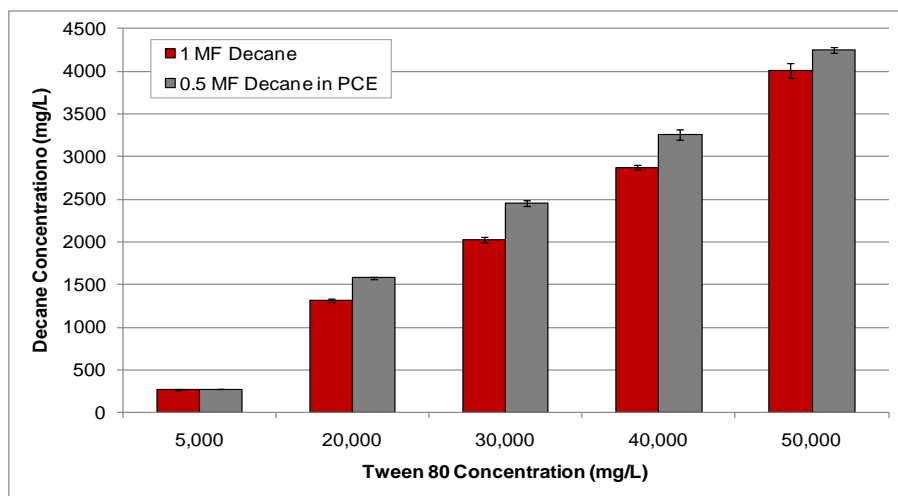


Figure R.1.4. Measured decane solubilities from a pure decane liquid and an a NAPL consisting of 1:1 (molar) PCE:decane at five concentrations of Tween 80.

The size of surfactant micelle prior to and after solubilization was characterized to provide insight into the solubilization behavior of the different organic constituents (Table R.1.1). The micelle diameter was found to increase with increasing solubility of the NAPL in the surfactant solution. For example, the percent increase in micelle size following solubilization of TCE and PCE was the greatest, which was attributed to the tendency for more polar organic compounds to partition into both the hydrophobic micelle core and the outer hydrophilic shell or palisade layer (Pennell et al. 1997). Considerably smaller increases in micelle diameter were observed when decane and dodecane were solubilized in 1% Tween 80 solutions. These straight chain hydrocarbons are very hydrophobic, and are therefore expected to partition primarily into the micelle core. Thus, the location or “locus” of solubilization in the micelle impacts the solubilization capacity for mixed NAPL systems. For example, the equilibrium micellar solubility of decane from a 1:1 mixture of PCE and decane was greater than that from the neat decane (Figure R1.4). This behavior was attributed to partitioning of PCE into the outer shell of the micelle, which acted to increase the size or “swell” the micelles. This behavior serves to increase the size of micelle core, creating a greater volume for strongly hydrophobic compounds, such as decane, to partition into within the micelle.

Table R.1.1. Measured changes in micelle size following NAPL solubilization in 1.0 % (wt.) Tween 80 solutions

	Average Micelle Diameter, Saturated Solution (nm)	Percent Increase
1% Tween 80	8.309 ± 0.25	-
TCE	27.44 ± 0.67	230.0%
PCE	14.72 ± 0.23	77.0%
Decane	10.00 ± 0.12	20.0%
Dodecane	10.20 ± 0.04	23.0%

Conclusions

Batch experiments conducted to examine the equilibrium micellar solubilization of PCE and TCE from a multi-component DNAPL in the absence, and in the presence of surfactant revealed the following key findings:

- Binary mixtures of TCE and PCE exhibited ideal dissolution behavior in water, which could be described using Raoult’s Law convention.
- Neat TCE and PCE exhibited classic Winsor Type I microemulsion formation in 1-5% Tween 80 solutions.

- PCE was preferentially solubilized relative to TCE from binary TCE- and PCE- DNAPL mixtures in both Tween 80 and Aerosol MA-80I micelles (i.e., anionic surfactant) over a range of mole fractions, indicating that Raoult's law convention could not be used to predict these aqueous concentrations.
- The location or "locus" of solubilization in the micelle impacts the solubilization capacity for mixed NAPL systems, where strongly hydrophobic compounds are expected to partition primarily into the micelle core while less hydrophobic compounds partition into both the core and palisade layer.

Furthermore, solute-micelle interactions are strongly dependent on the relative physio-chemical properties of the compounds. For example, PCE solubility was under predicted in the presence of strongly hydrophobic compounds such as decane, which act to swell the micelle core upon solubilization, increasing the overall micelle size. This behavior could directly influence the recovery of multicomponent DNAPLs when surfactant-enhanced aquifer remediation is employed for *in situ* treatment of DNAPL source zones. The results of these batch studies were also used to assist in the interpretation of mass removal and plume response in aquifer cell studies containing mixed DNAPL described in the following subsection.

III.1.1.2. Aquifer Cell Experiments

Results of source zone mass removal from multicomponent heterogeneous source zones: Ganglia-dominated source zones (AC 1 and AC 3)

To evaluate the dissolution of multicomponent source zones due to both water and surfactant flushing, a total of three aquifer cell experiments were completed with a source zone DNAPL consisting of a 1:1 molar mixture of TCE and PCE. The three aquifer cells (1.0 m length by 48 cm height with a 1.4 cm internal thickness) were packed to provide a variation in the initial SZA; AC1 and AC3 were designed to have a ganglia-dominated source zone, while AC2 contained a pool-dominated source zone (see below). This enabled the ability to evaluate the both the effect of surfactant enhanced flushing on mass removal from multicomponent source zones and the temporal evolution in mass discharge due to aqueous dissolution following preferential solubilization of one DNAPL over another from the multicomponent source zones.

Following establishment of steady flow in the aquifer cells and emplacement of the DNAPL source zones, the initial PF values, characterized using the light transmission system, were 0.38 and 0.36 for AC1 and AC3, respectively. These values indicate that the ganglia-dominated systems (AC1 and AC3) contained approximately 62 and 64 % ganglia over the course of each aquifer cell experiment and 38 and 36 % pools, respectively. The temporal evolution of the source zone and the associated down-gradient dissolved phase TCE and PCE concentrations are shown in Figure R.1.5 for AC1. Before introducing the surfactant, the source zone was ganglia-dominated, and the mass flux of both TCE and PCE was relatively uniform throughout the entire vertical height of the down-gradient plume area. The maximum flux-averaged effluent concentrations during this water flushing period were 440 and 100 mg/L for TCE and PCE,

respectively. Localized plume concentrations measured from the side-ports approaching the aqueous solubility, 550 mg/L TCE and 100 mg/L PCE, of both chlorinated solvents based on a Raoult's Law convention. During the first surfactant flood, flux-averaged TCE and PCE effluent concentrations increased to 1210 and 5240 mg/L, respectively, which represented an increase of 3- and 40-fold over the maximum observed concentrations during water flushing. Due to the greater aqueous solubility of TCE, TCE mass removal from the source zone was greater than PCE during water flushing, with 58 percent of the TCE mass removed from the DNAPL source zone, compared to only 12 percent for PCE prior to the first surfactant flood. This resulted in an overall source zone DNAPL mole fraction of 0.3 and 0.7 for TCE and PCE. Consistent with the equilibrium solubilization studies discussed above in Section III.1.1.1, PCE was preferentially solubilized relative to TCE during flushing with 40 g/L Tween 80 (Figure R.1.5 and R.1.6). After the first surfactant flushing period, only approximately 5 g of TCE mass was removed from the source zone, compared to 17 g of PCE. The significantly greater amount of PCE mass removal can be attributed to the increased mole fraction of PCE in the source zone and the preferential solubilization of PCE relative to TCE.

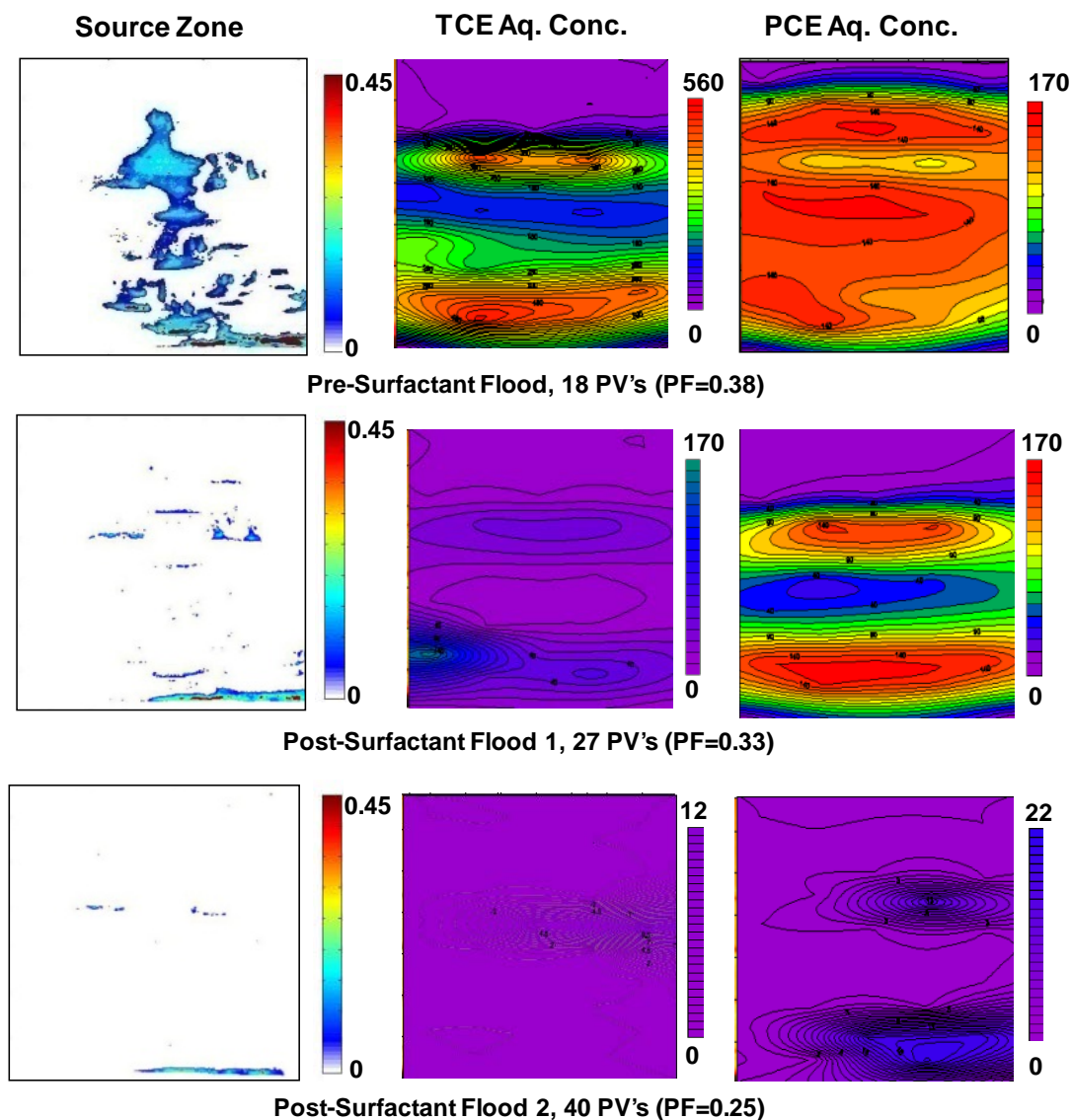


Figure R.1.5. Temporal evolution in DNAPL source zone and corresponding down-gradient dissolved phase mass flux for AC1 initial ganglia dominated source zone containing 1:1 (m/m) TCE:PCE-DNAPL source zone) prior to and following surfactant floods. Source zone DNAPL saturations are in volumetric fractions; downgradient TCE and PCE aqueous concentrations are mg/L.

Similar behavior was observed following the second surfactant flush; however, the mass removal efficiency was less than observed during the first surfactant flush. This observation was attributed to the decreased mass present in the source zone (with only 15 and 16 % of the total

mass remaining), which resulted in a decreased surface area available for dissolution. Similar behavior has been observed in a number of studies, where mass removal efficiency has decreased with extended aggressive mass removal approaches (MacDonald and Kavanaugh 1994, Londergan et al. 2001, Childs et al. 2006, Stroo et al. 2012).

Although surfactant flushing removed a significant portion of the source zone mass, the source zone remained ganglia-dominated both before and following the surfactant flushing periods (Figure R.1.5). This finding is contrary to the behavior typically observed both in numerical simulations and lab scale aquifer cell experiments that have quantified the DNAPL source zone saturation (Christ et al., 2006; Phelan and Abriola, 2006; Brusseau et al., 2008; DiFilippo et al., 2010; DiFilippo and Brusseau, 2011). Although the preferential depletion of ganglia has been observed, leaving only high saturation pools in the source zone, solubilization studies using high resolution magnetic resonance imaging (MRI) techniques have found that the gradual dissolution of pooled regions from heterogeneous source zones can result in the formation of ganglia once a certain volume of the DNAPL pool has dissolved (Zhang et al., 2007; Zhang et al., 2008; Werth et al., 2010). In effect, regions containing high-saturation DNAPL pools are converted to ganglia-dominated zones as the source zone mass is depleted, rather than remaining as high-saturation pools until complete DNAPL mass removal occurs. Due to the large volume of PCE mass removed during surfactant flooding, this could explain why the AC 1 source zone remained ganglia-dominated. Upon completion of the AC1 experiment and measurement of the DNAPL mass remaining in the system, it was determined that 72% of the TCE mass removed can be attributed to dissolution during water flooding, and the remaining 28% occurred during the surfactant flooding period (Figure R.1.6). Conversely, 80 % of the PCE mass removed during this aquifer cell experiment was due to surfactant enhanced dissolution, while the remaining 20% was due to aqueous dissolution (Figure R.1.6).

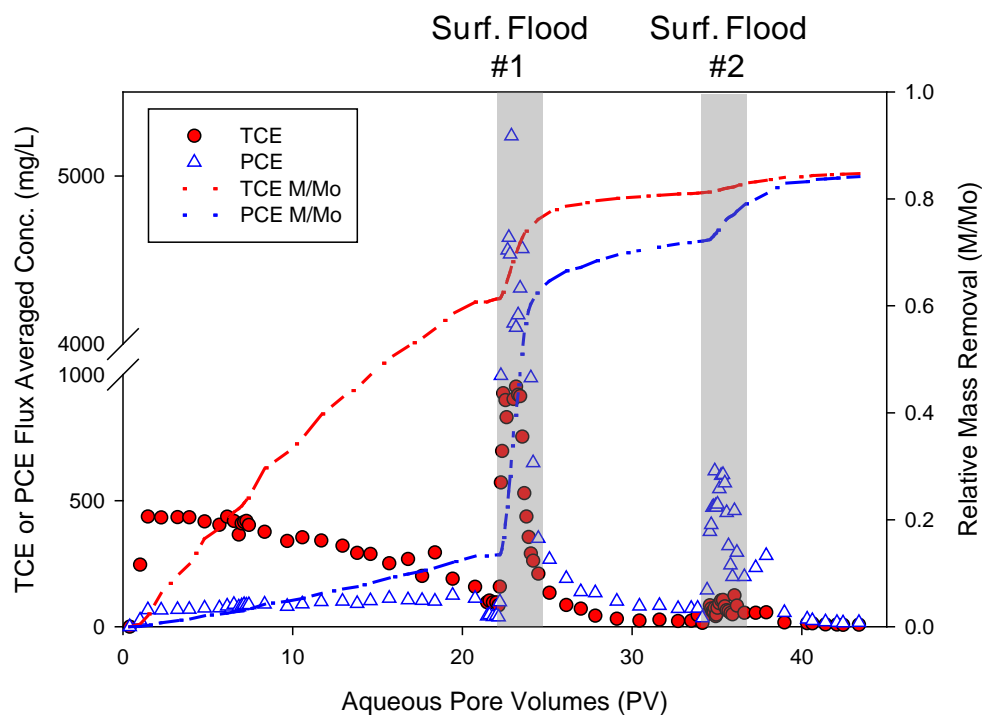


Figure R.1.6. TCE and PCE flux-averaged effluent concentrations and normalized mass removed as a function of pore volume for AC1. Flux averaged effluent concentrations during surfactant flood 1 (23 PV) and 2 (35 PV) are shown by the grey boxes.

Similar to AC1, AC3 was designed to contain a ganglia-dominated source zone consisting of a 1:1 (molar) TCE:PCE DNPL source zone. The experimental conditions in AC3 were similar to those in AC1, and additional aquifer cell further evaluated the influence of extended water flushing after surfactant flooding to evaluate the effect on downgradient mass discharge and overall DNAPL source zone mole fraction. Evolution of the DNAPL source zone saturation distribution profiles and corresponding down-gradient dissolved-phase plumes for AC3 are shown in Figure R.1.7. The GTP decreased following each surfactant flood, indicating that a significant portion of the mass removed can be attributed to dissolution of ganglia located in residual saturated zones throughout the source.

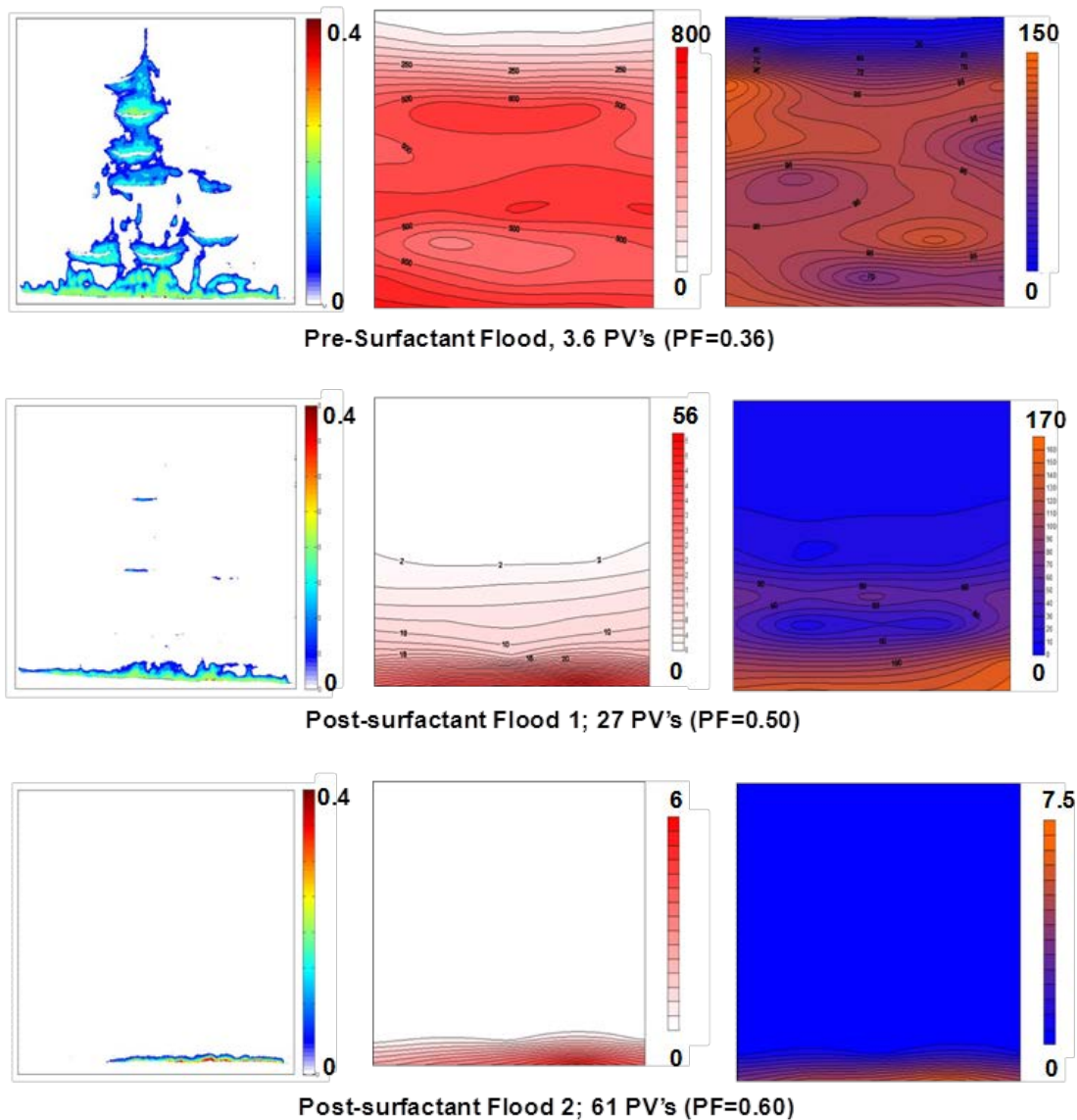


Figure R.1.7. Temporal evolution in DNAPL source zone (column 1) and corresponding down-gradient dissolved phase TCE (column 2) and PCE (column 3) mass flux for AC3 (initial ganglia dominated source zone containing 1:1 (m/m) TCE:PCE-DNAPL source zone) prior to and following surfactant floods. Source zone DNAPL saturations are in volumetric fractions; downgradient TCE and PCE aqueous concentrations are mg/L.

Figure R.1.8 depicts the flux-averaged effluent concentrations of TCE and PCE (left-y-axis) and the percent of TCE and PCE mass removed from the mixed DNAPL AC3 experiment as a function of volume eluted from aquifer cell (i.e., PVs). Prior to the first surfactant flood (15.5 PVs), flux-averaged effluent concentrations of TCE and PCE were approximately 163.2 and 91.6

mg/L, respectively, while the percent mass removal for TCE and PCE were 52.2 and 12.5 percent, respectively. These data clearly demonstrate that TCE was preferentially depleted from the mixed DNAPL due to aqueous dissolution, which was similar to the behavior observed in AC1, and has been observed in a number of other studies of dissolution from mixed organic liquids in non-equilibrium, porous media systems (Lesage and Brown, 1994; Brusseau, 1996; Roy et al., 2004). Following the first surfactant flood, which removed an additional 20 and 49 percent of the TCE and PCE mass, respectively, from the aquifer cell, flux-averaged effluent concentrations of TCE and PCE were reduced to approximately 26.2 mg/L and 39.1 mg/L, respectively. Following the second surfactant flood (45.0 PVs), an additional 2.7 percent of the TCE mass and 4.9 percent of the PCE mass were removed, with flux-averaged TCE effluent concentrations of 12.5 mg/L and PCE concentrations of approximately 10.3 mg/L. These results are consistent with experimental observations noted in AC1.

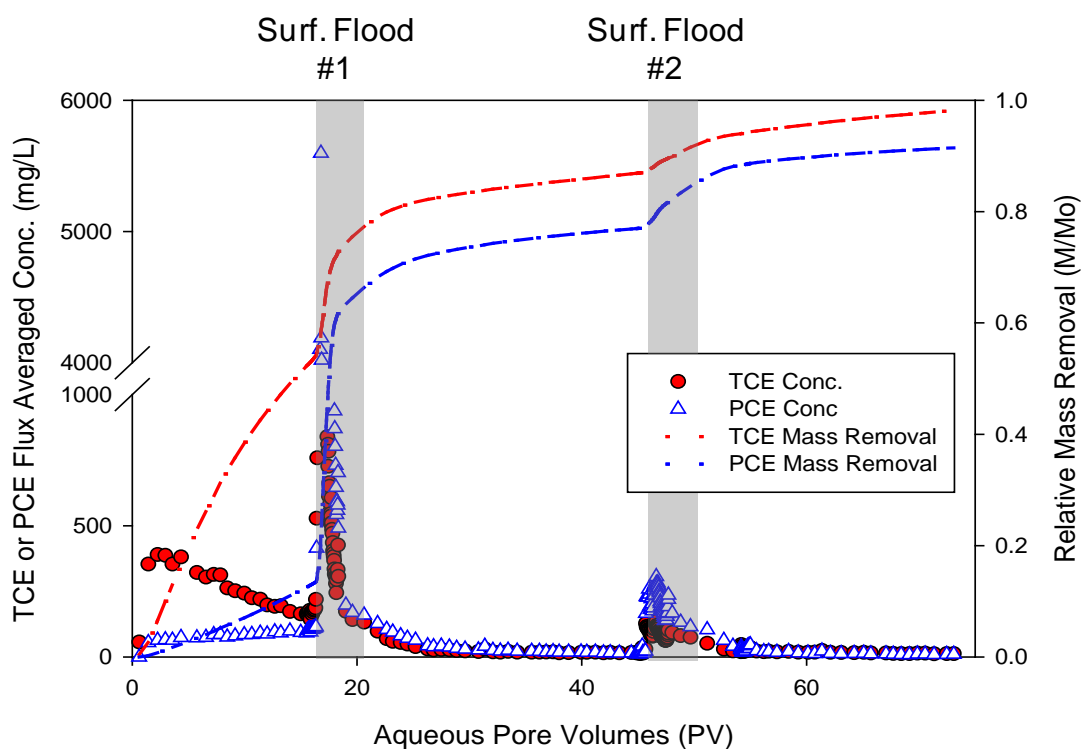


Figure R.1.8. TCE and PCE flux-averaged effluent concentrations (left axis) and fractional mass recovered (right axis) as a function of pore volume flushed through the aquifer cell for AC3. Flux averaged effluent concentrations during surfactant flood 1 (15.5 PV) and surfactant flood 2 (45 PV) are shown by the grey boxes.

Temporal changes in TCE and PCE flux averaged concentrations (left axis) due to aqueous dissolution and the average TCE and PCE mole fraction (right axis) with PV for the DNAPL

source zone are shown in Figure R.1.9. The direct comparison illustrates that flux averaged aqueous concentrations were strongly dependent on the source zone average TCE- and PCE- DNAPL mole fraction. Reduction in TCE mass due to preferential aqueous dissolution from the source and increasing overall PCE mole fraction resulted in an increased PCE mass discharge. During surfactant flushing, increased mass removal of PCE from the source zone relative to TCE, due to preferential solubilization, decreased the PCE mole fraction. After the first surfactant flood, the PCE mole fraction increased due to greater aqueous TCE dissolution, which affected the reduction in mass discharge of PCE from the mixed source. These findings indicate that the competitive solubilization during surfactant enhanced aquifer remediation can influence the molar composition of the NAPL source zone and alter the mass discharge characteristics of the source zone during active remediation.

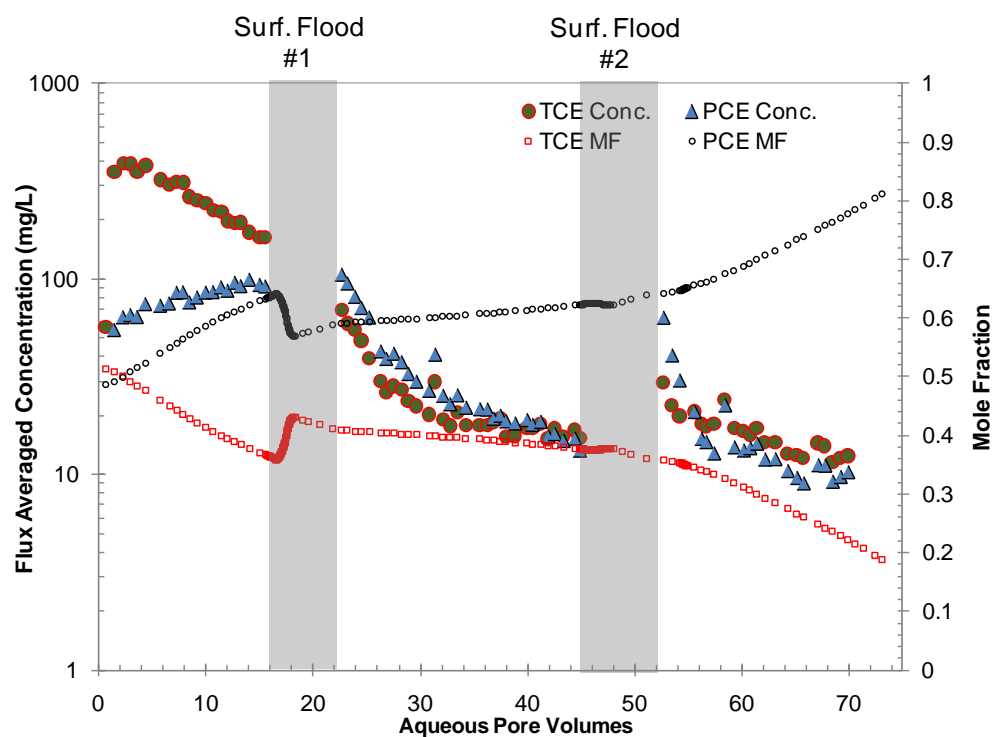


Figure R.1.9. TCE and PCE flux-averaged effluent concentrations (left axis) and source zone averaged DNAPL mole fraction (right axis) as a function of pore volumes flushed through AC3. Note that elevated effluent concentrations due to surfactant flooding were omitted (represented by gray boxes).

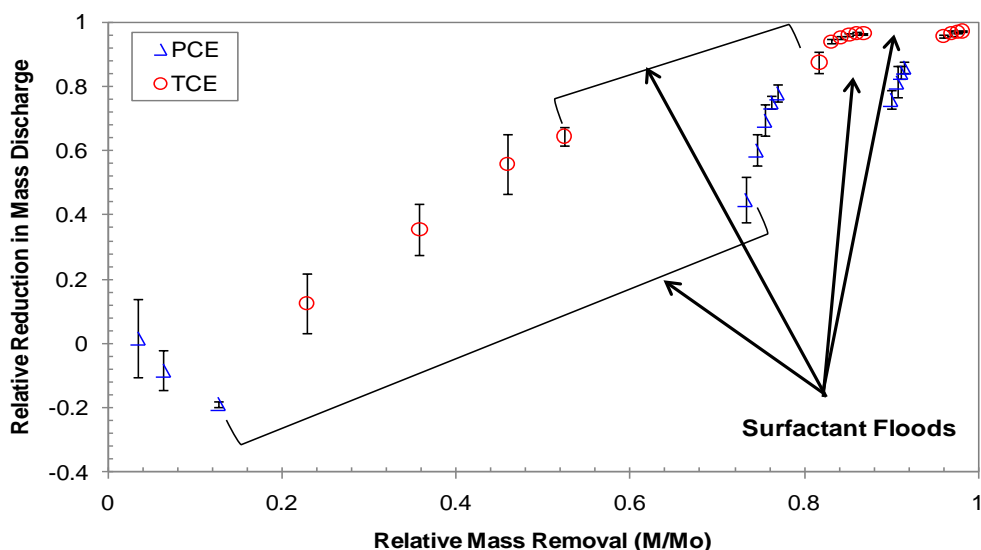


Figure R.1.10. Relative reduction in mass discharge for TCE and PCE in AC3 as a function of the relative mass removed for each component. A relative reduction <0 indicates an increase in mass discharge, while a relative reduction >0 indicates a decrease in mass discharge.

To further explore the preferential depletion of TCE and the effect of molar composition on mass discharge from the TCE and PCE 1:1 molar source, flux-averaged effluent concentration data during water flushing were expressed as relative reduction in mass discharge versus relative mass removal for TCE and PCE (Figure R.1.10). Each data point represents the arithmetic mean of 5 measurements (7.5 PVs) and the error bars represent one standard deviation from the mean. The relative reduction in TCE mass discharge increased significantly during the water flushing portion of the experiment due to the greater water solubility of TCE relative to PCE. This level of TCE removal resulted in negative reductions in mass discharge of PCE from the mixed source due to the changing molar composition (increasing PCE mole fraction; decreasing TCE mole fraction) within the DNAPL. An increase in the PCE mole fraction resulted in a greater PCE effective solubility and increased mass discharge. These findings are consistent with the down-gradient dissolved phase effluent concentrations and temporal change in mole fraction shown in Figure R.1.9, which indicates that PCE effluent concentrations increased as TCE was depleted from the source zone. Following surfactant flood 1, PCE mass discharge decreased significantly due to preferential solubilization of PCE-DNAPL mass removal. This behavior is unique to source zones that contain multicomponent DNAPL, and is driven by the preferential solubilization of the different components in the organic phase mixture. In contrast, changes in mass discharge from single component source zones tend to either remain constant or decrease as mass is removed (Stroo et al., 2003; Jawitz et al., 2005; Fure et al., 2006).

Results of source zone mass removal from multicomponent heterogeneous source zones: Pool-Dominated Source Zone (AC 2)

While A1 and AC3 were designed to contain ganglia-dominated source zones, AC2 was intended to yield a pool-dominated source zone, where the DNAPL was present predominantly at values greater than the residual value for the 20/30 mesh Accusand sand (saturation >0.11). Following addition of the 1:1 (molar) TCE:PCE and a 24 hour equilibration period, the source zone in AC2 was significantly pool-dominated, with an initial PF of 0.88 (Figure R.1.11). These values indicate that the pool-dominated aquifer cell (AC2) contained 12 % ganglia and 88 % pools. The presence of these pools that were located throughout the source zone resulted in temporal changes in mass discharge that differed from those observed in the ganglia-dominated aquifer cells (AC1 and AC3), both with respect to mass removal efficacy during surfactant and water flushing.

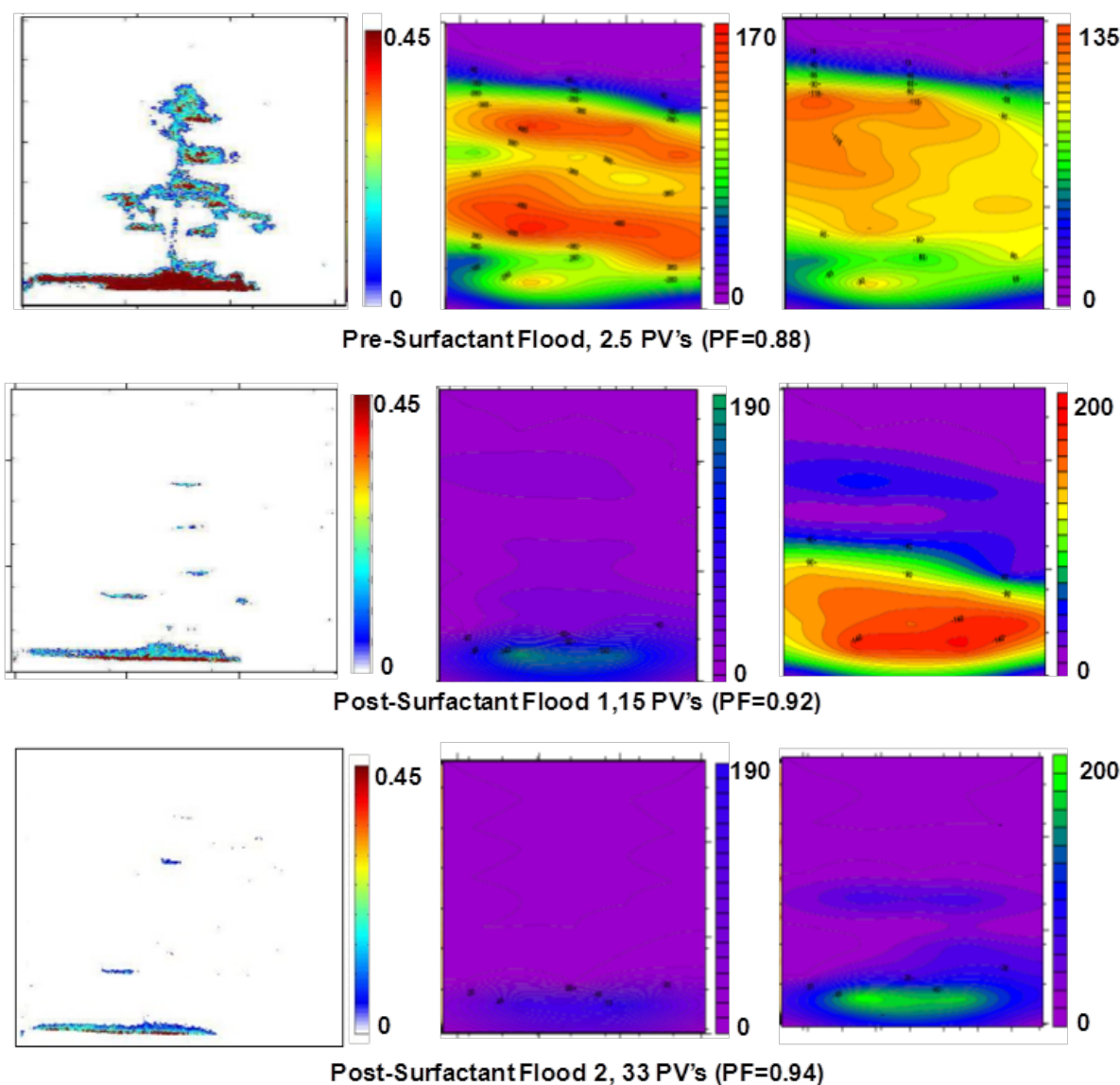


Figure R.1.11. Temporal evolution in source zone architecture (column 1), down gradient dissolved phase TCE (column 2) and PCE (column 3) mass flux from the pooled source zone consisting of 1:1 (m/m) TCE:PCE-DNAPL source zone in AC2. Source zone DNAPL saturations are in volumetric fractions; downgradient TCE and PCE aqueous concentrations are mg/L.

The pool-dominated source zone configuration (AC2) yielded initial maximum flux averaged effluent concentrations during the water flushing period of 292.3 mg/L and 65.3 mg/L, respectively, for TCE and PCE (Figure R.1.12). These values were lower than those observed in AC1 and AC3, and can be attributed to the poorly assessable areas of high saturation DNAPL

present as pools. This resulted in only approximately 11.1% and 1.8 % of the TCE and PCE mass removed from the DNAPL during the initial water flushing period. Furthermore, prior to the first surfactant flood, dissolved phase TCE and PCE concentrations reached a maximum value and were then declining rapidly after 8 PVs of water flushing. This sharp decline in concentrations was attributed to the rapid dissolution of the small volume of DNAPL present in the source zone as ganglia, which left behind DNAPL that was predominately located in high-saturation pools. This explanation was consistent with the observed increase PF values over time, based on light transmission measurements of the source zone (Figure R.1.11).

Following an initial water flushing period of 11 PVS, a 40 g/L (4% wt.) pulse of 4% Tween 80 solution was introduced in to the aquifer cell. This first surfactant flood removed an additional 28 and 32 percent of the TCE and PCE mass, respectively, present in the source zone. During surfactant flooding, TCE and PCE concentrations rose to 2,080 and 3,000 mg/L, respectively. The elevated concentrations of PCE during the first surfactant flush were attributed to the preferential solubilization behavior of PCE in Tween 80, as was observed in aquifer cells with ganglia-dominated source zones (AC1 and AC3). The concentrations of TCE and PCE observed in the effluent represented a 7- and 46- fold enhancement in solubility over the concentrations observed during the initial water flushing period, which was greater than that from the ganglia-dominated source zones. This trend was attributed to the lower mass flux values initially observed, and the greater amount of mass present at the beginning of this surfactant flushing period as compared to AC1 and AC3. Flux-averaged effluent concentrations of TCE were reduced to approximately 57.0 mg/L, whereas, flux-averaged effluent concentrations of PCE increased to approximately 123.3 mg/L during water flushing after the first surfactant flood. The second phase of surfactant flushing removed an additional 3 % of the TCE mass and 6 % of the PCE mass from AC3, and flux-averaged effluent concentrations of TCE and PCE were reduced to approximately 35.7 mg/L and 30.2 mg/L, respectively. The two surfactant floods removed a total of 55 % and 60 % of the initial TCE and PCE mass from the aquifer cell. Based on the light transmission analysis, the NAPL removed was predominately depleted from the upper regions of the source zone. This upper region contained smaller pools than those located on the lower confining layer (Figure R.1.11), which would be more accessible to flow in the aquifer cell during both water and surfactant flushing. Following completion of the second surfactant flood, approximately 70 additional PVs of water were flushed through the aquifer cell to estimate the time scale for reduction of the flux averaged concentration below detectable levels. This prolonged dissolution period resulted in relatively constant mass discharge from the aquifer cell, accounting for an additional 30 and 20 percent removal of TCE and PCE mass, respectively.

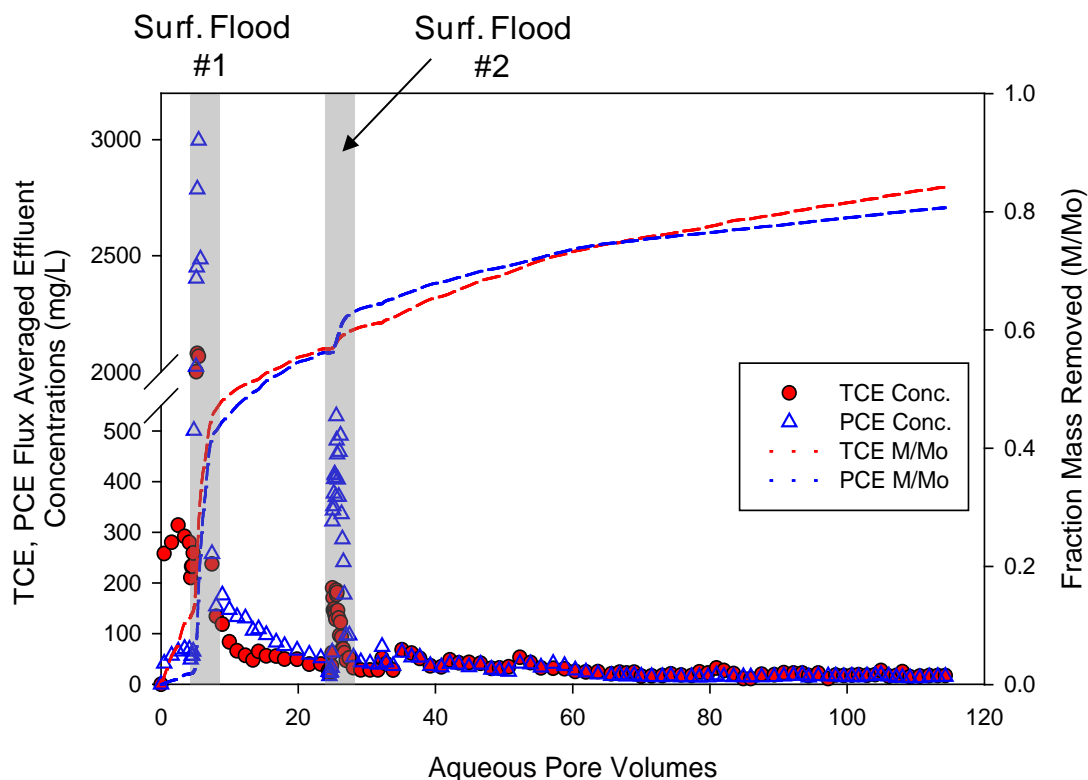


Figure R.1.12. TCE and PCE flux-averaged effluent concentrations (left axis) and fractional mass removed (right axis) from the pool dominated aquifer cell experiment (AC2). Flux averaged effluent concentrations during surfactant flood 1 (11 PV) and surfactant flood 2 (25 PV) are marked by the grey boxes.

Due to the high percentage of pools initially present in the source zone for AC2, the reduction in mass discharge and changes in DNAPL source zone mole fraction were different from the results obtained in AC1 and AC3. Figure R.1.13 depicts the source zone DNAPL mole fraction and flux-averaged effluent concentrations as a function of pore volumes flushed through the aquifer cell. Elevated TCE and PCE effluent concentrations measured during surfactant flushing were not included. As can be seen in Figure R.1.13, the lower TCE and PCE flux-averaged effluent concentrations during both water flushing and surfactant flushing resulted in a relatively constant DNAPL source zone mole fraction composition for both TCE and PCE, which continued throughout the entire experiment. This resulted in comparable dissolution behavior for both contaminants, which was not observed in either of the ganglia-dominated cells (AC 1 and AC3). This trend was also evident from the fractional mass removed curves shown in Figure R.1.12. For both TCE and PCE, the mass removed as a function of pore volume introduced exhibits a slight upward trend during all water flushing periods. This finding suggests that the SZA itself can control the long term dissolution behavior from heterogeneous, multicomponent source

zones. This is an important consideration when attempting to design remediation approaches for subsurface restoration of aquifers contaminated with mixtures of organic liquids in heterogeneous permeability fields.

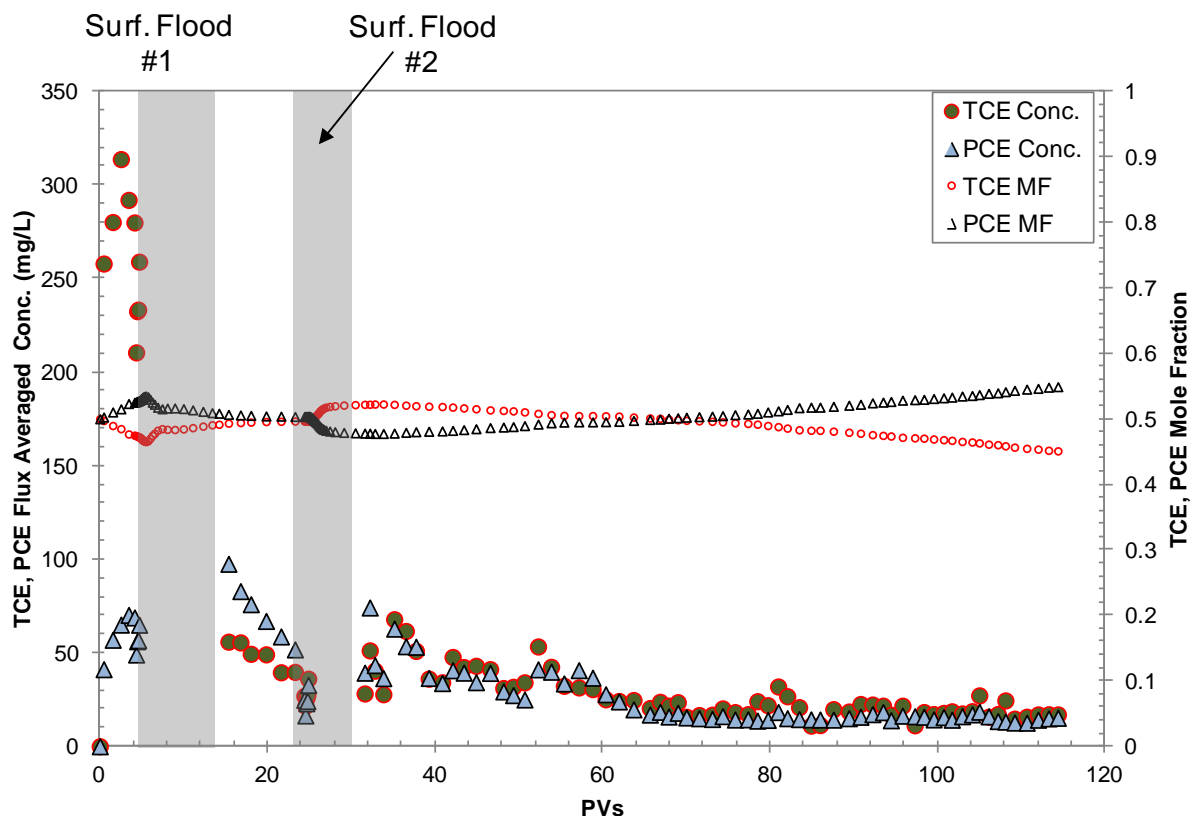


Figure R.1.13. TCE and PCE flux-averaged effluent concentrations during aqueous flushing alone and source zone averaged mole fraction as a function of pore volume for AC2. Flux averaged effluent concentrations during surfactant floods 1 and 2 were removed and are represented by grey boxes.

Results of Single component DNAPL source zone aquifer cells

While the purpose of AC1, AC2 and AC3 was to evaluate the mass flux behavior from multicomponent source zones before and after aggressive mass removal, AC4 was designed to study the dissolution of a single component source zone (TCE) due to aqueous dissolution alone. This resulting data set was later used for training of mathematical models. Light transmission analysis of the initial SZA yielded a PF of 0.47, indicating that the DNAPL source zone

consisted of approximately 53 % ganglia and 47 % pools. Evolution of the DNAPL source zone saturation distribution and corresponding down-gradient dissolved-phase plumes are shown in Figure R.1.14. The resulting DNAPL source zone distribution consisted of high-saturation pools located at the interface between low and higher permeability media, while ganglia-dominated regions were distributed throughout the vertical height of the source region. Mass removal from AC4 was the result of dissolution alone, as no surfactant was used to enhance mass removal. Initial aqueous flushing of the TCE-DNAPL resulted in preferential dissolution of higher surface area ganglia regions, which in turn, increased the source zone PF (Figure R.1.15). Following an initial monotonic increase in PF, the proportion of DNAPL mass remaining in pooled regions stabilized at 65% due to the slow dissolution from pooled regions and transition of higher saturation DNAPL zones to lower saturation, ganglia-dominated regions. Following removal of 80% of the DNAPL mass, the PF varied significantly as a large portion of the pools were reduced to saturations below the residual saturation threshold (18 %) , and rapidly dissolved, until all DNAPL mass was removed from the source zone.

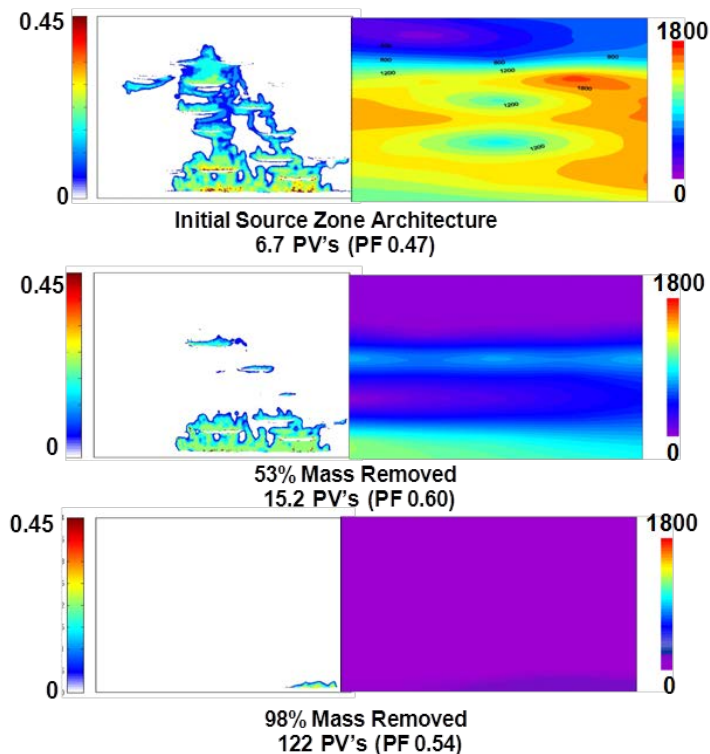


Figure R.1.14 Temporal evolution in source zone architecture and downgradient, dissolved phase TCE plume development in the neat TCE aquifer cell experiment (AC4). Source zone DNAPL saturations are in volumetric fractions; downgradient TCE aqueous concentrations are mg/L.

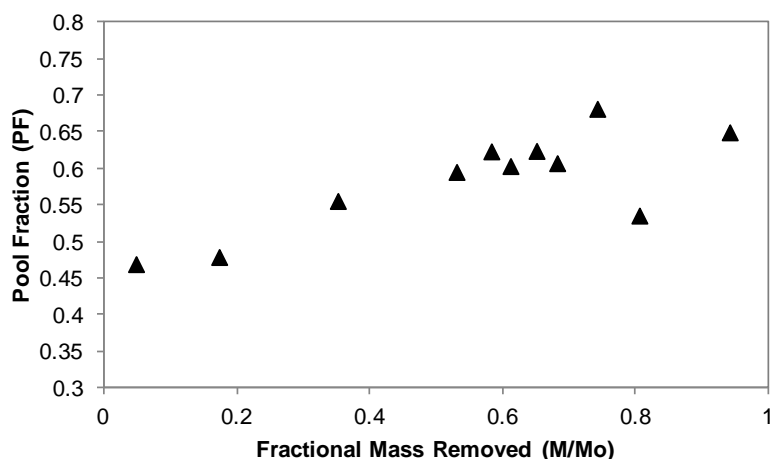


Figure R.1.15. Temporal changes in source zone PF as a function of TCE-DNAPL fractional mass removed.

Dissolved phase plume concentrations measured in down-gradient sampling ports indicated that TCE plume concentrations were initially detectable throughout the vertical height of the aquifer cell (Figure R.1.14, top), primarily due to dissolution from high surface area ganglia which resulted in TCE flux-averaged effluent concentrations and mass discharge rate of 820.5 mg/L and 1030 mg/day, respectively. As high surface area ganglia became depleted from the source zone, mass discharge decreased, and sustained dissolution from higher saturation pooled regions dominated. This resulted in a reduction in down-gradient TCE aqueous concentrations and multi-step flux averaged effluent behavior as mass removed from the source zone increased (Figure R.1.16). Similar behavior has been observed in previous studies of dissolution from heterogeneous DNAPL architectures (Zhang et al., 2008; Christ et al., 2010; DiFilippo and Brusseau, 2011). This effect resulted primarily from differences in dissolution kinetics between DNAPL pools and ganglia, which is primarily influenced by interfacial area available to flowing water and the DNAPL present in the source zone as either pools or ganglia. Upon transitioning to a pool dominated source zone, sustained mass loading resulted in a relatively constant flux-averaged effluent concentration until greater than 95% of the initial TCE-DNAPL mass had been removed.

To evaluate the full range of mass flux-mass removal due to aqueous dissolution for the TCE-DNAPL source zone, down-gradient dissolved phase concentrations and flux-averaged effluent concentrations were measured until no visible DNAPL was present in the source zone. Upon removal of all TCE-DNAPL detectable by light transmission, the final TCE flux averaged effluent concentration and mass discharge values were reduced to 0.36 mg/L and 0.632 mg/day, respectively. Post-experiment dissection and extraction of the source zone region suggest that the

volume of TCE-DNAPL present in the source zone had been reduced to less than 0.005 uL, and that TCE mass discharge was primarily attributed to the release of dissolved phase TCE from lower permeability lens located throughout the aquifer cell. This finding highlights the importance of understanding the capacity of low permeability zones to store dissolved contaminants due to diffusive mass transfer to and from low permeability zones, in this case the low permeability lenses that were suspended within the more transmissive background porous sand.

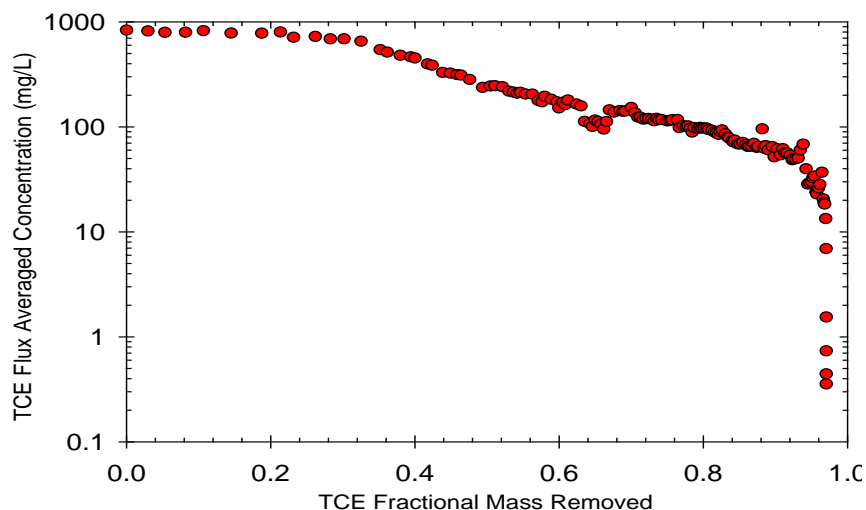


Figure R.1.16. TCE flux-averaged effluent concentration as a function of mass removed from the source zone for AC4.

To evaluate the influence of image scaling on SZA metrics, different DNAPL averaging technique were utilized to quantify the PF of AC4. This analysis was performed to investigate the effects of averaging window size and approach on source zone metrics obtained from the aquifer cells. The averaging approach used for source zone metrics is particularly important when developing simplified mass discharge models at the aquifer cell scale. These correlations are often developed using field scale simulations or applied to large scale systems, and thus, should account for differences in scale. Using the averaging methods presented by Christ et al. (2012), Figure R.1.17 shows the influence on the SZA and PF obtained for AC4 when different averaging windows are used.

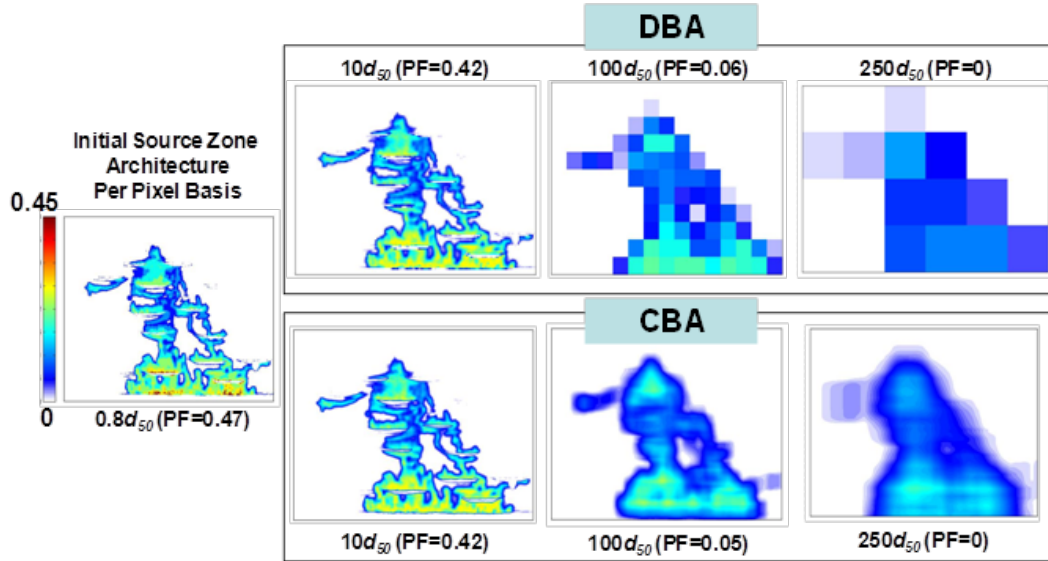


Figure R.1.17. Source zone morphology and PF at 10, 100 and 250 times the median sand grain size (d_{50}) for the initial SZA in AC4.

As the averaging window is increased for the discrete block averaging (DBA) and continuum block averaging (CBA) approaches, the PF value suggest that the source zone became more dominated by ganglia than pools. When the averaging window is further increased in size, the fraction of source zone DNAPL existing as high-saturation pools approaches zero. The trend of NAPL saturation becoming more ganglia dominated with increasing averaging window size is due to the fact that pool volume is determined based on volumetric saturation. Therefore, as the averaging window is increased, the saturation decreases since the total volume of DNAPL present is constant and the volume over which it is averaged increases to the entire domain. The effective saturation is then reduced below that of the residual saturation cutoff (e.g., 13%), resulting in all windows being considered as regions occupied by ganglia. Furthermore, while the averaging technique used significantly affected the boundaries and general shape of the DNAPL source zone saturation distribution (Figure R.1.17), the source zone metric (PF) was not strongly dependent, indicating that both averaging approaches could be used as an upscaling technique for aquifer cell experiments. Based on the results of Christ et al. (2010) detailed analysis, a 30 times the median grain size diameter ($30 \times d_{50}$) was determined to be optimum averaging window size, and this methodology was used to assess the evolution in mass flux from AC-4 (Figure R.1.18).

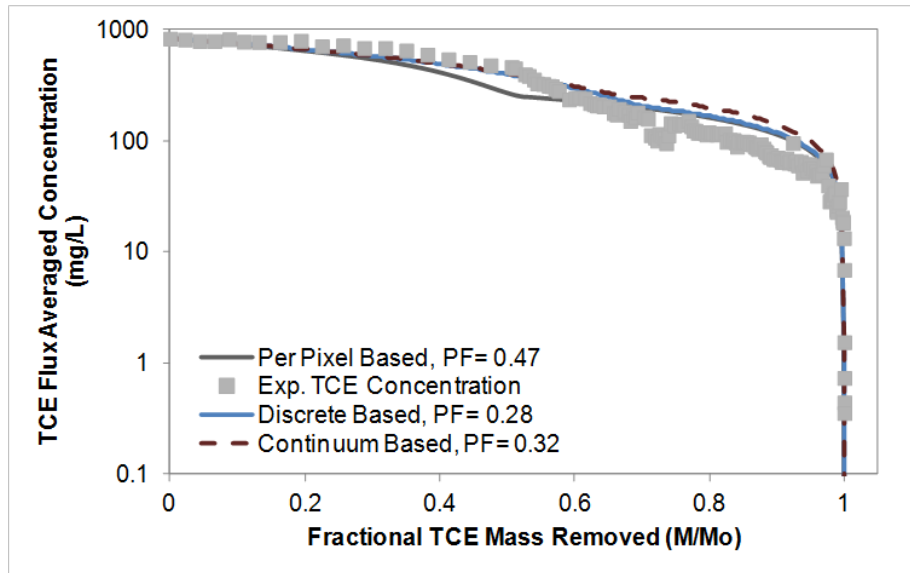


Figure R.1.18. Experimental flux averaged effluent concentrations and prediction based on the Christ 2010 upscaled model using a per-pixel averaging window, DBA and CBA.

Flux-averaged effluent curves developed using the upscaled model and the experimental effluent concentrations are shown in Figure R.1.18 along with the corresponding initial source zone PF. For the pixel based, discrete based and continuum based averaging the corresponding root mean square errors were 63, 50 and 68 mg/L, respectively. As shown in Figure R.1.18, the DBA approach resulted in the most accurate model prediction (middle graph in Figure R.1.18). While DBA resulted in the best match to the experimental results, both the per-pixel scale and CBA averaging approach results provided order-of-magnitude estimates of the mass removal-discharge mass removal behavior observed in AC4. Furthermore, the models were generally able to account for the changes in mass flux when the source zone transitioned from ganglia- to pool-dominated, as indicated by the drop in predicted curves at a relative mass removal (M/M_0) value of approximately 0.5. Previous simplified models have not been able to adequately account for this transition, which can result in over-estimation of the time scale needed to achieve significant reductions in mass flux.

Results of Markov-chain transitional probability aquifer cell experiment (AC5)

While the previous aquifer cell experiments focused on the dissolution of DNAPLs in source zones containing a combination of pools and ganglia, the permeability fields were relatively simple compared to most aquifer formations. Thus, the purpose of AC5 was to incorporate a permeability distribution that was based on geostatistical parameters obtained from a well-characterized field site. The simulated and actual permeability distributions are shown in Figure R.1.19, which was generated using a Markov Chain-Transitional probability scheme based on

the Herten site (Maji 2005). Following packing and establishment of steady flow within the aquifer cell, a series of tracer tests were conducted using fluorescent dyes and bromide to evaluate the overall flow properties of the aquifer cell and the influence of permeability contrasts on the transport behavior of non-reactive solutes. Non-reactive tracer tests are important for determining solute flow paths and residence times in this subsurface system since preferential flow and short-circuiting were expected to occur in the higher permeability media. The initial hydrodynamic characterization was completed by injecting a 1/3 PV pulse of tracer solution containing sodium bromide and sodium fluorescein at a seepage velocity of 2.4 m/d. Effluent tracer concentrations coupled with digital images of the tracer front (Figure R.1.20) showed that subsurface heterogeneity significantly influenced solute transport within the aquifer cell. The tracer exhibited preferential flow through zones of higher permeability and early breakthrough in the effluent (less than 1 PV), followed by prolonged tailing of the bromide breakthrough curves (Figures R.1.20 and R.1.21). The observed tracer behavior was attributed to heterogeneous flow field and physical non-equilibrium (i.e., back diffusion) between zones of high and low permeability located throughout the aquifer cell.

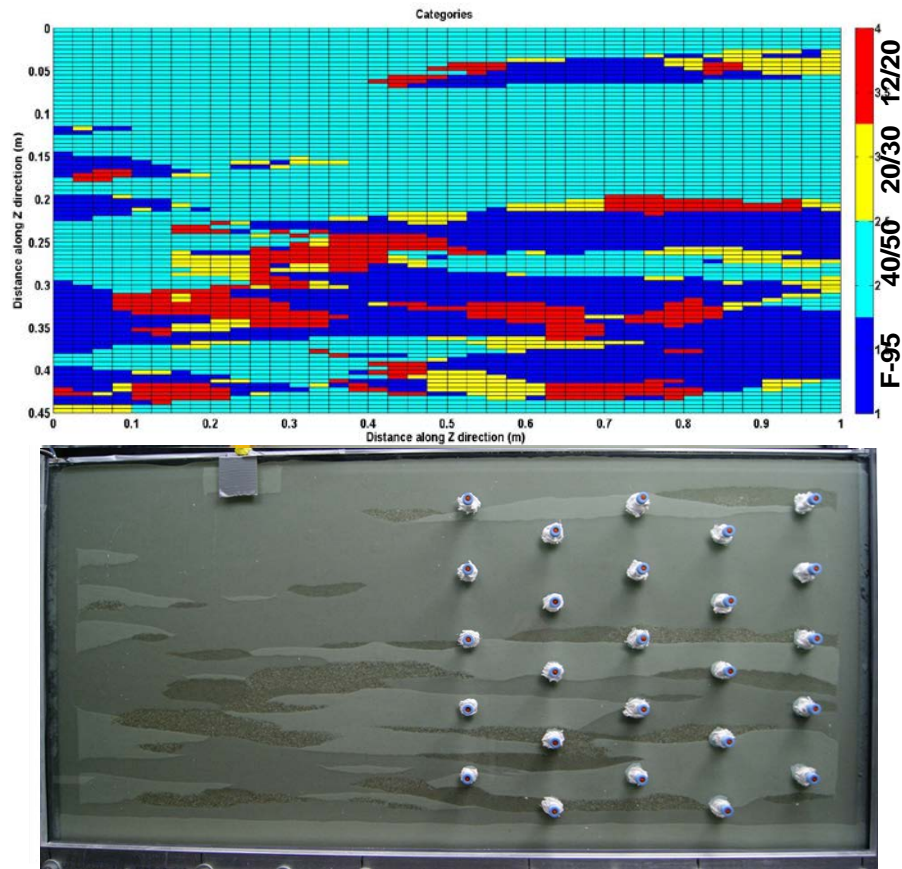


Figure R.1.19. Simulated (top) and actual (bottom) permeability distribution of aquifer cell 5 (AC5).

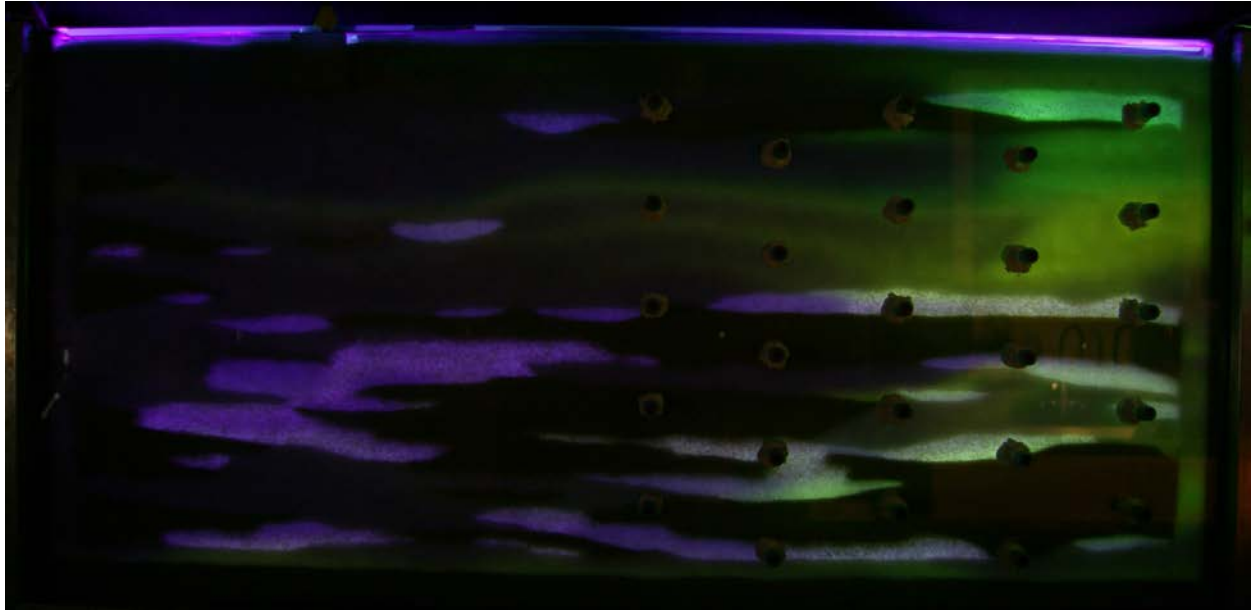


Figure R.1.20. Conservative tracer dye (sodium fluorescein) movement through AC5 (illuminated with 450 nm Kino-Flo Blue bulbs) at 0.5 PVs.

To improve our understanding of the overall flow properties of the aquifer cell and the influence of low permeability media on the storage and release of non-reactive solutes prior to DNAPL release in AC5, a second extended tracer test was completed using multiple tracers of varying molecular weight. Tracer transport through interconnected layers of the 12-20 and 20-30 mesh size fractions led to early tracer breakthrough (i.e. less than 1 pore volume) in the effluent and side-port samples. Flow interruptions resulted in small decreases (flow interruption 1) and increases (flow interruption 2) in effluent tracer concentrations. The observed changes in effluent concentrations following periods of flow interruption are indicative of rate-limited mass transfer between the lower and higher permeability layers. The relatively small magnitude of measured effluent concentration change immediately following a flow interruption was attributed to the duration of the interruption, and the averaging effect of the flux-averaged concentrations in the effluent chamber. A small degree of separation was observed between the PFBA and Br tailing portion of the effluent breakthrough curve (Figure R.1.22). This behavior was attributed to the different diffusion coefficient of the two tracers, suggesting that rate-limited diffusive mass transfer occurred between the high and low permeability lenses.

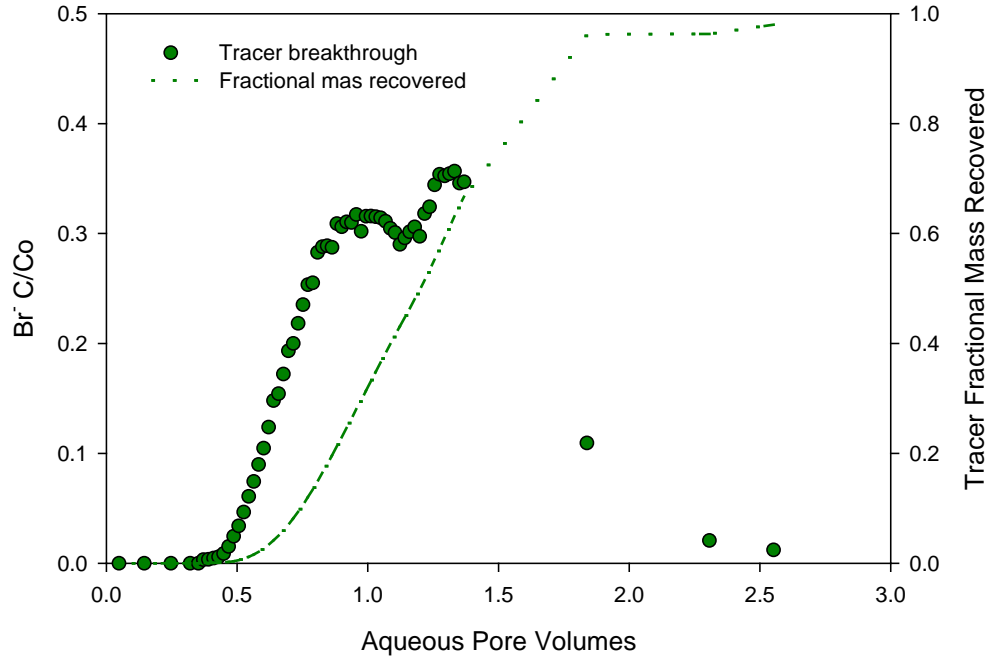


Figure R.1.21. Bromide tracer breakthrough (left axis) and fractional bromide mass recovered (right axis) during a 1/3 pulse conservative tracer test in AC5.

Based on the results of the extended conservative tracer test, it was assumed that diffusion contributed to tracer mass transfer into the low permeability lenses. This hypothesis was based on solute behavior following flow interruptions and difference in the tailing behavior for two different molecular weight solutes. Although this permeability distribution provided a two order of magnitude (1×10^{-10} to 1×10^{-12} m²) contrast between the coarsest background media and zones of low permeability lenses, it was important to assess the relative contributions of diffusive mass transfer between the low and high permeability zones and advective flow through the layers to the observed solute tailing. Therefore, a series of numerical simulations and sensitivity analyses were conducted using the aquifer cell permeability distribution to gain insight into the influence of permeability field heterogeneity on tracer transport and to investigate the times required for solute entry and release in the lower permeability zones (see Task III).

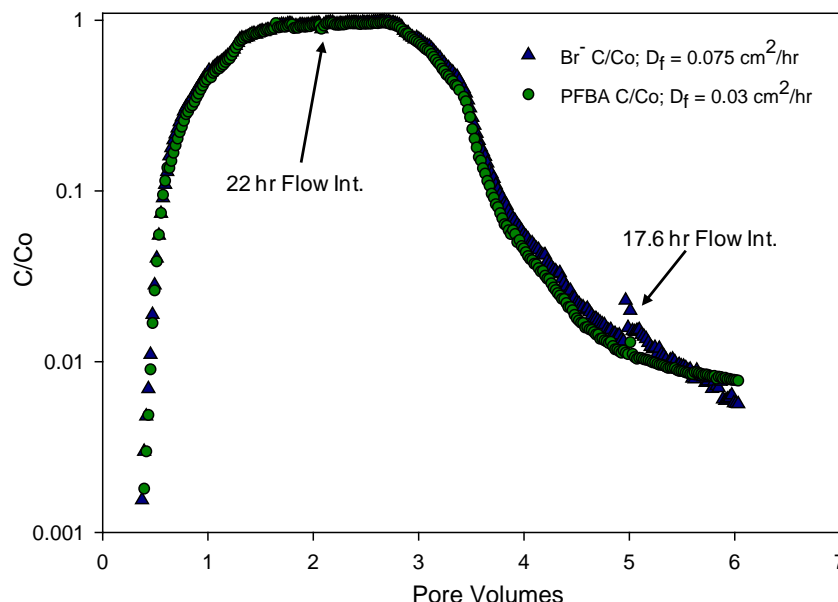


Figure R.1.22. Bromide and PFBA tracer breakthrough during the extended conservative tracer test in AC5.

Measured effluent and side port tracer concentrations were utilized to calibrate the model permeability field and to obtain dispersivity values. The modeling results verified experimental observations demonstrating that the flow interruption on the plateau of the breakthrough curve (BTC) resulted in a decrease in the effluent concentration, while on the interruption on the distal portion of the BTC resulted in an increase or spike in effluent concentration. This change was attributed to the redistribution of the tracer mass during the flow interruption due to molecular diffusion and rate-limited mass transfer between the high and low permeability media. The sensitivity analysis was then completed by varying the three main experimental parameters, which included the flow rate (decrease and increase during both loading and flushing, flow interruption durations (increase length), and the contrast between permeability of the background and the low permeability zones (increase).

The simulation results (next sub-section) indicate that when the permeability contrast between the background and low permeability media is approximately one order of magnitude, tracer mass storage and release from the low-permeability zones is relatively fast, resulting in only a limited concentration gradient between high and low permeability zones. Therefore, changing other parameters such as flow rate or duration of the flow interruption did not substantially enhance the effect of contaminant mass transfer. In contrast, when the simulated permeability contrast is increased by three orders-of-magnitude or more, advective flux within the low permeability zones is negligible and a sufficiently high concentration gradient exists at the beginning of the flow interruption to drive diffusion into lower permeability zones.

Following characterization of the hydrodynamic flow field in the aquifer cell, neat TCE-DNAPL was injected into AC5 and initial light transmission analysis measured a PF of 0.4 in the source zone. The presence of higher permeability zones located throughout the source zone region resulted in localized, high DNAPL saturations at the interface of the lenses containing either 12-20 mesh or 20-30 mesh Ottawa sands and 40-50 mesh or F-95 Ottawa sands. Due to the presence of these high saturation pools, TCE-DNAPL did not fully penetrate the entire vertical profile of the source zone region, resulting in the formation of high saturation pools in the two most transmissive lenses (12-20 and 20-30 mesh sands). Regions with lower DNAPL saturations (i.e., ganglia regions with residual saturations less than 18 %) predominately formed in the background 40-50 mesh Ottawa sand, and higher-saturation pools were only observed when TCE-DNAPL migrated through a 40-50 mesh region and encountered a lower permeability lens of F-95 sand. Down-gradient port measurements of dissolved-phase TCE concentrations indicated that the TCE plume developed throughout the height of the aquifer cell. The highest TCE concentrations (approximately 1,000 mg/L) were initially observed in regions located down-gradient from the source zone containing 40-50 mesh sands, where TCE-DNAPL predominantly was present as ganglia (Figure R.1.21). These higher concentrations were attributed to the faster dissolution rates of ganglia with greater interfacial area compared to the high-saturation pools.

Following the initial plume development period, when high concentration TCE measurements were relatively uniform within the transmissive regions of the aquifer, a significant decrease in concentration was observed in locations immediately down-gradient from the source zone regions containing ganglia (Figure R.1.23). This observation corresponded with the transition to a source zone regions composed predominantly of high saturation pools located in the 12-20 and 20-30 mesh regions. Effluent TCE concentrations reached an initial maximum of 511 mg/L at 1.9 PVs, and then decreased monotonically over the next 14 PVs, until a pseudo steady-state flux averaged concentration of approximately 314 mg/L was reached. The resulting decrease in mass discharge was approximately 37%, with localized high concentrations of TCE observed in down-gradient port samples. This multi-stage dissolution behavior has been observed in a number of 2-D laboratory scale dissolution studies with heterogeneous SZAs (Christ et al. 2010, DiFilippo and Brusseau 2011), and is attributed to the initial, rapid dissolution of ganglia from the source zone and followed by the sustained dissolution from pooled TCE-DNAPL.

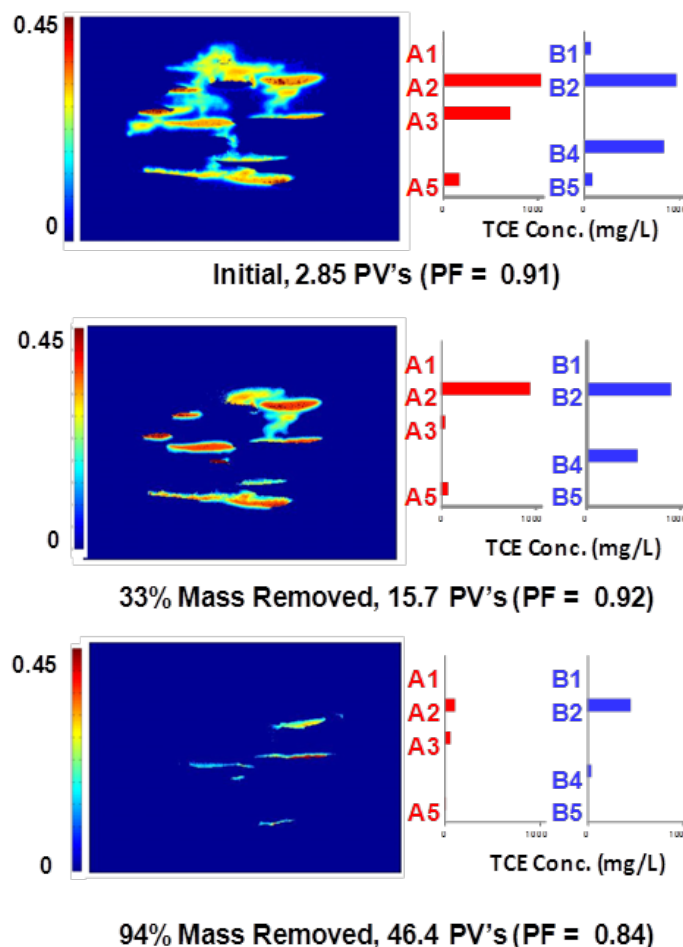


Figure R.1.23. Temporal evolution in SZA and down-gradient plume concentrations for AC5. The side-port concentration measurements were obtained from the first and second transect, while ports A4 and B3 were located within the low permeability zones and therefore were not sampled.

During the surfactant flushing phase of the AC5 experiment, TCE flux-averaged effluent concentrations reached a maximum of 6,100 mg/L, which is significantly lower than concentrations measured during surfactant flooding in aquifer cells containing more uniform permeability distributions (Suchomel et al. 2007). This most likely occurred due to the greater pore-water velocity through the higher permeability sands, resulting in rate-limited dissolution, and the non-uniform distribution of DNAPL throughout the vertical height of the source zone. Side port measurements obtained during the flow interruption at the conclusion of the surfactant flushing period revealed localized TCE concentrations as high as 12,000 mg/L immediately down-gradient of regions containing TCE-NAPL. A total of 16.3 g (11 mL), or 28 % of the initial TCE, mass was recovered during surfactant flushing.

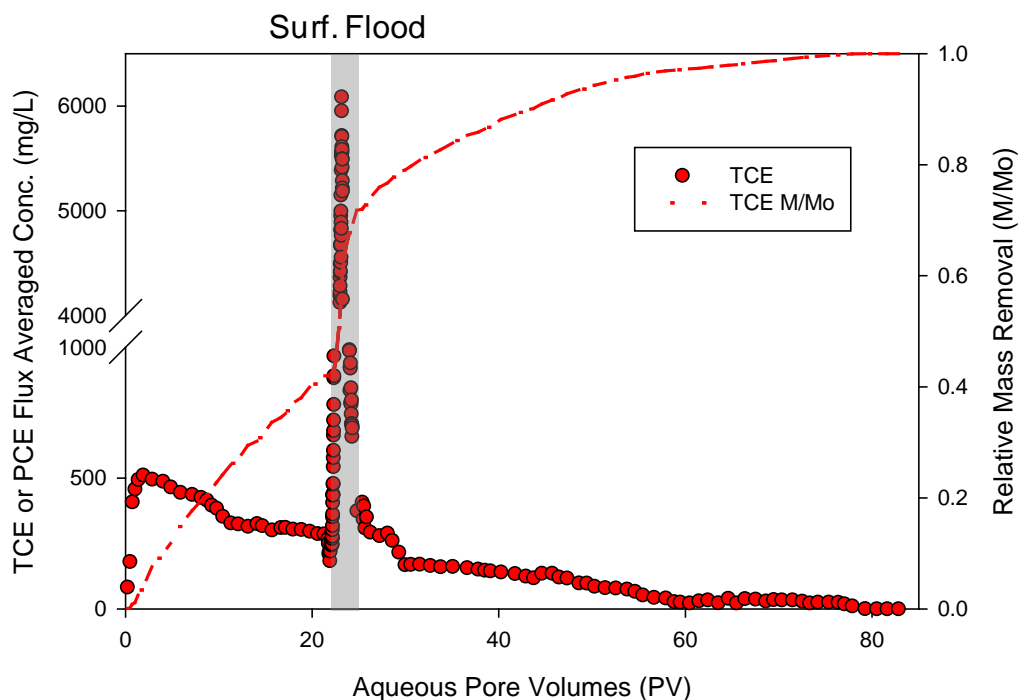


Figure R.1.24. TCE flux-averaged effluent concentrations as a function of pore volume from AC5. Flux averaged effluent concentrations during surfactant flooding (at 22 PV) are indicated by the grey box.

Side-port (Figure R.1.23) and flux-averaged effluent (Figure R.1.24) measurements revealed reductions in TCE concentrations following surfactant flushing, with a flux-averaged effluent concentration and percent reduction in mass discharge of 119 mg/L and 80%, respectively. Side port measurements and LT analysis indicated that the TCE mass discharge was predominantly due to dissolution of high saturation pools located in zones of 12-20 and 20-30 mesh sands that contained the remaining 25% of the DNAPL mass, resulting in a pool-dominated source zone with a PF that approached 1.0 (Figure R.1.23). TCE concentrations measured in side ports located down-gradient from the pooled regions provided additional evidence of the location of the remaining NAPL, with the highest TCE concentrations approaching 100 mg/L emanating from these higher permeability zones. Conversely, TCE concentrations measured down-gradient from source zone areas in lower permeability media (40-50 mesh and F-95 Ottawa sand) were below detectable levels (< 0.012 mg/L). Following complete dissolution of the observable DNAPL pools after 81 PV, effluent TCE concentrations rapidly decreased to below 0.3 mg/L, with no measurable concentrations of TCE in any of the sideport samples. Results from dissolution monitoring highlight the influence of subsurface heterogeneity on DNAPL SZA and plume evolution. TCE concentrations were directly correlated to the presence of upgradient

TCE-DNAPL mass, which in turn, varied by the presence of low and high permeability regions in the source zone.

Numerical Simulation of the tracer transport in Markov-Chain Permeability field

The conservative tracer transport in the aquifer cell packed with the Markov Chain permeability distribution was numerically simulated and a series of sensitivity analyses was conducted to gain insight into the influence of permeability field heterogeneity on tracer transport and to investigate the time periods required for solute entry and release in the lower permeability zones. The aquifer cell flow field was modeled using MODFLOW 2005 with a no-flow boundary condition assigned to all four boundaries of the two-dimensional 5x5 mm grid domain. Constant flow within the cell was simulated using two well-cells on the right and left sides of the domain. These well-cells were located at the vertical midpoint of a 2 cm wide vertical strip containing highly permeable material, and were modeled to represent the fully screened influent and effluent wells. A 2.3 pore volume (PV) pulse was used to simulate the conservative tracer test that was followed by flushing with clean water to mimic the pulse conditions in the 2-D aquifer cell experiment. A Crank-Nicolson finite difference method was utilized to simulate the tracer mass transport within the domain (the mass transport simulator is discussed in Section II.2.3.2.).

In order to investigate the effect of diffusion into and out of the low permeability zones, the experimental flow interruption periods were simulated during both the injection and flushing phases. These flow interruptions were modeled to occur at the same dimensionless time as those completed in the experimental aquifer cell. During these flow interruptions molecular diffusion was the only transport mechanism. Observations from both the model and the experimental data illustrate that the flow interruption on the plateau of the breakthrough curve (BTC) resulted in a decrease in the effluent concentration, while that on the distal portion of the BTC resulted in an increase or spike in effluent concentration. This change can be attributed to the redistribution of the tracer mass during the flow interruption due to molecular diffusion and rate-limited (rather than instantaneous) mass transfer between the high and low permeability media. The effect of the interruption on the effluent breakthrough curve is shown in Figure R.1.25. Both the experimental effluent data and the simulated breakthrough curves are illustrated in this figure. Measured effluent and side port tracer concentrations were utilized to calibrate the permeability field and to obtain dispersivity values. This numerical simulation revealed that the contrast between the permeability of the low permeability material and the background sand in the packed aquifer box must be adjusted to about one order of magnitude. Using the adjusted permeability field, the simulator was able to match the height of the change in effluent concentration after the flow interruptions (see Figure R.1.25).

A sensitivity analysis was then completed by varying the three main experimental parameters, which included the flow rate (decrease and increase during both loading and flushing, flow interruption durations (increase length), and the contrast between permeability of the background and the low permeability zones (increase). The simulation results indicate that when the

permeability contrast between the background and low permeability media is approximately one order of magnitude, tracer mass storage and release from the low-permeability zones was relatively fast, resulting in only a limited concentration gradient between high and low permeability zones. Therefore, changing other parameters such as flow rate or duration of the flow interruption did not substantially enhance the effect of contaminant mass transfer. In contrast, when the simulated permeability contrast was increased to three orders of magnitude or more, a sufficiently high concentration gradient exists at the beginning of the flow interruption to drive diffusion into lower permeability zones. Figures R.1.26 and R.1.27 illustrate the redistribution of the tracer in the domain during the flow interruption periods when the contrast between the permeability of the materials is increased to three orders of magnitude. Both figures reveal that during the flow interruption the sharp concentration contrasts begin to ‘soften’, resulting in a sudden change in effluent concentration when the flow resumes.

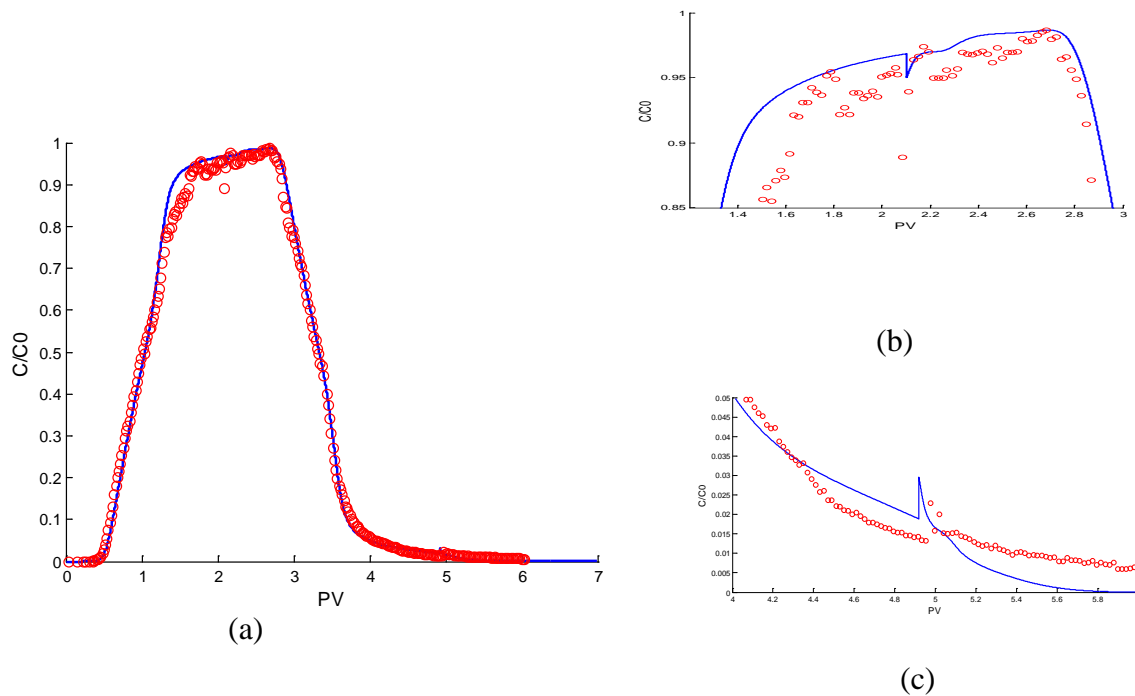


Figure R.1.25. Simulated and experimental effluent breakthrough concentration of the conservative tracer; (a) entire test duration; (b) and (c) magnified around the flow interruption periods at approximate pore volumes 2.0 and 4.7, respectively.

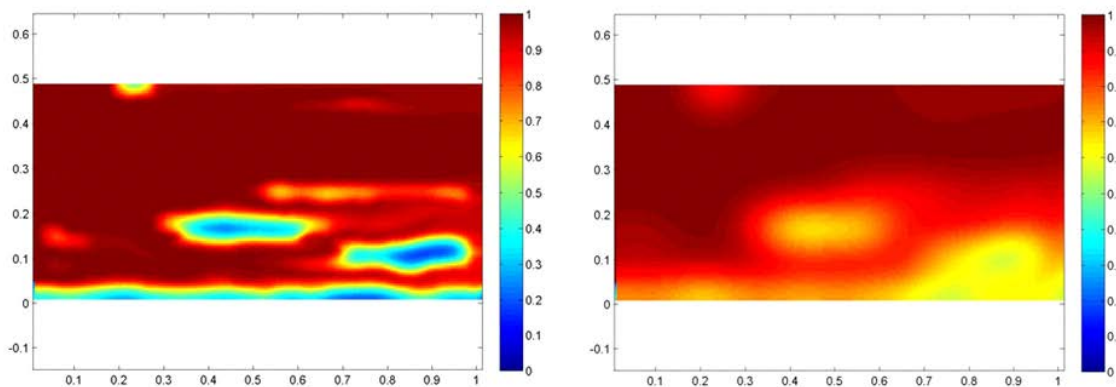


Figure R.1.26. Simulated distribution of normalized tracer concentration in the aquifer cell before (left) and after (right) a flow interruption during injection phase of a conservative tracer test.

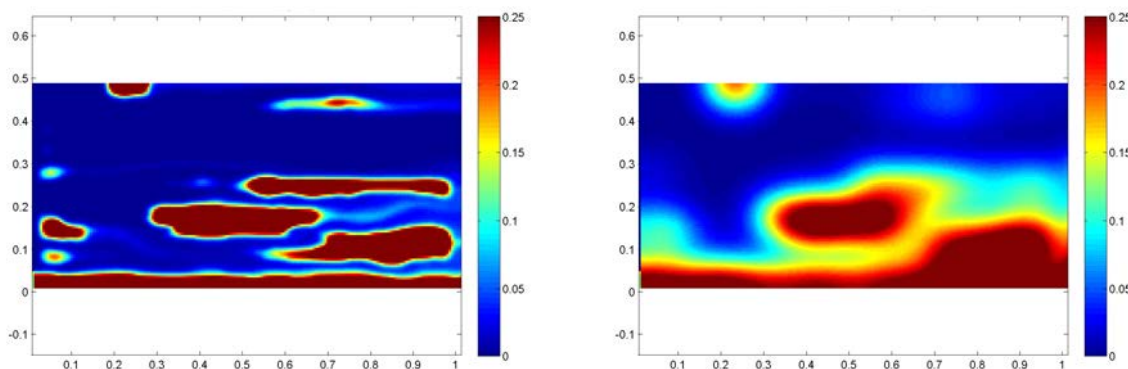


Figure R.1.27. Simulated distribution of normalized tracer concentration before (left) and after (right) a flow interruption during the flushing of the tracer out of the aquifer cell.

Conclusions of Plume Development and Response Aquifer Cell Studies

Results from the five aquifer cell studies completed under Task I advanced our understanding of the inter-relationships between the initial SZA, mass removal, mass flux reductions, plume evolution, and effluent concentrations emanating from mixed PCE/TCE- and neat TCE-DNAPL source zones. The resulting experimental data have provided insight into source plume evolution and supported the modeling work described in Sections III.1.2 and III.3. Below is a summary of the main findings of Task I.

Multi-component 1:1 (mole/mole) PCE- and TCE- NAPL aquifer cells

- Aggressive surfactant NAPL mass removal reduced PCE and TCE discharge from heterogeneous DNAPL source zones.
- Changes in NAPL source zone composition (i.e., molar ratios) differed during water flushing (i.e., aqueous dissolution) and surfactant flushing due to effects of preferential DNAPL solubilization (i.e., did not follow Raoult's law convention).
- Aqueous dissolution resulted in decreased mole fraction of the more soluble compound (TCE); whereas, micellar solubilization reduced the mole fraction of the less soluble compound (PCE).
- Mass discharge-mass removal relationships were directly related to DNAPL molar composition, with decreased reductions in mass discharge with increasing mole fraction.
- The initial DNAPL saturation distribution (e.g., ganglia vs. pools) controlled the long-term dissolution behavior of heterogeneous, multicomponent source zones.

Single-component TCE- NAPL aquifer cell

- Evaluation of image processing scaling methods using light transmission data obtained from AC4 indicate that an averaging window of $30 \times d_{50}$ provides the most reliable estimates of PF and the GTP ratio.
- Following substantial removal (80%) of the initial DNAPL mass, the PF decreased sharply as a large portion of the pools were reduced to saturations below the residual saturation threshold (18 %), and rapidly dissolved, until all DNAPL mass was removed from the source zone.

Markov-Chain permeability distribution aquifer cell

- Comparisons between experimental data and numerical simulation results indicate that when the permeability contrast between the background and low permeability media is approximately one order of magnitude, tracer mass storage and release from the low-permeability zones is relatively rapid, resulting in only a limited concentration gradient between high and low permeability zones.
- Multi-stage DNAPL dissolution behavior was attributed to the initial, rapid dissolution of ganglia from the heterogeneous source zone, followed by sustained dissolution from regions containing high-saturation pools located in high permeability lenses.

III.1.2. Numerical Simulations

III.1.2.1. Field-scale Numerical Simulations

This task resulted in the large library of 3-D field-scale numerical simulations used as training data in Task III. Figure R.1.28 shows a schematic representation of the different scenarios

included in the database for the SGS based simulation ensembles. Three representative examples for the different permeability field cases taken from these ensembles are displayed in Figure R.1.29. As demonstrated in Figure R.1.30, these ensembles alone resulted in a wide variety of source zone architectures with PF's ranging from near zero to greater than 0.8. This wide variety in PF and source zone spreading metrics provided a robust data set for training the models employed in Task III.

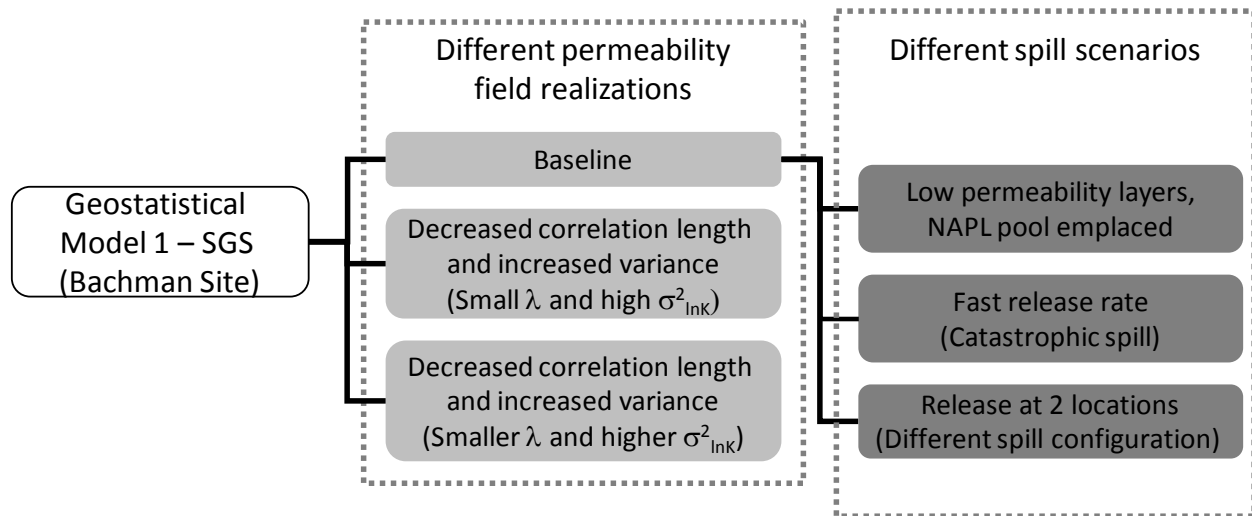


Figure R.1.28. Schematic representation of cases included in the database of 3-D simulations of DNAPL source zone architecture-plume response in a relatively homogeneous glacial outwash deposit.

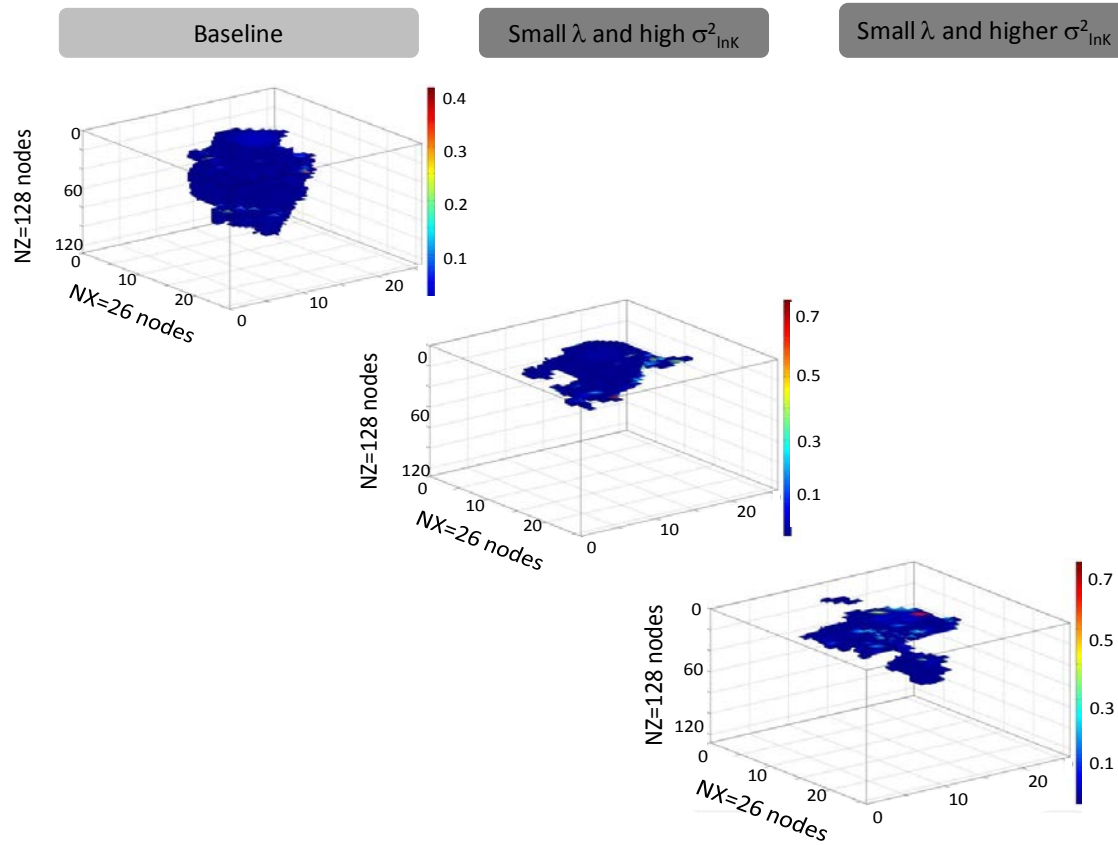


Figure R.1.29. Three examples of the DNAPL SZA for the cases where the permeability field was modified in a relatively homogeneous glacial outwash deposit.

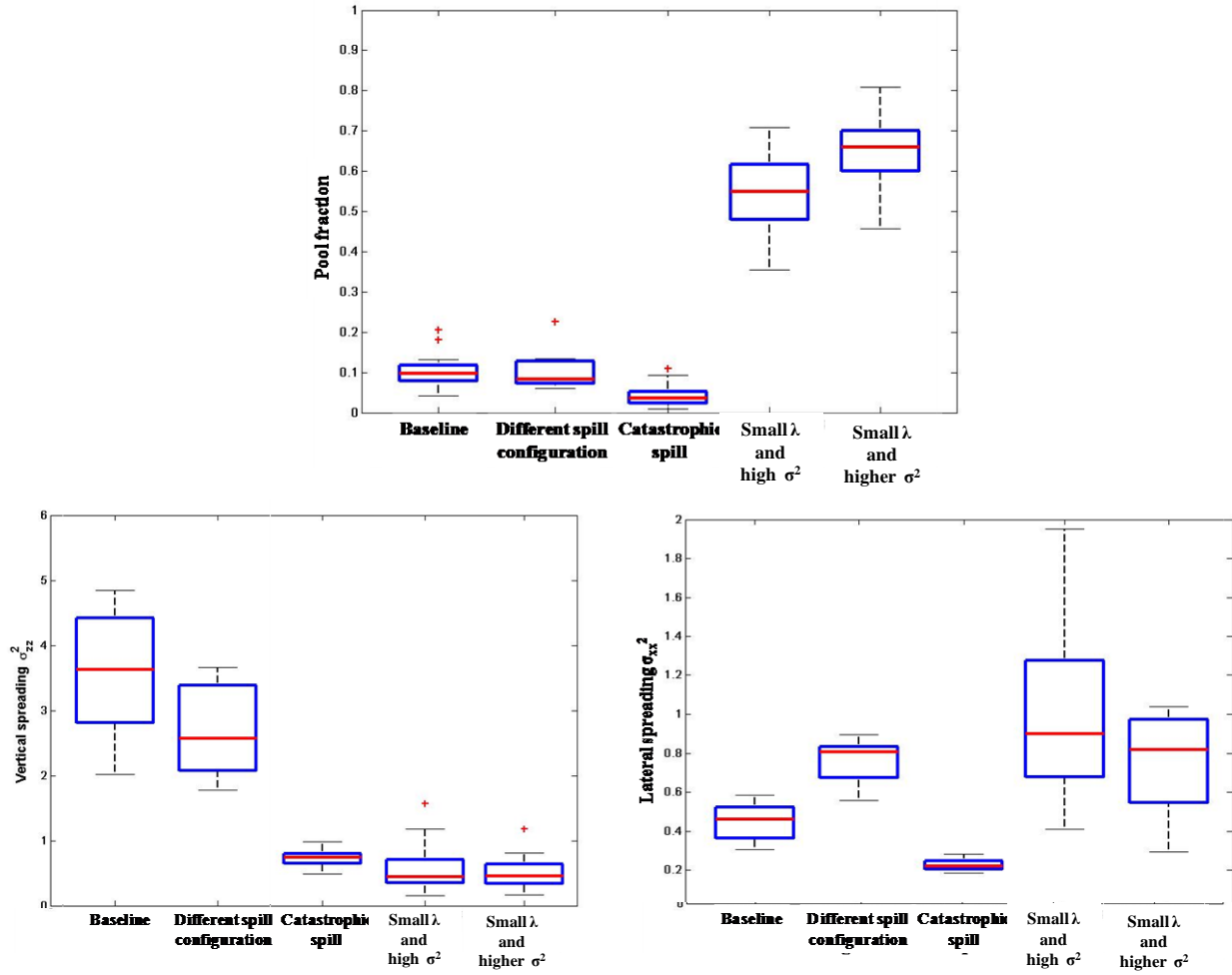


Figure R.1.30. Range of SZA metrics obtained from the database of 3D simulations in a relatively homogeneous glacial outwash deposit.

Simulations in permeability fields based upon the highly heterogeneous glaciofluvial deposit (Herten site; Maji, 2005) were also used as training data for Task III. Recall these ensembles investigated the influence of capillary pressure-saturation parameters; residual organic saturation; spill rate; hypothetical field structure; and dimensionality on the DNAPL migration and entrapment. Table R.1.2 summarizes the ensemble maximum, minimum, mean and standard deviation values for the source zone configuration metrics, including maximum PCE saturation (s_o^{max}), horizontal and vertical center of mass (x_{cm} and z_{cm}), horizontal and vertical spread (σ_{xx}^2 and σ_{zz}^2), GTP, and PF, for all simulation cases (see Tables M.1.4 and M.1.5 in the Section II.1.3 for descriptions of the cases).

Table R.1.2. Summary of ensemble statistics for PCE distribution metrics for highly heterogeneous glaciofluvial deposit

		S_z^{max}	x_{cm}	z_{cm}	σ_{xx}^2	σ_{zz}^2	GTP	PF
case 1	min	0.781	6.430	1.080	1.190	0.248	0.314	0.278
	max	0.917	10.400	3.820	6.160	6.580	2.590	0.761
LS-1Sor-M-1	mean	0.898	8.924	2.126	3.841	1.623	0.992	0.531
	stdev	0.041	0.964	0.652	1.358	1.488	0.554	0.117
case 2	min	0.911	6.310	1.470	0.264	0.664	0.433	0.149
	max	0.919	8.530	3.650	3.460	4.520	5.720	0.698
HPM-1Sor-M-1	mean	0.918	7.522	2.629	1.213	2.148	1.646	0.451
	stdev	0.002	0.630	0.535	0.737	1.184	1.396	0.160
case 3	min	0.780	6.390	1.080	1.190	0.248	0.318	0.279
	max	0.917	10.400	3.830	6.190	6.640	2.590	0.759
LS-4Sor-M-1	mean	0.897	8.924	2.139	3.876	1.685	1.005	0.530
	stdev	0.041	0.967	0.652	1.356	1.485	0.587	0.119
case 4	min	0.911	6.440	1.470	0.262	0.691	0.439	0.148
	max	0.919	8.530	3.630	3.480	4.560	5.760	0.695
HPM-4Sor-M-1	mean	0.918	7.556	2.590	1.212	2.118	1.608	0.458
	stdev	0.002	0.575	0.517	0.756	1.185	1.409	0.158
case 5	min	0.776	5.790	1.200	1.550	0.344	0.271	0.365
	max	0.918	10.700	4.420	8.650	6.850	1.740	0.787
LS-1Sor-S-1	mean	0.902	8.994	2.590	4.867	2.415	0.872	0.557
	stdev	0.042	1.319	0.755	1.908	1.796	0.395	0.117
case 6	min	0.913	6.210	1.760	0.559	0.787	0.248	0.343
	max	0.919	8.580	4.600	3.430	6.010	1.920	0.802
HPM-1Sor-S-1	mean	0.918	7.428	3.173	1.638	2.947	1.005	0.532
	stdev	0.001	0.708	0.728	0.804	1.605	0.525	0.137
case 7	min	0.787	6.730	1.600	0.633	0.607	0.403	0.150
	max	0.917	9.800	3.890	9.500	3.600	5.670	0.713
LS-1Sor-M-2	mean	0.896	8.205	2.926	2.968	2.056	1.563	0.437
	stdev	0.040	0.940	0.618	2.261	0.775	1.129	0.130
case 8	min	0.825	6.230	1.760	0.230	1.220	0.325	0.092
	max	0.919	8.840	4.250	4.820	4.480	9.880	0.755
HPM-1Sor-M-2	mean	0.912	7.707	3.398	0.980	3.105	2.268	0.365
	stdev	0.021	0.625	0.700	1.077	0.937	1.967	0.135
case 9	min	0.676	6.620	0.793	0.976	0.209	0.636	0.232
	max	0.916	9.250	2.110	3.350	2.980	3.310	0.611
LS-1Sor-F-1	mean	0.889	8.297	1.498	2.100	0.792	1.364	0.444
	stdev	0.056	0.707	0.356	0.749	0.599	0.617	0.091
case 10	min	0.506	6.630	1.070	0.245	0.381	0.920	0.147
	max	0.918	8.140	2.090	3.460	1.650	5.800	0.521
HPM-1Sor-F-1	mean	0.893	7.676	1.769	0.866	1.058	2.532	0.313
	stdev	0.092	0.428	0.252	0.710	0.350	1.192	0.100

In these highly heterogeneous permeability fields, capillary pressure-saturation parameters significantly influenced the DNAPL migration pathways, while the residual organic saturation had almost no influence on DNAPL distributions. Figure R.1.31 depicts three representative PCE saturation distributions (*min*, *mean* and *max* horizontal spread). With Leverett scaling, there is a larger entry pressure contrast between the extensive layers of lithofacies when compared to the HPM (Haverkamp and Parlange (1986)) Method, and this contrast decreases the likelihood that PCE will penetrate through the low permeability layers. As a result, with Leverett scaling, the PCE has a higher tendency to migrate horizontally. With HPM, the entry pressure contrast between continuous layers is smaller, thus less horizontal migration is observed.

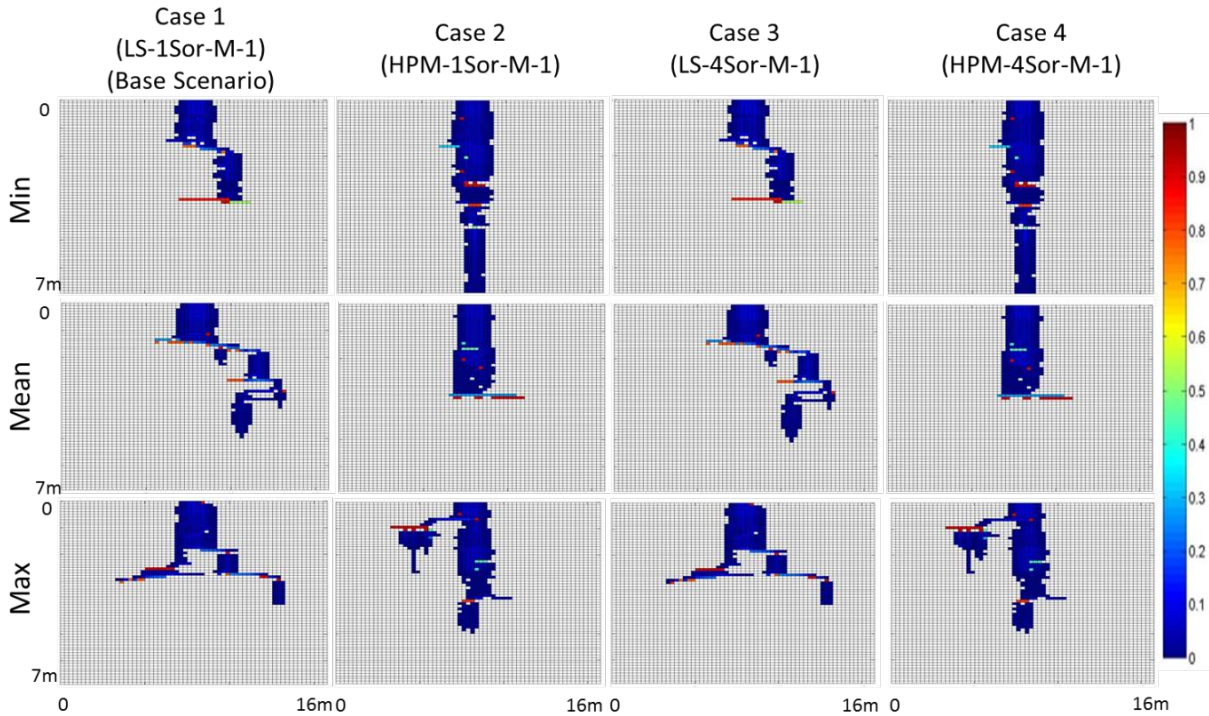


Figure R.1.31. Representative PCE saturation distributions in a highly heterogeneous glaciofluvial deposit – 2D simulations case 1 to case 4.

Table R.1.3 shows the result of a nonparametric two-sample Kolmogorov–Smirnov test ($K-S$ test) (Fasano and Franceschini, 1987) that was performed to quantify the difference between HPM and Leverett scaling. In the two-sample $K-S$ test, the null hypothesis is that the samples are drawn from the same distribution. The null hypothesis is rejected at a confidence level α if the $K-S$ test statistic is larger than the critical value for the test (Fasano and Franceschini, 1987). In this study, the two-sample $K-S$ test was performed with Minitab (Minitab, Inc., 2011). The highlighted values in Table R.1.3 suggest that for case 1 and case 2 (or case 3 and case 4), the

different sets of capillary pressure-saturation parameters (Leverett for cases 1 and 3 and HPM for cases 2 and 4) resulted in different distributions of s_o^{max} , x_{cm} , z_{cm} , and σ_{xx}^2 and therefore strongly influenced the resulting SZA quantified by these metrics. The test between case 1 and case 3 (or case 2 and case 4) does not show a statistical difference, which demonstrates that the residual organic saturation does not strongly influence the simulation of DNAPL infiltration and entrapment.

Table R.1.3. K-S Test Statistic for Cases 1 to 4 (Critical Value = 0.441, $\alpha = 0.05$). Values higher than the critical value at the given confidence level are highlighted

	s_o^{max}	x_{cm}	z_{cm}	σ_{xx}^2	σ_{zz}^2	GTP	PF
Case 1 vs. Case 2	0.947	0.736	0.526	0.842	0.315	0.368	0.368
Case 3 vs. Case 4	0.947	0.736	0.473	0.842	0.315	0.368	0.368
Case 1 vs. Case 3	0.052	0.052	0.052	0.105	0.157	0.105	0.105
Case 2 vs. Case 4	0.105	0.105	0.105	0.105	0.052	0.105	0.105

Likewise, the spill rate strongly affects the DNAPL spread, especially along the vertical direction (Table R.1.4). Figure R.1.32 shows representative PCE saturation distributions for different spill rates in a highly heterogeneous glaciofluvial deposit; case 1 and 2 were simulated assuming a medium spill rate (2 L/day), case 5 and case 6 were simulated assuming a slow spill rate (0.5 L/day), and case 9 and case 10 were simulated assuming a fast spill rate (20 L/day). Note that cases 1, 5, and 9 had the same permeability field, and likewise for cases 2, 6, and 10. In this way, the pathways for PCE are similar within the same realizations and the results are comparable. From Figure R.1.32, a clear decrease in the depth of penetration is observed with increasing spill rate. For the same realization and capillary pressure model, high saturation pools occur at similar locations. With increasing spill rate, both the horizontal and vertical spread are reduced; the PCE tends to be trapped in a smaller region with higher average saturation values in each cell. Table R1.3.3 quantifies these results using the *K-S* test and demonstrates that when Leverett scaling is used, statistical differences in the underlying distribution of metrics are observed in the high spill rate scenarios. The statistical analysis gives similar conclusions when HPM is used. In this case however, it appears that x_{cm} is not influenced by a change in spill rate.

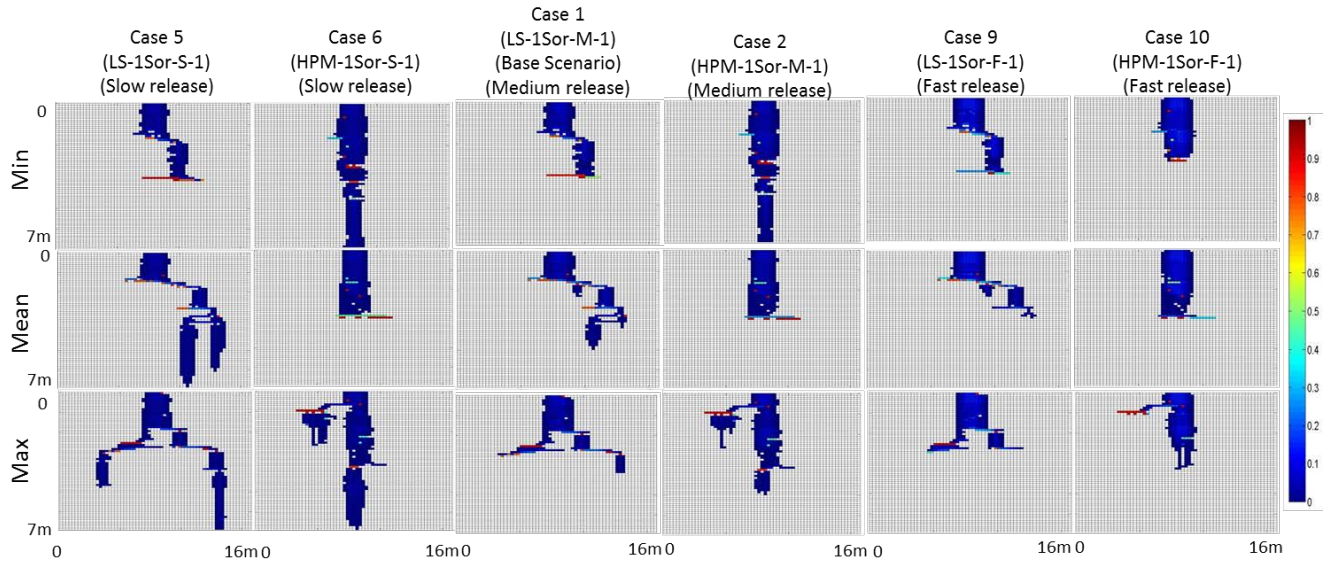


Figure R.1.32 Representative PCE saturation distributions for different spill rates in a highly heterogeneous glaciofluvial deposit - simulation case 1, case 2, case 5, case 6, case 9 and case 10.

Table R.1.4. K-S Test Statistic for Cases 1, 2, 5, 6, 9, and 10 (Critical Value = 0.435, $\alpha = 0.05$)

	S_o^{max}	\bar{S}_o	x_{cm}	z_{cm}	σ_{xx}^2	σ_{zz}^2	GTP	PF
Case 1 vs. Case 5	0.331	0.281	0.184	0.431	0.289	0.434	0.194	0.194
Case 1 vs. Case 9	0.481	0.584	0.426	0.536	0.634	0.492	0.484	0.484
Case 5 vs. Case 9	0.7	0.65	0.5	0.8	0.8	0.75	0.5	0.5
Case 2 vs. Case 6	0.423	0.431	0.142	0.486	0.321	0.294	0.315	0.315
Case 2 vs. Case 10	0.894	0.634	0.271	0.842	0.428	0.581	0.534	0.534
Case 6 vs. Case 10	0.95	0.85	0.3	0.9	0.6	0.75	0.65	0.65

The location of low permeability layers that make up the field structure has a critical influence on the predicted center of mass and spreading in the vertical direction. Simulation results for cases 1, 2, 7 and 8 are compared to explore the infiltration and entrapment behavior in different field formations (Figure R.1.33). Cases 1 and 2 are simulated in hypothetical permeability field 1, and cases 7 and 8 are simulated in hypothetical permeability field 2. Other simulation conditions, like the release rate (2 L/day), and the total volume released into the subsurface are exactly the same. The volumetric portions for each lithofacies are consistent in field 1 and 2, but the location of low permeability layers is different. In field 1, a large low permeability layer was present on the top boundary near where the PCE was released, while in field 2, no such low permeability layer was present around the release location. Figure R.1.33 shows the representative source zones for field 1 and field 2. As might be expected, these two modified permeability fields result in entirely different pathways, which greatly influenced the PCE pool locations. Results from the two-sample *K-S* test (Table R1.3.4) show that with Leverett scaling, the metrics quantifying permeability fields 1 and 2, z_{cm} , σ_{zz}^2 , GTP, and PF, tend to have different underlying distributions. When using HPM, these same metrics in addition to σ_{xx}^2 , reveal obvious, quantifiable differences between field 1 and field 2. Five out of the seven studied metrics in this work are sensitive to the location of low permeability layers, namely σ_{xx}^2 , z_{cm} , σ_{zz}^2 , GTP, and PF. The clear difference in metrics between field 1 and field 2 strongly suggests that the location of the low permeability layer with extensive horizontal correlation length is of great importance in simulating DNAPL entrapment and infiltration behavior. Therefore, the TP/MC approach has to be carefully designed when generating field realizations.

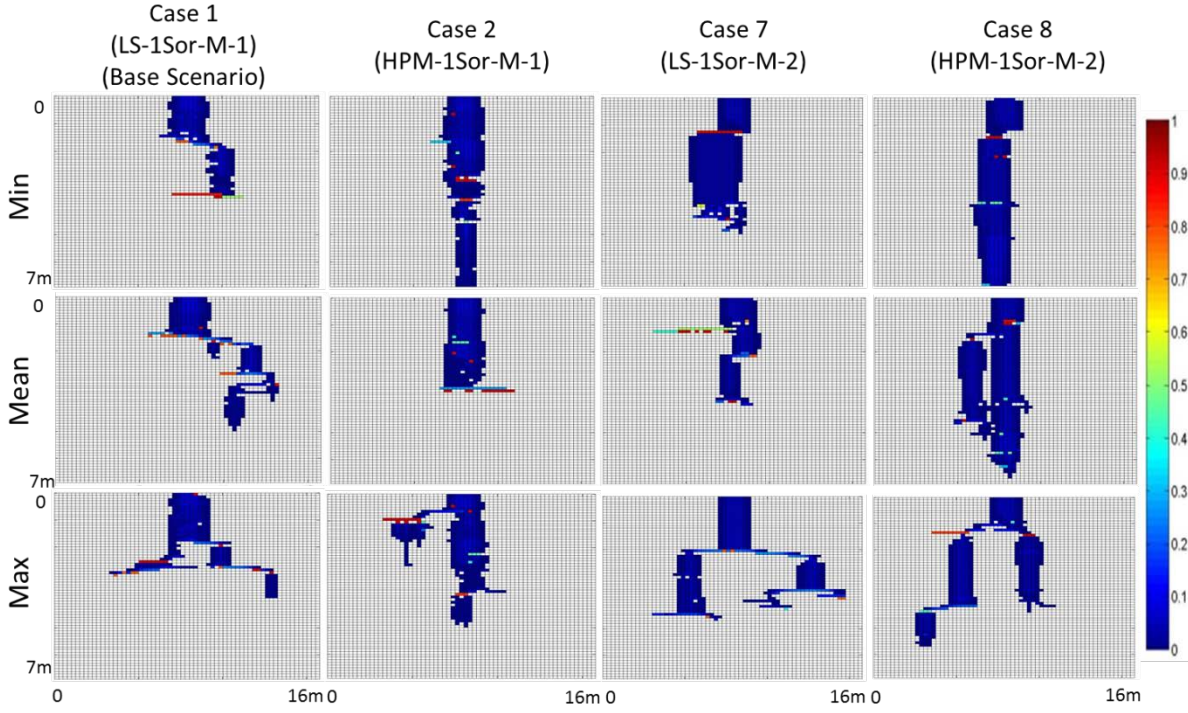


Figure R.1.33. Representative PCE saturation distributions for simulation in a highly heterogeneous glaciofluvial deposit -case 1, case 2, case7, and case 8.

Table R.1.5. *K-S* Test Statistic for Cases 1, 2, 7, and 8 (Critical Value = 0.435, $\alpha = 0.05$)

	s_o^{max}	x_{cm}	z_{cm}	σ_{xx}^2	σ_{zz}^2	GTP	PF
Case 1 vs. Case 7	0.178	0.347	0.744	0.394	0.486	0.534	0.534
Case 2 vs. Case 8	0.397	0.244	0.594	0.436	0.484	0.531	0.531

The results also suggest that there is a significant increase in maximum organic saturation (s_o^{max}) and PF in highly heterogeneous aquifers in comparison to those in mildly heterogeneous aquifers. The influence of spill rates on the prediction of s_o^{max} and GTP for highly heterogeneous aquifers tends to be different from that for mildly heterogeneous aquifers. To compare the values of x_{cm} , z_{cm} , σ_{zz}^2 , and σ_{xx}^2 for highly heterogeneous aquifers to those for mildly heterogeneous aquifers, these metrics were normalized according to the corresponding scale for the respective domain and converted into dimensionless quantities. The dimensionless quantities are listed in Table R1.3.5. All the values present in Table R1.3.5 are adjusted from the mean values of the simulations with Leverett scaling (e.g. case 5 and 9 for this study). Table R1.3.5 shows that the s_o^{max} obtained in highly heterogeneous aquifers is dramatically higher than that in mildly heterogeneous aquifers. In addition, the values for horizontal and vertical spread in highly heterogeneous aquifers are generally greater than those in mildly heterogeneous aquifers. The center of mass in the horizontal direction is similar for mildly and highly heterogeneous aquifers since the release areas are located at the center of the simulated region for all studies. For highly heterogeneous aquifers, z_{cm} tends to be 10% to 30% higher than it is for mildly heterogeneous aquifers. Note that neither the same volume nor the same PCE release rate was used for all the studies quantified in Table R1.3.5.

Table R.1.6. Dimensionless mean source zone metrics for highly and mildly heterogeneous aquifers

	s_o^{max}	x_{cm}	z_{cm}	σ_{xx}^2	σ_{zz}^2
This study (Herten site) (80L 0.5 L/day)	0.9018	0.562	0.370	0.019	0.049
This study (Herten site) (80L 20 L/day)	0.8885	0.519	0.214	0.008	0.016
Dekker and Abriola (2000) (Borden site) (75L 15 L/day)	0.0743	—	0.188	—	0.006
Christ et al. (2005) (Oscoda site) (32L 0.16 L/day)	0.354	0.472	0.331	0.014	0.026
Lemke et al. (2004) (Bachman Road site) (96L 0.24 L/day)	0.37	—	0.353	0.001	0.045

The influence of dimensionality was briefly investigated in this subtask. To obtain insight into PCE entrapment and infiltration behavior in 3-D, only 1 of the 20 realizations obtained for the 2D study was chosen as a representative domain and simulated under the 1, 2, 5, 6, 9, and 10 simulation cases. These six cases include Leverett scaling and HPM under slow, medium, and fast release rates, thus the influence of capillary pressure-saturation parameters and the spill rates on 3-D simulation of PCE migration can be examined. To facilitate the comparison of 2-D and 3-D simulation results, the 3-D DNAPL infiltration results were sliced along the center x - z cross

sections corresponding to the permeability field used in the 2-D simulation, as shown in Figure R.1.34. Metrics obtained from this slice are labeled “2-D in 3-D.” From Figure R.1.35, it is observed that the PCE migration pathways for 2-D and 3-D simulations under slow, medium, and fast spill rates are quite different. Although the same amount of PCE is released at the same rates in identical permeability fields, the different DNAPL architectures resulting from the 3-D and 2-D simulations may be explained by the migration of PCE in the 3rd dimension when encountering horizontal capillary barriers in 3-D, whereas in the 2-D domain the adjacent cross sections does not exist. The PCE pathways for the 2-D cross sections of the 3-D simulations are not continuous, but the 3-D simulations have pathways in other planes for the PCE to continue its vertical migration. Figure R.1.36 depicts the PCE pathways for 2-D and 3-D simulations with HPM. Clearly, the capillary pressure-saturation parameters strongly influence the PCE migration for both 2-D and 3-D simulations, since the PCE migration pathways are different between Leverett scaling and HPM. With HPM the pathway for PCE tends to be more continuous in the 3-D simulation than when Leverett scaling is used. However, there are still discontinuous pathways, which indicate PCE movement to adjacent planes. In general, the results suggest that dimensionality effects are mildly dependent on the capillary pressure-saturation methodology employed and that these results seem to lack a regular pattern that would allow one to assume the 2D simulation is an accurate reflection of the 3D simulation as originally reported by Christ et al. (2006). Thus, based on the aquifer realizations employed in this study, the results for 2-D simulations should not be extended to 3-D simulations in highly heterogeneous aquifers. Future work is needed for a more systematic study of 3-D behavior in highly heterogeneous permeability fields.

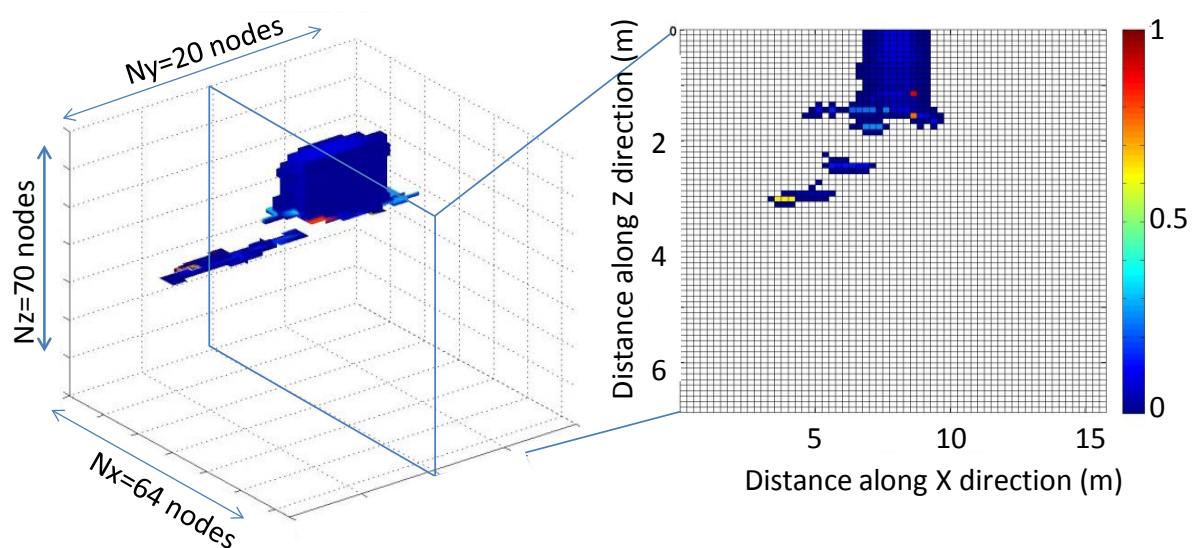


Figure R.1.34. 2-D simulation results extracted from 3-D simulation.

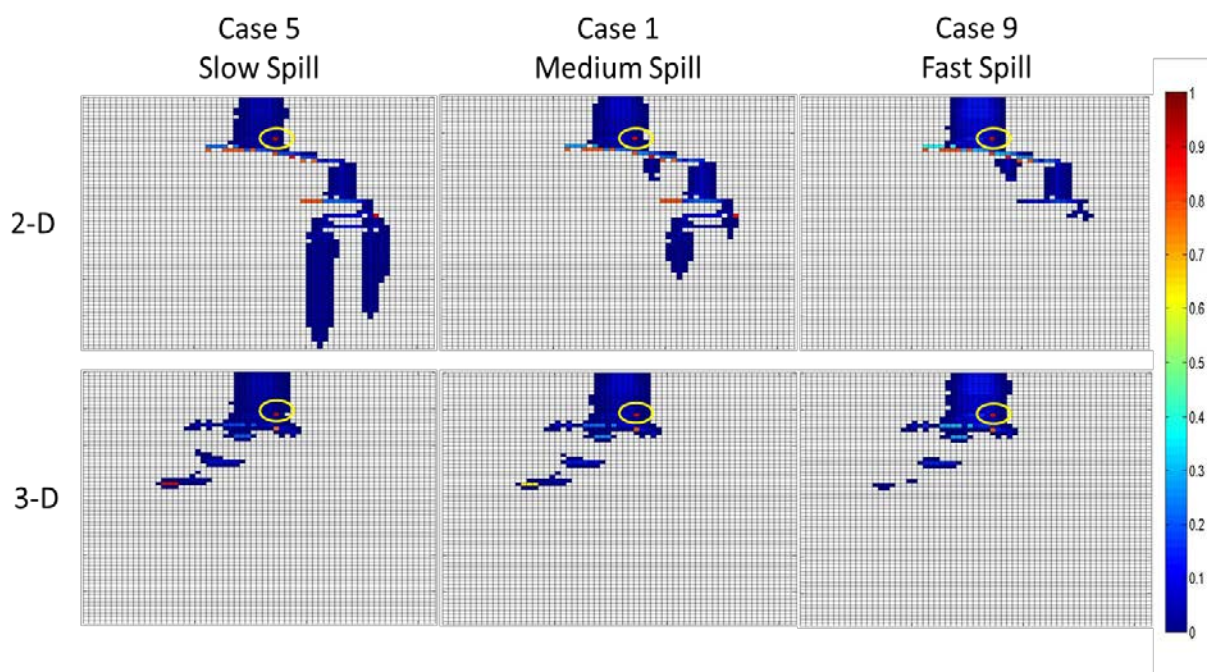


Figure R.1.35. 2-D and 3-D PCE saturation distribution with Leverett scaling.

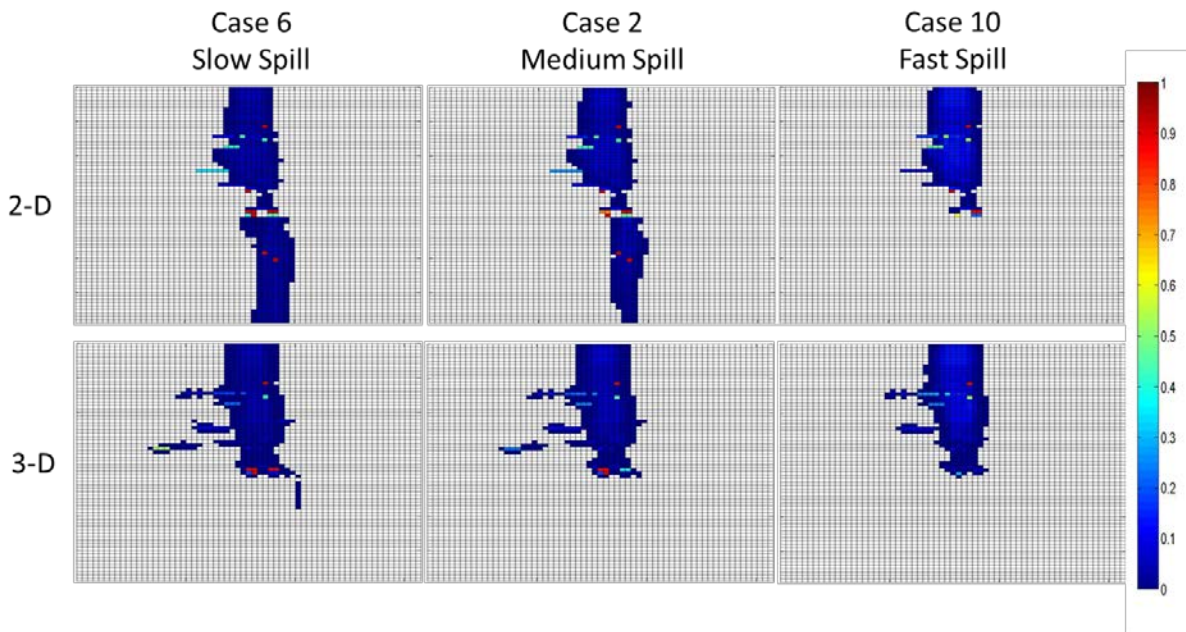


Figure R.1.36. 2-D and 3-D PCE saturation distribution with HP Method.

III.2. Refinement of In-Source Push-Pull Tests

III.2.1. Batch, Column, and Aquifer Cell Experiments

III.2.1.1. Liquid-Liquid Equilibrium Studies

Evaluation of equilibrium partitioning

The ternary phase diagram for each alcohol with TCE and water is shown in Figure R.2.1. Also shown in Figure R.2.1 is the UNIFAC prediction (dashed line) of the binodal curves that separate the two phase region from the DNAPL phase region (upper left curve) and the aqueous region (a small region, not visible in Figure R.2.1, located in the lower right corner of the phase diagram). Tie lines (solid lines) connect the two points corresponding to the measured, equilibrium compositions of the two phases. Any initial composition located between the binodal curves will separate into two phases each having a composition lying on the binodal curves that is connected by a tie line.

The nonlinear partitioning of each tracer between the TCE-DNAPL and aqueous phase is shown in Figure R.2.2. The nonlinearity in the partitioning behavior means that $K_p^{C_i}$ is a function of phase composition. (Herein partition coefficients refer to concentration based partition coefficients ($K_p^{C_i}$) with units of $[L^3/L^3]$ as opposed to mol fraction based partition coefficients ($K_p^{X_i}$) which are dimensionless) (Ervin et al., 2011).

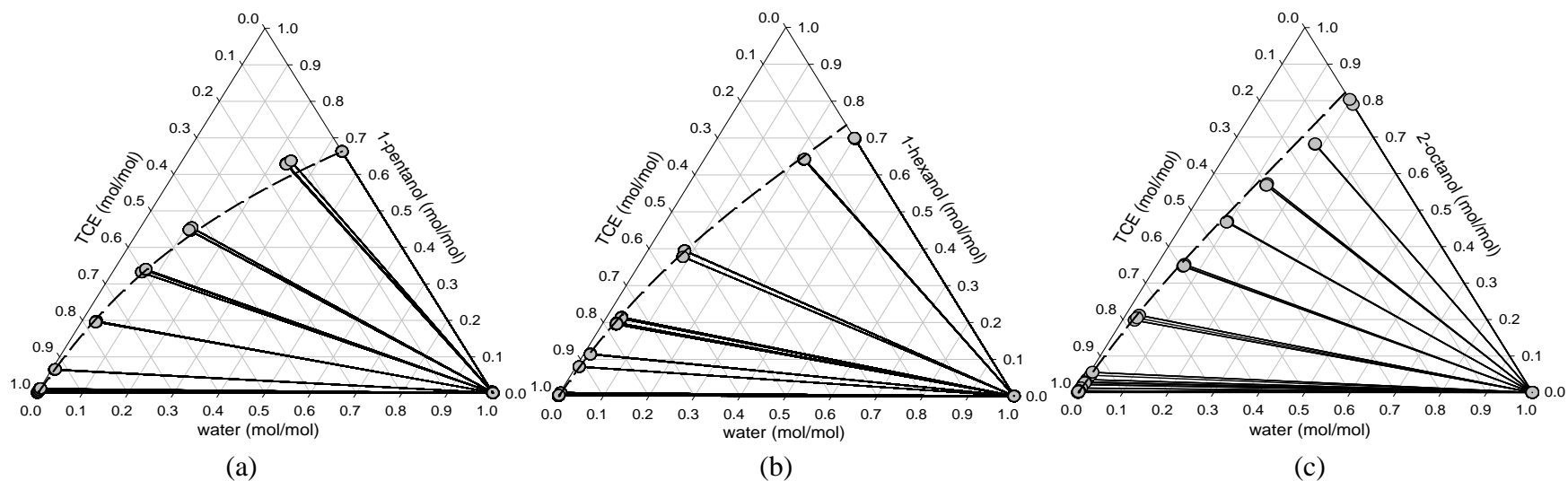


Figure R.2.1. Ternary phase diagrams at $22.0 \pm 0.1^\circ\text{C}$ for 1-pentanol (a), 1-hexanol (b), and 2-octanol (c) developed from liquid-liquid equilibrium batch experiments. Experimental data are shown as tie lines. UNIFAC predictions of the binodal curves defining each two phase region are shown as dotted lines. The binodal curve defining the aqueous phase is not visible but exists in the lower right corner of each phase diagram.

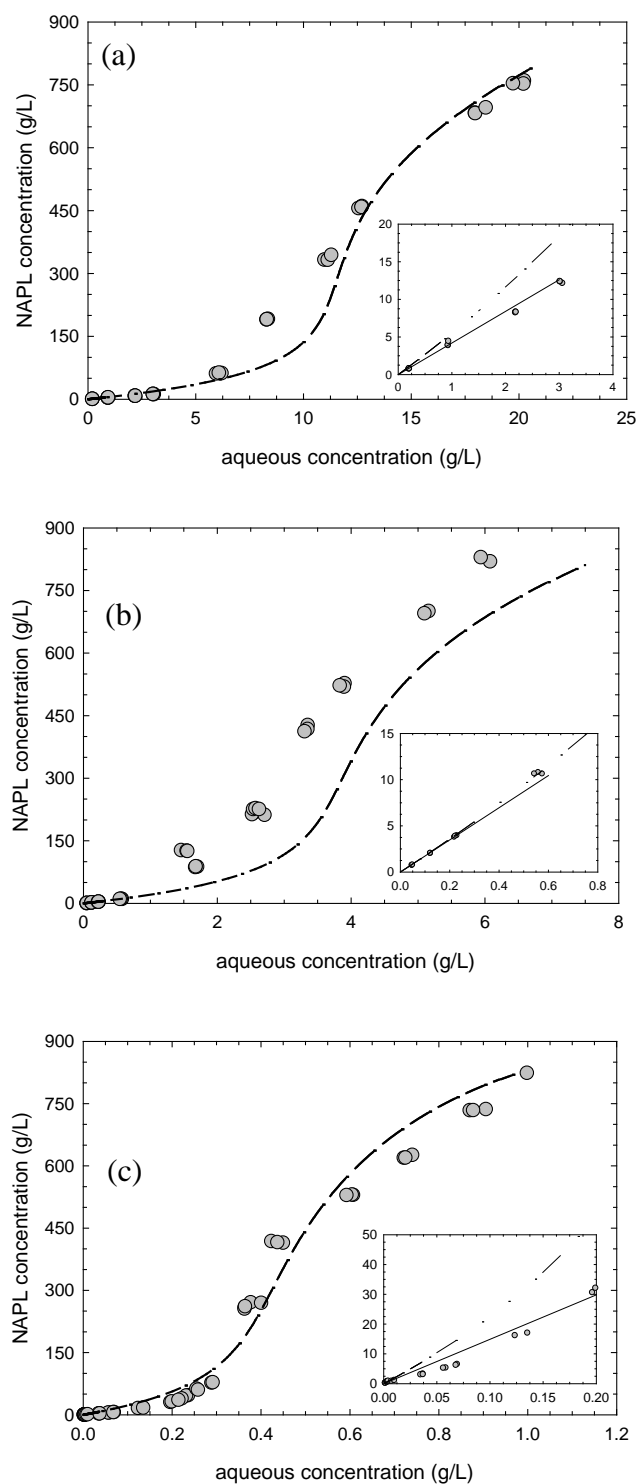


Figure R.2.2. The distribution of 1-pentanol (a), 1-hexanol (b), and 2-octanol (c) between the NAPL and aqueous phase at $22.0 \pm 0.1^\circ\text{C}$ as established by liquid-liquid equilibrium data (circles) and UNIFAC predictions (dashed line). Note that data span the range of possible aqueous concentrations but that differences in solubility necessitate change in the horizontal range for each panel. Insets show dilute range with the regressed, linear partitioning model (solid line).

Evident in Figure R.2.2 is a region at lower concentration where the partitioning data can be approximated as linear, above which the partition coefficient increases with increasing concentration. The assumption of linear partitioning appears to be applicable below approximately 3,000 mg/L, 600 mg/L and 200 mg/L for 1-pentanol, 1-hexanol and 2-octanol, respectively (Figure R.2.2). A linear, weighted, least squares regression was employed in the dilute region of each alcohol tracer to determine the linear partition model (Ramachandran et al., 1996). The resulting partition coefficients (at 22.0±0.1°C) for 1-pentanol, 1-hexanol and 2-octanol in a TCE-DNAPL/water system are 4.20±0.10, 17.4±0.2, and 149±8 L_{aq}/L_{DNAPL} , respectively (Ervin et al. 2011).

It is noted that all three of these measured values represent a different amount of partitioning than has been previously reported (Table R.2.1). The discrepancy between measured and literature values for the partitioning of 2-octanol (in a TCE/water system) is approximately 113%. This large discrepancy for 2-octanol is consistent with the fact that 2-octanol exhibited the greatest nonlinearity (Figure R.2.2). In addition, both K_p values for 2-octanol appearing in Table R.2.1 (317 and 332) were estimated based upon equivalent alkane carbon number (Dwarakanath and Pope, 1998; Thal et al., 2007). While these estimates may hold value when screening alcohols, the data shown in Figure R.2.2 demonstrate the need for careful measurement of partition coefficients prior to application.

Table R.2.1. Reported partition coefficients for 1-pentanol, 1-hexanol and 2-octanol

Tracer	$K_p^{C_i}$ (L_{aq}/L_{DNAPL})	Initial Aqueous Concentration for Measurement of $K_p^{C_i}$	Reference
1-pentanol	3.80 ^{a,c} 3.8 ^{b,c} 3.73 ^{a,d} 3.39 ^{a,c}	1000 mg/L 1000 mg/L range not reported ^d 500 mg/L	Dwarakanath and Pope, 1998 Wang et al., 1998 Willson et al., 2000 Thal et al., 2007
1-hexanol	18.6 ^{a,e} 18.6 ^{a,c} 18.6 ^{b,c} 18.0 ^{a,d} 18.2 ^{a,f} 12.4 ^{a,c}	not reported ^e 1000 mg/L 1000 mg/L range not reported ^d not applicable ^f 500 mg/L	Jin et al., 1997 Dwarakanath and Pope, 1998 Wang et al., 1998 Willson et al., 2000 Istok et al., 2002 Thal et al., 2007
2-octanol	317 ^{a,g} 332 ^{a,g}	not applicable ^g not applicable ^g	Dwarakanath and Pope, 1998 Thal et al., 2007

^a temperature was not reported, ^b 25°C, ^c single-point measurement, ^d regression of measurements at multiple concentrations though concentration range was not reported, ^e measurement method was not reported, ^f value estimated using method in Lyman et al. (1990), ^g estimated using an equivalent alkane carbon number for 2-octanol that was produced by employing the known 2-octanol partition coefficient between water and PCE-DNAPL (Ramsburg et al. 2005).

UNIFAC Modeling

The UNIFAC predictions of alcohol partitioning between the DNAPL and aqueous phases are also shown in Figure R.2.2 (dashed line). The group contribution parameters used in the UNIFAC prediction (Ervin et al., 2011) are able to predict the general shape over the entire partitioning range for each alcohol. The model performance is especially good for 1-pentanol and 2-octanol. The relatively poorer performance of UNIFAC when describing the partitioning of 1-hexanol results from an inability to accurately capture the 1-hexanol/water mutual solubility which shifts the curve to the right in Figure R.2.2. Note, however, that the shape of the UNIFAC prediction is similar to that of the data. In the dilute region, the UNIFAC model over predicts the amount of alcohol partitioning. The UNIFAC predictions of linear partition coefficients within the dilute regions are $5.8 \text{ L}_{\text{aq}}/\text{L}_{\text{DNAPL}}$, $18.4 \text{ L}_{\text{aq}}/\text{L}_{\text{DNAPL}}$ and $232.6 \text{ L}_{\text{aq}}/\text{L}_{\text{DNAPL}}$ for 1-pentanol, 1-hexanol and 2-octanol, respectively (Ervin et al. 2011). The superior UNIFAC predictions for the 1-hexanol within the dilute region are suspected to be spurious and related to the previously described inaccuracy in the 1-hexanol/water mutual solubilities.

The inability of UNIFAC to capture the 1-hexanol data was further examined by adjusting group interaction parameters in an attempt to visually fit the model to the 1-hexanol data (Ervin 2012). It was found that adjusting the $\text{H}_2\text{O}/\text{OH}$ interaction parameters enables the model to better predict the 1-hexanol data, but it must be recognized that the same adjustment leads to poorer UNIFAC model predictions for both 1-pentanol and 2-octanol. UNIFAC parameters are estimated from thousands of data points stored in the Dortmund Data Bank (Gmehling et al., 1977) and both H_2O and OH groups are well characterized interaction parameters. Therefore, even though adjustment of these parameters allows for better prediction of the hexanol data set, it is not recommended that these adjusted interaction parameters be employed when making predictions of LLE.

Adsorption of the Selected Tracers at the TCE-DNAPL/Water Interface

LLE experiments were also used to study interactions of the alcohol tracers and the aqueous/organic interface. Surface accumulation for 1-pentanol, 1-hexanol and 2-octanol at the DNAPL-aqueous interface was quantified by measuring equilibrium IFTs over a range of solute concentrations (200-1300 mg/L for 1-pentanol, 35-4600 mg/L for 1-hexanol, and 170-900 mg/L for 2-octanol). The two Langmuir parameters Γ_{∞} (maximum surface accumulation, $\text{M}\cdot\text{L}^{-2}$) and a_L (half saturation concentration, $\text{M}\cdot\text{L}^{-3}$) were obtained by fitting Equation R.2.1 to the IFT data using a nonlinear, least squares approach (see Ervin et al. 2011 for more detail).

$$\gamma = \gamma_0 - \Gamma_{\infty} RT \ln \left(1 + \frac{C_{aq}}{a_L} \right) \quad (\text{R.2.1})$$

In Equation R.2.1, C_{aq} is the bulk tracer concentration ($\text{M}\cdot\text{L}^{-3}$), and γ_0 and γ are the interfacial tensions ($\text{M}\cdot\text{T}^{-2}$) measured in the absence of the alcohol and at alcohol concentration C , respectively. Fitted isotherm parameters (shown in Table R.2.2) suggest that 2-octanol has a half saturation concentration (a_L) that is two orders of magnitude lower than that of 1-pentanol. The low a_L of 2-octanol implies that the interface becomes saturated at relatively low concentrations. The capacity of the interface (Γ_{∞}) was found to decrease with increasing alcohol carbon chain length, though all values are on the same order of magnitude. The interfacial capacities shown in

Table R.2.2 suggest that surface accumulation (at any given time during the column experiment) will represent a small fraction of the overall mass in the system.

Table R.2.2. Isotherm parameters for tracers at a TCE-DNAPL-water interface

Tracer	Γ_{∞} ($\mu\text{mol}/\text{m}^2$)	a_L ($\mu\text{mol}/\text{m}^3$)	a_L (mg/L)	R^2
1-pentanol	6.6 \pm 1.5	(2.6 \pm 1.1) $\times 10^7$	2330 \pm 1000	0.960
1-hexanol	4.8 \pm 0.5	(3.2 \pm 0.6) $\times 10^6$	330 \pm 60	0.989
2-octanol	3.6 \pm 0.4	(2.7 \pm 0.8) $\times 10^5$	35 \pm 11	0.936

Values determined by a nonlinear least squares fit of Equation R.2.1 to equilibrium interfacial tensions measured at 22 \pm 2°C. Uncertainties represent standard error in parameter estimates.

Liquid-Liquid Equilibrium Conclusions

The partitioning of three, straight-chain alcohols was found to be nonlinear functions (i.e., dependent upon phase composition). These findings, together with those in Wise et al. (1999), suggest a need for more thorough characterization of alcohol partition coefficients prior to application for source zone assessment. When nonlinearity is neglected, interpretation of partitioning tracer data leads to a systematic over estimations of NAPL saturation (Wise, 1999). The partitioning of many tracers, however, may be approximately linear at low concentration. Care must be taken when designing and interpreting the results from tests employing partitioning tracers as analysis may prove difficult due to the convoluted effects of poor characterization of $K_p^{C_i}$ (over estimation of S_n) and the hydraulic accessibility of the NAPL (under estimation of S_n). Few studies report the concentrations at which partition coefficients were measured, and those that do report the data employed to evaluate $K_p^{C_i}$ often evaluate the partition coefficient at concentrations that are much lower than those introduced to the subsurface (Jawitz et al., 1998; Brooks et al., 2002; Meinardus et al., 2002; Jalbert et al., 2003; Ramsburg et al., 2005; Moreno-Barbero et al., 2007; Hartog et al., 2010). The injection concentrations employed in these field tests may be within the linear partitioning range, but without thorough characterization of the tracer/NAPL interactions, the range over which the linear assumption is valid remains unknown. While the use of low injection concentrations minimizes the potential implications relating to nonlinear partitioning, concentrations must be high enough to avoid the influence of tracer-soil interactions and analytical detection limits. Our thermodynamically rigorous characterization of 1-pentanol, 1-hexanol and 2-octanol interactions with TCE suggests that concentrations should not exceed 3,000 mg/L, 500 mg/L and 200 mg/L, respectively, if the data analysis is to be simplified by assuming linear partitioning.

Transport models, and consequently, saturation estimates are very sensitive to the partition coefficient. Though UNIFAC offers an effective tool for predicting alcohol/chlorinated ethene/water phase behavior, the group contribution method tends to over predict the partition coefficients in the dilute range (where data appear linear). This over prediction of the partition coefficient may lead to underestimation of NAPL saturation. Therefore, measurement of the partition coefficient over the range of concentrations to be employed provides the best foundation for accurate estimates of NAPL saturation from partition tracer test data.

The equilibrium sorption isotherms developed in this work show that 1-pentanol, 1-hexanol and 2-octanol do accumulate at the aqueous/DNAPL interface. This surface accumulation may regulate tracer mass flux across this interface (Ferrari et al., 1997; Liggieri et al., 1997; Ravera et al., 1997; Ravera et al., 2000). However, the maximum accumulation of the three tracers is small (on the order of micrometers per square meter). To understand the implications of surface accumulation, the equilibrium sorption isotherms need to be incorporated into a transport model that can quantify the effect surface accumulation has on overall transport.

III.2.1.2. Non-equilibrium Tracer Transport

Column Experiments

Column experiments were conducted to explore the relative importance of the processes that may control the extent and rate of interphase alcohol tracer partitioning in domains containing uniformly entrapped TCE-DNAPL (Ervin et al. 2011). In contrast to previous investigations, independent measurement and/or estimation of system physical and chemical properties leads to unambiguous data interpretation and eliminates the need for curve fitting. Focus is placed on conditions which promote non-equilibrium mass exchange to elucidate the processes controlling the temporal distribution of the solute within the multiphase environment. We specifically examine the importance of aqueous and NAPL resistances to tracer mass transfer. This is done through a series of column experiments and model simulations, using the representative alcohol tracers.

Breakthrough curves from the column tracer experiments are presented in Figure R.2.3, with experimental parameters listed in Table R.2.3. Comparison of the curve for the non-partitioning tracer (Figure R.2.3a) with that for each alcohol tracer (Figures R.2.3b-d) reveals the influence of partitioning – retardation during transport. Note that predictions of the tracer transport were made using known values of the TCE-DNAPL saturation and tracer partition coefficients.

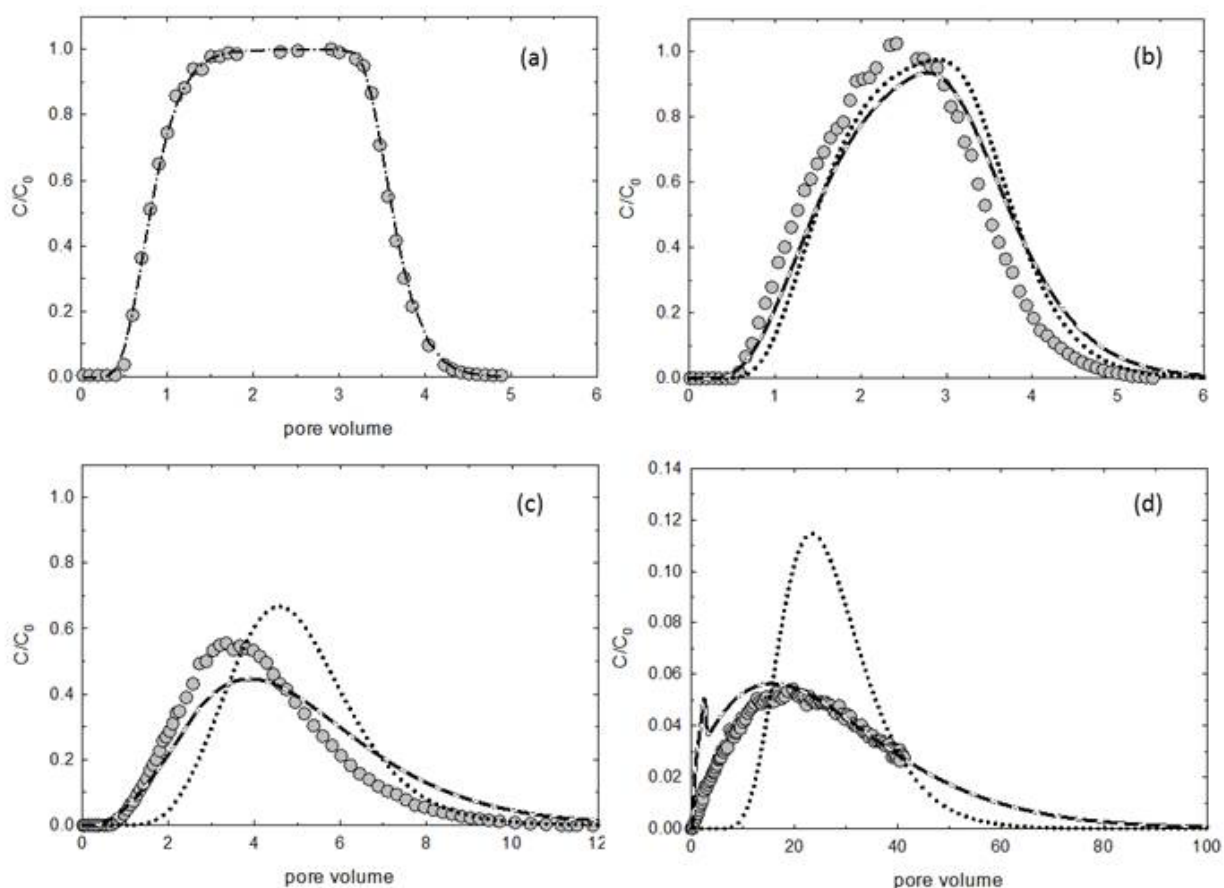


Figure R.2.3. Breakthrough curves for bromide (a), 1-pentanol (b), 1-hexanol (c), and 2-octanol (d) tracer tests conducted at $22 \pm 2^\circ\text{C}$. Dispersivity was fit (dash-dot) to bromide data. Predictive simulations using measured values for the partition coefficients are also shown using equilibrium (dotted), linear driving force (solid), and dual diffusion (dashed) models. Values of the partition coefficient employed in these simulations were 4.20, 17.4, and $149 L_{aq}/L_{NAPL}$ for 1-pentanol, 1-hexanol, and 2-octanol, respectively, at $22.0 \pm 0.1^\circ\text{C}$. Note that linear driving force and dual diffusion models produce nearly identical results, the pore volume scale changes for each panel, and the normalized concentration scale changes for panel d.

Table R.2.3. Parameters related to column experiments and simulations

sand (Ottawa, IL)	45-50 mesh	45-50 mesh
uniformity index (U_i)	1.09	1.09
median grain diameter (d_{50})	0.326 mm	0.326 mm
column length (L)	5.0 cm	4.9 cm
pore volume (PV)	36 mL	35 mL
porosity (n)	0.39	0.39
TCE-NAPL saturation (S_n)	16.8%	13.1%
ganglia diameter ^a (d_{NAPL})	0.297 mm	0.297 mm
flow rate (Q)	2.2 mL·min ⁻¹	0.56 mL·min ⁻¹
pore water velocity (v)	0.32 cm·min ⁻¹	0.091 cm·min ⁻¹
dispersivity (α)	3.2 mm	1.5 mm
molecular diffusivity in water (D_{aq}) ^b 1-pentanol 1-hexanol 2-octanol	 0.80×10 ⁻⁵ cm ² ·s ⁻¹ 0.76×10 ⁻⁵ cm ² ·s ⁻¹ 0.65×10 ⁻⁵ cm ² ·s ⁻¹	
molecular diffusivity in TCE (D_n) ^c 1-pentanol 1-hexanol 2-octanol	 2.4×10 ⁻⁵ cm ² ·s ⁻¹ 2.2×10 ⁻⁵ cm ² ·s ⁻¹ 1.9×10 ⁻⁵ cm ² ·s ⁻¹	
lumped mass transfer coefficient (\hat{k}) ^d 1-pentanol 1-hexanol 2-octanol	 2.34×10 ⁻³ s ⁻¹ 2.19×10 ⁻³ s ⁻¹ 1.98×10 ⁻³ s ⁻¹	 - - 8.45×10 ⁻⁴ s ⁻¹
pulse width – all pulses (PW)	2.3 PV	10.3 PV
influent concentration (C_0) 1-pentanol 1-hexanol 2-octanol	 1070 mg·L ⁻¹ 380 mg·L ⁻¹ 180 mg·L ⁻¹	 - - 195 mg·L ⁻¹
effluent recovery 1-pentanol 1-hexanol 2-octanol ^e	 98.8% 94.6% 70.4%	 - - 89.6%

^a Calculated using correlation of Ramsburg et al. (2011). ^b Calculated using the correlation of Hayduk and Laudie (1974) at 22°C. ^c Calculated with correlation of Wilke-Chang at 22°C. ^d Calculated using the correlation of Powers et al. (1992) at 22°C. ^e Effluent recovery lower due to incomplete quantification of BTC tail.

The influence of mass transfer is apparent in the breakthrough curves. All of the equilibrium transport predictions offer the poorest description of the BTCs, with deviations most noticeable for the strongest partitioning tracer (2-octanol). The influence of diffusion within the DNAPL on the partitioning kinetics was explored by comparing the dual diffusion model to the linear driving force model (see Ervin et al. 2011 for details). Dual diffusion and linear driving force (i.e., completely mixed DNAPL) scenarios produce predictions that are coincident, suggesting that diffusion within the NAPL singlets occurs rapidly relative to transport to the NAPL-water interface. Sensitivity analyses (not shown) determined that diffusional resistance in the NAPL phase does not become important until the radius of the ganglia droplet is doubled. From this analysis, it appears that diffusional resistance within the NAPL may be important for tracer mass transport through regions containing pools, but is not controlling mass transfer for the entrapped ganglia systems examined herein. Additional sensitivity analyses (not shown) were conducted to determine whether or not the laboratory data could be reproduced by fitting the value of the mass transfer coefficient in either the linear driving force or dual diffusion models. Results suggest that adjustment of the mass transfer coefficient does not improve the ability of either model to fit the 1-hexanol or 2-octanol effluent data.

To more broadly explore the effects of uniform DNAPL saturation on the equilibrium assumption, the linear driving force model was employed to identify a velocity at which the local equilibrium assumption (LEA) is a reasonable approximation of the partitioning process (taken here to be 5% difference between the simulated BTCs). The 18 simulation results shown in Figure R.2.4 are for the partitioning alcohols and porous medium examined here, with transport lengths of 5, 10 and 100 cm.

These illustrative results, presented in terms of the hydraulic residence time within the zone $\left(\frac{L}{nS_{aq}v} \right)$, and the partitioning index (defined here as $S_n K_p^{C_i}$),

suggest that strong non-equilibrium conditions may be present when using tracers with high partition coefficients, or where local saturations may be high. It is interesting that the tracers with the higher partition coefficients are frequently used to assess DNAPL saturation in the field due to the need for tracer separation when interrogating large volumes. Local exchange for these tracers, however, may be occurring under conditions of non-equilibrium.

Actual source zones, characterized by low overall saturations, typically comprise heterogeneous saturation distributions. Here, the local equilibrium assumption may be less appropriate due to flow bypassing and less accessibility to the DNAPL surface area (Moreno-Barbero and Illangasekare, 2005, 2006). Where DNAPL is accessible, the local length scale (characteristic length of contact between the tracer solution and DNAPL) will govern the applicability of the LEA. Unfortunately, confirmation of the LEA applicability or selection of an appropriate non-equilibrium model formulation requires that contact times (or lengths) are known *a priori* across the unknown DNAPL architecture.

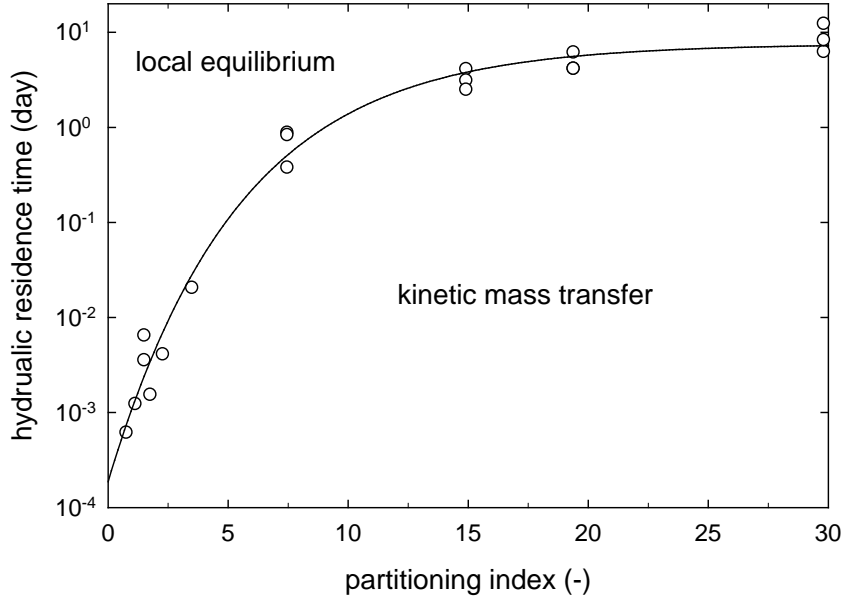


Figure R.2.4. Limitation of the local equilibrium assumption for partitioning alcohols in zones of uniformly entrapped DNAPL. The hydraulic residence time within the zone is $\frac{L}{nS_{aq}v}$, and the partitioning index is defined to be $S_n K_p^{C_i}$. The line is shown as a visual guide for the simulation results shown as open circles.

Conclusions from Column Experiments

Laboratory experiments and mathematical modeling were coupled to examine the partitioning of the three representative tracers under non-equilibrium conditions in systems comprised of TCE-DNAPL ganglia. Results suggest that a linear driving force model employing a mass transfer coefficient correlation developed from NAPL dissolution experiments is able to reproduce BTCs generated in the 1-D column systems (Ervin et al. 2011). Results also demonstrate that non-equilibrium effects increase with increasing partition coefficient and increasing NAPL saturation, suggesting that the validity of the LEA should be checked for the solute having the highest partition coefficient. While the column experiments were designed to be in non-equilibrium, the flow rate of the 2-octanol experiment would have had to be reduced to 0.01 mL/min (i.e., 0.5% of the initial rate) before the linear driving force model predictions were within 5% of those produced by an equilibrium simulation.

Tracer Partitioning In DNAPL Pools

The longer diffusional path length in a DNAPL pool (relative to ganglia), may mean that diffusion within the DNAPL is more relevant to tracer transport in regions having pooled DNAPL. To study kinetic processes controlling tracer transport in regions of pooled DNAPL, partitioning tracer tests were conducted in

a 2-D aquifer cell with a source zone comprised of a large TCE-DNAPL pool. Concentration data were modeled to examine the feasibility of employing mass transfer correlations developed to describe dissolution from a NAPL pool when describing the kinetic mass transfer for partitioning tracers. The aquifer cell experiments described in this section used Ottawa Federal Fine (30-140 mesh) for the background sand and F-70 Ottawa Sand was used to create low permeability lenses and layers. The lens structure (Figure R.2.5) was comprised of a 1 cm thick F-70 lens (28.2 cm long) at the up-gradient end of the box. Triangular mounds (3.6 cm tall) were placed on each end of the lens in an effort to direct the TCE-DNAPL to fill the area above the lens, creating a large pool. This structure was not meant to mimic an observed structure within the subsurface. Rather, it was an alternative to previous use of similarly contrived, coarse lenses placed within a lower permeability matrix (e.g. Nambi and Powers, 2003; Moreno-Barbero and Illangasekare, 2006). Parameters pertaining to the packing structure are shown in Table R.2.4. Details related to the experimental procedure can be found in the Section II.2.2.2, as well as in Ervin (2012).

The TCE-DNAPL distribution and corresponding light transmission results are shown in Figure R.2.6. Light transmission results determine the PF as 0.96, 0.94 and 0.93 on a pixel by pixel basis, a discrete block averaging basis and a continuum averaging basis, respectively (Christ et al., 2012).

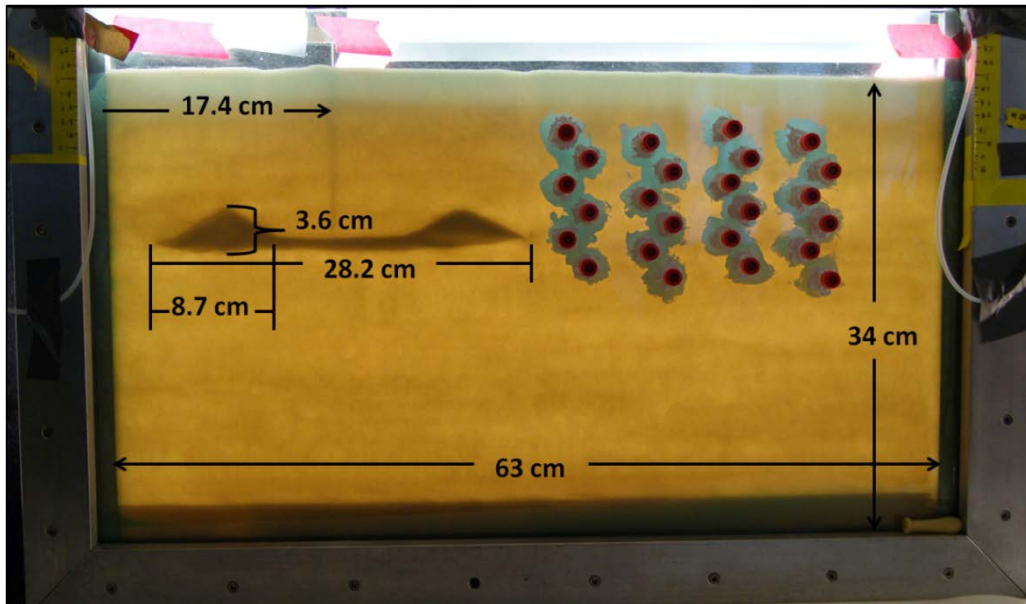


Figure R.2.5. Packing structure used to create the pooled source zone.

Table R.2.4. Relevant 2-D box parameters

Parameter	Value
Mass Ottawa Federal Fine	4868 g
Mass F-70	521 g
Packed Height	34 cm
Average Bulk Density	1.54 g/cm ³
Average Porosity	0.42
Total Pore Volume	1303 mL
TCE-DNAPL Volume	13.5 mL
Overall TCE-DNAPL Saturation	1.04%
Initial Pool Fraction	
Pixel x Pixel	0.96
Discrete Block Averaging	0.94
Continuum Averaging	0.93

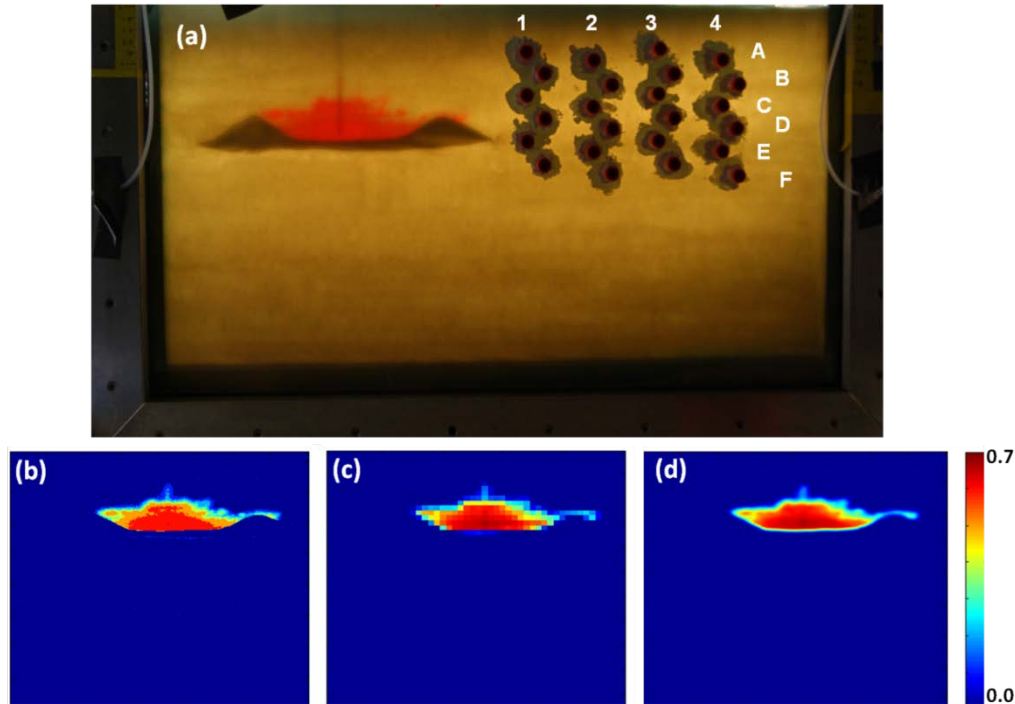


Figure R.2.6. 2-D aquifer cell used to examine partitioning tracer transport in a pooled TCE-DNAPL source zone. The photograph (a) sampling port labels (columns 1- 4 and rows A-F). Light transmission results are shown as a pixel by pixel saturation estimation (b), discrete averaging saturation estimation (c), and continuum averaging saturation estimation (d).

The tracer pulse (0.31 PV) containing bromide (10 mM), 1-pentanol (980 mg/L), 1-hexanol (380 mg/L), and 2-octanol (135 mg/L) in a background solution of Milli-Q water saturated with TCE was delivered to the aquifer cell at a rate of 4.9 mL/min with flow moving from left to right (in Figure R.2.6). Effluent samples were continuously collected over 4-5 minute intervals throughout the test using a fraction collector (Retriever II, ISCO). Additionally, 250 μ L samples were collected from the array of sampling ports (immediately downstream of the pool) approximately every pore volume using a 1 mL gas tight Hamilton syringe.

In contrast to column experiments conducted using uniform residual TCE-DNAPL saturations, the breakthrough of each tracer in the 2-D box occurred at approximately the same time (Figure R.2.7). The lack of tracer separation in the effluent was attributed to the larger volume of the 2-D system, relative to that of the pool (TCE-DNAPL pool comprises 1% of the total volume); therefore, most of the tracer flowing through the system did not contact the pool (i.e., flow bypass). Although the overall (effective) saturation employed for the pool

experiments (1%) is lower than that employed for the ganglia column experiments (16.8%), local saturations in the pool experiments were much greater (~70%).

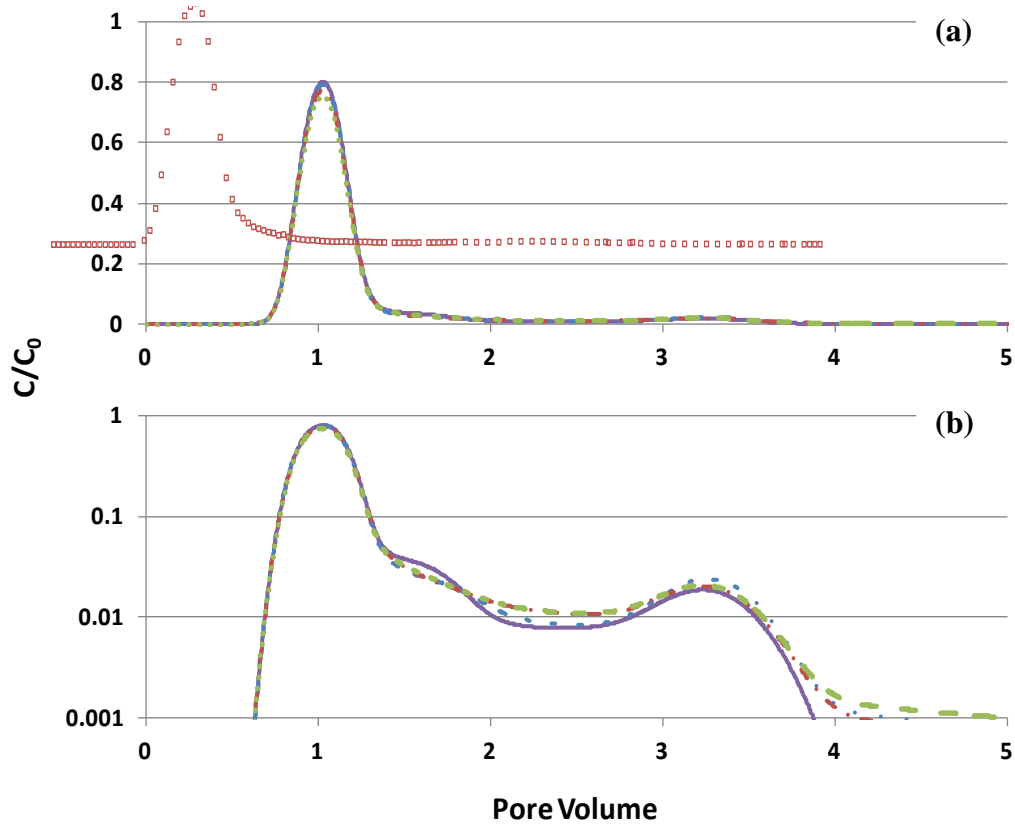


Figure R.2.7. Effluent data and model simulations for the aquifer cell experiment containing the isolated pool. Bromide (circles and solid line), pentanol (diamonds and dashed line), hexanol (squares and dash-dot line) and 2-octanol (triangles and dotted line) are included. The model was fit to the bromide data by adjusting dispersivity. All partitioning tracer breakthrough curves were subsequently predicted using this fitted dispersivity.

Five mass transfer correlations developed from NAPL pool dissolution studies as well as two correlations developed from ganglia dissolution studies were evaluated for use with the linear driving force model. It was determined (see Ervin 2012 for details) that the Nambi and Powers (2003) correlation (developed from a DNAPL pool dissolution study) and the Powers et al. (1992, 1994) correlations (developed from ganglia dissolution studies) are all able of providing good predictions of partitioning tracer transport. By comparison of the sum of squared errors, it was determined that the Nambi and Powers (2003) correlation performs slightly better than the other two correlations. Additionally, the Nambi

and Powers correlation includes a saturation term which may be useful for predicting transport in source zones with heterogeneous DNAPL saturations. The only adjustable parameter in the model is longitudinal dispersivity (0.13 cm) which was fit to bromide data. Note here that transverse dispersivity is assumed to be 10% of the longitudinal value. Overall, the model appears to capture the general shape of the effluent breakthrough curve produced in the experiment (Figure R.2.7). When viewed on the log-scale, it becomes apparent that the model is able to capture the slight dip and recovery in concentrations seen between approximately 1.8 and 3 pore volumes, but that it over predicts the subsequent increase in concentrations. The remainder of the tail concentrations (> 4 PV) is well captured by the model.

Tracer concentrations in the samples collected from the ports were used to construct local BTCs in an effort to examine the influence of the pool on the spatial distribution of tracer concentrations within the box. These local BTCs were subsequently examined by interrogating local concentration predictions produced during each of the aforementioned model simulations. Simulations for each partitioning tracer match the data well for most ports. The dispersivity value fit to the bromide effluent curve was used to predict tracer BTCs at each sampling port. Illustrative results are shown for Columns 1 and 2 of the sampling ports (Figure R.2.8). Note that because of the geometry of the sampling port array (Figure R.2.6), results for column 3 are similar to column 1 and those for column 4 are similar to column 2. In column 1, predictions for port 1E slightly under predict maximum C/C_0 values, but still capture the general shape of the data. For port 1D, the port most affected by the combination of the low permeability berm and the TCE-DNAPL pool, the simulations accurately capture the data. In column 2, the data for all of the ports, except 2D are well reproduced. However, even the predictions at port 2D are able to capture the overall shape and low C/C_0 values seen in the data.

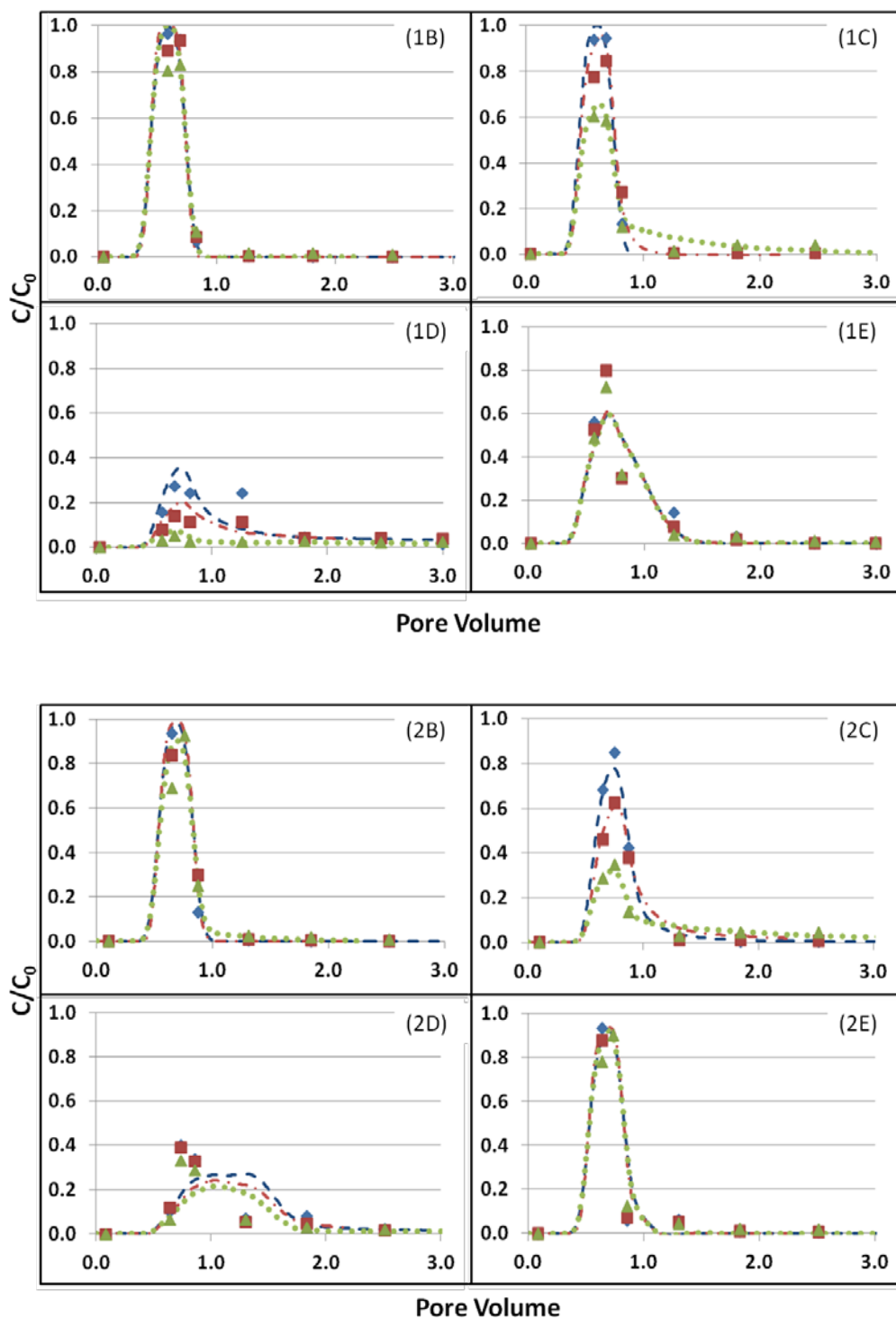


Figure R.2.8. Comparison of tracer concentrations in the sampling ports (columns 1 and 2) to those predicted by the model. 1-pentanol (diamonds, dashed line), 1-hexanol (squares, dash-dot line) and 2-octanol (triangles, dotted line) are included. Panel labels correspond to specific ports show in Figure R.2.6.

Comparison between columns 1 and 2 suggests a fine-scale local variation in concentration. Though these two sets of ports (column 1 versus column 2) are only vertically offset by 1 cm, the differences in the breakthrough curves are distinct (e.g. ports C, D, and E for columns 1 and 2). This shows that the scale of vertical heterogeneity around the low permeability berm and TCE pool is on the order of 1 cm, highlighting the importance of precise alignment of the local ports in the model domain. Nevertheless, results of this experiment suggest that the Nambi and Powers (2003) correlation in concert with the linear driving force model is capable of describing tracer partitioning (absorption and dissolution) within DNAPL pools.

Conclusions for lone pool experiment

Results demonstrated that a 2-D linear driving force model employing the Nambi and Powers (2003) correlation for the mass transfer coefficient, a correlation developed from DNAPL dissolution experiments, is able to predict partitioning tracer transport for the experiment. Model predictions were able to capture the behavior of both the effluent data and local port BTCs downgradient of the TCE-DNAPL pool. When coupled with the results from our column experiment, the results from the pooled aquifer cell experiment allow for quantitative understanding of partitioning tracer transport at both end members of PF.

III.2.1.3. Push-Pull Test Design

Three push-pull tests, each employing a different combination of injection and extraction rates, were conducted in 2D aquifer cell experiments. A description of the aquifer cell is provided in the Section II.2.2.2. Greater detail on the experiments is available in Ervin 2012. In brief, three different packing structures were used to create a low, mid and high PF source zone. Combinations of fast (8.5 mL/min) and slow (0.05 mL/min) flow rates were selected in an attempt to highlight the difference in transport time scales between ganglia and pools. Target flow rates for each experiment are shown below in Table R.2.5. A fast flow rate of 8.5 mL/min was chosen because it provides a similar pore water velocity to that employed in the non-equilibrium column experiments. The slow flow rate was 0.5 mL/min. This slow flow rate represents a compromise between a desire to achieve 2-octanol equilibrium partitioning and the practicability of using slow flow (i.e., long test durations in the field).

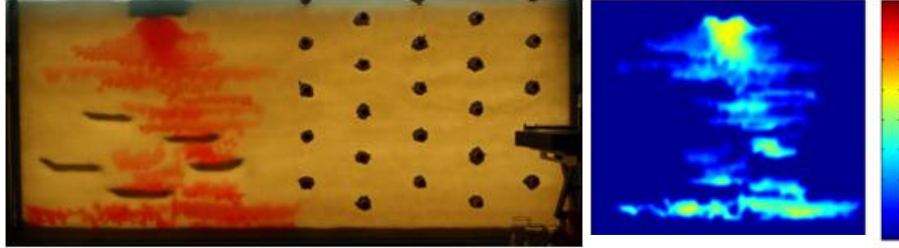
Table R.2.5. Tracer test flow rates for mixed source zone experiments

Condition	Push		Pull	
	Q (mL/min)	v (m/hr)	Q (mL/min)	v (m/hr)
1	8.5	0.25	8.5	0.25
2	0.5	0.02	8.5	0.25
3	8.5	0.25	0.5	0.02

Using a fast flow rate for both phases of a test (condition 1) is most favorable for field implementation because of the cost and organizational issues associated with running long field tests. The increased residence time due to the slow push in condition 2 should allow more tracer mass to partition into the DNAPL. The fast “pull” phase would then force the system into non-equilibrium, possibly visualizing any diffusional resistance to mass transport in the DNAPL pools as long tailing signals. Condition 3 switches the order of flow rates used in condition 2 to force the tracers all the way through the source zone and then allow for partitioning during the pull phase to be close to equilibrium. By changing the injection and extraction flow rates of each push-pull test, the three experiments should show if differences in transport time scales between ganglia dominated and pool dominated systems can be manipulated to estimate PF.

In each of these nine push-pull experiments, approximately 1800 mL of an aqueous tracer solution containing bromide, 1-pentanol, 1-hexanol and 2-octanol was flowed through the source zone from the left end-chamber (Figure R.2.8). To ensure that the tracer solution flowed completely through the source zone, the presence of each partitioning tracer was verified in aqueous samples taken from the first two columns of ports immediately downgradient of the source. Flow was then reversed and background solution was flowed through the box from the right end-chamber. Effluent samples were collected from the left end chamber with a fraction collector (Retriever II, ISCO) in 20 mL increments during this “pull” phase until the tracer tails began to flatten out. Then, samples were collected approximately every 900 mL until tracer concentrations fell below the detection limit. All background solutions used after DNAPL was released into the box were saturated with TCE to minimize TCE-DNAPL dissolution from the source zone. All tracer concentrations were below their detection limit (see Section II.2.1) before the experiment was terminated and the next experiment initiated. It should be noted that though TCE saturated water was used in attempt to minimize TCE-DNAPL dissolution from the source zone, DNAPL mass was lost from each source zone due to both dissolution and volatilization.

low pool fraction (pf = 0.26)



mid pool fraction (pf = 0.55)



high pool fraction (pf = 0.68)



Figure R.2.9. Initial TCE-DNAPL saturation distributions in the 2D aquifer cell for the low, mid and high PF experiments. Shown on the left are photographs of each aquifer cell (100 cm in length, 44 cm in packed height and 1.5 cm in thickness). Shown on the right are light transmission images of saturation distribution. All color bars range from no saturation (blue) to a saturation of 0.4 (red).

A detailed description of the results from each of the nine experiments is available in Ervin (2012). Discussed here are the comparisons across experiments to assess the influence of flow rate and PF on the tracer recover curves. Push-pull recovery curves for the three partitioning tracers employed with the fast-slow flow condition showed little differentiation between the three PFs used here. Even the tails of the 2-octanol recovery curves were similar, and do not distinguish between pool dominated and ganglia dominated source zones. The slow-fast flow scenario developed slight differences at relatively early time among the three PFs with 2-octanol signals separated in order, low, mid, high PF. However, the shapes are too similar to conclusively differentiate between PFs, especially when

considering the loss in fidelity expected with field data. Data from the tails of these 2-octanol recovery curves, showed no separation, indicating that tailing is not as dependent on PF as was hypothesized before conducting these tests. The amount of TCE-DNAPL used to create these source zones (~30 mL) is relatively small; it may be that the approximately 10 additional milliliters of pooled TCE in the high PF box (compared to the low PF box) does not appreciably increase tailing. Interestingly, the fast-fast 2-octanol data sets are the only recovery curves that show a difference between all three PFs, though the recovery curve in the high PF experiment lies between those obtained in the low and mid PF boxes. This, along with the fact that the other flow rate combinations are unable to distinguish between pool fractions, suggests that PF may not be an appropriate metric to be quantified using these push-pull tests.

Equilibrium Push-Pull Model

The most common method for analyzing push-pull tracer tests is to fit an analytical solution to the recovery curve data (Istok et al., 2002). It is important to note that the geometry in many push-pull studies (e.g. Schroth et al., 2001; Istok et al., 2002) has a radial flow field. Therefore, the analytical solutions found in these works were developed for radial or cylindrical coordinate systems. The experiments conducted for this work were completed in rectangular 2-D aquifer cells so that light transmission could be used to more accurately estimate PF. Therefore an analytical push-pull model developed by Gelhar and Collins (1971) was employed to model the BTCs in this rectangular geometry. The analytical solution is as follows:

$$\frac{C}{C_0} = \frac{1}{2} \operatorname{erfc} \left[\frac{\frac{V_{ext}}{V_{inj}} - 1}{\left(\frac{4\alpha}{x_{max}} \left(2 - \left(1 - \frac{V_{ext}}{V_{inj}} \right) \right) \right)^{1/2}} \right] \quad (\text{R.2.2})$$

where α is the dispersivity [L] and x_{max} is the maximum travel distance of each tracer [L]. For bromide, the x_{max} is taken to be V_{inj} divided by the aquifer cell cross sectional area and the porosity (Istok et al., 2002). For each of the partitioning tracers, x_{max} is the maximum travel distance of bromide, divided by the partitioning tracer retardation coefficient. Assumptions implicit in this analytical solution include equilibrium partitioning, uniform flow field, and a uniform distribution of DNAPL saturation.

The analytical solution is fit to the bromide data to determine dispersivity (α). This dispersivity is used in all subsequent fits of the partitioning tracer data to obtain the value of x_{max} that corresponds to each tracer. All fits are carried out by minimizing the sum of squared error between the data and the BTC produced by

the analytical model. Essentially, this model determines the apparent dispersion of each partitioning tracer compared to the dispersion observed in the breakthrough of the non-partitioning tracer (bromide). All of the excess spreading in the partitioning tracers is assumed to result from *equilibrium* interactions between the partitioning tracer and DNAPL. Under this assumption, the retardation coefficient for each tracer can be calculated as:

$$R = \frac{x_{\max}^{Br^-}}{x_{\max}^{part}} \quad (R.2.3)$$

where $x_{\max}^{Br^-}$ is the bromide x_{\max} and x_{\max}^{part} is the x_{\max} of the partitioning tracer. The overall average saturation can be estimated:

$$S_n = \frac{R-1}{K_p^{C_i} + R-1} \quad (R.2.4)$$

Best fit estimates of the saturations obtained using the analytical solution were compared to the known saturation for each of the three tracers in the nine experiments. Representative good performance of the analytical solution is shown in Figure R.2.10. Generally, predictions of 1-pentanol BTCs using the fit dispersivity and measured source zone saturation capture the data. However, the model is unable to capture the degree of excess spreading present in the 1-hexanol BTCs using the measured saturation. Fitting the analytical solution to the 1-hexanol data provides gross over estimates of saturation, even though the model is capable of capturing the shape of the 1-hexanol data sets. Model performance is worse for the 2-octanol recover curves. Here, the analytical solution is unable to capture the shape of the asymmetric 2-octanol curves, no matter how high a saturation value is used. The analytical solution always produces symmetric curves that breakthrough at $V_{\text{ext}}/V_{\text{inj}} = 1$. Increasing saturation only increases the apparent dispersion in the recovery curve.

To facilitate a quantitative comparison across all 27 partitioning tracer curves, we employ the ratio of the saturation obtained from the analytical solution to the known saturation (Table R.2.6). It is interesting to note that in the best cases the saturation estimates obtained from the analytical solution are an order of magnitude greater than the actual saturation in the interrogated source zone. Over estimation of NAPL saturations when using the analytical solution to interpret data from push-pull partitioning tracer tests has also been noted in other studies. Davis et al. (2002) found that the analytical solution resulted in average saturation estimates that were 3-4 times higher than the actual overall saturation, but did not offer an explanation of the overestimation. Istok et al. (2002) also found that applying the analytical solution to push-pull BTC resulted in an overestimation of average saturation, but did not report the magnitude of the overestimates. They

did, however, suggest that the overestimation is due to kinetic processes that are not accounted for in the analytical solution.

The asymmetry in the recovery curve was further explored as a potential source of the gross overestimation of the TCE-DNAPL saturations. Here the experiment shown in Figure R.2.10 were refit using only early ($V_{\text{ext}}/V_{\text{inj}} \leq 1$) or late ($1 \leq V_{\text{ext}}/V_{\text{inj}} \leq 3$) time data in the recovery curves. Estimated saturations for these fits are shown in Table R.2.7 along with the saturation estimated when the analytical solution is fit using the entire recovery curve. Notice that fitting the early time data decreases the accuracy of the saturation estimate, but fitting late time data increases accuracy. This illustrates the asymmetry in the curve produced by phenomena occurring related to the early time data, but the high concentrations control the fit when all the data are used.

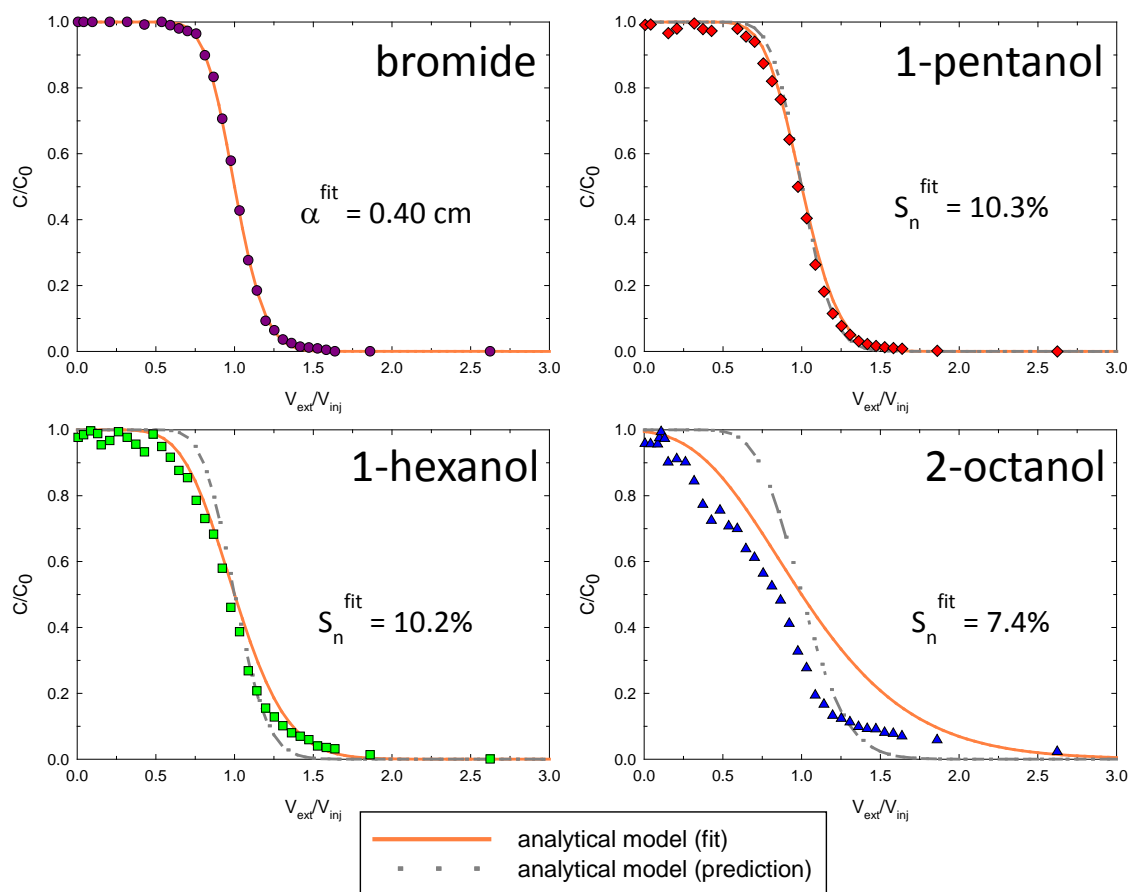


Figure R.2.10. Representative experiment (Mid PF, Fast-Fast Flow) for which the analytical solution has relatively good performance. Shown here are data (symbols) for each tracer and two simulations, a fit of the analytical solution to the data by adjusting only TCE-DNAPL saturation, and a prediction using the actual TCE-DNAPL saturation determined via light transmission (0.8%).

Table R.2.6. Ratios of saturation estimates obtained with the analytical solution to those measured via light transmission. Bold values represent the experiment shown in Figure R.2.10

1-pentanol estim : meas		pool fraction		
		low	mid	high
flow	fast-fast	25.7	12.9	14.2
	slow-fast	16.3	14.2	6.7
	fast-slow	8.2	36.9	10.4

1-hexanol estim : meas		pool fraction		
		low	mid	high
flow	fast-fast	25.7	12.8	21.2
	slow-fast	11.4	13.9	9.6
	fast-slow	9.6	33.6	13.2

2-octanol estim : meas		pool fraction		
		low	mid	high
flow	fast-fast	7.8	9.3	20.8
	slow-fast	9.8	12.3	6.5
	fast-slow	7.9	17.1	12.3

Table R.2.7. Comparison of saturation values obtained by fitting different sections of the recovery curves shown in Figure R.2.10

		TCE-DNAPL saturation (%)		
		pentanol	hexanol	octanol
measured		0.8	0.8	0.8
fit with	all data	10.3	10.2	7.4
	$0 \leq V_{\text{ext}}/V_{\text{inj}} \leq 1$	18.8	17.4	8.9
	$1 \leq V_{\text{ext}}/V_{\text{inj}} \leq 3$	0.7	3.9	0.2

Model Choices for 2D Laboratory-Scale Simulations

For the simulation of laboratory experiments, Equation M.2.9 was solved in two spatial dimensions. The hydraulic conductivity was assumed isotropic. A value of 0.7 for the Van Genuchten parameter n_{vg} [-] was employed because it has been previously used to model similar sands (Rathfelder and Abriola, 1996).

Because the model was confined, there was no advective or dispersive flux through the top or bottom boundaries. The flow rate was controlled by prescribing the head (from experimental piezometric head readings) in the fully screened inlet and outlet wells. These wells were modeled as very high permeability columns added to the sides of the domain. The exact locations of the tubing used for experimental injection and extraction were modeled inside the screened wells. Also, no dispersive flux was allowed on either side of the domain. Tracer transport was simulated with the linear driving force model formulation presented in Section II.2.3.1. The longitudinal dispersivity was determined by fitting to the bromide data and the vertical dispersivity is assumed to be 0.1*longitudinal dispersivity. The lumped mass transfer coefficient was evaluated using a modified Nambi and Powers (2003) correlation. Light transmission images of the experimental system before TCE-DNAPL injection allowed for the exact geometry of the 2-D box (i.e. the location of low and high permeability layers) to be input into the model domain. The exact TCE-DNAPL saturation distribution was added to the domain using light transmission results after TCE-DNAPL injection. Hydraulic conductivity values for each sand type were estimated from intrinsic permeability and then refined using known experimental velocities and piezometric head readings.

The domain was discretized into 5 mm x 5 mm grid blocks, which is similar to the averaging window used to estimate PF from the light transmission pictures. A time step of 20 seconds was used for all simulations, upon determining that a smaller time step produced the same BTCs. The flux-averaged tracer concentrations were recorded at the effluent well (right-hand side of the aquifer cell).

The Role of Mass Transfer

The numerical linear driving force model employed to examine the pooled box source zone was used to examine the push-pull recovery curves. For all nine push-pull tests, the model domain was constructed from light transmission results that measured the exact packing structure and TCE-DNAPL distribution. Dispersivity was fit to each bromide data set. Alcohol tracer recovery curves were predicted based on these fitted dispersivity values and the measured partition coefficients. For full details about the modeling of each experiment, please see Ervin (2012). Presented here is a summary of the results obtained for the 2-octanol recovery curve for the high PF, fast-fast experiment (Figure R.2.11). Notice that the 2-octanol data represent a recovery curve with a large amount of asymmetry and several inflection points. When uniform permeability, uniform saturation and equilibrium partitioning is assumed, neither the analytical nor the numerical model can capture the data (both are smooth, symmetric curves). Note that the minor differences between the analytical and numerical models are related to the numerical model being solved in 2-D (i.e., longitudinal and transverse dispersivities). When exact knowledge of the permeability field and saturation distribution is employed with mass transfer kinetics established by the Nambi and Powers (2003) correlation, the model can well capture all features of the observed recovery curve. These represent end members in the knowledge and assumptions that can be made (homogenous versus complete knowledge of heterogeneity). Relaxing the idea of having perfect knowledge of permeability yields a simulation that also captures the data well. This however, presumes perfect knowledge of the saturation distribution which is unlikely for any real application of this push pull tracer technique. Thus, we also relax the amount of knowledge presumed about the saturation distribution and assumed a known average saturation (i.e., uniform permeability and saturation distributions). Under these assumptions, the kinetic simulation still represents a good approximation of the data; far better than what is capable with the analytical solution. This demonstrates that mass transfer kinetics is the most important aspect (in comparison to permeability, saturation distribution and mass transfer kinetics) when attempting to describe asymmetric recovery curves. This observation suggests techniques which upscale the mass transfer coefficient based upon features of the source zone may hold promise for in source assessment of DNAPL architecture (see Section III.4.2).

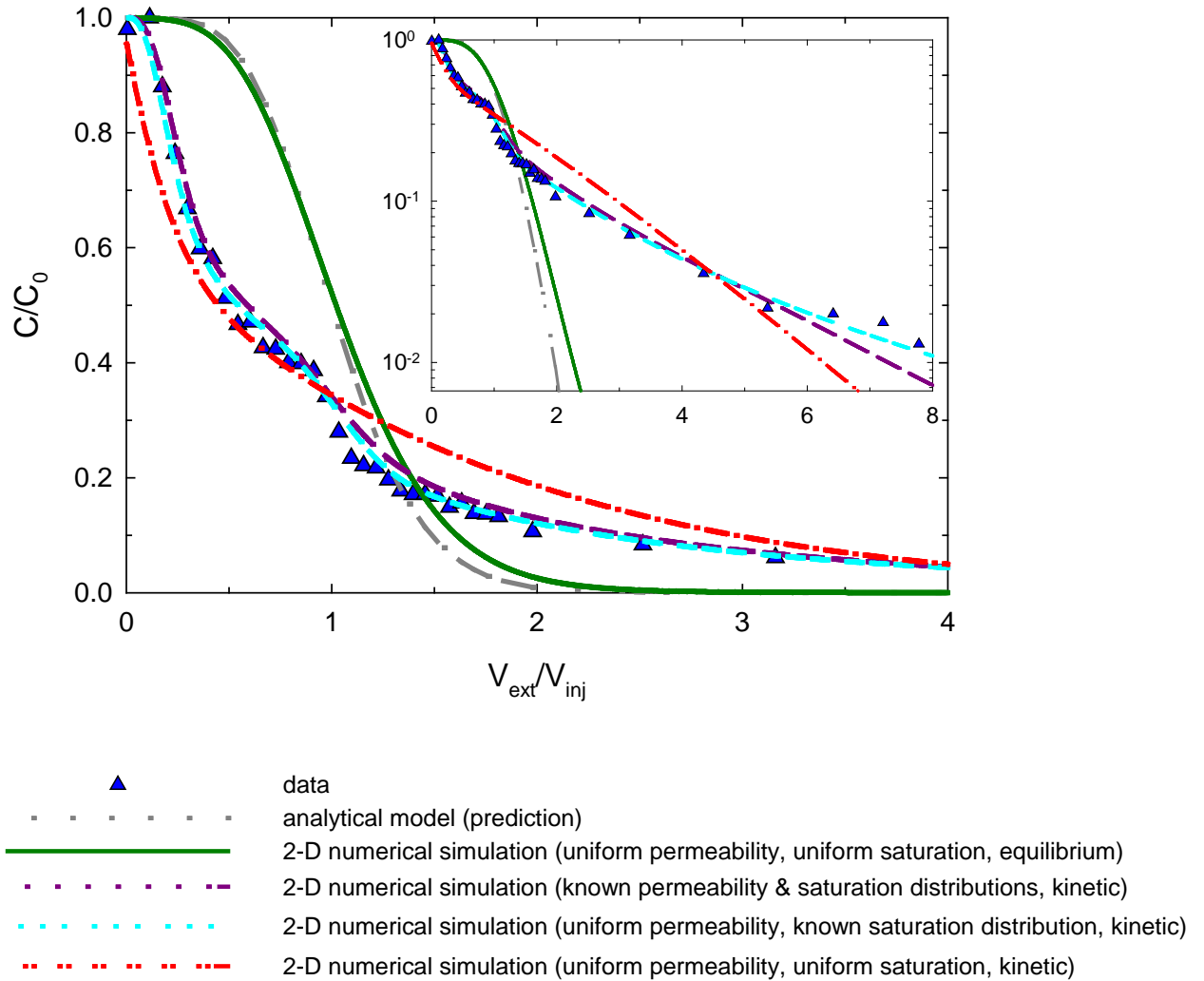


Figure R.2.11. 2-octanol recovery curve for the high PF, fast-fast flow experiment used here to illustrate the influence of the major simplifying assumptions associated with the analytical solution.

Conclusions from 2-D box experiments

Push-pull tests were conducted in three source zones of low, mid and high PF. Three combinations of fast and slow flow rates were employed to determine if the difference in transport time scales between ganglia and pools can be manipulated to differentiate pool dominated source zones from ganglia dominated source zones. Results indicate that all three flow rate combinations (fast injection, fast extraction; slow injection, fast extraction; fast injection, slow extraction) provide similar recovery curves. Also, the push-pull tracer tests do not appear to be sensitive to PF. As slow flow rates are costly (in both time and money) to run in

the field, it is beneficial that the fast push, fast pull test provides the same results as the other two flow rate combinations.

Cell data comparisons with model simulations also reveal that the inclusion of kinetic exchange is necessary to interpret asymmetric recovery curves. A 2-D numerical model including a linear driving force expression parameterized by the correlation of Nambi and Powers (2003) is able to accurately reproduce partitioning tracer recovery curves. This model was used to show that the assumptions of equilibrium partitioning and uniform saturation distribution are the two assumptions that prevent the analytical solution from being able to capture the behavior of the higher partitioning tracers. It was also shown that a model assuming kinetic partitioning, but prescribing only average uniform saturation and permeability values can produce a reasonable approximation of the 2-octanol recovery curves.

III.2.1.4. Interpreting Asymmetric Recovery Curves in Push Pull Tracer Tests

Our interest in push-pull partitioning tracer tests was based upon the idea that these tests may provide localized information about SZA. Results presented in the previous sections suggest that these recovery curves may not be particularly sensitive to PF, per se. The average saturation within the interrogated volume appears to be a more readily attainable output of this type of in source testing. Interestingly, though, the assumption of equilibrium partitioning when interpreting recovery curve data was found to lead to gross overestimates of the DNAPL saturation. Kinetic descriptions of the mass exchange must be included to obtain reasonable approximations of the saturation. However, even with the inclusion of kinetic mass transfer, there are instances where recovery curves for strongly partitioning solutes (e.g., 2-octanol) are highly asymmetric, leading to poorer estimates of saturation. In practice, asymmetric recovery curves are often set aside due to the difficulties in interpreting the curves with an analytical solution(s). Thus interest here is placed on coupling simple metrics of SZA with the kinetic limitations to elucidate an empirical method for interpreting asymmetric recovery curves. To better elucidate the causes of asymmetry we examined a series of 40, highly simplified, synthetic, SZAs. Push-pull partitioning tracer tests employing 2-octanol were then simulated with each simple source zone using a numerical model that includes the influence of the kinetics and precise SZAs. Interrogation of the simulation results identified common points of inflection in the recovery curves which were correlated to features of the DNAPL distribution.

Highly Simplified SZAs

Forty simple source zones (Figure R.2.12) were created to produce domains with TCE-DNAPL source zones that vary in vertical and horizontal distribution, distance of DNAPL to the injection/extraction well, total DNAPL mass, and local TCE-DNAPL saturation. The highly simplified SZAs were then used within the previously described 2D push pull numerical model to generate recovery curves for 2-octanol under the fast-fast flow condition. The model domain for the these

simulations is the same as the aquifer cells used for the experiments described in the previous section (100 cm length x 44 cm height). A dispersivity of 0.5 cm was selected for use in all simulations as this value is representative of the dispersivities fit to conservative tracer data in our 2D box experiments. The permeability was based upon that of the 40-50 mesh sand. Also shown in Figure R.2.12 are realization numbers (1 through 40) and the saturation values of all grid cells that contain TCE-DNAPL. In each realization (except for realization 12) all cells in the domain containing DNAPL have the same saturation value. This saturation value varies from realization to realization, but is consistent within each realization. Realization 12 has an area of high saturation within a region of low saturation, and therefore has two saturation values as depicted in Figure R.2.12.

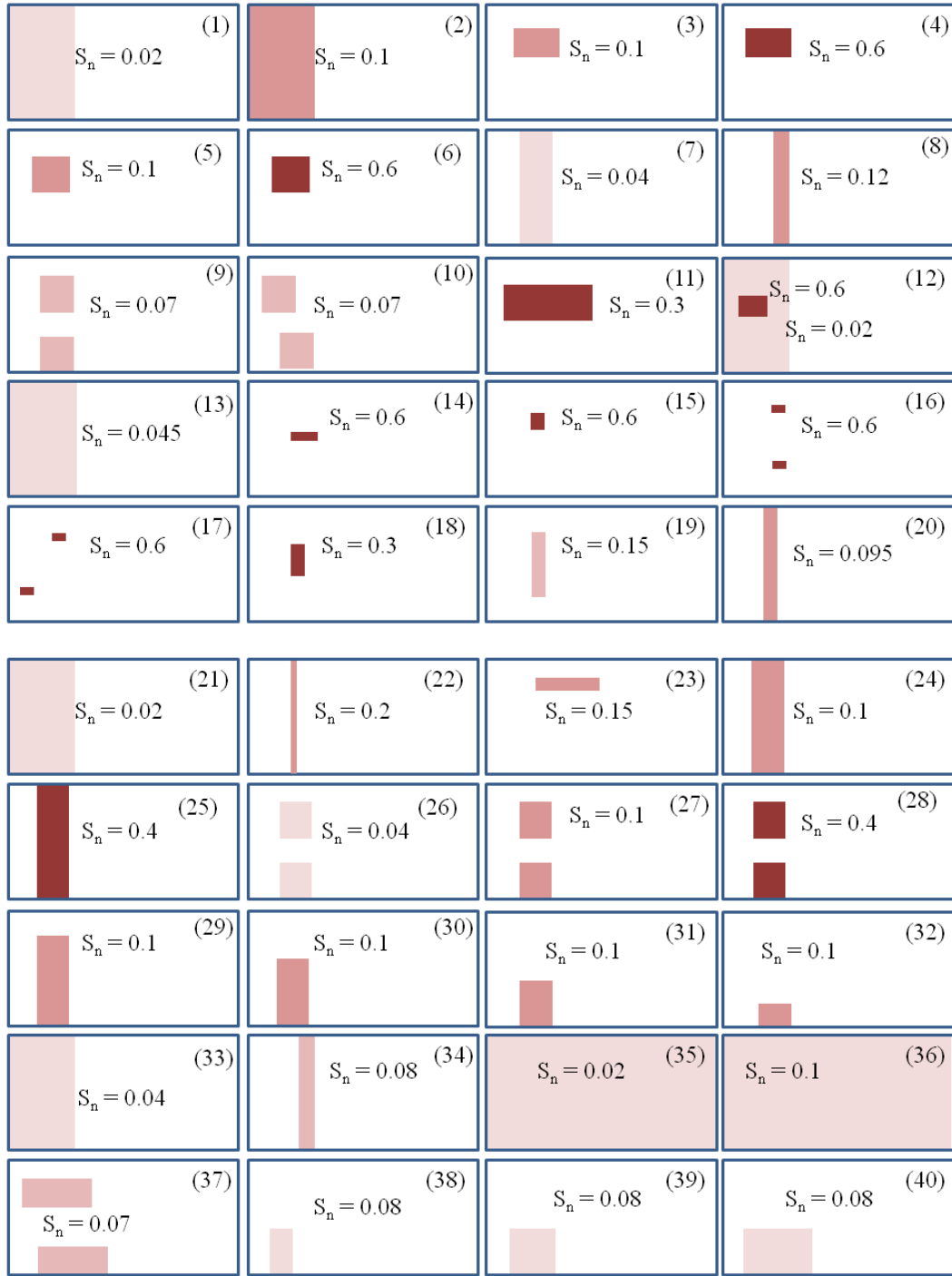


Figure R.2.12. Representations of the forty highly simplified source zones employed in the development of the empirical approach to interpreting asymmetric recovery curves in push-push partitioning tracer tests.

Interpretation

Detailed analysis of each simulation is available in Ervin (2012). What is presented here are results which highlight the empirical interpretation. The source zones presented in Figure R.2.12 were first examined to determine if push-pull tests are capable of distinguishing vertical differences in DNAPL SZA. Simulations employed here include those where DNAPL occupied 100% of vertical (simulation #24), 80% of vertical (simulation #29), 60% of vertical (simulation #30), 40% of vertical (simulation #31), and 20% of vertical (simulation #32). These five source zones produce five distinct curves (Figure R.2.13), suggesting that the shape of the recovery curve depends on the vertical distribution of DNAPL. There are a few important characteristics of these curves. First, there is an inflection point early in each recovery curve where the slope of the concentration signal levels out. The C/C_0 value of this inflection point appears to decrease as more of the vertical domain is occupied with DNAPL. Also, on some of the curves, there is a second inflection point (around $V_{\text{ext}}/V_{\text{inj}} = 1.5$) where concentrations level out and start to tail.

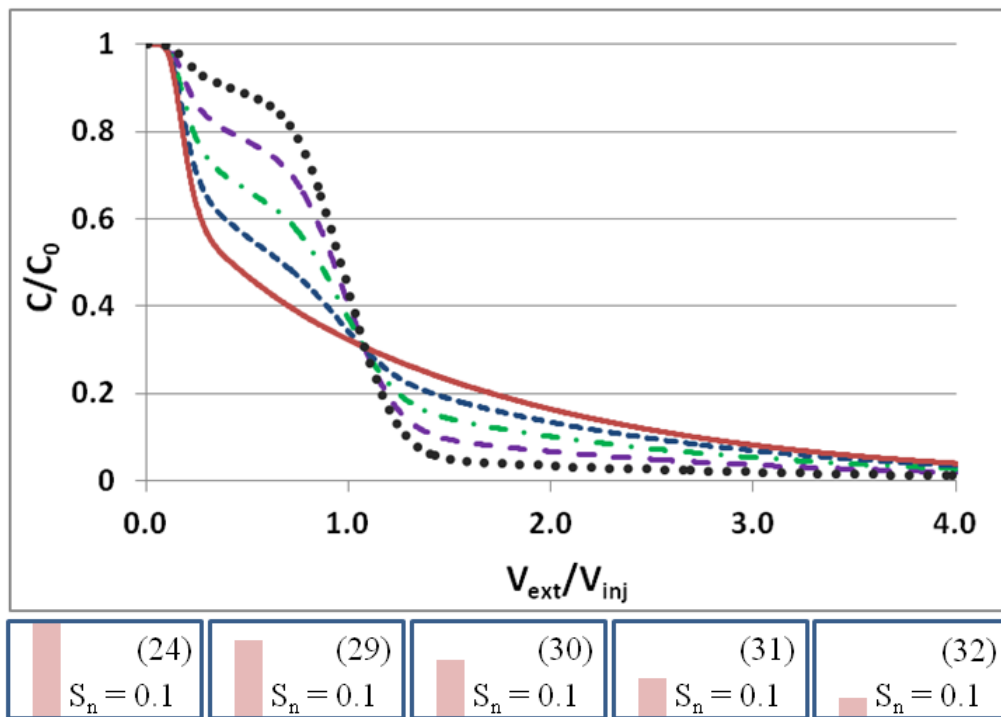


Figure R.2.13. 2-octanol recovery curves resulting from push-pull tests conducted in realizations 24 (solid), 29 (short dash), 30 (dot dash), 31 (short dash) and 32 (dotted). Also included are the diagrams of the corresponding source zones.

This inflection point is most obvious in domains where less of the vertical dimension contains DNAPL, and is not present in domains where the vertical dimension is completely filled with DNAPL. The recovery curves shown in Figure R.2.13 suggest that for the same horizontal distribution and distance from the injection/extraction well, these push-pull tests respond to variations in the percent of the vertical domain containing DNAPL saturation (%Z).

The influence of horizontal distribution is best visualized by considering a series of simulations conducted using realizations 7, 8, and 21 (Figure R.2.14). These realizations all cover the entire vertical domain (%Z =100), have the same TCE-DNAPL mass, have the same distance from the injection/extraction well to the back edge of the DNAPL mass, but differ in distance between the injection/extraction well and the front edge of the DNAPL mass. These three realizations result in separated curves in the early portion of the recovery curve, that all recovery curves become coincident at $V_{\text{ext}}/V_{\text{inj}} = 0.6$. These results demonstrate that the closer the DNAPL front is to the injection/extraction well, the earlier C/C_0 concentrations drop from a value of 1.0. 2-octanol should behave like a conservative tracer in the area between the well and the DNAPL front (assuming no tracer/porous media interaction). The reason for the C/C_0 value to drop below 1.0 is either because enough tracer mass has been pumped out of the system or because tracer interactions with the DNAPL are causing retardation. The bromide signals of each of these curves (not shown) drop from 1.0 much later than the 2-octanol curves; therefore, the early drop in the 2-octanol must be related to tracer partitioning.

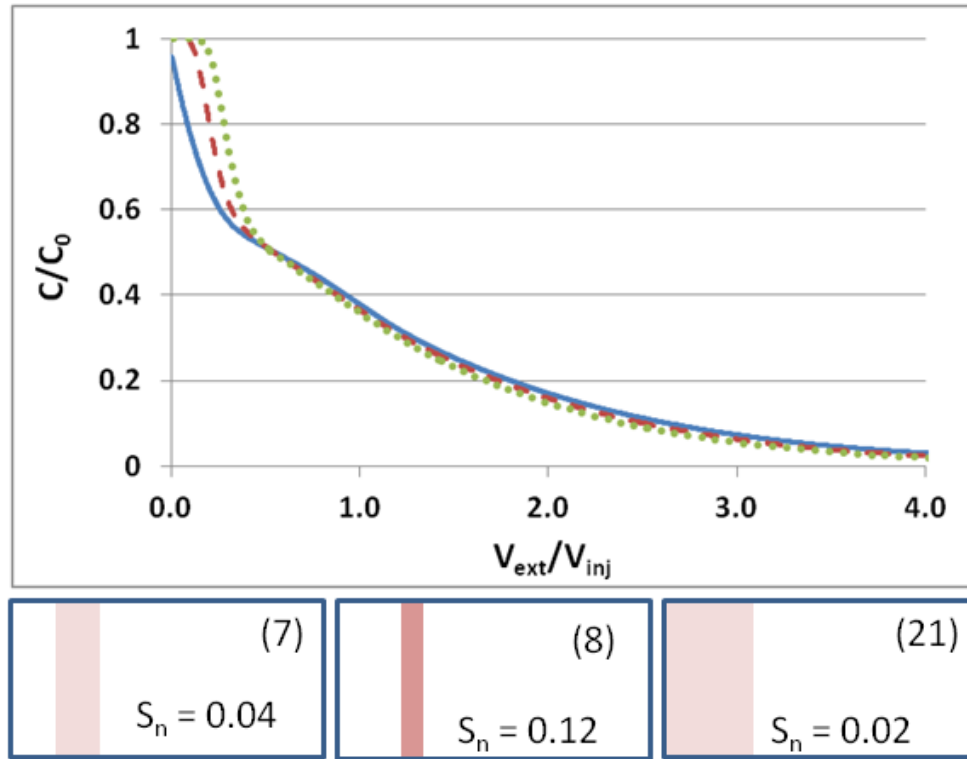


Figure R.2.14. 2-octanol recovery curves resulting from push-pull tests conducted in realizations 7 (dashed), 8 (dotted), and 21 (solid). Also included are the diagrams of the corresponding source zones.

Analysis of the results presented above, as well as recovery curves produced by the other realizations (see Ervin (2012) for details), indicate that three key aspects of an asymmetric recovery curve (Figure R.2.15) may provide information on SZA: i) the point at which C/C_0 concentrations fall from a nominal value of 1.0; ii) the C/C_0 value corresponding to the first inflection point; iii) the C/C_0 value corresponding to the second inflection point. The goal then was to correlate these features of the recovery curve to features of the DNAPL distribution. The horizontal distance from the well to the DNAPL front (D_{front}) can be approximated using the average DNAPL saturation in the contaminated region (S_n) and $(V_{\text{ext}}/V_{\text{inj}})^*$, which is defined to be the value of $V_{\text{ext}}/V_{\text{inj}}$ at which C/C_0 falls below 0.980, by using Equation R.2.5. Note that D_{front} in Equation R.2.5 is supplied in terms of the fraction of the horizontal distance interrogated by the tracers (i.e., x_{max} , as previously defined, and taken to be V_{inj} divided by the aquifer cell cross sectional area and the porosity). Equation R.2.5 represents a correlation ($R^2=0.94$) developed using recovery curves from the 40 simplified source zones. Exponents of regressed parameters are shown as (value \pm standard deviation).

$$\left(V_{ext}/V_{inj}\right)^* = (0.0153 \pm 0.0037)(D_{front})^{(0.922 \pm 0.083)} (S_n)^{(0.174 \pm 0.028)} \quad (R.2.5)$$

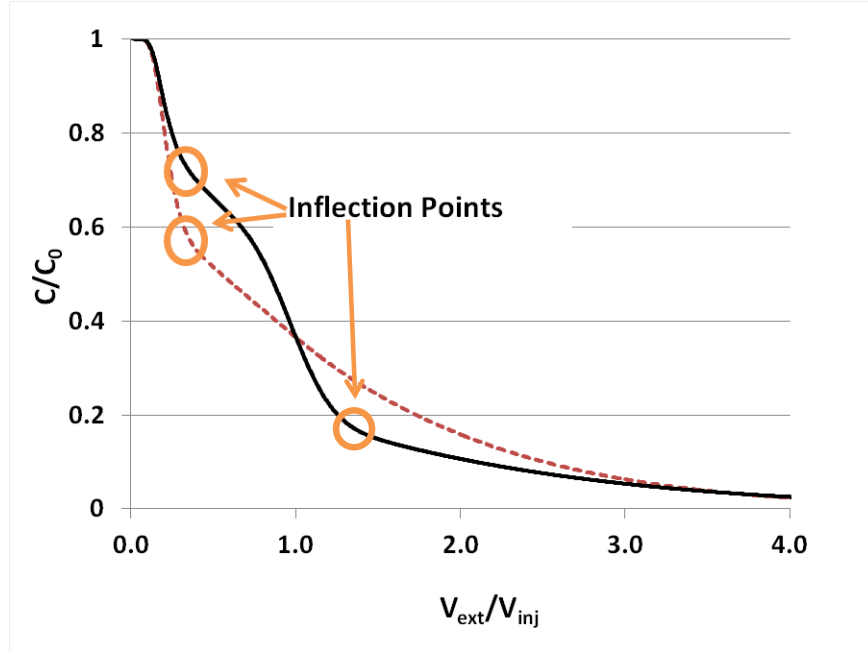


Figure R.2.15. Example of inflections in asymmetric recovery curves.

Analysis of each recovery curve suggested a linear relationship between %Z and the value of C/C_0 corresponding to the first inflection point (Equation R.2.6, $R^2 = 0.95$). The second inflection was best correlated to saturation and %Z (Equation R.2.7, $R^2=0.93$). It should be noted here that realizations with DNAPL in the entire vertical domain do not have a second inflection point, so Equation R.2.7 is based upon the 24 realizations for which %Z<100. Regressed parameters are shown with the (value \pm standard deviation).

$$\left(\frac{C}{C_o}\right)_{1st} = \frac{(225 \pm 6) - \%Z}{(230 \pm 9)} \quad (R.2.6)$$

$$\left(\frac{C}{C_o}\right)_{2nd} = (0.0093 \pm 0.0023) S_n^{(-0.241 \pm 0.039)} \%Z^{(0.564 \pm 0.070)} \quad (R.2.7)$$

Equations R.2.5-R.2.7 create a system of equations related to specific, identifiable features of an asymmetric recovery curve that can be employed to produce features of the DNAPL saturation distribution within the volume interrogated

during a push-pull partitioning tracer test. There are caveats to this analysis, the most important of which is that these results are only strictly valid for the system in which they were developed. A field push-pull test will be complicated by radial flow and the potential for DNAPL to be localized within one sector of the well circumference. Heterogeneous geology may necessitate the use of the bromide curve to determine which features of the recovery curves are due to the flow field and which are due to interactions with the DNAPL. Moreover, the field data will not be as complete or smooth as these simulations. Thus, without high quality data sets, inflection points may be miscalculated or missed completely. These caveats notwithstanding, the empirical approach was tested against independent data sets obtained from 2D aquifer cell experiments (Ervin, 2012). Shown here is an illustrative application related to the 2-octanol recovery curve in the mid PF, fast-fast experiment (Figure R.2.16). The features of this curve produce the following estimates of the SZA using Equations R.2.5-R.2.7: $D_{\text{front}} = 17\%$ of x_{max} , which with an x_{max} of 68 cm means the DNAPL is 12 cm from well; $\%Z = 59$; and S_n within the contaminated domain = 0.18. These estimates were found to compare favorably with the actual DNAPL distribution. As can be seen in Figure R.2.17, the estimated D_{front} is a reasonable uniform approximation of the heterogeneous DNAPL front. The actual $\%Z$ in the experiment was 50 compared to the estimated 59. Comparison of the estimated saturation requires the actual saturations be weighted by the $\%Z$ of each contaminated region (see Figure R.2.17) as shown in Equation R.2.8.

$$S_{n,\text{weighted}} = \frac{S_{n1} \%Z_1 + S_{n2} \%Z_2 + S_{n3} \%Z_3 + S_{n4} \%Z_4 + S_{n5} \%Z_5}{100} \quad (\text{R.2.8})$$

Where, S_{n1} , S_{n2} , S_{n3} , S_{n4} and S_{n5} are the average saturation calculated for each of the five TCE-DNAPL regions boxed in Figure R.2.17. The weighted average saturation in the aquifer cell experiment is then 0.14, which compares reasonably well to the value 0.18 obtained using the empirical approach.

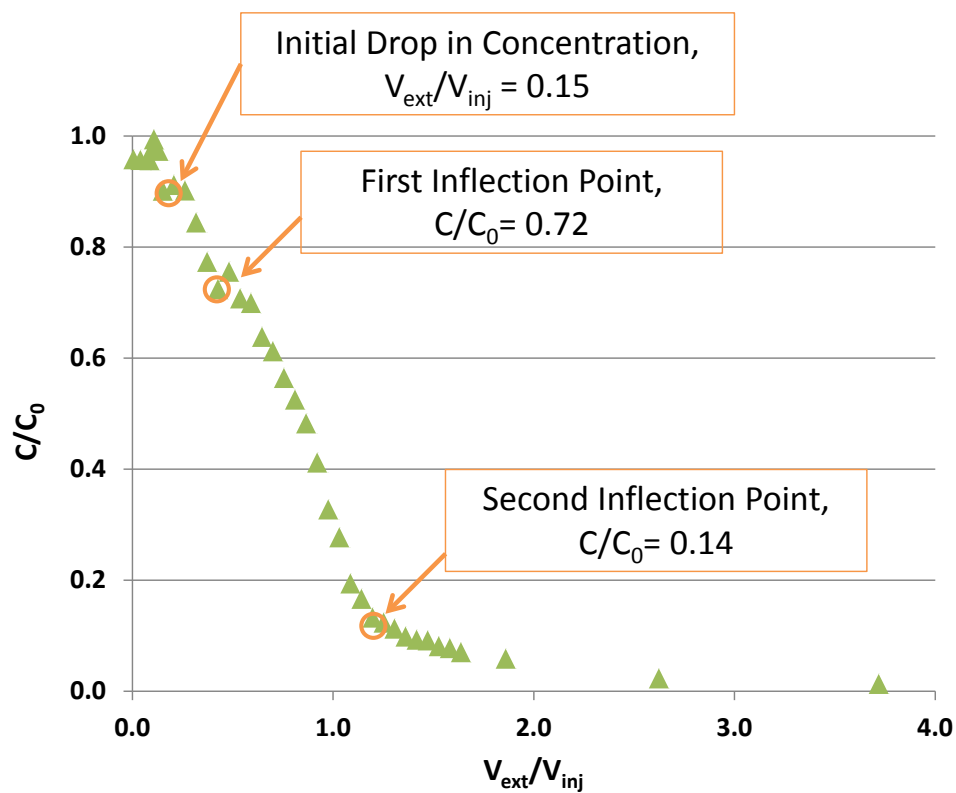


Figure R.2.16. Interpretation of an asymmetric recovery curve using the empirical approach developed in this research. The data shown here are those from the 2-octanol recovery curve produced from the mid PF, fast-fast experiment.

Estimated $D_{\text{front}} = 12 \text{ cm}$

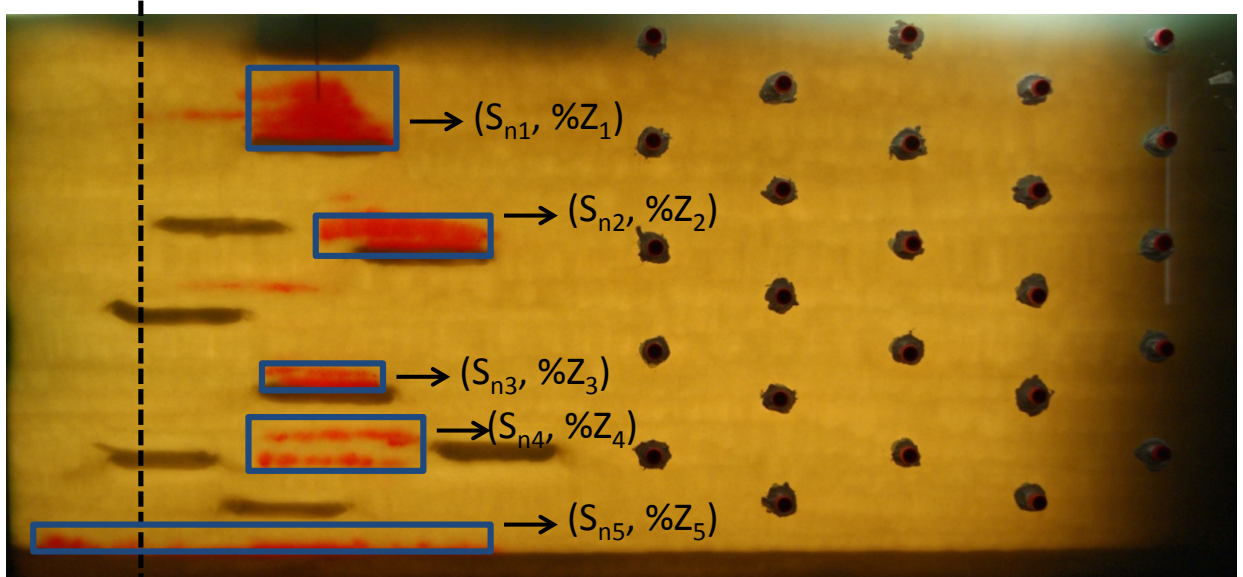


Figure R.2.17. Light transmission image of DNAPL architecture in the mid PF, fast-fast experiment used to illustrate the empirical approach to interpreting asymmetric recovery curves obtained during push-pull partitioning tracer tests. The boxed regions correspond to those used in Equation R.2.8.

The above illustration using 2-octanol as a partitioning tracer in a push pull test, demonstrate how asymmetric recovery curves may be used to produce estimates of DNAPL source zone features. If a recovery curve has both inflection points discussed in this analysis, it may be able to provide three pieces of information: i) the distance between the injection/extraction well and the DNAPL front; ii) the percent of the vertical domain that contains DNAPL; iii) the average local saturation of the DNAPL. This analysis cannot determine the vertical location of the DNAPL. For example, if it is determined that $\%Z=60$, this analysis cannot indicate whether the DNAPL is in the bottom 60% percent of the domain, the top 60% of the domain or spaced throughout the vertical domain. Additionally, the analysis does not give information on the horizontal extent of the domain. However, it appears that these curves can be used to estimate more than just the overall average saturation of a source zone.

Conclusions for the Interpretation of Recovery Curves

The ability of the selected features of the recovery curve to describe DNAPL SZA needs to be examined in much greater depth for more realistic source zones. However, the preliminary analysis conducted herein indicates that because of these features, push-pull tests may be useful for estimating more than just overall DNAPL saturation. It may be that the strength of this analysis lies in better differentiating between source zones characterized by greater vertical spreading

(characteristic of younger source zones) from source zones with more localized hot spots (characteristic of aged source zones).

III.2.2. Push-Pull Tracer Test Model Development

III.2.2.1. Fine-Scale 3D Simulator

In the previous sections, experimental results were presented for examining the behavior of DNAPL releases in highly heterogeneous (Markov Chain model) formations as well as for tracer partitioning at the laboratory scale. Due to their strong link to experimental results, the simulation results describing these experiments were also presented in the previous sections. The reader is referred to Section III.1.1.2, subsection *Batch and Aquifer Cell Experiments/Results of Markov-chain transitional probability aquifer cell experiment*, respectively Section III.2.1.3, subsection *The Role of Mass Transfer*.

Field-scale 2D and 3D results obtained with the fine-scale simulator for the purpose of developing and applying an upscaled push-pull model are presented together with the presentation of the upscaled model, see Section III.4.2.

III.2.2.2. Tracer Push-Pull Sensitivity and Inverse Modeling

Implementation of Adjoint Sensitivity Method

In this section, we present an implementation of the adjoint sensitivity method (M.2.24-M.2.28) for the problem of investigating the sensitivity of tracer aqueous phase concentration to DNAPL saturation in a push-pull test. With the calculated sensitivity matrix, we are able to back estimate the distribution of DNAPL saturation through observed tracer concentrations. The flow field, boundary conditions, and load terms in the transport model need to be set up in a manner that reflects the adjoint model described in Section II.2.3.3. The flow field is calculated in the same manner as when forward simulations are run, and then the flow field is reversed because we use backward time τ in the derivation of the adjoint states equations. The second-type boundary condition, which is adopted in the forward push-pull tracer transport model, becomes a third-type condition in the adjoint states equations. The transport model is run once for each observation, coupled with each adjoint run, the sensitivity matrix of tracer concentration to DNAPL saturation can then be obtained.

We demonstrate the efficiency of the adjoint sensitivity method to investigate the sensitivity of tracer concentration to DNAPL saturation when the number of concentration observations is much smaller than the number of parameters. After that, we compare two tracers with differing partitioning coefficients to examine their performance. We also investigate the influence of tracer injection concentration and load term on the sensitivity matrix.

We first explore the utility of this adjoint sensitivity approach using a three-dimensional hypothetical source zone containing a heterogeneous DNAPL (TCE)

distribution (figure R.2.18), which is a 3.5m long, 3.5m wide, and 2m high domain. The single push-pull well is located at the center of this domain. Two-dimensional uniform planar flow is assumed around the push-pull well, and non-equilibrium interphase mass transfer is described by a linear approximation to the diffusion flux across a stagnant film separating two phases. Here we adopt the heterogeneous TCE saturation distribution depicted in figure R.2.19. We specifically investigate how the tracer concentration breakthrough curves in the well will change with the perturbation of saturation distributed within the interrogated zone. The flow and media properties in addition to some of the model input parameters are listed in table R.2.8.

Table R.2.8. Important input parameters for modeling

Flow and media properties	
Diffusion coef. (m^2/s)	7.75E-10
Longitudinal dispersivity (m)	0.03
Transverse dispersivity (m)	0.003
Keq of Hexanol	17
Keq of Octanol	149
D ₅₀ (mm)	0.328
Unity Index	1.09
Porous media density (g/cm^3)	1.67
Porous media porosity	0.35
Distribution coef. (cm^3/g)	0.00001
Qinj, Qext (m^3/s)	1.5E-4
Push Duration (h)	1
Pull Duration (h)	4
Model parameters	
Domain dimensions (m)	3.5*3.5*2
Grid size (m)	0.05*0.05*0.4

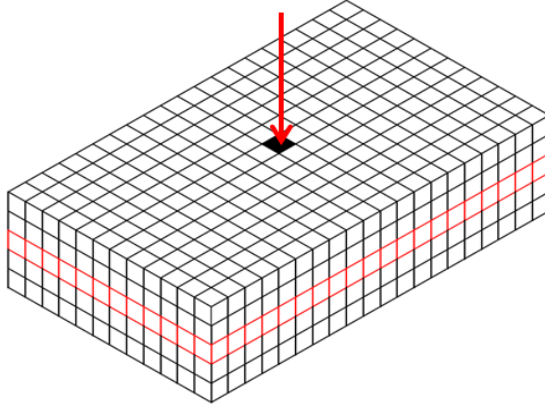


Figure R.2.18. Skeleton diagram of study area.

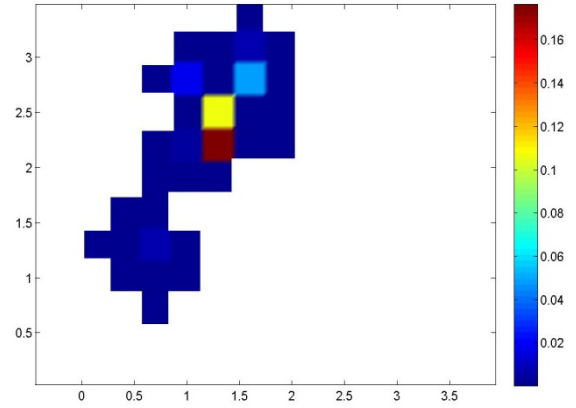


Figure R.2.19. DNAPL saturation distribution.

The assumptions of this push-pull model are (1) homogeneous two-dimensional Cartesian flow field (planar), (2) heterogeneous three-dimensional Cartesian transport model, (3) heterogeneous DNAPL distribution, (4) non-equilibrium interphase mass transfer, (5) no effect of mass injection on flow field, (6) no effect of porosity, dispersion tensor, fluid velocity, source or sink flow rates on DNAPL saturation.

For scenario 1, we first demonstrate the efficiency of the adjoint sensitivity method to obtain the sensitivity matrix of tracer concentration to DNAPL saturation when the number of observations is much smaller than the number of parameters. We push a pulse of octanol tracer solution into the well with a flow rate of 1.5×10^{-4} m³/s for our hour. After that, the tracer is extracted from the well with the same flow rate, for four hours. Here octanol is chosen for its high partition coefficient to investigate how the sensitivities of tracer concentration with respect to DNAPL saturation change at different time steps during the pull phase. In addition, the mass transfer correlation presented by Powers et al. (1994) is adopted here as the expression of mass transfer coefficient in the control equation for the push-pull tracer test.

To verify the performance of the adjoint sensitivity method, we first compared the sensitivity matrix at the end of the pull phase that was obtained using the adjoint sensitivity method to that observed by running the forward model according to the change of saturation value in each grid (figure R.2.20). Examination of the figure reveals that the detailed values and patterns of these two sensitivity matrices are similar, confirming the reliability of the adjoint approach for calculating sensitivities.

At early stages during the pull phase, the tracer concentration in the push-pull well decreases rapidly, leading to a high positive sensitivity of the tracer concentration to DNAPL saturation around the push-pull well. However, at later

times, the mass of tracer that was captured in the DNAPL phase will continue to partition to the aqueous phase. Thus more significant sensitivities occur where DNAPL exists. Furthermore, an increase in DNAPL saturation causes a reduction in tracer concentration (negative sensitivity). Sensitivities of tracer concentration to DNAPL saturation at 1h, 2h, 3h and 4h during the pull phase are shown in figure R.2.21.

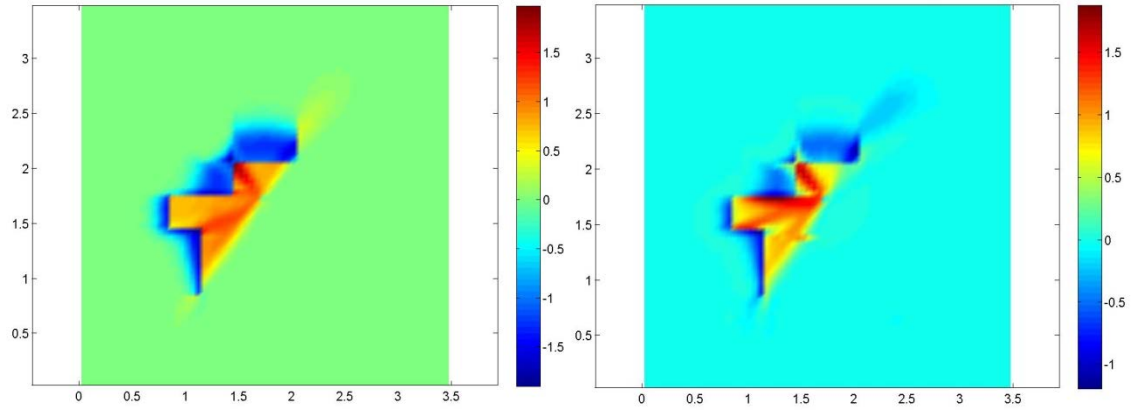


Figure R.2.20 Sensitivity of tracer concentration in aqueous phase with respect to DNAPL saturation at the end of pull phase. The left figure is obtained using the adjoint sensitivity method, the right figure is obtained by running the forward model many times.

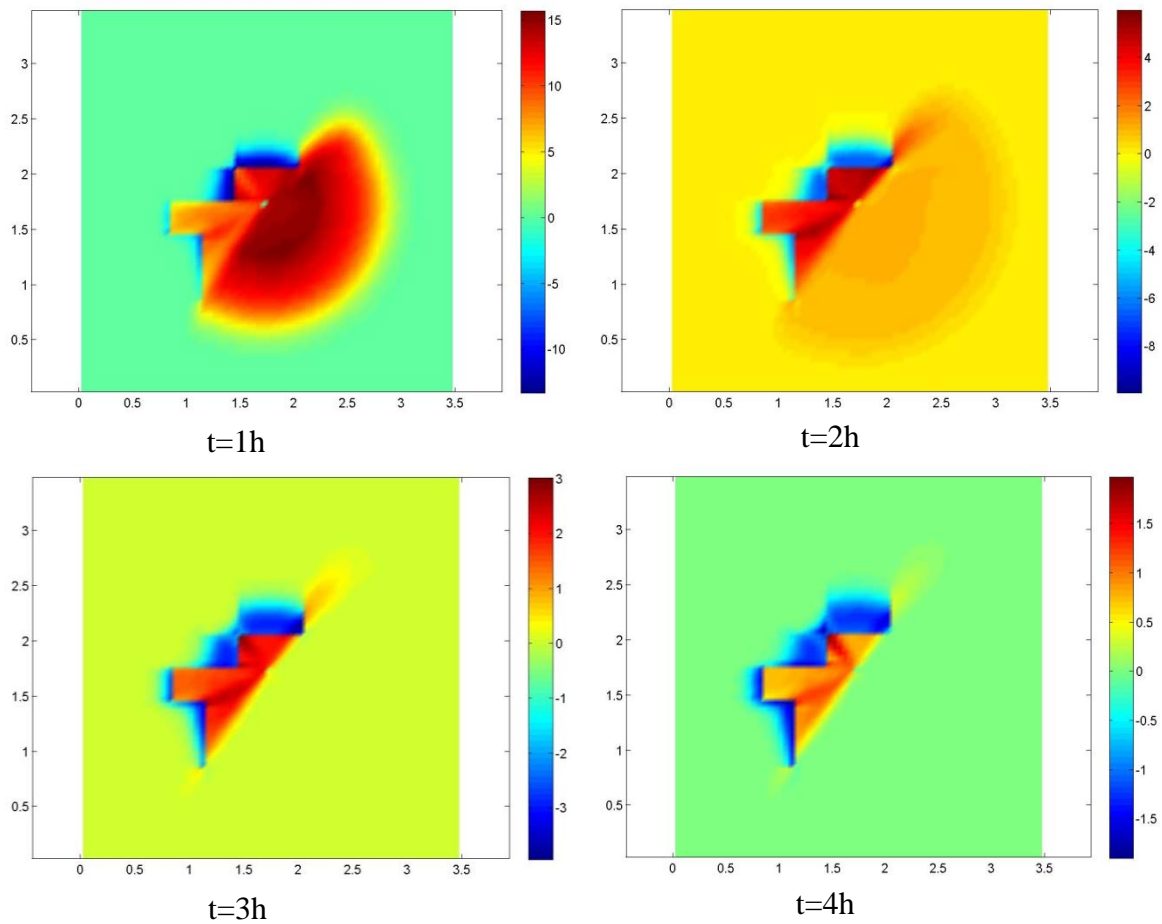


Figure R.2.21. Sensitivity of tracer concentration in aqueous phase to DNAPL saturation at different time steps during the pull phase.

Next two partitioning tracers (hexanol and octanol) with different partitioning coefficients are injected into the push-pull well to explore the differences in predicted sensitivity matrices.. Two DNAPL saturation distributions are considered. The first (figure R.2.22) is normally distributed with a mean value of 0.5 and variance of 0.05. The other DNAPL saturation distribution is the same as the previous case. In addition, for the following simulations, we adopt the expression of mass transfer coefficient obtained by [Nambi and Powers in 2003]. All the other simulation parameters are the same as the previous case.

The sensitivity matrices at four different time steps during the pull phase are shown in figures R.2.23 and R.2.24. As expected, the higher partitioning tracer has the higher sensitivity to DNAPL saturation, consistent with the fact that the DNAPL can capture more tracer mass. For example, the largest absolute value of the sensitivity at the end of the pull phase for octanol at the location where DNAPL exists is almost 1.9 and 2 with these two scenarios; this same metric has an absolute value of 0.035 and 0.02 for hexanol. These differences between sensitivity values for the two tracers are more significant at the later time stages during the pull phase.

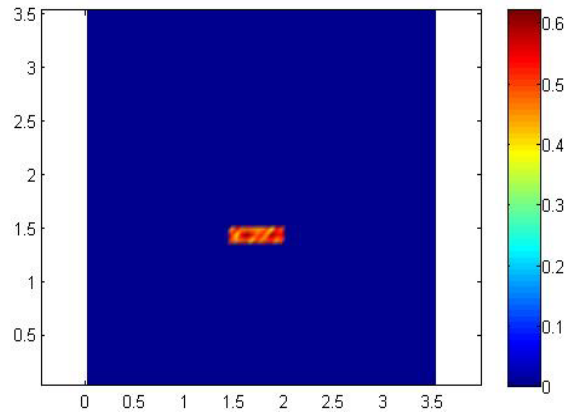


Figure R.2.22. DNAPL saturation distribution.

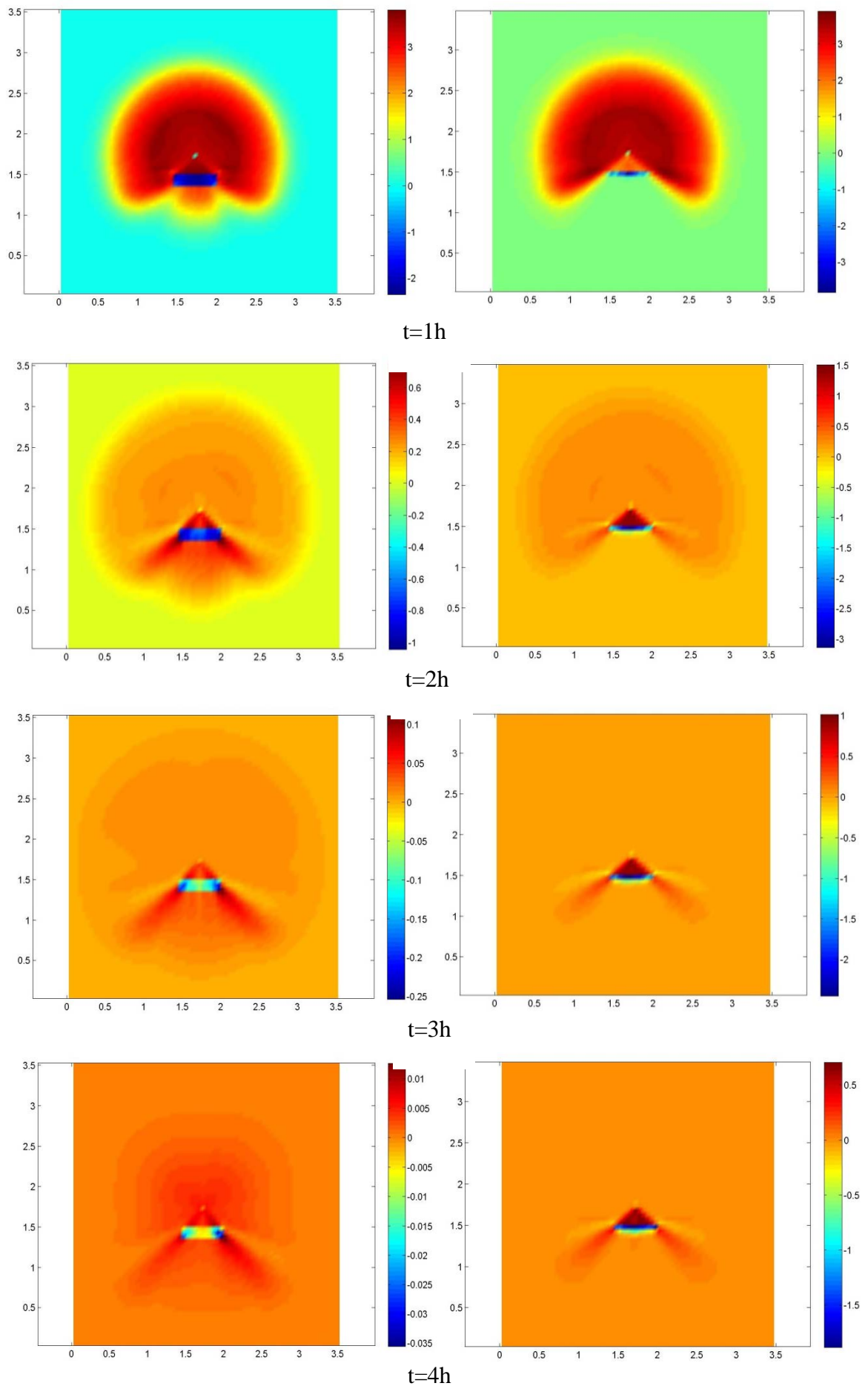


Figure R.2.23. Sensitivity of tracer concentration to DNAPL saturation at four time steps during the pull phase. Left four figures are the sensitivity matrices of Hexanol, and the right four figures are the sensitivity matrices of Octanol.

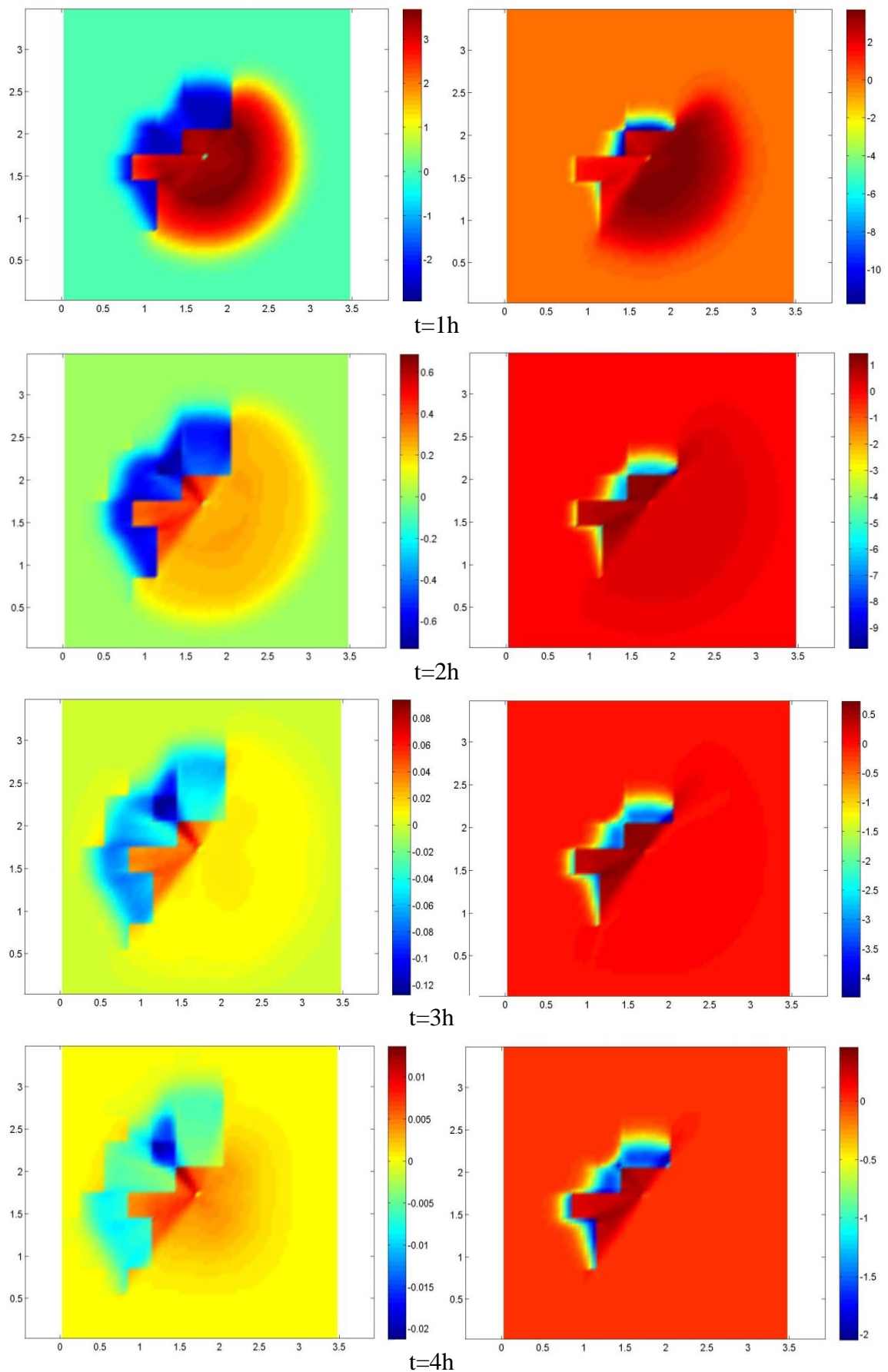


Figure R.2.24 Sensitivity of tracer concentration to DNAPL saturation at four time steps during the pull phase. Left four figures are the sensitivity matrices of Hexanol, and the right four figures are the sensitivity matrices of Octanol.

The influence of different tracer injection concentrations and different injection and extraction flow rates is also studied here to further explore the behavior of the sensitivity matrix. Scenario 2 is the “baseline” that was used for the previous simulation. Scenarios 1 and 3 are variations of the baseline scenario, where the injection concentration decreases from 370mg/L to 100mg/L, and then increases from 370mg/L to 600mg/L. Figure R.2.25 shows three plots of sensitivity values for hexanol concentration with respect to DNAPL saturation at 4h into the pull phase for the three injection concentrations. As expected, the higher the injection concentration, the higher the sensitivity.

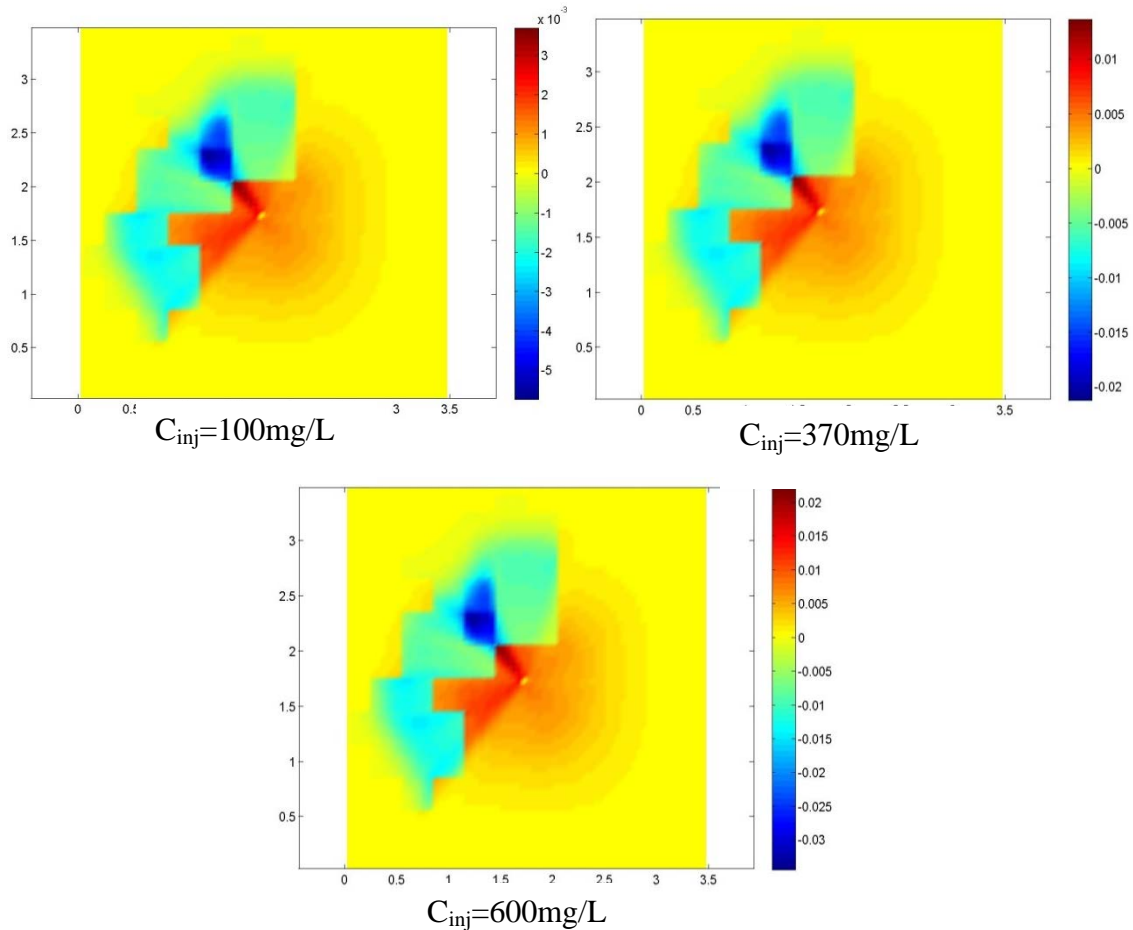


Figure R.2.25. Sensitivity of tracer concentration to DNAPL saturation with different tracer injection concentrations at 4h of the pull phase.

We also explore the influence of different injection and extraction rates on the sensitivity matrices. Values are listed in Table R.2.9 and computed sensitivities are presented in Figure R.2.26. As can be seen, if injection flow rate is reduced, the values of the sensitivities decrease. On the other hand, when the extraction flow rate decreases, with the same injection flow rate, the sensitivity matrix also has smaller values. Furthermore, with the fast-fast injection-extraction rates, the differences between the sensitivity values are more significant, which means that

the DNAPL location and the location of high DNAPL saturations can be easier obtained using fast-fast flow rates. This is consistent with the experiment presented in Section III.2.1.3 that the fast-fast flow rates can get better ratios of saturation estimates obtained with the analytical solution to those measured via light transmission.

Table R.2.9. Three different scenarios for injection and extraction flow rates

	Scenario 1	Scenario 2	Scenario 3
Injection flow rate (m^3/s)	$8\text{e-}5$	$1.5\text{e-}4$	$1.5\text{e-}4$
Extraction flow rate (m^3/s)	$1.5\text{e-}4$	$1.5\text{e-}4$	$8\text{e-}5$

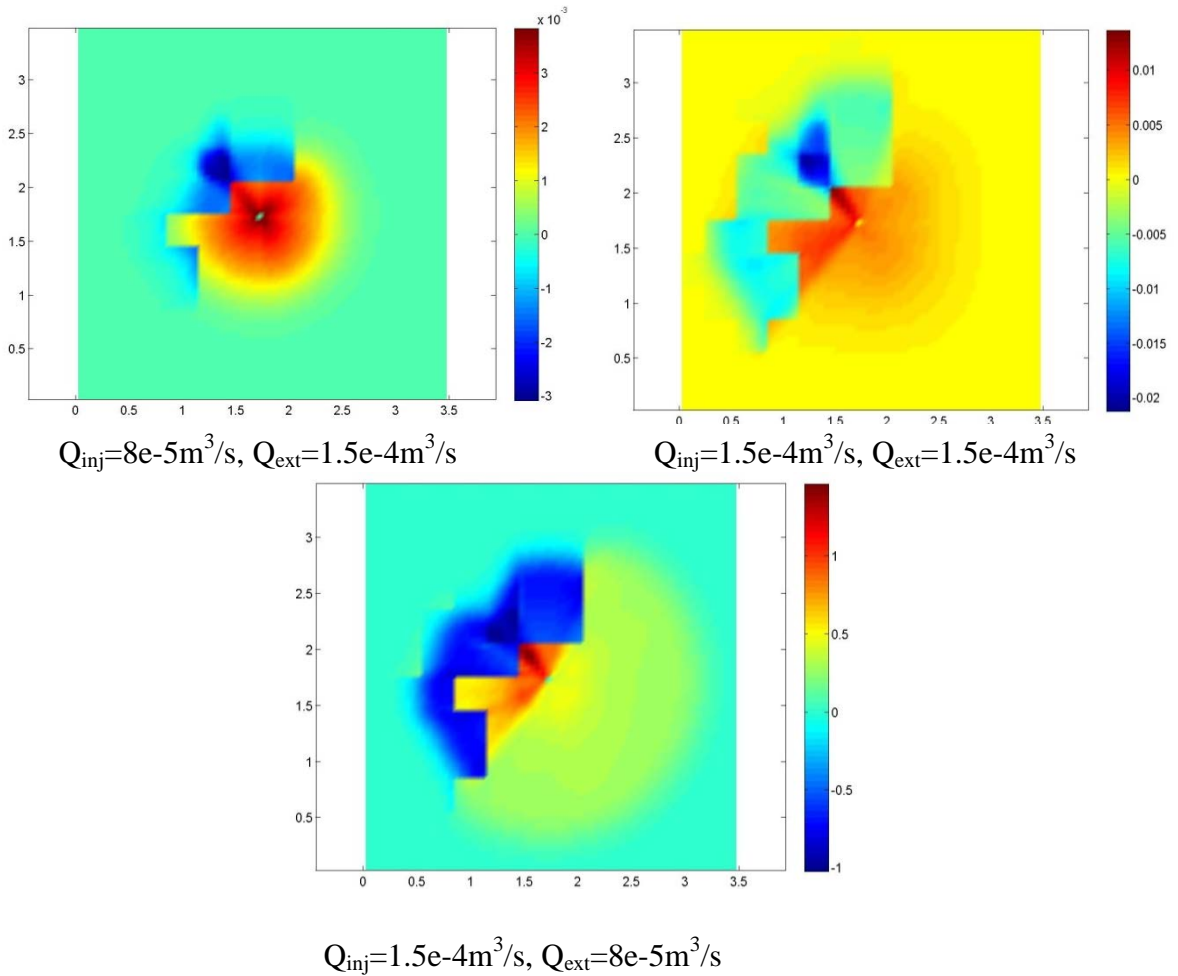


Figure R.2.26. Sensitivity of tracer concentration to DNAPL saturation with different injection and extraction flow rates at 4h of the pull phase.

Application to the estimation of DNAPL saturation

Two different sample applications are presented. These involve the identification of DNAPL saturation in the aquifer described previously, in which DNAPL is located at one layer of the domain. Measurements of tracer concentration are taken at different time steps during the pull phase. For the first example, the heterogeneously distributed DNAPL saturation is located at one corner of the domain. For the second example, the DNAPL locations changes and we increase the size of the domain and also the injection and extraction flow rates. Although the method is directly applicable to a system with a three-dimensional DNAPL saturation distribution, two-dimensional DNAPL saturation distributions were selected for the applications for ease of illustration.

The overall simulation steps to back estimate the DNAPL saturation distribution are: (1) provide an initial guess of the DNAPL saturation distribution, (2) calculate the tracer concentration in the push-pull well at different time steps during the pull phase, (3) use the adjoint sensitivity method to obtain the sensitivity matrix, (4) apply the Gauss-Newton method to back estimate the DNAPL saturation distribution, i.e., find the distributions that minimizes the difference between calculated and observed tracer concentration, (5) update the DNAPL saturation with the calculated Gauss-Newton descent step, (6) repeat the steps (2) to (5) until some stopping criterion is met.

The “real” DNAPL saturation distributions used for obtaining the tracer concentration measurements are presented in figure R.2.27. The tracer concentration is sampled every two minutes (4900 observations) , The problem of parameter estimation is, thus, strongly underdetermined. The specified DNAPL saturation distributions both follow a normal distribution with mean value of 0.5 and variance of 0.05. Each is located a different distance from the push-pull well (0.35m and 0.71m), with the total mass of 5475g in each location.

The initial guess for DNAPL saturation is that we assume a little DNAPL everywhere in the domain. Here we use the octanol as the partitioning tracer to test the method’s ability to recover the metrics of DNAPL saturation. We focus on three metrics of DNAPL saturation: mean saturation value, total mass, and closest distance from the push-pull well.

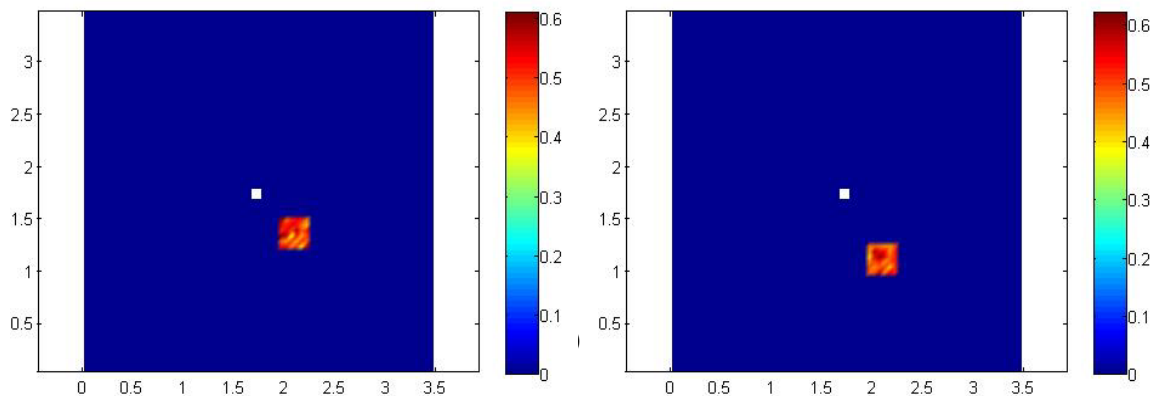


Figure R.2.27. “Real” DNAPL saturation distributions for first example.

Estimated DNAPL saturation distributions are presented in figure R.2.28. Here the estimated saturation pattern is a circular ‘ring’ surrounding the well; given uniform radial flow, the concentration signal yields no information on directional angle. As can be seen, the estimated distances from the well location are very similar to the real values, with the estimated values of 0.39m and 0.78m, respectively. In addition, the estimated total masses are 5700.57g and 5818.02g, with the relative mass error of 4.12% and 6.26%. Here we take the difference between the estimated and real value of total mass divided by DNAPL total mass as the measure of relative mass error. However, the estimated mean saturation values are 0.32 and 0.31, both smaller than the real value of 0.5. The estimated DNAPL saturation distribution spreads the DNAPL out around the push-pull well, such that a lower mean value of DNAPL saturation yields the same tracer concentration in the well compared to the case with DNAPL located in just one area.

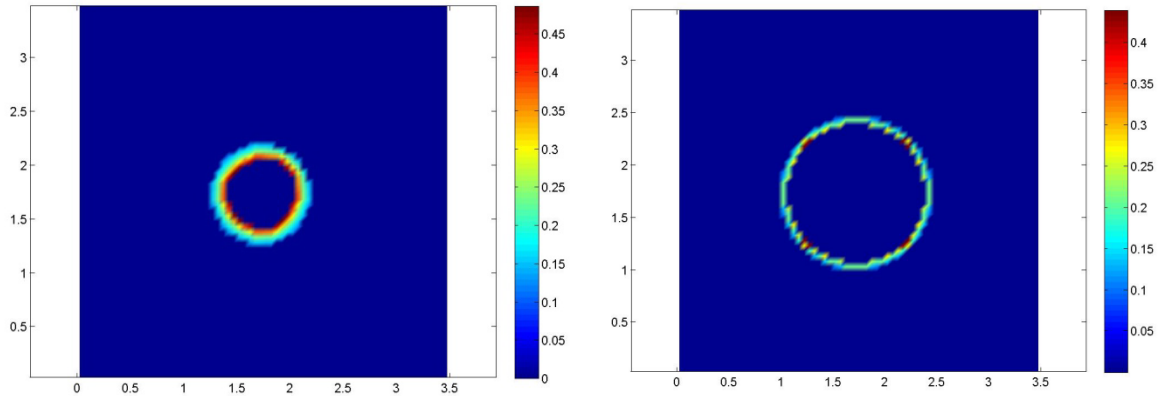


Figure R.2.28. estimated DNAPL saturation distributions for first example.

The second example involves an increased domain size of 5m*5m*2m, and increased injection and extraction flow rates of $2.5e-4m^3/s$. The “real” DNAPL saturation distribution is also changed to more be more spread out, distributed in a rectangular pattern. The two DNAPL saturation distributions are shown in figure R.2.29, with different distances from the well. The push-pull well is still located

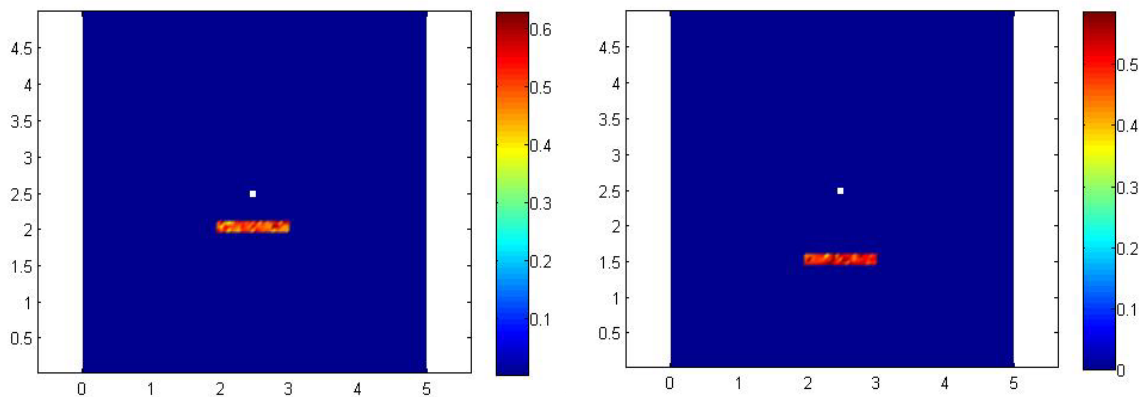


Figure R.2.29. “Real” DNAPL saturation distributions for second example.

at the center of the domain. For the first DNAPL saturation (left), the shortest distance from the well to DNAPL location is 0.5m, and the longest distance is 0.71m. The shortest and longest distances from the push-pull well to the DNAPL location are 1m and 1.12m in the second example. The total mass of TCE is 13797g, with the average saturation of 0.5. All the other simulation parameters are the same as before.

The estimated DNAPL saturation distributions are presented in figure R.2.30. Here the estimated total masses are 14082g and 14281g, respectively, with relative mass errors of 2.07% and 3.51%. The estimated distances of DNAPL from the well location are 0.7m and 1.1m, which are values between the values of the shortest and longest distances of the “real” DNAPL. Comparing the estimated mean saturation values with the real ones, the results suggest that the estimated values (0.38 and 0.33) are still smaller than the real ones.

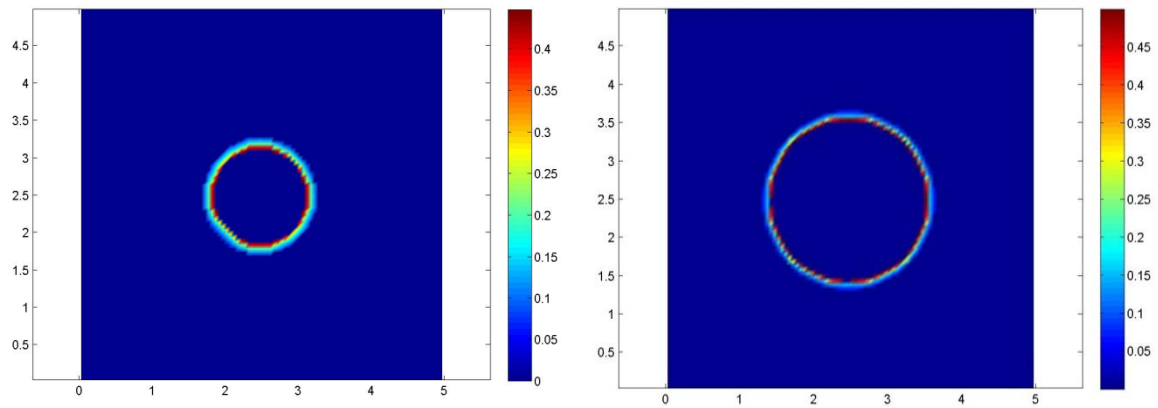


Figure R.2.30. Estimated DNAPL saturation distributions for second example.

When we compare the first example with the second one, since the “real” DNAPL saturation distributions of the second example are more spread near the well, the estimated total mass and mean saturation value are both more accurate than the first example. In addition, comparing the two cases in the same example, when the DNAPL location is nearer to the push-pull well, the metrics of estimation of total mass, average DNAPL saturation, and distance of DNAPL from the well are better than the case with the DNAPL location further from the well. This suggests that we can get a better estimate of source metrics with the DNAPL location near the push-pull well and for distribution that spread more around the well.

Conclusions

Comparing different partitioning tracers, as expected, the higher partitioning tracers yield higher sensitivities. Ongoing efforts are being directed towards coupling the developed adjoint sensitivity model with tracer concentration observations to back estimate features of the saturation distribution with more realistic DNAPL saturation distributions and flow field. The non-linear least

squares estimation approach being implemented using Gauss-Newton method demonstrated the method's efficiency to back estimate the DNAPL characteristics. Here an initial guess of the saturation distribution is updated iteratively until a selected stopping criterion is met.

Results to date suggest that the adjoint sensitivity method can be used to provide good estimates of local DNAPL mass and distance from the push-pull well. Estimates of average DNAPL saturation are more difficult to obtain without some directional information (angle from the well). The estimation of source zone characteristics was shown to be more accurate with a more spread saturation distribution and at smaller distances from the well.

III.3. Processing Methods for Identification of Source Zone Features

III.3.1. Machine Learning Results

Here we demonstrate the performance of our proposed standard machine learning regression algorithm, as well as the integrated manifold regression algorithm and multi-task manifold learning algorithms, using the hydrological data which were gathered from Sequential Gaussian Simulation (SGS). Three data sets are considered: In data set-1, we combined three different spill scenarios (DNAPL infiltration, entrapment and dissolution). Scenario 1 of data set 1 (Table R.3.1) is the "baseline" and was reported in Christ et al. (2010) (see Case 1 in Table M.1.4). Briefly, an ensemble of 16 equally probable realizations of a 3D permeability field was obtained from (Lemke et al., 2004). These realizations were generated by means of sequential Gaussian simulation geo-statistical methods and were based upon an aquifer located in Oscoda, Michigan, USA. For the whole ensemble, simulation of different hypothetical spill scenarios was conducted by means of UTCHEM as outlined in Section II.1.3 of this report. The baseline scenario consisted of a release of 128 liters of PCE for a period of 400 days located in a 4x5 grid area centered in the top layer of the domain (see Table R.3.1).

Table R.3.1. Conditions of the 3 different data sets generated for the machine algorithm implementation

Matrix Properties	Data set 1			Data set 2		Data set 3	
Variogram Parameters	Horizontal	Vertical		Horizontal	Vertical	Horizontal	Vertical
Nugget	0.333	0.333		0.333	0.333	0.333	0.333
Range (m)	7	1.07		4.66	0.72	4.66	0.72
Integral Scale (m)	2.33	0.36		1.55	0.24	1.55	0.24
$\sigma^2 \ln(K)$	0.29			1		1.5	
Mean Hydraulic Conductivity, (m/d)	16.8			16.8		16.8	
Anisotropy Ratio kv/kh	0.5			0.5		0.5	
Spill conditions	Scenario 1	Scenario 2	Scenario 3				
Spill Volume (L)	128	128	128	128		128	
Spill Duration (d)	400	4	400	400		400	

Following infiltration and entrapment, MT3DMS was used to simulate dissolution under natural gradient conditions and the source zones with their corresponding down-gradient transect concentration data were obtained at every 20 time steps. Scenarios 2 and 3 of data set 1 are variations of the baseline scenario. Scenario 2 (Case 3, Table M.1.4) consists of a catastrophic release, with the same release volume and location as the baseline scenario but a release period of 4 days. Scenario 3 (Case 2 of Table M.1.4) of data set 1 consists of the same volume and release period as the baseline but a different release location. In this scenario the release was located in the top layer of the 3D domain in 2 off-center block areas (as shown in Table R.3.1). We used this combined data set 1 as the input to our algorithm to explore the extent to which strong performance can be maintained as we increase the complexity and variability of the underlying scenarios. The spill scenario used in scenario 1 of data set 1 is used for data sets 2 and 3 (Cases 5 and 6 in Table M.1.5). The difference in these sets rested on the statistical properties used for obtaining the permeability realizations. As shown in Table R.3.1, modifications to the statistics include smaller correlation length values (integral scale) for data sets 2 and 3, and higher lognormal transformed permeability variance ($\sigma^2 \ln(K)$) of 1.00 and 1.5 for data set 2 and 3 respectively. Additionally, in order to test the performance of the regression function under a wide range of conditions, we combine these three data sets (data set-4) as the input of our algorithms.

As an example of the results of this process, the hyper-parameter settings of the SGS data set-1 for both the standard regression framework and the integrated algorithm are provided in Table R.3.2 (a). In the case of standard regression, for each of a number of combinations of σ_1, σ_2 and σ_{SR} , 10-fold cross validation is used to evaluate the empirical performance of the regression procedure. The final values of σ_1, σ_2 and σ_{SR} are chosen as those with the smallest error. For the integrated approach, we use these same values for $\sigma_1, \sigma_2, \sigma_{SR}$ and employ 10-fold cross validation to determine γ_1, γ_2 and γ_3 . For the multi-task learning, the hyper-parameters selected previously are used, and we only need to select γ_p . In our experiment, $\gamma_p = 0.5$. The hyper-parameter selection for the TP/MC data set is shown in Table R.3.2 (b), where for this data set $\gamma_p = 2$. For the Bayesian regression, the noise in the original data set is small, so we set the initial variance of metrics β as 0.01 and for the prior distribution for \mathbf{w} , we set $\alpha = 1$.

Table R.3.2 (a). The hyper-parameters setting of standard procedure and integrated algorithm for data set-1

		σ_1	σ_2	σ_{SR}	γ_1	γ_2	γ_3
Standard Regression Procedure	f_p	30	1	15	x	x	x
	M_p	40	5	10	x	x	x
	M_g	20	5	10	x	x	x
Integrated Regression Procedure	f_p	30	1	15	0.5	1000	400
	M_p	40	5	10	0.5	500	50
	M_g	20	5	10	0.5	20	0.5

Table R.3.2 (b). The hyper-parameters setting of standard procedure and integrated algorithm for TP\MC model

		σ_1	σ_2	σ_{SR}	γ_1	γ_2	γ_3
Standard Regression Procedure	f_p	200	0.5	300	x	x	x
	M_p	100	10	500	x	x	x
	M_g	100	5	300	x	x	x
Integrated Regression Procedure	f_p	200	0.5	300	0.1	20	40
	M_p	100	10	500	0.1	1	20
	M_g	100	5	300	2	10	2

In our experiment, the sizes of data sets 1 to 3 are 500, 600 and 900 respectively. For these three data sets, we apply 10-cross validation which means that we use 90% of the data for training and the remaining 10% of data for test. However, data set-4 combines all SGS data such that its size is 2000. When training data are plentiful, there is little to be gained by employing the more complex

processing method in which the physical constraints among the three parameters are explicitly enforced. Therefore, we decided to randomly select half of the data from the data set for training and use the balance for testing, repeating this procedure 10 times. When the training data size is small, enforcing the physical relationship among the three quantities allows for the same (or close to the same) level of performance as in the data-rich case. This is important since it means we have a method for doing as well with less training data (which may be expensive to collect or time consuming to simulate) as with large collections of training data. Also, it reduces the time and space complexity for running the training algorithm. For the TP/MC model, there are 7000 samples for the training data set. Thus as we did for data set 4, we used half of the data set (e.g. 3500 data) for training and the other half for testing.

Table R.3.3 (a): The Statistical Result of standard procedure, integrated algorithm and multi-task learning using data set-1

	Range of Metric	Standard Manifold Regression		Integrated Manifold Regression		Multi-task Manifold Regression	
		median error	EPcte	median error	EPcte	median error	EPcte
f_p	0 ~ 1	0.0522	91.60%	0.0508	90.60%	0.0491	80.80%
M_p^a	0.59 ~ 44.62	2.3073	75.20%	2.1551	85.80%	2.1125	83.40%
M_g^a	0 ~ 201.4	6.3012	84.00%	5.6241	92.80%	5.1427	89.60%

Table R.3.3 (b): The Statistical Result of standard procedure, integrated algorithm and multi-task learning using data set-2

	Range of Metric	Standard Manifold Regression		Integrated Manifold Regression		Multi-task Manifold Regression	
		median error	EPcte	median error	EPcte	median error	EPcte
f_p	0 ~ 1	0.0433	94.60%	0.042	91.50%	0.0406	85.80%
M_p^a	0.61 ~ 139.5	2.6745	89.10%	2.4659	89.10%	2.3318	86.80%
M_g^a	0 ~ 114.4	1.0397	92.00%	1.0071	91.60%	0.9205	90.60%

Table R.3.3 (c): The Statistical Result of standard procedure, integrated algorithm and multi-task learning using data set-3

	Range of Metric	Standard Manifold Regression		Integrated Manifold Regression		Multi-task Manifold Regression	
		median error	EPcte	median error	EPcte	median error	EPcte
f_p	0 ~ 1	0.0359	94.60%	0.0343	93.20%	0.0338	86.10%
M_p^a	0.60 ~ 159.7	5.4644	85.00%	4.0768	87.80%	3.8294	87.60%
M_g^a	0 ~ 91.6	2.5878	97.50%	1.0144	94.70%	0.991	93.60%

Table R.3.3 (d): The Statistical Result of standard procedure, integrated algorithm and multi-task learning using data set-4

	Range of Metric	Standard Manifold Regression		Integrated Manifold Regression		Multi-task Manifold Regression	
		median error	EPcte	median error	EPcte	median error	EPcte
f_p	0 ~ 1	0.0644	87.30%	0.06	87.20%	0.0565	82.80%
M_p^a	0.59 ~ 159.7	5.6545	86.90%	5.3627	89.90%	4.6909	86.20%
M_g^a	0 ~ 201.4	2.148	93.80%	1.8739	92.50%	1.761	93.00%

Table R.3.3 (e): The Statistical Result of the standard procedure, integrated algorithm and multi-task learning using sparse data generated by the TP\MC model

	Range of Metric	Standard Manifold Regression		Integrated Manifold Regression		Multi-task Manifold Regression	
		median error	EPcte	median error	EPcte	median error	EPcte
f_p	0 ~ 1	0.019	89.50%	0.0181	93.00%	0.0169	90.00%
M_p^b	0 ~ 57.3	3.0246	84.60%	2.4502	89.80%	2.1464	88.40%
M_g^b	0 ~ 23.8	0.3242	94.00%	0.235	91.30%	0.2011	89.30%

^aMass in pools and ganglia is measured in kilograms.

^bMass in pools and ganglia is measured in grams.

The range of metrics for the experiment and the statistical results of the standard regression framework the integrated algorithm, and multi-task learning are provided in Tables R.3.3 (a)-(d) for the SGS data set. The error is the absolute value of the difference between the estimation metric and the true metric value. Tables R.3.3 (a)-(d) present the median error which gives the upper error bound of half of the test data set. In the tables, the superior performance of multi-task manifold regression is clearly evident compared to standard manifold regression and integrated manifold regression. Thus, enforcing the physical relationship among these three metrics facilitates the accuracy of the regression procedure.

Comparing the median error of multi-task manifold regression for data sets 1-4, indicates that the error for f_p in data sets 1 to 3 is less than 0.05, but the error for f_p is a bit higher in data set-4 due to the added variability from combining all three SGS data sets. Referring again to data set-4 the median error of M_p is less than 5 kg and that of M_g is less than 2 kg. Indeed, ganglia mass here is relatively easy to determine because the morphology of the concentration images changes significantly when ganglia vanish. The result in Table R.3.3 (d) shows that even with a small training data set, the performance of multi-task manifold learning is still promising.

For the TP/MC data set in Table R.3.3 (e), the median error of f_p is less than 0.017, the median error of M_p is less than 3 grams and the median error of M_g is around 0.2 grams. Comparing these results to those of the SGS data, we see that even with the sparsely sampled data set, performance does not significantly degrade. Moreover, the accuracy is actually better than SGS data, since the TP/MC data were generated under one condition. This demonstration has validated the generalization ability of our proposed manifold regression framework.

We also calculated the Empirical Percentage of times for which the true metrics fell within the confidence intervals, denoted as EPcte in Table R.3.3. The 85% confident interval is defined as $[\hat{t}_i - 1.44\hat{s}_i, \hat{t}_i + 1.44\hat{s}_i]$ where the output of Bayesian regression is $N(\hat{t}_i, \hat{s}_i^2)$ for each test data. The EPcte of all the metrics using multi-task manifold regression is around 85% for both the SGS and TP/MC data sets. This indicates that the confidence interval estimates are in fact quite accurate.

Table R.3.4. The statistical result of multi-task manifold regression using SGS data set-4 and TP/MC sparse data

		Mass in pools		Mass in Ganglia		Pool fraction	
		50% Error	90% Error	50% Error	90% Error	50% Error	90% Error
Absolute error	SGS Data Set 4	4.7 kg	28 kg	1.8 kg	17 kg	0.056	0.19
	TP/MC	2.1 g	8.7 g	0.20 g	1.8 g	0.017	0.083
Relative error	SGS Data Set 4	40%	245%	31%	148%	9.10%	59%
	TP/MC	19%	122%	57%	100%	1.80%	9.90%

To gain a better understanding of the performance of the multi-task approach, in Table R.3.4, we provide the 50% (i.e., median) and 90% statistics both for absolute as well as relative error. Here, the absolute error is defined as $|t - \hat{t}|$ where t is the true metric, \hat{t} is the estimation from our regression function, while the relative error $\frac{|t - \hat{t}|}{t} \times 100\%$ compares the absolute error to the true metric. For PF observations generated using the SGS model, the 50% absolute error level is 0.06 meaning half the time we are within 0.06 of the true PF. When measured relative to the true PF, the 50% level is a bit over 9%. At the 90% level, the absolute PF error is about 0.19 while the relative error reaches 59%. In the case of the TP/MC, despite the sparsity of the data, the PF performance at both the 50% and 90% levels is substantially improved. We hypothesize that this is due to the homogeneity of the spill conditions used in the TP/MC simulation. The SGS data set-4 contains relatively few examples from spills where we varied the statistical permeability model as well as the release rate and release configuration. In the TP/MC case only the permeability fields were stochastically generated and then with a common transition probability matrix. No variation in the spill configuration was considered. Moreover, the number of data in the TP/MC case was far higher than in the SGS data set-4. Both of these conditions then resulted in improved performance of our approach in the case of the TP/MC data.

For the estimation of M_p and M_g , Table R.3.4 indicates what we achieve reasonable performance at the 50% level but clearly see some deterioration at 90%. To understand this better, scatter plots of absolute error versus relative error for both mass in pools and mass in ganglia are shown in Figure R.3.2 for the SGS data set and Figure R.3.3 for the TP/MC data set, respectively. The asterisk indicates each test data, the red dashed lines are 50% error for both absolute error and relative error and the blue dashed lines are 90% error. The dashed line of each color divides the absolute error versus relative error plots into four parts. Most of the asterisks are located in the quadrant close to the origin where both the relative and absolute errors are small. We also see that few of the test data are located in the “upper-right” meaning that there are few cases where both the absolute error and relative error are large. Therefore we are led to conclude that the majority of the cases contributing to the large error results in Table R.3.4 correspond to a situation where either the absolute error is large but the relative error is smaller or vice versa.

To gain a better understanding of this phenomenon we need to consider in a bit more detail the relationship of relative error, absolute error, and the true metric value. We calculate the relative error as

$$\varepsilon_r = \frac{|t - \hat{t}|}{t} \times 100\% = \frac{\varepsilon_a}{t} \times 100\%$$

where ε_r denotes relative error and ε_a denotes absolute error. Here the true metric is $t = \varepsilon_a / \varepsilon_r \times 100\%$. Thus, in those cases where ε_r is high and ε_a is low, the true metric is typically small and we are overestimating the quantity of interest. Alternatively, in the case where ε_a is large and ε_r small, t is large, this low relative error may be less of a problem.

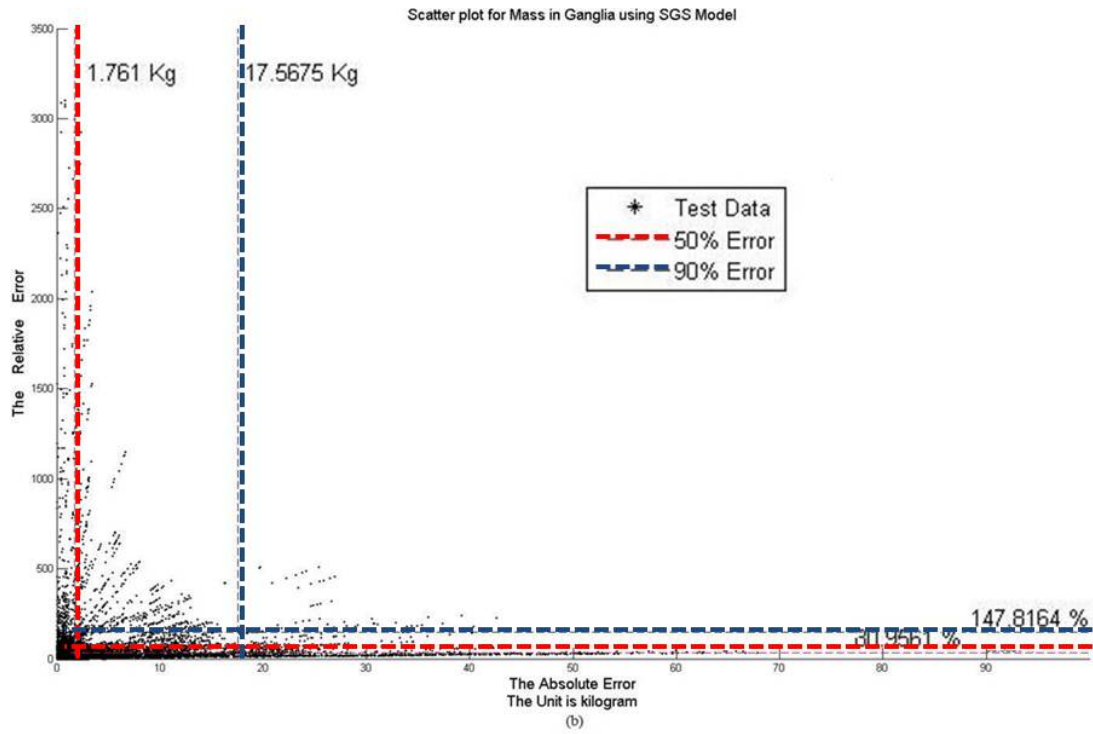
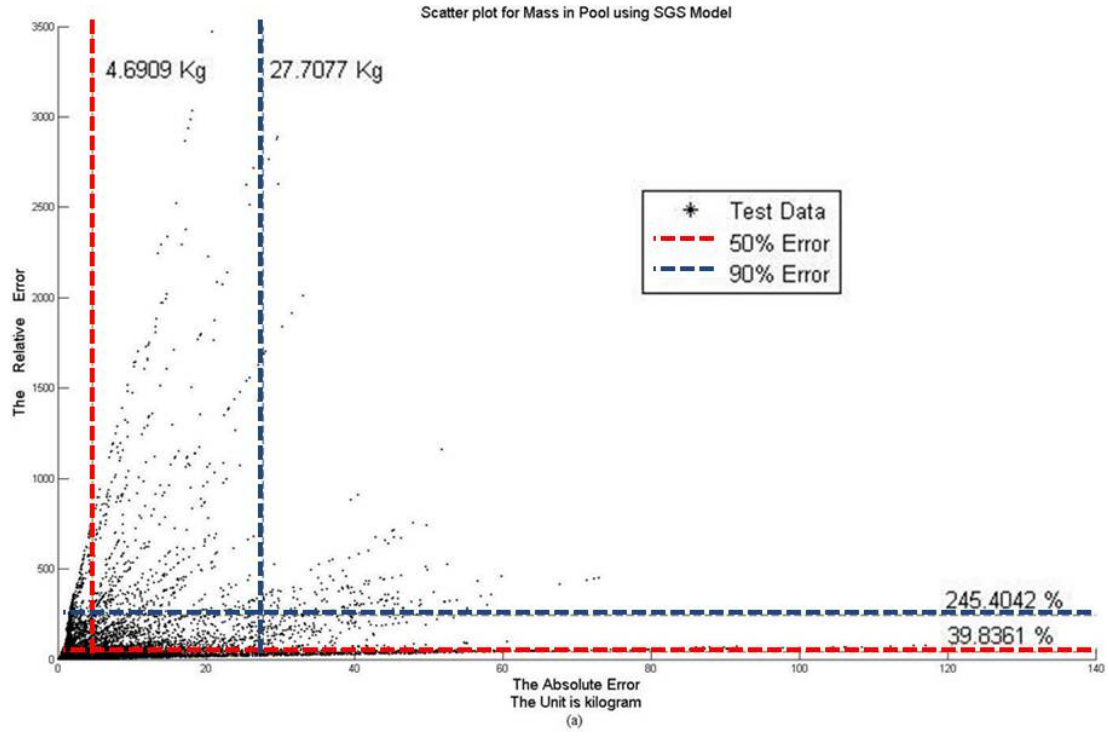


Figure R.3.2. The absolute error vs relative error scatter plots of M_p and M_g from SGS data set-4 using multi-task manifold regression.

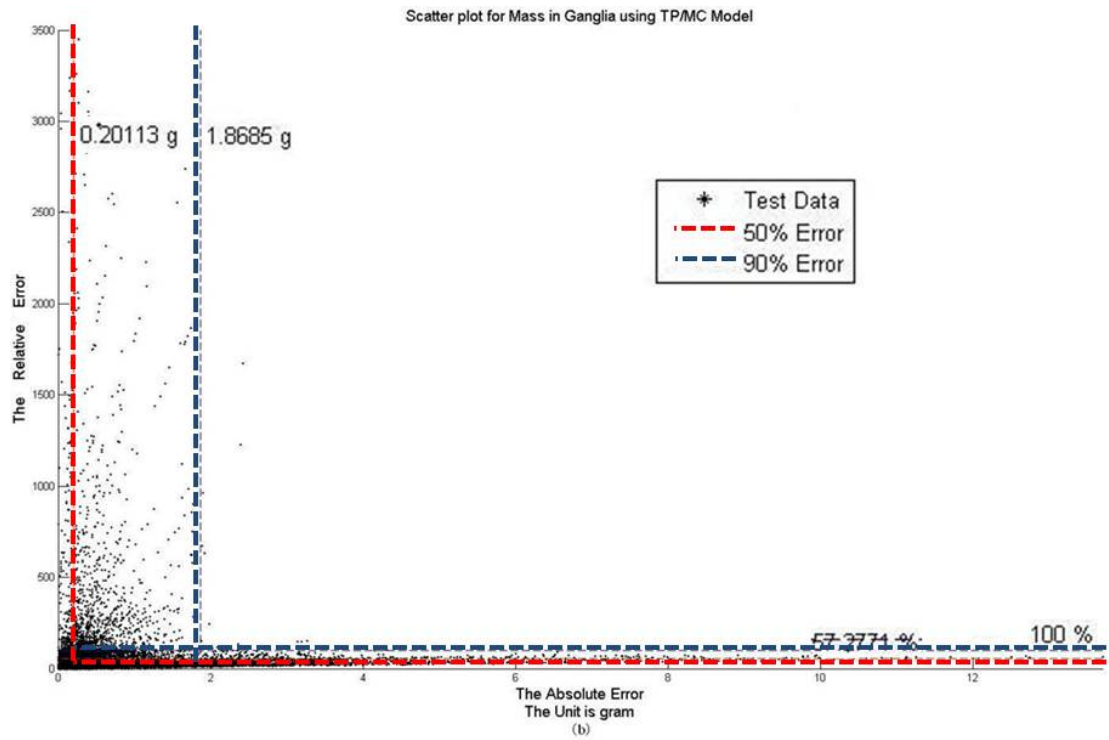
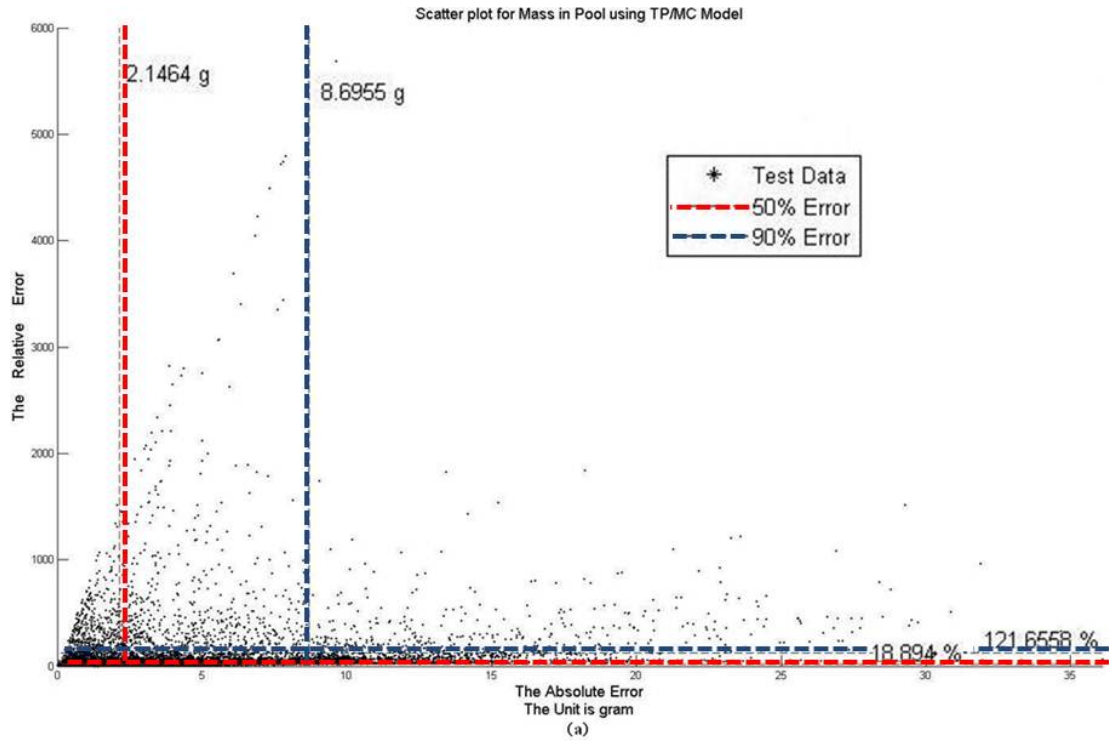


Figure R.3.3. The absolute error vs relative error scatter plots of M_p and M_g from TP/MC data set using multi- task manifold regression.

III.3.2. Machine Learning Conclusions

We have proposed three approaches based on the use of machine learning regression techniques to estimate a number of metrics characterizing the structure of a subsurface contaminant source zone given observations of down-gradient concentration. In the standard machine learning approach, first, we presented a collection of morphology-based features which relate structure in the observed data to that of the unobserved contaminant distribution. Second, we have employed a manifold embedding method, Laplacian Eigenmaps, to reduce the dimension of the training data set. After that, the spectral regression method was applied to embed the test data in the same space as the training data set. Third, linear Bayesian regression techniques were used to estimate the metrics from the low dimensional representation of the test data. In the integrated algorithm, we found the global optimal solution of the dimension reduction function and regression function. In the multi-task manifold learning framework, we used the physics relating the three metrics as constraint to improve the performance of the regression function. Finally, we extended our proposed manifold regression methods to sparse concentration data. These experiments validate the performance of the overall approach for the determination of important source zone metrics.

All of the release scenarios examined herein are for pure DNAPL spills. Under real field conditions, however, the presence of multi-component DNAPLs, and/or the formation of reaction daughter products, will complicate efforts to identify source zone metrics. Thus, an understanding of the dissolution behavior of DNAPL mixtures in representative heterogeneous systems will be essential to proper data interpretation. During the initial spill and redistribution period that occurs following a DNAPL release or infiltration below the water table, the organic liquid composition will be relatively uniform. As a DNAPL source zone ages, however, dissolution will vary spatially and temporally based upon the aqueous solubility and mole fraction of each constituent present in the organic liquid phase. Components with the largest aqueous solubilities will preferentially dissolve from the DNAPL. This process will occur most rapidly in transmissive zones of the aquifer formation that contain entrapped ganglia (i.e., high specific surface area). Although the concentrations of each constituent may persist over different time scales and at different magnitudes, the mass removal behavior (i.e., change in the relative concentration versus mass removed or time) is unlikely to differ substantially from that which would be observed for a single-component DNAPL (e.g., TCE-DNAPL) under the same conditions. This consistency is attributed to the fact that dissolution behavior is largely dominated by the initial source zone metrics (e.g., pool fraction). Thus, provided that the initial concentration of a mixed DNAPL (e.g., TCE + PCE, or TCE in oil) is known or can be estimated, it is anticipated that the metric identification algorithms presented above, as well as the upscaled models derived for pure DNAPLs (see Section III.4.1), may be adapted to estimate mass distribution metrics and to predict plume evolution.

Accounting for potential changes in dissolution behavior arising from abiotic or biotic transformations, such as when a mixed DNAPL evolves due to the back-

partitioning of a transformation (daughter) product into the parent DNAPL, is challenging and was beyond the scope of this project. However, if one assumes that the mass of daughter product (e.g., cis-DCE) that back partitions into the DNAPL is relatively small compared to the parent compound (e.g., TCE) or the dominant constituent (e.g., oil), changes in the mole fraction would be minimal. As a consequence, the general shape of the dissolved-phase signal would not be expected to change substantially under most conditions.

III.4. Development of Simplified Modeling Tools

III.4.1. Upscaled Model for Mass Depletion

III.4.1.1. Model Refinement and Validation

Using the expanded set of source zone dissolution behavior realizations produced in this research (Tables M.1.5 and M.1.6 in Section II.1.3), a revised correlation for the parameter β in the Christ et al. (2006) upscaled screening model (equation M.4.1 in Section II.4.2) was developed:

$$\beta = 0.972GTP^{0.2152} \quad \text{for } 0.41 < GTP < 1.82.$$

Figure R.4.1 shows the successful application of this new correlation to source zones with GTP outside the range of the original correlation developed in Christ et al. (2006). This correlation can be substituted in the screening models developed in Christ et al. (2006, 2010) to better predict source zone dissolution behavior across a wider range of source zone scenarios.

In addition to the refinement of the β correlation, the upscaled model was also enhanced to more accurately reflect the variety of source zone behaviors that may be observed in the field, with special attention directed towards two stage mass flux behavior, indicative of a transition from ganglia to pool dominated behavior. The refined model quantifies DNAPL mass discharge by partitioning the source zone into ganglia dominated and pool dominated regions. As described in the publication Christ et al. (2010), the simplified upscaled model (Christ et al., 2006) was modified to predict flux averaged, down-gradient concentration (or mass discharge) as a function of mass removal in 2-stage mass recovery scenarios by incorporating the pool fraction (PF), initial flux-averaged concentration (C_o), and fraction of flux-averaged concentration eluting from pool regions (f_x^P):

$$\frac{C_{out}^{Total}}{C_{eq}} = 2 - \left(1 - \frac{f_x^P \overline{C_o}}{C^{eq}} \right) \left(\frac{PF \cdot \left(\frac{M}{M_o} \right)}{PF_0} \right)^{0.5} - \left(1 - \frac{(1 - f_x^P) \overline{C_o}}{C^{eq}} \right) \left(\frac{(1 - PF) \left(\frac{M}{M_o} \right)}{1 - PF_0} \right)^{1.5 \left(\frac{1 - PF_0}{PF_0} \right)^{-0.26}} \quad (R.4.1)$$

By incorporating a parameter representing the fraction of down-gradient contaminant flux emanating from DNAPL pool zones, we were able to predict 2-stage mass recovery behavior with reasonable accuracy (see Figure R.4.2).

Conceptually, this model partitions the source zone into two simultaneously dissolving zones, each assumed to represent either pools or ganglia. The contribution to down-gradient flux from each of these zones is assumed to be additive. This upscaled model provides a new screening tool that can be employed to obtain order-of-magnitude estimates for new or aged sites exhibiting single or two-stage mass recovery behavior.

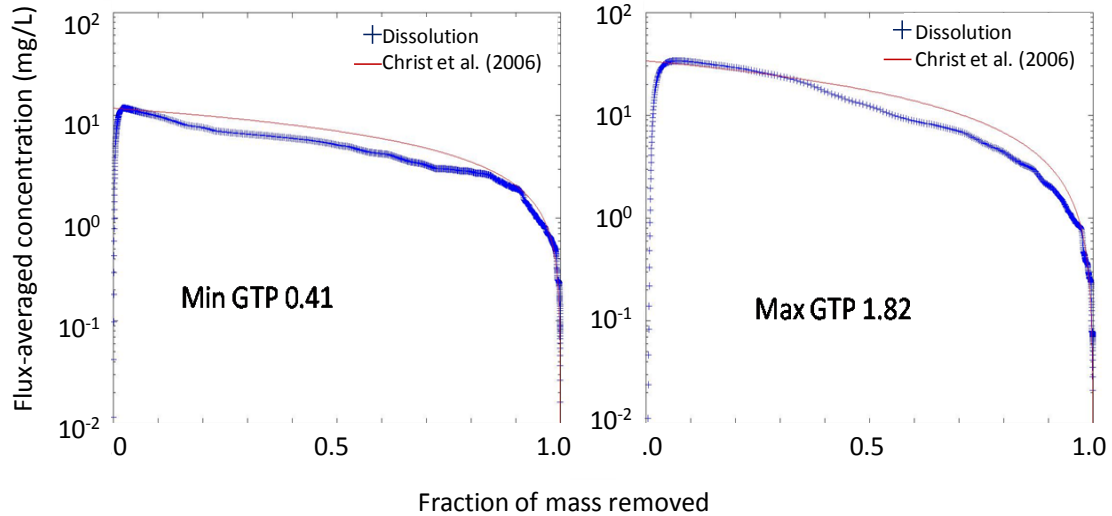


Figure R.4.1 Prediction of dissolution behavior using Christ et al. (2006) model for low GTP SZAs generated by changing the correlation length of the original permeability fields.

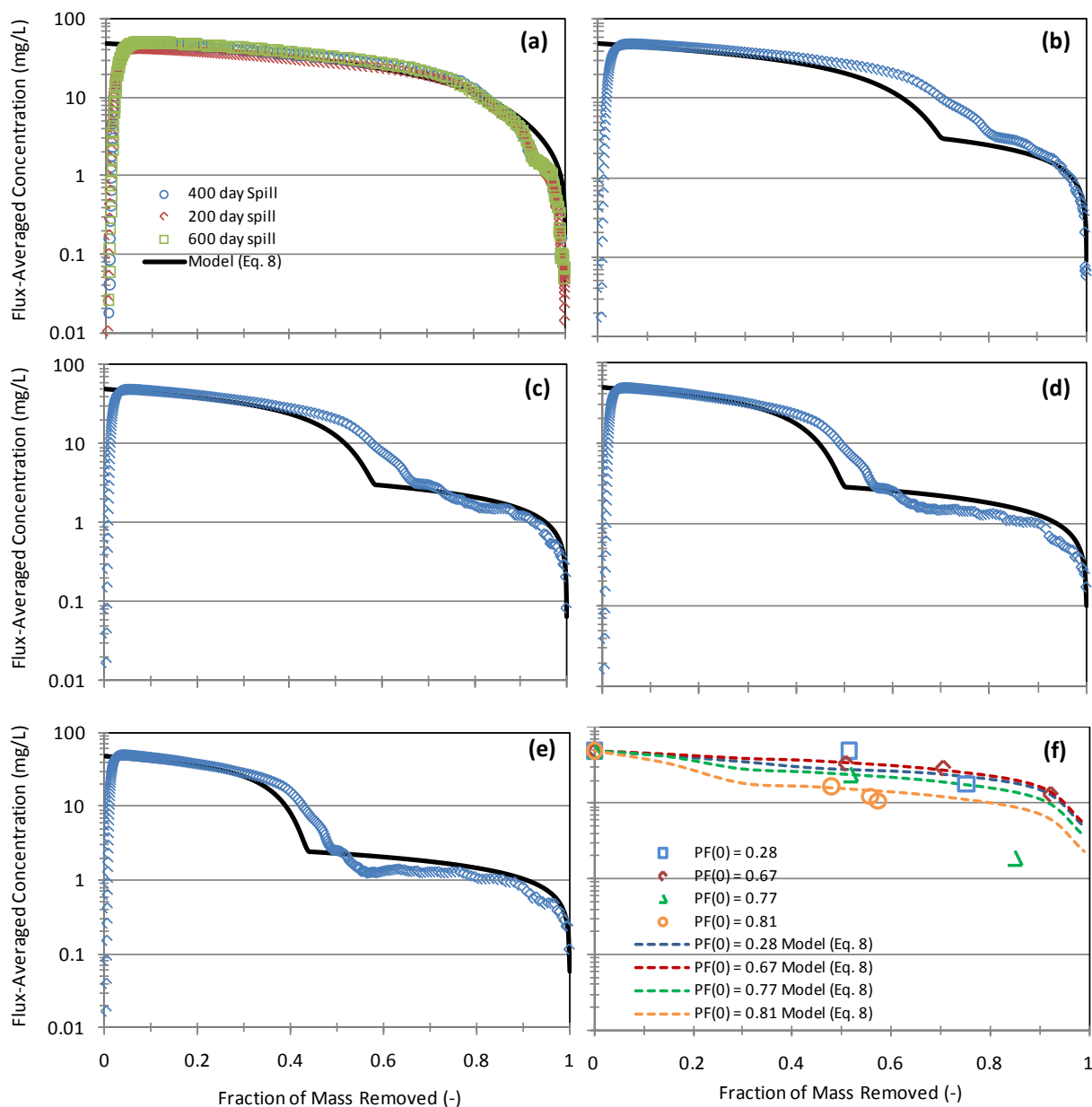


Figure R.4.2. Two-domain upscaled model comparison to numerical simulation results for (a) 200-, 400-, and 600-day spill simulations with no emplaced NAPL, (b) – (e) 400-day simulations with various volumes of NAPL emplaced at pools (See Christ et al., 2010 for a full description), and (f) comparison to 2-D aquifer cell experiment results of Suchomel and Pennell (2006). Equation 8 refers to equation R.4.1.

III.4.2. Upscaled Models for Push-Pull Tracer Tests

The goal of this research subtask was to develop a simplified upscaled model for application to the analysis of partitioning tracer tests. Results described in Section III.2, point to the importance that rate limited interphase partitioning and variations in the spatial distribution of DNAPL play in the determination of extraction well breakthrough curve behavior.

III.4.2.1. Model Development

2D Fine Scale Simulation of Partitioning Tracer Tests

To generate representative breakthrough (observation) data for upscaled model development, a series of tracer test simulations was performed with the fine scale simulator (described in section II.2.3) extracted two dimensional subdomains (see Section II.4.3.3). Tracer test simulations were performed under conditions representative of field tracer tests. A pulse of a group of tracers, including one non-partitioning (conservative), i.e., bromide, and two partitioning alcohol tracers, i.e., 1-hexanol, and 2-octanol, was introduced to the domain. Tracers were uniformly injected across the left-hand boundary of each two dimensional subdomain and a flux-averaged concentration at the right-hand boundary was observed. One pore volume (1PV) of the tracer solution was injected, and followed by background solution flushing until either more than 99 percent of the injected mass was recovered or 40 PV of background solution was flushed through the domain. Tracer characteristics and simulation conditions are summarized in Tables M.1.4 and M.1.5 (Section II.1.3). For each 2D domain (from a total of 180 domains) four tracer tests were simulated with flow rates ranging from 1 to 40 (mL/min).

All simulations were performed in a finely discretized (5x5 mm) two-dimensional domain of dimensions 120 x 40 cm. This level of discretization was chosen to permit resolution of the local flow field within the heterogeneous blocks at a scale consistent with the use of local (laboratory scale) mass transfer coefficients. These simulations produced 480 sets of tracer breakthrough curves for further analysis (observation tracer data).

Effective Mass Transfer Rate Coefficient Estimation

The purpose of this step is to lump the influence of all heterogeneities, i.e., heterogeneities in the permeability field and in the organic mass distribution, into an effective mass transfer coefficient. A one-dimensional form of the upscaled model developed in Section II.4.3.3 was used to model the simulated data.

An effective mass transfer coefficient was fit individually for all 480 analyzed tracer tests. The non-partitioning tracer data first were used to fit the effective porosity and dispersivity. These fitted values were then embedded in the model, and the upscaled model was fit to the breakthrough curves of the 1-hexanol and 2-octanol tracers. A single effective mass transfer coefficient was used to simultaneously fit both tracer breakthrough curves. However, the 2-octanol data were weighted 5 times more than the 1-hexanol in the optimization algorithm.

These weights were chosen based upon the higher potential of 2-octanol to partition into the DNAPL (partition coefficient of $149 L_{aq}/L_{NAPL}$ for 2-octanol versus $17.4 L_{aq}/L_{NAPL}$ for 1-hexanol). The fit was performed using the `lsqcurvefit` function from MATLAB optimization tool that solves non-linear curve fitting problems in the least squares sense. To obtain a quantitative understanding of the goodness of the fits, the mean squared error (MSE) between the observed and predicted breakthrough curves was calculated separately for each test. Figure R.4. depicts the distribution of MSE for all 480 simulations. Box plots present the distribution of MSEs classified according to the characteristics of the permeability fields. In both sets, more than 90 percent of the simulations fall within a range 2.7 times the standard deviation around the mean. Predicted and observed tracer breakthrough curves are shown for four representative simulations on Figure R.4. (b). These examples are selected to represent different MSE value ranges.

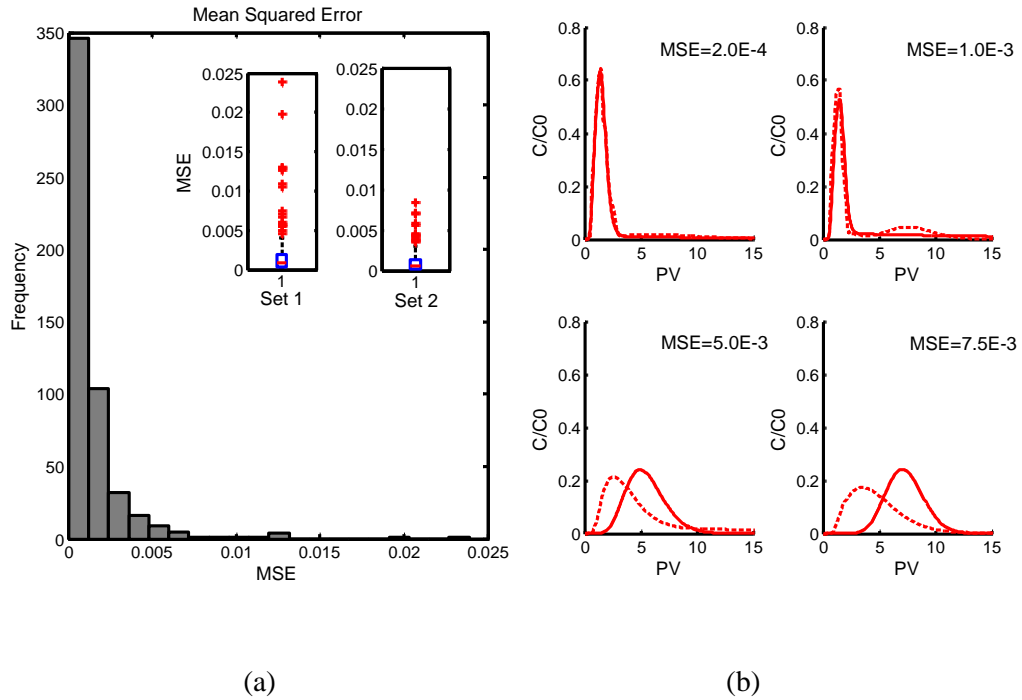


Figure R.4.3. Mean squared errors between the fit and observed breakthrough curves; (a) Distribution of mean squared errors between breakthrough curves for all simulations; and (b) demonstration of breakthrough curves for 4 samples representative of different MSE value ranges; solid lines show prediction and dashed lines represent observation data.

Mass Transfer Correlation Development

Once effective mass transfer rate coefficients were obtained for a wide range of source-zone configurations, a statistical analysis was performed to develop a constitutive equation descriptive of the mass transfer rate as a function of source-zone metrics. The potential predictors were divided into three groups: (1) permeability field characteristics, i.e., average and variance of $\ln K$ and vertical correlation length of the permeability field (λ_z); (2) DNAPL mass distribution characteristics, i.e., overall average organic saturation (\bar{S}_n), pool fraction ratio (used as $1 + \text{PF}$), center of mass in x and z directions (dimensionless forms \bar{x}/L and \bar{z}/H), and variances of mass distribution around center of mass in x and z directions (dimensionless forms σ_{xx}^2/L^2 and σ_{zz}^2/H^2); and (3) the flow characteristics i.e., average Reynolds number ($Re = qL/\nu$) in the domain, where the characteristic velocity is the Darcy velocity, the domain dimension is the length scale, and ν is the kinematic viscosity of aqueous phase.

The above variables are physically independent; however, they may be numerically correlated. A matrix scatter plot (not shown here) was used to diagnose the potential interdependencies between predictors in this group. Results showed that the R^2 values between the vertical spreading and center of mass in the vertical direction and the horizontal spreading values, was 0.92, and 0.82, respectively, indicating a strong numerical correlation between these variables. Thereafter these variables were excluded from the analysis. All other variables were considered as potential predictors.

A multivariable power function was selected for the form of the predictive model. This form was selected because with a logarithmic transformation, a Multiple Linear Regression (MLR) model could be used to develop the model in a systematic way. The predictor variables were estimated in dimensionless forms, and a combined dimensionless group also represented the upscaled mass transfer coefficient:

$$\frac{\bar{Sh}}{Sc} = \beta_0 \cdot x_1^{\beta_1} \cdot x_2^{\beta_2} \cdot \dots \cdot x_N^{\beta_N} \quad (\text{R.4.2})$$

here $x_{1,2,\dots,N}$ are the predictor variables. The effective mass transfer coefficient ($\hat{k}, [T^{-1}]$) was described as the ratio of an upscaled Sherwood ($\bar{Sh} = \hat{k}L^2/D_{aq}$) and the Schmidt ($Sc = \nu/D_{aq}$) numbers.

Multiple models with an increasing number of predictors were created. At each stage one variable was added to the best model of the previous stage, and the best model was evaluated based on three main statistics: adjusted r-squared; standard error of the model: S; and predicted residual sums of squares: PRESS (Helsel and Hirsch 2002). The normal distribution of residuals, variance inflation factor (an index for the severity of multicollinearity between variables), and statistical significance of the coefficients were checked for all models.

Table R.4.1 summarizes the coefficients, standard error of coefficients, and the corresponding R^2 values of the best model at each step for up to five predictors. The R^2 value increases from model 1 to 5 at the cost of adding more variables. The best overall model was selected by comparing the improvement in the statistics of the models when more variables are added. Figure R.4.4 shows how these statistics improve when more predictors are added. The graphs on the top row of this figure present the absolute values of the statistics, and the graphs on the bottom show the percentage of the improvement after adding additional predictors. The improvement percentages are calculated in comparison to the statistics of the first model. As Figure R.4.4 suggests, the improvement in prediction accuracy is insignificant for the first four models. At least one percent gained improvement in all three statistics was chosen as the criterion for adding more parameters. Based on this criterion, Model 4 was chosen as the best model:

$$\frac{\bar{sh}}{sc} = 446.68 \times Re^{0.929} (1 + PF)^{-3.74} \left(\frac{\sigma_{zz}^2}{H^2} \right)^{0.523} (\bar{S}_n)^{0.584} \quad R^2=0.833 \quad (R.4.3)$$

According to this model, the Reynolds number, pool fraction ratio, spreading of the organic mass in vertical direction, and effective saturation are the most important variables that control the effective mass transfer coefficient in the domain. Figure R.4.5 depicts the predictive performance of Model 4 for all observation data points.

Table R.4.1. Coefficients and standard errors of the developed regression models

Model ¹ #		1	2	3	4 ²	5
Number of variables (<i>N</i>)		1	2	3	4	5
<u>variable</u>	<u>coefficient</u>	<u>coefficient \pm SE</u>				
-	$\log(\beta_0)$	3.32 ± 0.1	1.92 ± 0.08	2.09 ± 0.07	2.65 ± 0.11	2.73 ± 0.12
σ_{zz}^2/H^2	β_1	1.05 ± 0.05	1.05 ± 0.03	0.70 ± 0.04	0.52 ± 0.05	0.52 ± 0.05
<i>Re</i>	β_2		0.93 ± 0.03	0.93 ± 0.03	0.93 ± 0.03	0.93 ± 0.03
1 + PF	β_3			-3.41 ± 0.03	-3.70 ± 0.34	-3.70 ± 0.34
$\overline{S_n}$	β_4				0.584 ± 0.09	0.603 ± 0.09
\bar{x}/L	β_5					0.26 ± 0.10
σ_{lnK}^2	β_6					
R^2 (pred)		0.41	0.78	0.817	0.831	0.835

1. Equation M.4.5 describes the general form of the regression models.
2. Selected as the best model

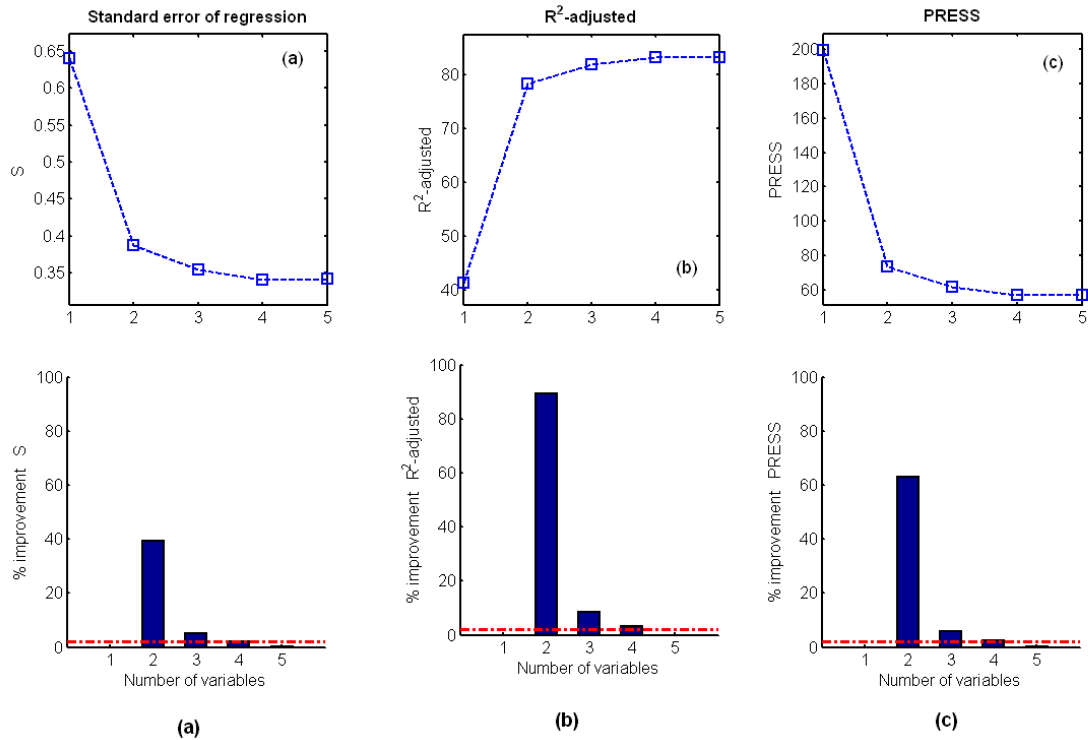


Figure R.4.4. Selecting the best model based on the statistics of the regression models; (a) standard error of the models; (b) adjusted R-squared value; (c) prediction error sum of squares: PRESS; The graphs on the top row present the absolute value of the statistics. The graphs on the bottom show the gained improvement by adding one more predictor parameter at a time to the model. The horizontal lines on the lower row figures mark the one-percent improvement criterion.

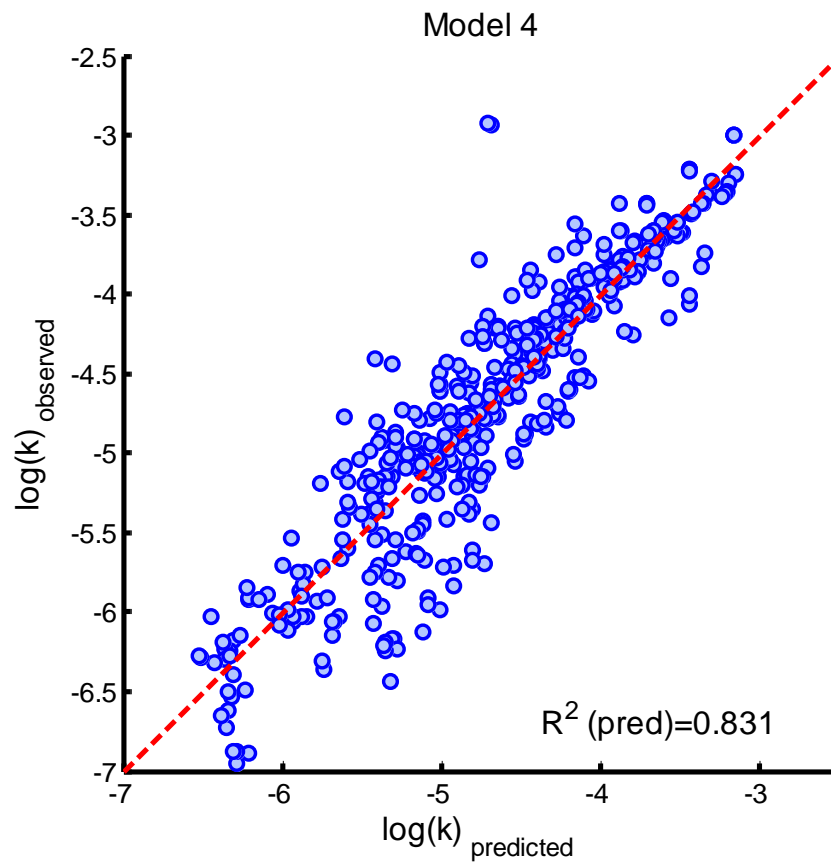


Figure R.4.5. Predicted versus observed effective mass transfer coefficients for the best model (model 4).

III.4.2.2. Model Verification

New Simulation Dataset

A dataset independent of the training data was used to evaluate the predictive capability of Model 4. In addition to the evaluation of the general performance of the model, this test was designed to explore the effect of the domain length on the effective mass transfer rate coefficient, since the training dataset consisted of source-zone realizations of uniform sizes.

Nine new two-dimensional domains with the same size as the ones used in the training process were chosen ($L \times H$ domain size). These realizations were generated from 3D realizations of Set 2 following the same approach described for the training data (see section II.1.3). Each of the domains was then used to generate three elongated hypothetical realizations of lengths $2L$, $3L$, and $4L$, consisting of repetitive modules of the primary realization. Following this approach 36 realizations were obtained. Tracer test simulations and effective mass transfer rate estimates were performed for two different flow rates (10 and 40 mL/min).

Figure R.4.6 illustrates the predictive performance of the developed model (Model 4 selected as best model) for all 72 test data points (9 series, 4 lengths, 2 flow rates). The R-squared value between the model's predicted and observed values is higher than 0.9, indicating a high prediction precision.

Experimental data comparison

To further examine the predictive capability of the developed model, model predictions were compared with experimental observations from a two-dimensional aquifer cell experiment (Ervin, 2012) (see Section III.2.1.2). Dimensions of the experimental aquifer cell and partitioning tracer test experimental conditions were similar to those of numerical simulations used to generate the upscaled model. This resemblance provides a unique possibility to test the performance of the developed model against experimental data.

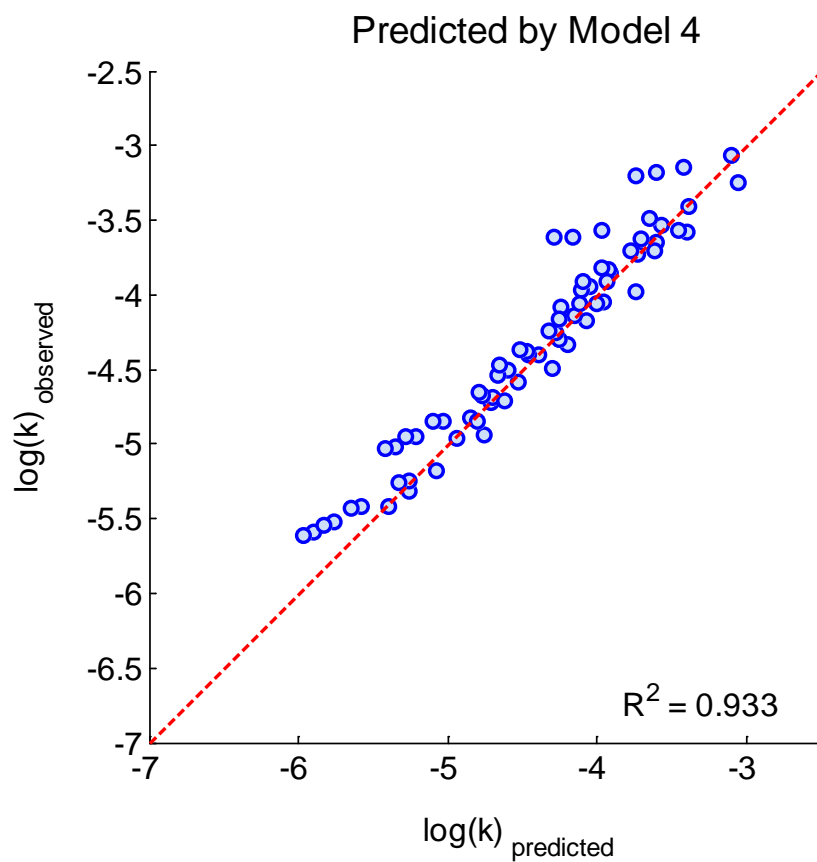


Figure R.4.6. Predicted versus observed effective mass transfer coefficients for the test dataset.

The aquifer cell consisted of Ottawa Federal Fine sand as the background, and F-70 Ottawa sand formed the low permeability zones within the background. Dimensions of the box, sand structure, and DNAPL distribution within the box are shown in Figure R.4.7. A one-centimeter thick F-70 lens (28.2 cm long) was placed at the up-gradient end of the box, and triangular low permeability zones (3.6 cm tall) formed on each end of the lens in an effort to direct the TCE-DNAPL to fill the area above the lens. Aquifer cell parameters are summarized in Table R.4.2. The flow in the cell was driven by implying a constant head pressure on two fully penetrated vertical source lines on the left and right hand sides of the domain. A pulse of 0.31 PV tracer solution was followed by flushing with background solution at 4.9 mL/min . The tracer solution consisted of bromide, 1-hexanol, and 2-octanol tracers. The tracer and background flushing solutions were saturated with TCE to assure no NAPL dissolution took place during the test.

The one-dimensional upscaled model was used to simulate this experiment. The overall mean TCE saturation, 1.1 %, was assigned to the entire domain. Conservative tracer data were used to fit the effective porosity and dispersivity of the model. For partitioning tracers, the interphase mass transfer rate was estimated by regression Model 4. Predictor variables were estimated based on a grid size-wise consistent with the regression model requirements ($30.6 \times 7.6 \text{ cm}$ blocks in horizontal and vertical directions, respectively). Table R.4.2 summarizes the box experiment parameters as well as estimated values of the predictor variables.

Figure R.4.8 demonstrates the predictive performance of Model 4 for two partitioning tracers. The arrival time of the peak of the curves is successfully predicted. To explore the significance of this observation, a sensitivity analysis (not shown here) proved that in this setup both the peak arrival time and the peak magnitude are sensitive to the effective mass transfer rate coefficient.

Additional model validation simulations with published experimental data may be found in (Boroumand, 2013).

Table R.4.2. Parameters of the first aquifer cell experiment used for model verification

Parameter	Value
<u>Cell parameters</u> ¹	
Box Dimensions (cm)	$70 \times 42 \times 1.5$
Packed Height (cm)	32.5
Mass Ottawa Federal Fine (g)	4868
Mass F-70 (g)	521
Average Bulk Density (g/cm^3)	1.54
Average Porosity	0.42
Total Pore Volume (mL)	1303
TCE-DNAPL Volume (mL)	13.5
Overall TCE-DNAPL Saturation (%)	1.04
<u>Tracer test parameters</u>	
Flow Rate (mL/min)	4.9
Reynolds Number	0.0074
<u>Mass distribution measures</u>	
PF ²	0
$\overline{S_n}$	0.011
\bar{z}/H	0.135
\bar{x}/L	0.240
σ_{zz}^2/H^2	0.0015
σ_{xx}^2/L^2	~ 0

1. Cell parameters from Ervin (2012)
2. PF is computed for an averaging grid consistent with the resolution used in model development

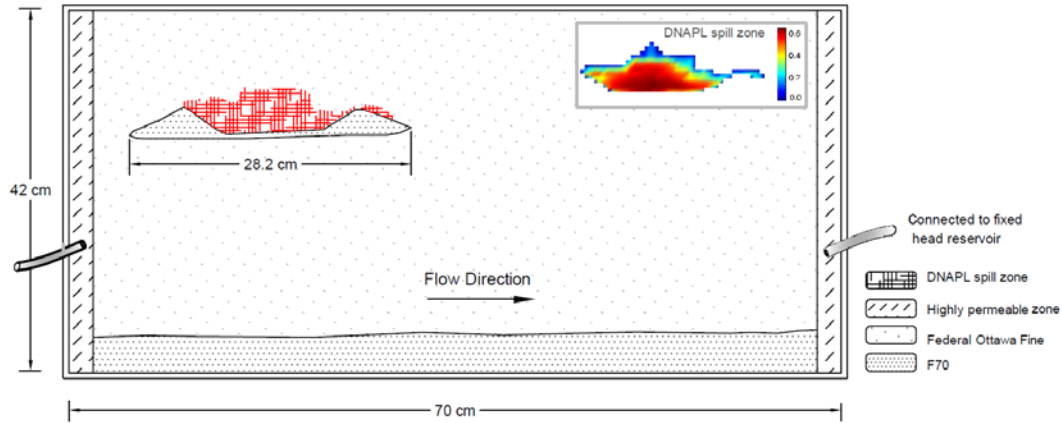


Figure R.4.7. First two-dimensional aquifer cell test used to verify developed model, Ervin (2012).

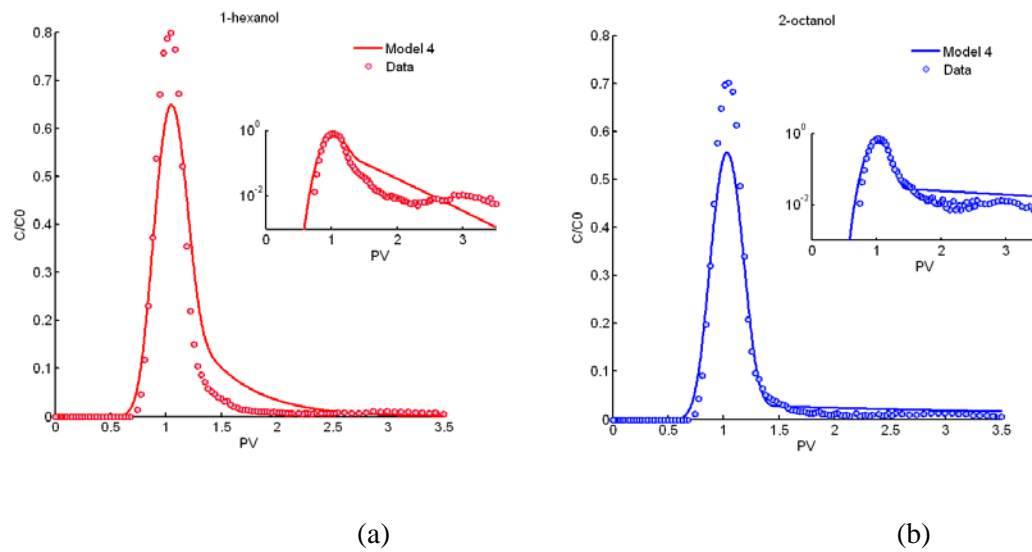


Figure R.4.8. Breakthrough curves for the partitioning tracer test conducted by Ervin (2012); (a) 1-hexanol tracer; (b) 2-octanol tracer; circles show the measured effluent concentration, solid lines are BTCs predicted by the developed upscaled model. The smaller figures on the upper right corner show the same BTCs on a logarithmic scale.

III.4.2.3. Conclusions for Upscaled PPTT Model Development

The effective mass transfer coefficient was numerically estimated for 480 tracer tests in 180 DNAPL realizations. Regression analysis was performed to study the correlation between the upscaled mass transfer coefficient and different characteristics of the realizations. The predictive potential of the model was explored by testing it on a second dataset. The model was verified against three sets of existing partitioning tracer test experiments. The results of the analysis can be summarized as:

- An upscaled, one dimensional transport simulator, incorporating a linear driving force mass transfer relationship, is capable of capturing the major breakthrough features of partitioning tracer tests in heterogeneous DNAPL source zone systems
- The most significant parameters influencing the magnitude of the upscaled mass transfer coefficient were vertical spreading of the NAPL, Reynolds number, PF, and average saturation, in that order.
- For relatively small injection domains, the metrics of heterogeneity in the NAPL distribution tend to control observed tracer breakthrough (permeability field heterogeneity does not have a large effect on effective mass transfer)
- In applying upscaled models, it is important to use a consistent approach to estimate (scale) DNAPL SZA metrics.

III.4.2.4. Assessment of Source Zone Features, using Push-Pull Data

Model Choices for 3D Field-Scale Applications

To verify the upscaled tracer model in for a 3D push-pull tracer test, fine-scale simulations were performed in a 3D domain of size $8.0 \times 8.0 \times 0.8$ (m). The interrogated zone is discretized into a $5 \times 5 \times 5$ (cm) grid. The test well is positioned at the horizontal center of the domain. It is assumed that the screened zone of the well is 0.4 (m). The sink/source terms are assigned to 8 adjacent nodes along the well-screen, which is located at mid-depth of the domain. This arrangement causes the flow to be injected into a 40-cm-height zone at the center of the domain. No-flow boundary conditions ($\frac{\partial \phi}{\partial z}=0$) are applied to both the top and bottom boundaries of the 3D domain. Variable-head boundary conditions, consistent with the imposed flow field, are applied to the other four faces of the domain.

Model Choices for Upscaled Simulations

The same finite-difference model used for the fine scale simulations was modified to simulate the test under the upscaled conditions. The major differences between the upscaled and fine scale simulators are listed below:

- i) In the upscaled model, field parameters, i.e., NAPL saturations, permeability, and porosity, are constant effective values within the interrogation zone.
- ii) The flow field in the upscaled model is estimated based on the radially symmetric approximation:

$$v(r) = \frac{Q}{2 \cdot \pi \cdot h \cdot n \cdot r} \quad (\text{R.4.4})$$

where Q is the pumping rate, r is the distance from the well, and h and n are the length of the screened zone of the well and the effective porosity, respectively.

iii) The upscaled mass transfer correlation expression (R.4.3) is incorporated into the upscaled model to represent the mass transfer of tracer between the NAPL and aqueous phase.

iv) The radius of influence (travel distance) of each tracer was assumed equal to the radius of influence of the conservative tracer.

Before using the developed upscaled model in 3D space, the validity of the model for application to a spatially variable velocity field was investigated and shown to effectively capture the observed extraction well breakthrough behavior (see Boroumand (2013) for more detail.

The three-dimensional simulator was next used to simulate PPTTs in numerically generated heterogeneous source zones. Two 3D DNAPL realizations were chosen from the numerically generated dataset discussed in Section III.1.2. Each tracer test was simulated with the fine scale model as well as the upscaled model. The NAPL realizations used for these simulations are illustrated in Figure R.4.9 (a) and Figure R.4.10 (a). A comparison of fine and upscaled breakthrough curves are presented in Figure (c,d) and Figure (c,d) for linear and logarithmic scales. Use of the logarithmic scale allows one to see the prediction accuracy for the tailing (late time concentrations). Figure R.4.11 presents a comparison of upscaled model predictions with those obtained assuming local equilibrium for 2-octanol in one case (Example 5). All MSEs between the observed and predicted BTCs with rate limited and equilibrium assumptions are reported in Table R.4.4. Note that MSEs are significantly (2 orders of magnitude) smaller when the rate limited model is used.

Breakthrough curves in the logarithmic scale show that the prediction error increases for late time concentrations. The error is more pronounced for the conservative tracer, and decreases as the partition coefficient increases. This suggests that the source of the error is not in the partitioning rate. It should be noted that the fine scale results are obtained with a 3D model in which mass transfer into the upper and lower layers of the interrogated zone is permitted through the transverse dispersion and diffusion processes. This phenomenon is not captured in the upscaled model which assumes horizontal, radially symmetric transport. It is postulated that this leads to a discrepancy between the BTCs at very low concentrations.

Table R.4.3. Parameters of the upscaled model used for simulation of PPTTs in heterogeneous domains

	NAPL saturation \overline{S}_n (%)	Vertical Spreading σ_{zz}^2/H^2	Pool Fraction PF
Example 4	0.205	0.072	0.448
Example 5	0.690	0.085	0.169

Table R.4.4. Mean squared errors for upscaled simulations

Example	Type	Model	MSE		
			Bromide	DMP	2-octanol
1	Radially Symmetric	2D	2.2E-3	-	-
		3D	2.2E-3	-	-
2	Radially Symmetric	2D	-	-	2.87E-4
		3D (rate-limited)	0.70E-3	-	0.80E-3
		3D (equilibrium)		-	0.51E-2
3	Radially Symmetric	2D	-	-	1.9 E-3
		3D (rate-limited)	0.73E-3	-	0.54E-3
		3D (equilibrium)		-	0.67E-2
4	Heterogeneous	Rate-limited	3.45E-4	-	3.82E-4
		Equilibrium		-	0.20E-2
5	Heterogeneous	Rate-limited	9.4E-5	7.8E-5	1.56E-4
		Equilibrium		8.4E-4	8.02E-3

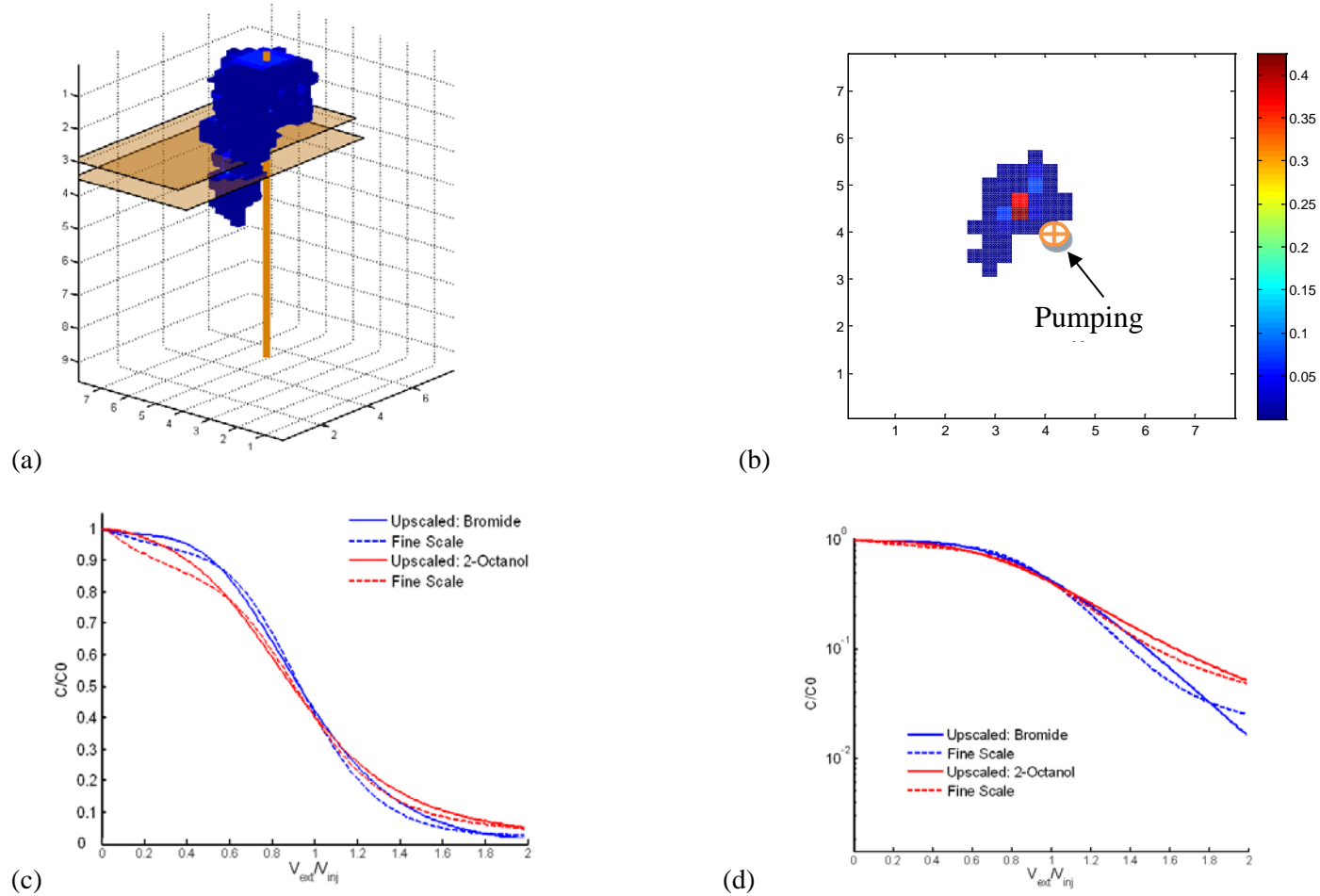


Figure R.4.9. Forward simulation of a PPTT in a heterogeneous source zone (Example 4); (a) 3D heterogeneous NAPL realization and location of the test well, horizontal planes mark the interrogation zone; (b) a horizontal cross section at the middle of the interrogation zone; (c) and (d) concentration breakthrough curves of the pull phase at the well location, in linear and logarithmic scales, respectively. MSE values are reported in Table R.4.4.

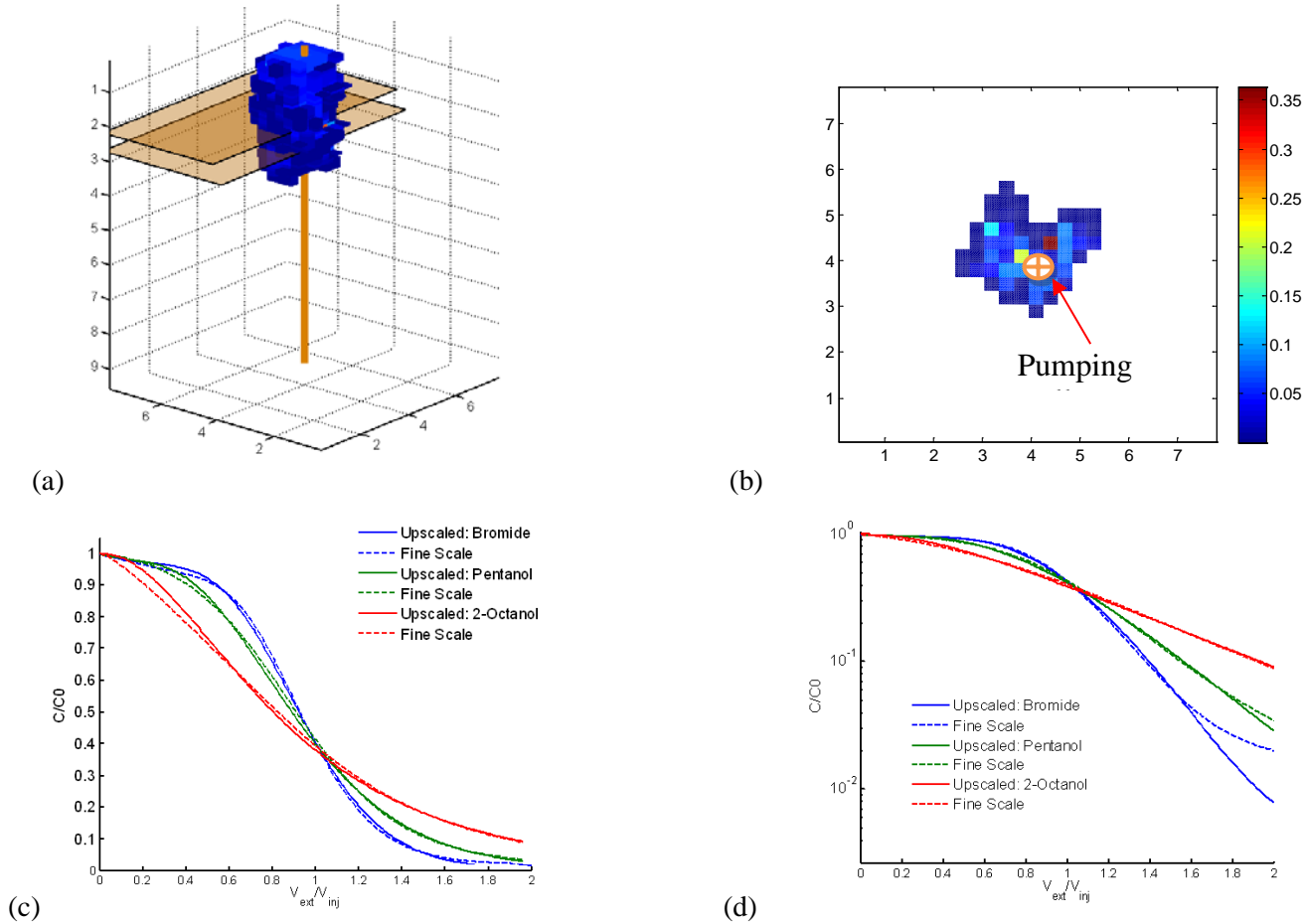


Figure R.4.10. Forward simulation of a PPTT in a heterogeneous source zone (Example 5); (a) 3D heterogeneous NAPL realization and location of the test well, horizontal planes mark the interrogation zone; (b) a horizontal cross section at the middle of the interrogation zone; (c) and (d) concentration breakthrough curves of the pull phase at the well location, in linear and logarithmic scales, respectively. MSE values are reported in Table R.4.4.

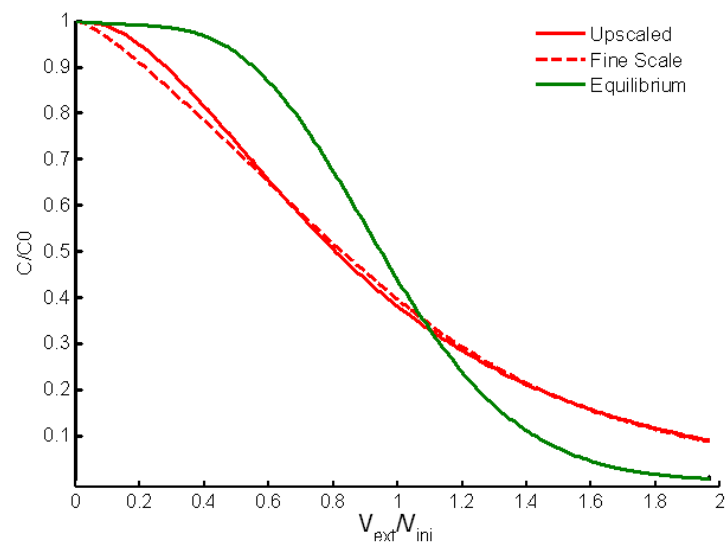


Figure R.4.11. Equilibrium and rate-limited prediction of a PPTT in a heterogeneous region; dashed line shows observed BTC for 2-octanol; solid lines show the upscaled and equilibrium predictions (Example 5). MSEs are reported in Table R.4.4.

Sensitivity Analyses

The major utility of the upscaled model is to implement it in a parameter estimation algorithm to determine the source zone characteristics. To guide this parameter estimation, a sensitivity analysis was first performed. The Push-Pull Tracer Test performed as Example-5 was selected as the basis of the comparison. Details of this analysis are presented in Boroumand (2013). Conclusions are briefly summarized below.

- 1) Results suggest that the late time breakthrough concentration is sensitive to all three predictor variables (NAPL saturation, vertical spreading, and pool fraction ratio). However, the sensitivity is more pronounced for average saturation.
- 2) An investigation of sensitivity to the ratio of injection and extraction rates rejects the hypothesis that changing the ratio of these flow rates can provide additional information for parameter estimation.

Parameter Estimation

To explore the utility of the upscaled model for local parameter estimation, the three parameters appearing in the upscaled mass transfer coefficient expression (effective vertical spreading, pool fraction, and NAPL saturation) were concurrently estimated for each tracer test by fitting model output to the observed data. Here the `lsqcurvefit` function from the MATLAB optimization tool was used to minimize the mean squared errors between the breakthrough curves obtained from fine scale and upscaled simulations. The optimization algorithm used for the least squares minimization is the Trust-Region-Reflective (TRR). After optimization, the residuals and Jacobian were transferred to the `nlparci` function to evaluate the 95% confidence intervals of the estimated parameters. The parameter estimation was performed in two steps: first, the conservative tracer data were used to fit the effective porosity and effective dispersivity of the upscaled model and then the partitioning tracer data were used to estimate the effective NAPL saturation, pool fraction ratio, and vertical spreading. Two partitioning tracers were used, and their BTCs were fit simultaneously.

The applicability of the parameter estimation approach described above was demonstrated by evaluation of the upscaled variables for a series of 2D domains. A total of 50 2D tracer test simulations in heterogeneous source zones were randomly selected from the pool of 480 simulations described above. Estimation accuracy was quantified by the correlation coefficient between the estimated and actual values (R^2) and the root-mean-square deviation (RMSD). Figure R.4.12 compares estimated parameters against with their actual values for all 50 domains. The correlation coefficients between the estimated and observed values are 0.82, 0.79, and 0.45 for vertical spreading of NAPL, pool fraction, and NAPL saturation, respectively. The RMSD values for vertical spreading of NAPL, pool fraction, and NAPL saturation are 0.065, 0.133, and 0.021, respectively. These

values can be normalized by the range of actual values of each variable to obtain a comparable metric (NRMSD), yielding NRMSD values for vertical spreading of NAPL, pool fraction, and NAPL saturation of 0.971, 0.173, and 0.255, respectively. The decreasing order of R-squared values between the predicted and actual values is consistent with the order of variable significances in the developed upscaled correlation. However, the NRMSD metric indicates that the relative prediction error for vertical spreading is higher than that for pool fraction and NAPL saturation. The scatter plot in Figure R.4.12 (a) reveals a consistent upward bias in vertical spreading estimates that explains the high R-squared of the data. Additional analysis suggests that the difference between estimated and actual upscaled parameters is related to the MSE between the observed and upscaled breakthrough curves. These observations confirm that the suggested approach can be used to estimate the upscaled parameters.

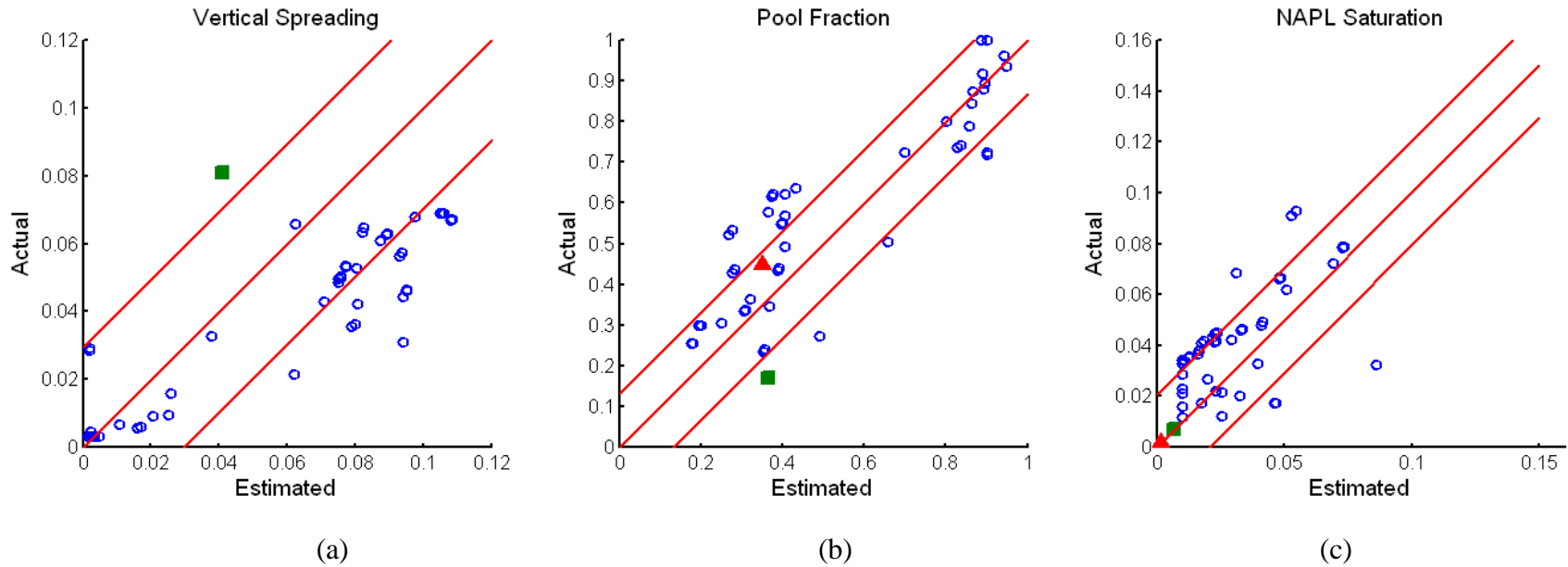


Figure R.4.12. Comparison of estimated and actual values for: (a) vertical spreading, (b) pool fraction, and (c) NAPL saturation. Blue circles show values of parameters obtained for 2D simulations; red triangles and green squares show values of parameters for 3D simulations, in Examples 4 and 5, respectively. The middle 45-degree-line represents the perfect estimation and the other two lines mark root-mean-square deviation below and above perfect estimation. Vertical spreading of Example 4 is an outlier and is not shown on plot (a); see Table R.4.5 for its values.

Table R.4.5. Estimated source zone parameters with PPTTS conducted in heterogeneous source zones; parameters are estimated using the upscaled model developed in this research and the local equilibrium model

			Parameter		
		Method	NAPL saturation \bar{S}_n (%)	Vertical Spreading σ_{zz}^2/H^2	Pool Fraction PF
Example 5	Actual	-	0.690	0.081	0.169
	Rate-limited analysis	Fit (linear)	0.660	0.041	0.365
		Fit (Log)	0.584	0.010	0.490
	Equilibrium analysis	2-octanol	8.590	N/A	N/A
		DMP	10.70	N/A	N/A
Example 4	Actual	-	0.205	0.072	0.449
	Rate-limited analysis	Fit (linear)	0.185	0.252	0.351
		Fit (Log)	0.260	0.488	0.010
	Equilibrium analysis	2-octanol	4.31	N/A	N/A
		DMP	3.85	N/A	N/A

Table R.4.6. Margin of error for the estimated parameters with rate-limited analysis

		NAPL saturation \bar{S}_n (%)	Vertical Spreading σ_{zz}^2/H^2	Pool Fraction PF
Example 5	Fit (linear)	± 0.004	$\pm >10$	$\pm >10$
	Fit (Log)	± 0.004	$\pm >10$	$\pm >10$
Example 4	Fit (linear)	± 0.005	$\pm >10$	$\pm >10$
	Fit (Log)	± 0.006	$\pm >10$	$\pm >10$

The 3D PPTT simulations presented above were used to explore the utility of the parameter estimation approach for three-dimensional heterogeneous source zones. Similar to the approach used for predictive simulation of PPTTs, observed tracer test data were numerically generated by a fine scale model that employed a local scale mass transfer coefficient. Estimated and actual values of the upscaled parameters are summarized in Table R.4.5. These values are shown on Figure R.4.12 along with the data points corresponding to the 2D domains. Inspection of Figure R.4.12 suggests that for the 3D examples considered here, the estimates of pool fraction and NAPL saturation parameters fall within the standard deviation zones calculated based on 2D simulations. This suggests that the prediction accuracy of these variables is consistent for 2D and 3D simulations. However, the estimates of vertical spreading fall out of the standard deviation zone and do not match with 2D simulations. For both 3D examples considered here, the predicted values of the average NAPL saturation are remarkably close to the perfect estimation line. The error margins (Table R.4.6) of the estimated saturations are smaller than 3.0 percent of the estimated values. In contrast, the confidence intervals for the vertical spreading and pool fraction are significantly larger (larger than 100% of the estimated value). Notice that the actual values of the effective NAPL saturation in the 3D simulations are less than one percent. These values are lower than the minimum NAPL saturation in the 2D simulations. This difference may help explain poorer estimation of vertical spreading in the 3D cases. More 3D cases will need to be evaluated to fully explore the utility and limitations of this estimation approach. This would require developing new NAPL release simulations under more diverse conditions to obtain local zones with higher effective NAPL saturation, and diverse pool fraction and vertical spreading parameters.

Parameter estimation based on local equilibrium assumption: The common method for analyzing a push-pull tracer test is to use a local equilibrium assumption and to model partitioning similarly to linear equilibrium sorption. The relationship between the fit retardation factor, equilibrium partition coefficient, and NAPL saturation can be used to estimate the NAPL saturation:

$$S_n = \frac{R - 1}{R + K_{eq} - 1} \quad (R.4.5)$$

To compare the performance of the developed parameter estimation algorithm with that of the conventional method, a 1D radial model capable of modeling equilibrium partitioning was fit to the results of the fine scale simulations. Equation R.4.5 was used to estimate NAPL saturations. Given that the model has to be fit separately for different partitioning tracers, different NAPL saturation estimates are obtained for each tracer. The estimated parameters based on the local equilibrium assumption are reported in Table R.4.5 along with the actual values and the results of the rate-limited interpretation. This comparison reveals that, for both examples, the local equilibrium assumption results in substantial estimation errors and over-prediction of the NAPL saturation, an observation that is consistent with the results of an experimental study of PPTTs in an aquifer cell (see Section III.2.2).

Conclusions for assessment of source zone features using tracer test data

Existing models for interpretation of partitioning tracer tests rely on a local equilibrium partitioning assumption. Analysis of partitioning push-pull tracer tests conducted by Istok et al. (2002), however, suggested that an equilibrium model is inadequate to describe the observed

separation between the tracers breakthrough curves. The research presented here supports conclusions of this earlier work and demonstrates the potential utility of an upscaled linear driving force model for the analysis of tracer data. Partitioning tracer tests, performed in 2D domains with injection and extraction wells on opposite sides of the domains and in 3D domains with a single injection and extraction well at the center of the domains, were analyzed. These simulations represent conditions of inter-well and push-pull partitioning tracer tests, respectively. The utility of the upscaled model to estimate vertical spreading, PF, and NAPL saturation was demonstrated in 2D simulations. The 3D simulations considered here provided estimates for average NAPL saturation with an absolute error of 3.0 percent or less. However, the accuracy of estimates for vertical spreading and PF was not consistent among the limited examples examined. The mathematical model and parameter estimation algorithm developed in this research is the first attempt to analyze PPTTs based on rate-limited partitioning and is shown to be useful for characterizing source zone features.

IV. Conclusions and Implications for Future Research / Implementation

The previous sections in Chapter III have detailed the results of research conducted to develop and implement tools for DNAPL source zone metric quantification and the prediction of associated plume response to DNAPL mass removal. The integration of these tools with the collection of appropriate site data will form the foundation for a site characterization and assessment protocol. The intent of this Protocol is to provide a framework to guide site managers in the assessment of existing data and the efficient collection of additional data, as well as in the evaluation and selection of an appropriate remedial/management strategy.

Figure C.1.1 presents a flow chart which outlines the suggested Protocol. Here, once a DNAPL site has been selected, available data on the site geology/stratigraphy are collected and matched to a representative site subsurface permeability model. The permeability models are then linked to a library of machine learning regression functions. The research summarized in Section III.3 demonstrated both the feasibility and methodology for the development of such functions. In this research, however, applications were limited to a small number of site permeability distributions. Future work will be required to develop a more comprehensive regression library for Protocol use. This library would include regression functions trained on a variety of site conditions (permeability distributions) typical of known contaminated formations. If a regression library is not available, the methodology developed and presented in this research could be implemented to develop a site-specific regression function. Such an exercise, however, would be simulation intensive and likely require additional site data collection.

After a site-matched regression function is obtained, site managers would employ this function, along with measured plume transect data, to estimate source zone metrics. To reduce uncertainty in identifying transect ‘hot spots’, the location of transect measurements and collection of transect data would be guided by sampling methodologies developed under previous SERDP research (ER-1293). Once source zone metrics have been estimated, the Protocol employs the upscaled screening model presented in Section III.4 to predict the likely response of the plume to source zone mass removal. This information will then guide preliminary site remediation decisions and future in-source data collection. *In situ* push-pull partitioning tracer test analysis techniques developed in this research (see Sections III.2 and III.4) will be useful in this latter phase of site characterization to estimate local average DNAPL saturation and mass distribution, should the screening analysis suggest that more aggressive remediation strategies are warranted.

High level conclusions from each subtask of this research are described below.

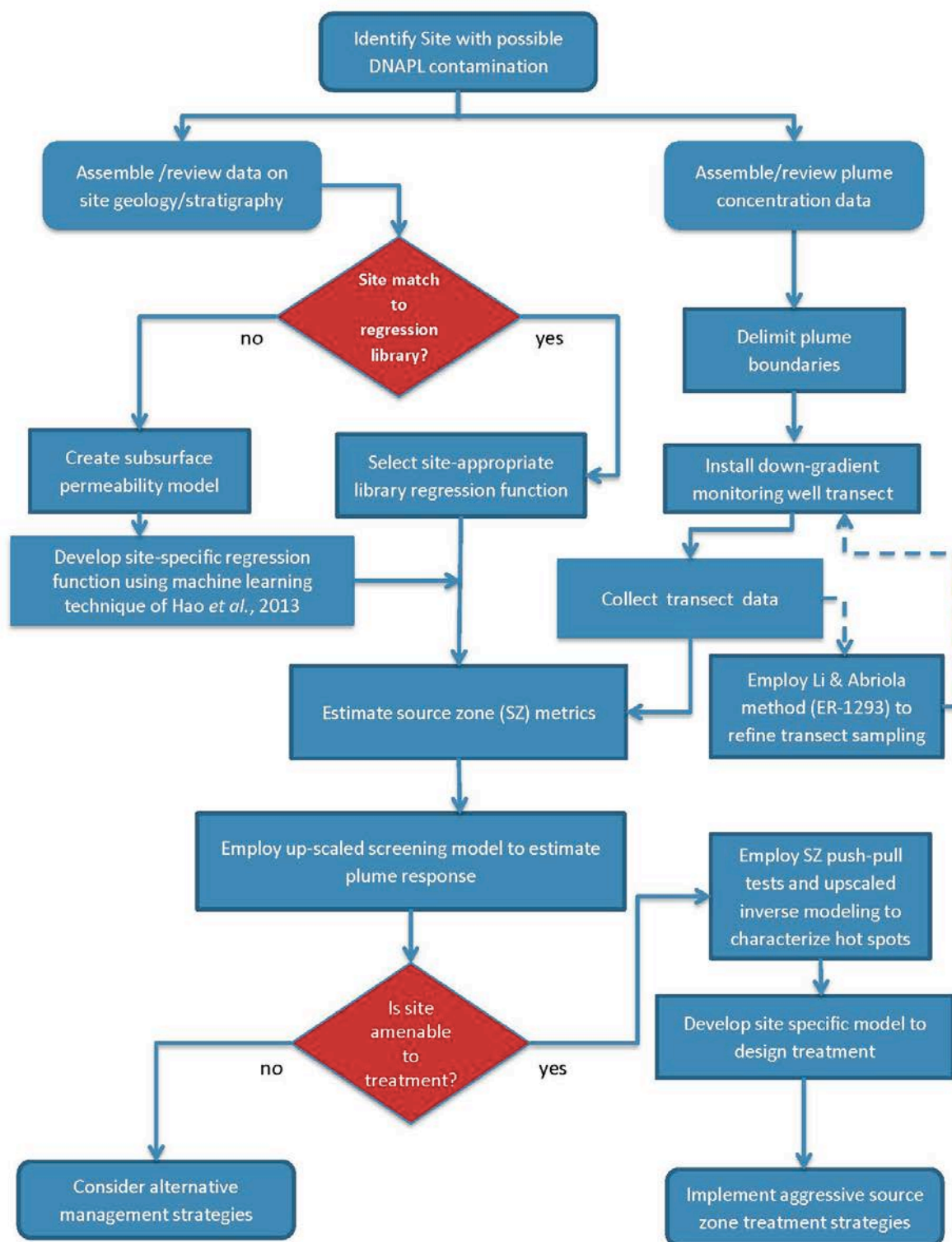


Figure C.1.1. Flow chart outlining the suggested Protocol.

IV.1. Data Generation for Metric Identification and Protocol Evaluation

Multi-component 1:1 (mole/mole) PCE- and TCE- NAPL aquifer cells

- Binary mixtures of TCE and PCE exhibited ideal dissolution behavior in water, which could be described using a Raoult's Law convention.
- Changes in NAPL source zone composition (i.e., molar ratios) differed during water flushing (i.e., aqueous dissolution) and surfactant flushing due to preferential solubilization of DNAPL constituents.
- Mass discharge-mass removal relationships were directly related to DNAPL molar composition, with decreased reductions in mass discharge with increasing mole fraction.
- The initial DNAPL saturation distribution (e.g., ganglia vs. pools) controlled the long-term dissolution behavior of heterogeneous, multi-component source zones.

Single-component TCE- NAPL aquifer cell

- Evaluation of image processing scaling methods using light transmission data indicated that an averaging window of $30 \times d_{50}$ provides the most reliable estimates of pool fraction (PF) or the ganglia to pool (GTP) ratio.
- Following substantial removal ($> 80\%$) of the initial DNAPL mass, PF decreased sharply as a large portion of the pools were reduced to ganglia, and rapid dissolution proceeded until all ($> 99\%$) DNAPL mass was removed from the source zone.

Markov-Chain permeability distribution aquifer cell

- Comparisons between experimental data and numerical simulation results indicated that when the permeability contrast between the background and low permeability media is approximately one order-of-magnitude, mass storage and release from the low-permeability zones is relatively rapid, resulting in only a limited concentration gradient between high and low permeability zones
- Multi-stage DNAPL dissolution behavior was attributed to the initial, rapid dissolution of ganglia from the heterogeneous source zone, followed by sustained dissolution from regions containing high-saturation pools located in high permeability lenses.

Field-scale numerical simulations

- 3D modeling results supplemented extensive experimental work to create a large library of simulation data. The generated library spans a large range of source zone geometries and metrics, suitable for the development and comprehensive assessment of source zone characterization methods under Task III.
- Modeling results suggested that NAPL release rate coupled with capillary pressure parameters and the distribution of low permeability layers significantly influenced the SZA, which increased variability in the down-gradient plume response.
- Consistency between SZA metrics computed in 2D and 3D was not observed in highly heterogeneous permeability fields reported here, suggesting previously reported dimensionality similarities are restricted to relatively homogeneous domains.

IV.2. Refinement of In-Source Push-Pull Tests

Batch, column and aquifer cell experimental tracer test results

- Transport models, and, consequently, SZA estimates from push-pull tests, are very sensitive to the tracer partition coefficient between water and NAPL, highlighting the importance of conducting careful assessments of K_p .
- Such assessments conducted for 1-pentanol, 1-hexanol, and 2-octanol demonstrate that the nonlinear partitioning of each alcohol may be approximated with a linear function below tracer concentrations of 3,000 mg/L, 600 mg/L and 200 mg/L, respectively.
- UNIFAC and other group contribution methods may over predict partition coefficients for these alcohols leading to underestimates in NAPL saturations determined using partitioning tracer tests employed in any well configuration.
- Diffusion limitations within the NAPL and surface accumulation on the NAPL do not appear to limit tracer partitioning in source zones. In fact, kinetics for the reversible absorption of alcohol tracers are well described using mass transfer correlations developed for pure-component NAPL dissolution.
- Analytical models for push-pull tracer tests typically assume equilibrium, linear partitioning in a homogenous medium containing a uniform saturation of NAPL. Of these assumptions, the most critical appears to be that of equilibrium partitioning. Incorporation of kinetic partitioning, even with the assumption of uniform NAPL saturation, provides a reasonable explanation of asymmetric recovery curves obtained in heterogeneous 2-D aquifer cell experiments. Further inclusion of the NAPL distribution, even with the assumption of homogenous media, results in highly accurate predictions of tracer transport.
- An empirical approach was employed to describe the asymmetry in recovery curves obtained in 2-D domains. This approach suggests the potential for using push-pull data to identify the distance to NAPL and the fraction of the vertical domain occupied by the NAPL.

Tracer Push-Pull Sensitivity and Inverse Modelling

- Application of a coupled adjoint sensitivity method to the partitioning tracer test problem can quantify the sensitivity of well observations to perturbations in the DNAPL saturation.
- The spatial distribution of sensitivities depends strongly on the location and shape of the DNAPL region surrounding the injection/extraction well, with higher sensitivities observed for tracers that have larger partitioning coefficients.
- The Gauss-Newton method, coupled with the sensitivity matrix, can be used to estimate the DNAPL total mass, mean saturation, and distance from the push-pull well.

IV.3. Processing Methods for Identification of Source Zone Features

- Machine learning methods can be used to successfully estimate source zone architecture metrics, including pool fraction, mass of DNAPL occupying pools, and mass of DNAPL occupying ganglia, from snapshot observations of concentrations within a down-gradient transect
- A fundamentally new machine learning processing method has been developed that employs ideas from manifold learning and embedding for estimating each metric individually
- The above approach has been extended using ideas from multi-task learning to determine the three metrics jointly, based on enforcing a physical relationship among the three
- Validation simulations have demonstrated that a strong performance of the SZA metric identification method can be obtained both with densely sampled data and with a more limited sampling of concentration data, as would be representative of measurements from laboratory experiments and typical field characterization efforts.

IV.4. Development of Simplified Modeling Tools

Upscaled Model for Mass Depletion

- An upscaled model that simplifies effective source zone behavior by conceptualizing NAPL dissolution from pool and ganglia zones predicted flux-averaged down gradient concentrations with reasonable accuracy using the initial source zone pool fraction, the initial flux-averaged concentration eluting from the source zone, and the initial fraction of that flux eluting from pool zones.
- This revised model improved on the upscaled model developed under previous SERDP sponsorship by enabling the prediction of two-stage mass recovery behavior that may be observed in the field, especially at “aged” sites.
- This tool provides a convenient method for obtaining screening-level predictions for source zone management, without the need to run extensive source zone characterization studies (e.g., full-size PITT or long term concentration analysis).

Upscaled Push-Pull Tracer Test Model Development

- An upscaled, one dimensional transport simulator, incorporating a linear driving force mass transfer relationship, is capable of capturing the major breakthrough features of partitioning tracer tests in two and three-dimensional heterogeneous DNAPL source zone systems.
- The most significant parameters influencing the magnitude of the upscaled mass transfer coefficient are vertical spreading of the NAPL, Reynolds number, PF, and average saturation, in that order.
- For relatively small injection domains, the metrics of heterogeneity in the NAPL distribution tend to control observed tracer breakthrough (permeability field heterogeneity does not have a large effect on effective mass transfer).

- In applying upscaled models, it is important to use a consistent approach to estimate (scale) DNAPL SZA metrics.

Assessment of source zone features using tracer test data

- Existing models for interpretation of partitioning tracer tests rely on a local equilibrium partitioning assumption. The research presented here demonstrates that an equilibrium formulation is inadequate to describe tracer test observations and demonstrates the potential utility of an upscaled linear driving force model for the analysis of tracer data.
- The utility of the upscaled model to estimate vertical spreading, PF, and NAPL saturation was demonstrated in 2D simulations.
- The 3D simulations considered here provided estimates for average NAPL saturation with an absolute error of 3.0 percent or less. However, the accuracy of estimates for vertical spreading and PF was not consistent among the limited examples examined. Future research will be required to explore the utility and refinement of this method for a larger sample of three dimensional source zone scenarios.

V. Literature Cited

- Abriola, L.M., C.D. Drummond, E.J. Hahn, K.F. Hayes, T.C.G. Kibbey, L.D. Lemke, K.D. Pennell, E.A., Petrovskis, C.A. Ramsburg, and K.M. Rathfelder. 2005. Pilot-scale demonstration of surfactant-enhanced PCE solubilization at the Bachman road site. 1. Site characterization and test design. *Environmental Science and Technology*, 2005. **39**(6): 1778-1790.
- Abriola, L.M., K. Rathfelder, M. Maiza, and S.Yadav. 1992. VALOR_Code_Version_1[1].0.pdf. Ann Arbor, Michigan.
- Abriola, L.M., P. Goovaerts, K.D. Pennell and F.E. Löffler. 2008. Development of assessment tools for evaluation of the benefits of DNAPL source zone treatment. *SERDP Project ER-1293, Final Report*.
- Annable, M.D., Jawitz, J.W., P.S.C. Rao, D.P. Dai, H. Kim, and A.L. Wood. 1998b. Field evaluation of interfacial and partitioning tracers for characterization of effective NAPL-water contact areas. *Ground Water* **36**(3): 495-502.
- Annable, M.D., P.S.C. Rao, K. Hatfield, W.D. Graham, and C.G. Enfield. 1998a. Partitioning tracers for measuring residual NAPL: Field-scale test results. *Journal of Environmental Engineering*, June, 498-503.
- Basu, N. B., A. D. Fure, and J. W. Jawitz. 2008. Predicting dense nonaqueous phase liquid dissolution using a simplified source depletion model parameterized with partitioning tracers. *Water Resour. Res.* **44**: W07414, doi:10.1029/2007WR006008.
- Belkin, M. and P. Niyogi. 2003. Laplacian eigenmaps for dimensionality reduction and data representation. *Neural Computation* **15**: 1373–1396.
- Bengio, Y., J-F Paiement, P. Vincent, O. Delalleau, N. Le Roux and M. Ouimet. 2003. *Out-of-Sample Extensions for LLE, Isomap, MDS, Eigenmaps, and Spectral Clustering*. In *Advances in Neural Information Processing Systems*, MIT Press: 177--184.
- Bernardez, L. A. 2008. Investigation on the locus of solubilization of polycyclic aromatic hydrocarbons in non-ionic surfactant micelles with ¹H NMR spectroscopy. *Colloids and Surfaces A: Physicochemical and Engineering Aspects* **324**(1-3): 71-78.
- Bernardez, L. A. and S. Ghoshal. 2004. Selective solubilization of polycyclic aromatic hydrocarbons from multicomponent nonaqueous-phase liquids into nonionic surfactant micelles. *Environmental science & technology* **38**(22): 5878-5887.
- Bertsekas, D. P. 1999. Nonlinear programming.
- Bishop, C. M. 2006. *Chapter 1.Introduction*. Pattern Recognition and Machine Learning. M. Jordan, J. Kleinberg and B. Schölkopf.
- Bishop, C. M. 2006. *Chapter 3.Linear Models for Regression*. Pattern Recognition and Machine Learning. M. Jordan, J. Kleinberg and B. Schölkopf.
- Bishop, C. M. 2006. *Chapter 12.Continuous Latent Variables*. Pattern Recognition and Machine Learning. M. Jordan, J. Kleinberg and B. Schölkopf.

Bishop, C. M. 2006. *Pattern Recognition and Machine Learning*. Springer.

Boroumand, A. 2013. *An assessment of the rate limited liquid-liquid interphase mass transfer in DNAPL source-zones: Modeling techniques and applications in site characterization*. Doctoral Dissertation, Tufts University.

Bradford, S.A., K.M. Rathfelder, J. Lang, and L.M. Abriola. 2003. Entrapment and dissolution of DNAPLs in heterogeneous porous media. *Journal of Contaminant Hydrology* **67**:133-157.

Brooks, M.C., M.D. Annable, P.S.C. Rao, K. Hatfield, J.W. Jawitz, W.R. Wise, A. L. Wood, C. G. Enfield. 2002. Controlled release, blind tests of DNAPL characterization using partitioning tracers. *Journal of Contaminant Hydrology* **59**: 187-210.

Brusseau, M. L. 1996. *Complex Mixtures and Groundwater Quality*. EPA Environmental Assessment Source Book. J. R. Boulding. Chelsea, MI, Ann Arbor Press: 113-131.

Brusseau, M. L., E. L. Difiippo, J. C. Marble and M. Oostrom. 2008. Mass-removal and mass-flux-reduction behavior for idealized source zones with hydraulically poorly-accessible immiscible liquid. *Chemosphere* **71**(8): 1511-1521.

Brusseau, M.L., Rao, P.S.C., 1989. Sorption nonideality during organic contaminant transport in porous-media. *Critical Reviews in Environmental Control* **19**(1): 33-99.

Carle, S. F. 1999. TPROGS-Transitional Probability Geostatistical Software, Version 2.1, User MAnnual. Hydrologic Sciences Group University of California, Davis CA.

Carroll, K. C. and M. L. Brusseau. 2009. Dissolution, cyclodextrin-enhanced solubilization, and mass removal of an ideal multicomponent organic liquid. *J Contam Hydrol* **106**(1-2): 62-72.

Cassiani, G., L. F. Burbery, and M. Giustiniani. 2005. A note on in situ estimates of sorption using push-pull tests. *Water Resour. Res.* **41**: W03005, doi:10.1029/2004WR003382.

Chaiko, M., R. Nagarajan and E. Ruckenstein. 1984. Solubilization of single-component and binary mixtures of hydrocarbons in aqueous micellar solutions. *Journal of Colloid and Interface Science* **99**(1): 168-182.

Childs, J., E. Acosta, M. D. Annable, M. C. Brooks, C. G. Enfield, J. H. Harwell, M. Hasegawa, R. C. Knox, P. S. Rao, D. A. Sabatini, B. Shiau, E. Szekeres and A. L. Wood. 2006. Field demonstration of surfactant-enhanced solubilization of DNAPL at Dover Air Force Base, Delaware. *J Contam Hydrol* **82**(1-2): 1-22.

Christ, J. A., C. A. Ramsburg, K. D. Pennell and L. M. Abriola. 2006. Estimating mass discharge from dense nonaqueous phase liquid source zones using upscaled mass transfer coefficients: An evaluation using multiphase numerical simulations. *Water Resour. Res.* **42**.

Christ, J. A., C. A. Ramsburg, K. D. Pennell and L. M. Abriola. 2010. Predicting DNAPL mass discharge from pool-dominated source zones. *Journal of Contaminant Hydrology* **114**(1-4): 18-34.

Christ, J. A., K. D. Pennell and L. M. Abriola. 2012. Quantification of experimental subsurface fluid saturations from high-resolution source zone images. *Water Resour. Res.* **48**(1): W01517.

Christ, J.A., C.A. Ramsburg, L.M. Abriola, K.D. Pennell and F.E. Löffler. 2005a. Coupling aggressive mass removal with microbial reductive dechlorination for remediation of DNAPL source zones: A review and assessment. *Environmental Health Perspectives* **113**(4): 465-477.

Christ, J.A., L.D. Lemke, and L.M. Abriola. 2005b. Comparison of two-dimensional and three-dimensional simulations of dense nonaqueous phase liquids (DNAPLs): Migration and entrapment in a nonuniform permeability field. *Water Resour. Res.* **41**(1): W01007.

Cooling, M.R., Khalfoui, B. Newsham, D.M.T. 1992. Phase-equilibria in very dilute mixtures of water and unsaturated chlorinated hydrocarbons and of water and benzene. *Fluid Phase Equilibria* **88**(1-2): 217-229.

Costanza, J. and Davis, W. M. 2000. Rapid detection of volatile organic compounds in the subsurface by membrane introduction into a direct sampling ion-trap mass spectrometer. *Field Analyt. Chem. Technol.* **4**: 246–254. doi: 10.1002/1520-6521(2000)4:5<246::AID-FACT4>3.0.CO2-W

Darnault C.J.G., J.A. Throop, D.A. DiCarlo, A. Rimmer, T.S. Steenhuis, J.Y. Parlange. 1998. Visualization by light transmission of oil and water contents in transient two-phase flow fields. *J. Contam. Hydrol.* **31**(3-4): 337-348.

Darnault, C. J. G., D. A. DiCarlo, A. R. Jacobson, T. W. J. Bauters, J. A. Throop, C. D. Montemagno, J.-Y. Parlange and T. S. Steenhuis. 2001. Measurement of Fluid Contents by Light Transmission in Transient Three-Phase Oil-Water-Air Systems in Sand. *Water Resour. Res.* **37**(7): 1859-1868.

Datta-Gupta, A., S. Yoon, D.W. Vasco, and G.A. Pope. 2002. Inverse modeling of partitioning interwell tracer tests: A streamline approach. *Water Resour. Res.* **38**(6): Art No. 1079.

Davis, B. M., J. D. Istok and L. Semprini. 2002. Push-pull partitioning tracer tests using radon-222 to quantify non-aqueous phase liquid contamination. *Journal of Contaminant Hydrology* **58**(1-2): 129-146.

Davis, B. M., J. D. Istok and L. Semprini. 2005. Numerical simulations of radon as an in situ partitioning tracer for quantifying NAPL contamination using push-pull tests. *Journal of Contaminant Hydrology* **78**(1-2): 87-103.

Dekker, T.J. and L.M. Abriola. 2000. The Influence of Field-Scale Heterogeneity on the Surfactant-Enhanced Remediation of Entrapped Nonaqueous Phase Liquids. *J. Contaminant Hydrology* **42**:219-251.

Deng C., X. H., Jiawei Han. 2007. Spectral regression: a unified subspace learning framework for contentbased image retrieval. Proceedings of the 15th international conference on Multimedia. New York, NY, USA: 403–412.

- Diallo, M. S., L. M. Abriola and W. J. Weber. 1994. Solubilization of nonaqueous phase liquid hydrocarbons in micellar solutions of dodecyl alcohol ethoxylates. *Environmental science & technology* **28**(11): 1829-1837.
- DiFilippo, E. L. and M. L. Brusseau. 2011. Assessment of a simple function to evaluate the relationship between mass flux reduction and mass removal for organic-liquid contaminated source zones. *J Contam Hydrol* **123**(3-4): 104-113.
- DiFilippo, E. L., K. C. Carroll and M. L. Brusseau. 2010. Impact of organic-liquid distribution and flow-field heterogeneity on reductions in mass flux. *J Contam Hydrol* **115**(1-4): 14-25.
- Dwarakanath, V., K. Kostarelos, G. A. Pope, D. Shots and W. H. Wade. 1999. Anionic surfactant remediation of soil columns contaminated by nonaqueous phase liquids. *Journal of Contaminant Hydrology* **38**(4): 465-488.
- Dwarakanath, V., Pope, G.A., 1998. New approach for estimating alcohol partition coefficients between nonaqueous phase liquids and water. *Environmental Science and Technology* **32**, 1662-1666.
- Enfield, G.C., A.L. Wood, F.P. Espinoza, M.C. Brooks, M. Annable, and P.S.C. Rao. 2005. Design of aquifer remediation systems: (1) Describing hydraulic structure and NAPL architecture using tracers. *Journal of Contaminant Hydrology* **81**: 125-147.
- Ervin, R. E. 2012. Assessment of Partitioning Tracers for Estimation of DNAPL Source Zone Architecture. Ph.D. Dissertation, Tufts University.
- Ervin, R.E., Boroumand, A.B., Abriola, L.M. and C.A. Ramsburg. 2011. Kinetic limitation on tracer partitioning in ganglia dominated source zones. *Journal of Contaminant Hydrology* **126**:195-207.
- Essaid, H.I., and K.M. Hess. 1993. Monte-Carlo simulations of multiphase flow incorporating spatial variability of hydraulic-properties. *Ground Water* **31**:123-134.
- Farthing, M.W., M.A. Seyedabbasi, P.T. Imhoff, and C.T. Miller. 2012. Influence of porous media heterogeneity on nonaqueous phase liquid dissolution fingering and upscaled mass transfer. *Water Resources Research* **48**.
- Fasano, G., Franceschini, A. 1987. A multidimensional version of the Kolmogorov–Smirnov test. *Monthly Notices of the Royal Astronomical Society* (ISSN 0035-8711) **225**: 155–170.
- Ferrari, M., Liggieri, L., Ravera, F., Amodio, C., Miller, R. 1997. Adsorption kinetics of alkylphosphine oxides at water/hexane interface 1. Pendant drop experiments. *Journal of Colloid and Interface Science* **186**: 40-45.
- Fredenslund, A., Jones, R.L., Prausnitz, J.M. 1975. Group-contribution estimation of activity coefficients in nonideal liquid-mixtures. *AIChE Journal* **21**(6): 1086-1099.
- Fure, A. D., J. W. Jawitz and M. D. Annable. 2006. DNAPL source depletion: linking architecture and flux response. *Journal of Contaminant Hydrology* **85**(3-4): 118-140.

- Gelhar, L.W. and M.A. Collins. 1971. General analysis of longitudinal dispersion in nonuniform flow. *Water Resour. Res.* **7**(6) DOI: 10.1029/WR007i006p01511
- Gmehling, J., Rasmussen, P., Fredenslund A., 1982. Vapor-liquid-equilibria by UNIFAC group contribution – revision and extension 2. *Industrial and Engineering Chemistry Process Design and Development* **21**: 118-127.
- Gmehling, J., U. Onken and W. Arlt. 1977-1990. Vapor-Liquid Equilibrium Data Collection. *Chemistry Data Series*, **Vol. I**, Parts 1-8, Dechema, Frankfurt/Main, Germany.
- Gossett, J.M. 1987. Measurement of Henry's Law Constants for C1 and C2 chlorinated hydrocarbons. *ES&T*, **21**(2):202-208.
- Guilbeault, M.A., Parker, B.L., Cherry, J.A. 2005. Mass and flux distributions from DNAPL Zones in sandy aquifers. *Ground Water* **43**(1): 70–86.
- Guodong Guo, Y. F., Charles R. Dyer, Thomas S.Huang. 2008. Image-based human age estimation by manifold learning and locally adjusted robust regression. *IEEE Transactions On Image Processing* **17**.
- Haggerty, R., Harvey, C.F., Freiherr von Schwerin, C. and Meigs, L.C. 2004. What controls the apparent timescale of solute mass transfer in aquifers and soils? A comparison of experimental results. *Water Resour. Res.* **40**: W01510, doi:10.1029/2002WR001716.
- Haggerty, R., S. W. Fleming, L. C. Meigs, and S. A. McKenna. 2001. Tracer tests in a fractured dolomite: 2. Analysis of mass transfer in single-well injection-withdrawal tests. *Water Resour. Res.*, **37**(5): 1129 – 1142.
- Hall SH, Luttrell SP, Cronin WE. 1991. A method for estimating effective porosity and ground-water velocity. *Ground Water* **29**: 171–174.
- Hanchuan, P., L. Fuhui and C. Ding. 2005. Feature selection based on mutual information criteria of max-dependency, max-relevance, and min-redundancy. *Pattern Analysis and Machine Intelligence, IEEE Transactions on* **27**(8): 1226-1238.
- Hansen, H.K., Rasmussen, P., Fredenslund, A., Schiller, M., Gmehling, J. 1991. Vapor-liquid equilibria by UNIFAC group contribution. 5. Revision and extension. *Industrial and Engineering Chemistry Research* **30**(10): 2352-2355.
- Harbaugh, A. W. 2005. MODFLOW-2005, the U.S. Geological Survey Modular Ground-Water Model-The Ground-Water Flow Process. *U.S. Geological Survey Techniques and Methods Book* 6.
- Hartog, N., Cho, J., Parker, B., Annable, M.D. 2010. Characterization of a heterogeneous DNAPL source zone in the Borden aquifer using partitioning and interfacial tracers: Residual morphologies and background sorption. *Journal of Contaminant Hydrology* **115**: 79-89.
- Haverkamp, R., and J. Y. Parlange. 1986. Predicting the water-retention curve from particle-size distribution: 1. Sandy soils without organic matter. *Soil Sci.* **142**: 325–339.

Hayduk, W., Laudie, H. 1974. Prediction of diffusion coefficients for nonelectrolytes in dilute aqueous solutions. *AIChE Journal* **20**(3): 611-615.

Helsel, D. R. and R. M. Hirsch. 2002. Statistical Methods in Water Resources. *USGS Techniques of Water-Resources Investigation Book 4*.

Hoag, George E., and Michael C. Marley. 1986. Gasoline Residual Saturation in Unsaturated Uniform Aquifer Materials. *Journal of Environmental Engineering* **112** (3): 586. doi:10.1061/(ASCE)0733-9372(1986)112:3(586).

Horvarth, A.L, F.W Getzen, and Z. Maczynska. 1999. IUPAC-NIST Solubility Data Series 67. Halogenated Ethanes and Ethenes with Water. *Journal of Physical and Chemical Reference Data* **28**(2):395-627.

Hu, Q. H. and M. L. Brusseau. 1995. Effect of Solute Size on Transport in Structured Porous-Media. *Water Resour. Res.* **31**(7): 1637-1646.

Huang, J., J. A. Christ, and M. N. Goltz. 2010. Analytical solutions for efficient interpretation of single-well push-pull tracer tests. *Water Resour. Res.* **46**: W08538, doi:10.1029/2008WR007647.

Imhoff, P.T. and K. Pirestani. 2004. Influence of mass transfer resistance on detection of nonaqueous phase liquids with partitioning tracer tests. *Advances in Water Resources* **27**(4): 429-444.

Imhoff, P.T., Jaffé, P.R., Pinder G.F. 1994. An experimental study of complete dissolution of a nonaqueous phase liquid in saturated porous media. *Water Resour. Res.* **30** (2): 307-320.

Istok, j. D., J. A. Field, M. H. Schroth, B. M. Davis and V. Dwarakanath. 2002. Single-well "push-pull" partitioning tracer test for NAPL detection in the subsurface. *Environmental Science & Technology* **36**(12).

Istok, J.D., J.A. Field, M.H. Schroth, B.M. Davis, and V. Dwarakanath. 2002. Single-well "push-pull" partitioning tracer test for NAPL detection in the subsurface. *Environmental Science and Technology* **36**(12): 2708-2716.

Istok, J.D., M. D. Humphrey, M. H. Schroth, M. R. Hyman, K. T. O'Reilly. 1997. Single- well "push-pull" test for in situ determination of microbial activities. *Ground Water* **35**: 619–630.

Jackson, R. E. and V. Dwarakanath. 1999. Chlorinated Decreasing Solvents: Physical-Chemical Properties Affecting Aquifer Contamination and Remediation. *Ground Water Monitoring & Remediation* **19**(4): 102-110.

Jafvert, C. T., P. L. van Hoof and J. K. Heath. 1994. Solubilization of non-polar compounds by non-ionic surfactant micelles. *Water Research* **28**(5): 1009-1017.

Jalbert, M., Dane, J.H., Bahaminyakamwe, L. 2003. Influence of porous medium and NAPL distribution heterogeneities on partitioning inter-well tracer tests: a laboratory investigation. *Journal of Hydrology* **272**: 79-94.

- James, A.I., W.D. Graham, K. Hatfield, P.S.C. Rao, and M.D. Annable. 1997. Optimal estimation of residual non-aqueous phase liquid saturations using partitioning tracer concentration data. *Water Resour. Res.* **33**(12): 2621-2636.
- James, A.I., W.D. Graham, K. Hatfield, P.S.C. Rao, and M.D. Annable. 2000. Estimation of spatially variable residual nonaqueous phase liquid saturations in nonuniform flow fields using partitioning tracer data. *Water Resour. Res.* **36**(4): 999-1012.
- Jawitz J.W., M.D. Annable, G.G. Demmy, and P.S.C. Rao. 2003. Estimating nonaqueous phase liquid spatial variability using partitioning tracer higher temporal moments. *Water Resour. Res.* **39**(7): 1192.
- Jawitz, J. W., A. D. Fure, G. G. Demmy, S. Berglund and P. S. C. Rao. 2005. Groundwater Contaminant Flux Reduction Resulting from Nonaqueous Phase Liquid Mass Reduction. *Water Resour. Res.* **41**: W10408.
- Jawitz, J.W., M.D. Annable, P.S.C. Rao, and R.D. Rhue. 1998. Field implementation of a Winsor type I surfactant/alcohol mixture for in situ solubilization of a complex LNAPL as a single-phase microemulsion. *Environmental Science and Technology* **32**: 523-530.
- Jin M., G.W. Butler, R.E. Jackson, P.E. Mariner, J.F. Pickens, G.A. Pope, C.L. Brown, D.C. McKinney. 1997. Sensitivity models and design protocol for partitioning tracer tests in alluvial aquifers. *Ground Water* **35**(6): 964-972.
- Jin, M., Delshad, M., Dwarakanath, V., McKinney, D.C., Pope, G.A., Sepehrnoori, K., Tilburg, C.E., Jackson, R.E. 1995. Partitioning tracer test for detection, estimation and remediation performance assessment of subsurface nonaqueous phase liquids. *Water Resour. Res.* **31** (5): 1201–1211.
- Kaluarachchi, J.j. and C. Parker. 1992. Multiphase flow with a simplified model for oil entrapment. *Transp. Porous Media* **7**(1).
- Kram, M.L., Keller, A.A., Rossabi, J., Everett, L.G. 2001. DNAPL characterization methods And approaches, Part 1: performance comparisons. *Ground Water Monitoring and Remediation* **21** (4): 109–123.
- Kueper, B. H., and J. I. Gerhard. 1995. Variability of point source infiltration rates for two-phase flow in heterogeneous porous media. *Water Resour. Res.* **31**: 2971– 2980.
- Lemke, L. D., L. M. Abriola and P. Goovaerts. 2004. Dense nonaqueous phase liquid (DNAPL) source zone characterization: Influence of hydraulic property correlation on predictions of DNAPL infiltration and entrapment. *Water Resour. Res.* **40**(1).
- Lemke, L.D., and L.M. Abriola. 2006. Modeling dense nonaqueous phase liquid mass removal in nonuniform formations: Linking source-zone architecture and system response. *Geosphere* **2**(2):74-82.
- Lemke, Lawrence D. 2004a. Dense nonaqueous phase liquid (DNAPL) source zone characterization: Influence of hydraulic property correlation on predictions of DNAPL

infiltration and entrapment. *Water Resour. Res.* **40** (1): 1-16. doi:10.1029/2003WR001980. <http://www.agu.org/pubs/crossref/2004/2003WR001980.shtml>.

Lemke, L.D., L.M. Abriola, and J.R. Lang. 2004b. Influence of hydraulic property correlation on predicted dense nonaqueous phase liquid source zone architecture, mass recovery, and contaminant flux. *Water Resour. Res.* **40**(12): W12417.

Lesage, S. and S. Brown. 1994. Observation of the dissolution of NAPL mixtures. *Journal of Contaminant Hydrology* **15**(1-2): 57-71.

Leverett, M. C. 1941. Capillary behavior in porous solids, *Pet. Dev. Technol.* **142**: 152– 169.

Liggieri, L., Ravera, F., Ferrari, M., Passrone, A., Miller, R. 1997. Adsorption kinetics of alkylphosphine oxides at water/hexane interface 2. Theory of the adsorption with transport across the interface in finite systems. *Journal of Colloid and Interface Science* **186**: 46-52.

Londergan, J. T., H. W. Meinardus, P. E. Mariner, R. E. Jackson, C. L. Brown, V. Dwarakanath, G. A. Pope, J. S. Ginn and S. Taffinder. 2001. DNAPL Removal from a Heterogeneous Alluvial Aquifer by Surfactant-Enhanced Aquifer Remediation. *Ground Water Monitoring Remediation* **21**: 57-67.

Lui, Y. M. 2012. Advances in matrix manifolds for computer vision. *Image and Vision Computing* **30**(6–7): 380-388.

Lyman, W. J., Reehl, W. F., Rosenblatt, D. H. 1990. *Handbook of Chemical Property Estimation Methods*; American Chemical Society, Washington, DC.

Ma, L., M. M. Crawford and J. Tian. 2010. Local Manifold Learning-Based k-Nearest-Neighbor for Hyperspectral Image Classification. *IEEE TRANSACTIONS ON GEOSCIENCE AND REMOTE SENSING* **48**(11): 4099-4109.

MacDonald, J. A. and M. C. Kavanaugh. 1994. Restoring contaminated groundwater: An achievable goal? *Environmental Science and Technology* **28**(8): 362A-368A.

Magnussen, T., Rasmussen, P., Fredenslund, A. 1981. UNIFAC parameter table for prediction of liquid-liquid equilibria. *Industrial and Engineering Chemistry Process Design and Development* **20** (2): 331-339.

Maji, R. 2005. Conditional stochastic modelling of DNAPL migration and dissolution in a high-resolution aquifer analog. University of Waterloo, Canada. Doctoral Thesis.

MATLAB. 2008. *The MathWorks Inc., Natick, Massachusetts*.

Mayer, A. and S.M. Hassanizadeh. 2005. Soil and groundwater contamination: Nonaqueous phase liquids. *Water Resources Monograph* **17**. American Geophysical Union, Washington DC.

McCray, J. E., G. Bai, R. M. Maier and M. L. Brusseau. 2001. Biosurfactant-enhanced solubilization of NAPL mixtures. *J Contam Hydrol* **48**(1-2): 45-68.

- McCray, J. E., T. B. Boving and M. L. Brusseau. 2000. Cyclodextrin-enhanced solubilization of organic contaminants with implications for aquifer remediation. *Ground Water Monitoring & Remediation* **20**(1): 94-103.
- Meinardus, H.W., V. Dwarakanath, J. Ewing, G.J. Hirasaki, R.E. Jackson, M. Jin, J.S. Ginn, J.T., Londergan, C.A. Miller, and G.A. Pope. 2002. Performance assessment of NAPL remediation in heterogeneous alluvium. *Journal of Contaminant Hydrology* **54**: 173-193.
- Mendoza-Sanchez, I., Cunningham, J. 2007. Efficient algorithm for modeling transport in porous media with mass exchange between mobile fluid and reactive stationary media. *Transport in Porous Media* **68** (3): 285-300.
- Michalak, A. M., and P. K. Kitanidis. 2004. Estimation of historical groundwater contaminant distribution using the adjoint state method applied to geostatistical inverse modeling. *Water Resour. Res.* **40**: W08302, doi:10.1029/2004WR003214.
- Mitchell, T. M. 1997. *Chapter 2. Concept Learning and the General-to-Specific Ordering*. Machine Learning, McGraw-Hill Science/Engineering/Math.
- Moran, M. J., J. S. Zogorski and P. J. Squillace. 2007. Chlorinated solvents in groundwater of the United States. *Environmental science & technology* **41**(1): 74-81.
- Moreno-Barbero, E. and T.H. Illangasekare. 2005. Simulation and performance assessment of partitioning tracer tests in heterogeneous aquifers. *Environmental and Engineering Geoscience*, **11**(4): 395-404.
- Moreno-Barbero, E. and T.H. Illangasekare. 2006. Influence of dense nonaqueous phase liquid pool morphology on the performance of partitioning tracer tests: Evaluation of the equilibrium assumption. *Water Resour. Res.* **42**(4): Art. No. W04408
- Moreno-Barbero, E., Kim, Y., Seaton, S., Illangasekare, T.H. 2007. Intermediate scale investigation of nonaqueous phase liquid architecture on partitioning tracer test performance. *Vadose Zone Journal* **6** (4): 725-734.
- Nagarajan, R., M. A. Chaiko and E. Ruckenstein. 1984. Locus of solubilization of benzene in surfactant micelles. *88* **13**: 2916-2922.
- Nagarajan, R., M. Barry and E. Ruckensteinf. 1985. Unusual Selectivity in Solubilization by Block Copolymer Micelles *Langmuir* **2**(2): 210-215.
- Nambi, I, M., and S. E. Powers. 2003. Mass transfer correlations for nonaqueous phase liquid dissolution from regions with high initial saturations, *Water Resour. Res.* **39**(2): 1030–1040.
- Nambi, I. 1999. Dissolution of non-aqueous phase liquids in in heterogenous subsurface systems, Clarkson University, Potsdam, N.Y.
- Nambi, I.M. and S.E. Powers. 2003. Mass transfer correlations for nonaqueous phase liquid dissolution from regions with high initial saturations. *Water Resour. Res.* **39**(2) doi:10.1029/2001WR000667.

National Research Council. 2005. *Contaminants in the subsurface: source zone assessment and remediation*. National Academies Press, Washington, DC.

Nelson, N. T., Q. Hu and M. L. Brusseau. 2003. Characterizing the contribution of diffusive mass transfer to solute transport in sedimentary aquifer systems at laboratory and field scales. *J Hydrol* **276**(1-4): 275-286.

Neupauer, R. M., and J. L. Wilson. 1999. Adjoint method for obtaining backward-in-time location and travel time probabilities of a conservative groundwater contaminant. *Water Resour. Res.* **35**(11): 3389–3398.

Neupauer, R. M., and J. L. Wilson. 2001. Adjoint-derived location and travel time probabilities for a multidimensional groundwater system. *Water Resour. Res.* **37**(6): 1657–1668.

Park, E., and J. C. Parker. 2005. Evaluation of an upscaled model for DNAPL dissolution kinetics in heterogeneous aquifers. *Adv. Water Resour.* **28**: 1280–1291, doi:10.1016/j.advwatres.2005.04.002

Parker, J.C. and E. Park. 2004. Field-scale DNAPL dissolution kinetics in heterogeneous aquifers. *Water Resour. Res.* **40**: W05109, doi: 10.1029/2003WR002807.

Pennell, K. D., A. M. Adinolfu, L. M. Abriola and M. S. Diallo. 1997. Solubilization of dodecane, tetrachloroethylene, and 1,2-dichlorobenzene in micellar solutions of ethoxylated nonionic surfactants. *Environmental Science and Technology* **31**(5): 1382-1389.

Pennell, K. D., G. A. Pope and L. M. Abriola. 1996. Influence of Viscous and Buoyancy Forces on the Mobilization of Residual Tetrachloroethylene during Surfactant Flushing. *Environmental Science and Technology* **30**(4): 1328–1335.

Pennell, K. D., M. Jin, L. M. Abriola and G. A. Pope. 1994. Surfactant enhanced remediation of soil columns contaminated by residual tetrachloroethylene. *Journal of Contaminant Hydrology* **16**(1): 35-53.

Phelan, T. J. and L. M. Abriola. 2006. Modeling dense nonaqueous phase liquid mass removal in nonuniform formations: Linking source-zone architecture and system response. *Geosphere* **2**(2): 74-82.

Pitterle, M. T., R. G. Andersen, J. T. Novak and M. A. Widdowson. 2005. Push-pull tests to quantify in situ degradation rates at a phytoremediation site. *Environmental Science & Technology* **39**(23): 9317-9323.

Powers, S. E., L. M. Abriola and W. J. J. Weber. 1992. An experimental investigation of nonaqueous phase liquid dissolution in saturated subsurface systems: Steady state mass transfer rates. *Water Resour. Res.* **28**(10): 2691-2705.

Powers, S.E., L.M. Abriola, and W.J. Weber, Jr. 1994. An Experimental Investigation Of Nonaqueous Phase Liquid Dissolution In Saturated Subsurface Systems - Transient Mass-Transfer Rates. *Water Resour. Res.* **30**(2): 321-332.

Prak, D. J. and P. H. Pritchard. 2002. Solubilization of polycyclic aromatic hydrocarbon mixtures in micellar nonionic surfactant solutions. *Water Res* **36**(14): 3463-3472.

Ramachandran, B.R., Allen, J.M., Halpern, A.M. 1996. The importance of weighted regression analysis in the determination of Henry's Law constants by static headspace gas chromatography. *Analytical Chemistry* **68**: 281-286.

Ramsburg, C.A. and K.D. Pennell. 2002. Density-modified displacement for DNAPL source zone remediation: Density Conversion Using a Partitioning Alcohol. *Environmental Science & Technology* **36**(9): 2082-2087.

Ramsburg, C.A., J.A. Christ, S.R. Douglas, and A. Boroumand. 2011. Analytical modeling of degradation product partitioning kinetics in source zones containing entrapped DNAPL. *Water Resour. Res.* **47**. DOI:10.1029/2010WR009958. Article Number: W03507.

Ramsburg, C.A., K.D. Pennell, L.M. Abriola, G. Daniels, C.D. Drummond, M. Gamache, H-L Hsu, E.A. Petrovskis, K.M. Rathfelder, J.L. Ryder, and T. P. Yavaraski. 2005. Pilot-scale demonstration of surfactant-enhanced PCE solubilization at the Bachman Road site. 2. System operation and evaluation. *Environmental Science and Technology* **39**: 1791-1801.

Ramsburg, C.A., Thornton, C.E., Christ, J.A. 2010. Degradation product partitioning in source zones containing chlorinated ethene DNAPL. *Environmental Science and Technology*. Available Online doi:10.1021/es102536f.

Rao, P.S.C., M.D. Annable, and H. Kim. 2000. NAPL source zone characterization and remediation technology performance assessment: recent developments and applications of tracer techniques. *Journal of Contaminant Hydrology* **45**: 63-78.

Rasmuson, A., Neretnieks, I. 1980. Exact solution of a model for diffusion in particle and longitudinal dispersion in packed-beds. *AIChE Journal* **26** (4): 686-690.

Rathfelder, K. and L.M. Abriola. 1996. Mass conservative numerical-solutions of the head-based Richards Equation – Reply. *Water Resour. Res.* **32**(3): 761.

Rathfelder, K.M., Abriola, L.M., Singletary, M.A., Pennell, K.D. 2003. Influence of surfactant-facilitated interfacial tension reduction on chlorinated solvent migration in porous media: Observations and numerical simulation. *Journal of Contaminant Hydrology* **64** (3-4): 227-252.

Ravera, F., Ferrari, M., Liffieri, L., Miller, R. 1997. Adsorption kinetics of alkyl phosphine oxides in water/alkane systems with transfer across the interface. *Progress in Colloid and Polymer Science* **105**: 346-350.

Ravera, F., Ferrari, M., Liggieri, L. 2000. Adsorption and partitioning of surfactants in liquid-liquid systems. *Advances in Colloid and Interface Science* **88**: 129-177.

Refael C. Gonzalez, R. E. W. 2010. *Chapter 2. Digital Image Fundamentals*. Digital Image Processing, Prentice Hall.

Refael C. Gonzalez, R. E. W. 2010. *Chapter 9. Morphological Image Processing*. Digital Image Processing, Prentice Hall.

Riddick J.A. and W.B. Bunger, Techniques of Chemistry, Vol. II, 3rd edn., Wiley Interscience, New York, 1970.

Roy, J. W., J. E. Smith and R. W. Gillham. 2004. Laboratory evidence of natural remobilization of multicomponent DNAPL pools due to dissolution. *Journal of Contaminant Hydrology* **74**(1-4): 145-161.

Saenton, S., Illangasekare, T.H. 2007. Upscaling of mass transfer rate coefficient for the numerical simulation of dense nonaqueous phase liquid dissolution in heterogeneous aquifers. *Water Resour. Res.* **43**: W02428.

Shawe-Taylor, J. and N. Cristianini. 2004. *Chapter 3. Properties of Kernels*. Kernel Methods for Pattern Analysis, Cambridge University Press.

Schnaar, G., Brusseau, M.L. 2005. Pore-Scale characterization of organic immiscible-liquid morphology in natural porous media using synchrotron x-ray microtomography. *Environmental Science and Technology* **39**: 8403-8410.

Schroth, M.H., and J.D. Istok. 2006. Models to determine first-order rate coefficients from single-well, push-pull tests. *Ground Water* **44**(2): 275-283.

Schroth, M.H., J.D. Istok, R. Haggerty. 2001. In situ evaluation of solute retardation using single-well push-pull tests, *Advances in Water Resources* **24**: 105-117

Schwarzenbach, R. P., P. M. Gschwend and D. M. Imboden. 2003. *Environmental Organic Chemistry*. Wiley Interscience.

Shiau, B.-J., D. A. Sabatini and J. H. Harwell. 1994. Solubilization and Microemulsification of Chlorinated Solvents Using Direct Food Additive (Edible) Surfactants. *Ground Water* **32**(4): 561-569.

Stroo, H. F., A. Leeson, J. A. Marqusee, P. C. Johnson, C. H. Ward, M. C. Kavanaugh, T. C. Sale, C. J. Newell, K. D. Pennell, C. A. Lebron and M. Unger. 2012. Chlorinated ethene source remediation: lessons learned. *Environmental science & technology* **46**(12): 6438-6447.

Stroo, H. F., M. Unger, C. H. Ward, M. C. Kavanaugh, T. M. Vogel, A. Leeson, J. A. Marqusee and B. P. Smith. 2003. Remediation chlorinated solvent source zones. *Environmental science & technology* **37**: 224A-230A.

Suchomel, E. J. and K. D. Pennell. 2006. Reductions in contaminant mass discharge following partial mass removal from DNAPL source zones. . *Environmental science & technology* **40**: 6110-6116.

Suchomel, E. J., C. A. Ramsburg and K. D. Pennell. 2007. Evaluation of trichloroethene recovery processes in heterogeneous aquifer cells flushed with biodegradable surfactants. *Journal of Contaminant Hydrology* **94**: 195-214.

Taylor, T. P., K. D. Pennell, L. M. Abriola and J. H. Dane. 2001. Surfactant enhanced recovery of tetrachloroethylene from a porous medium containing low permeability lenses , 1. Experimental studies. *Journal of Contaminant Hydrology* **48**(3-4): 325-350.

Thal Jr., A.E., Knox, R.K., Sabatini, D.A. 2007. Estimating Partition Coefficients of Tracers. *Groundwater Monitoring and Remediation* **27** (4): 135-142.

Tidwell, V. C. and R. J. Glass. 1994. X ray and visible light transmission for laboratory measurement of two-dimensional saturation fields in thin-slab systems. *Water Resour. Res.* **30**(11): 2873-2882.

Tomich, J.F., R.L. Dalton, H.A. Deans, and L.K. Shallenberger. 1973. Single-well tracer method to measure residual oil saturation. *Journal of Petroleum Technology*, February.

Totten, C.T., Annable, M.D., Jawitz, J.A., Delfino, J.J. 2007. Fluid and porous media property effects on dense nonaqueous phase liquid migration and contaminant mass flux. *Environmental Science and Technology* **41**: es061639r.

USEPA. 2003. 40 CFR Part 136 Appendix B, Definition and procedure for the determination of the method detection limit-Revision 1.11. US Environmental Protection Agency.

Wang, P. Dwarakanath, V., Rouse, B.E., Pope, G.A., Sepehrnoori, K. 1998. Partition coefficients for alcohol tracers between nonaqueous-phase liquids and water from UNIFAC solubility method. *Advances in Water Resources* **21** (2): 171-181.

Wang, X. 2013. Dense Nonaqueous Phase Liquid (DNAPL) Source Zone Characterization in Highly Heterogeneous Permeability Fields. *A thesis present to Tufts University in fulfillment of the thesis requirement for the degree of Master of Sciences*.

Werth, C. J., C. Zhang, M. L. Brusseau, M. Oostrom and T. Baumann. 2010. A review of non-invasive imaging methods and applications in contaminant hydrogeology research. *J Contam Hydrol* **113**(1-4): 1-24.

Willson, C.S., O. Pau, J.A. Pedit, and C.T. Miller. 2000. Mass transfer limitation effects on partitioning tracer tests. *Journal of Contaminant Hydrology* **45**: 79-97.

Wise, W.R., D. Dai, D., E.A. Fitzpatrick, L.W. Evans, P.S.C. Rao, and M.D. Annable. 1999. Nonaqueous phase liquid characterization via partitioning tracer tests: A modified Langmuir relation to describe partitioning nonlinearities. *Journal of Contaminant Hydrology* **36**: 153-165.

Wise, W.R. 1999. NAPL characterization via partitioning tracer tests: Quantifying effects of partitioning nonlinearities. *Journal of Contaminant Hydrology* **36**: 167-183.

Zhang, C., C. J. Werth and A. G. Webb. 2007. Characterization of NAPL source zone architecture and dissolution kinetics in heterogeneous porous media using magnetic resonance imaging. *Environmental science & technology* **41**(10): 3672-3678.

Zhang, C., C. J. Werth and A. G. Webb. 2008. Investigation of surfactant-enhanced mass removal and flux reduction in 3D correlated permeability fields using magnetic resonance imaging. *J Contam Hydrol* **100**(3-4): 116-126.

Zhang, Y. and W.D. Graham. 2001. Spatial characterization of a hydrogeochemically heterogeneous aquifer using partitioning tracers: Optimal estimation of aquifer parameters. *Water Resour. Res.* **37**(8): 2049-2063.

Zhu, W., Xu, L., Ma, J., Yang, R., Chen, Y. 2009. Effect of the thermodynamic properties of W/O microemulsions on samarium oxide nanoparticle size. *Journal of Colloid and Interface Science* **340**: 119–125.

VI. Appendices

VI.1. A. Supporting Data

VI.2. B. List of Scientific/Technical Publications

VI.2.1. B.1. Articles in peer-reviewed journals

Chen, M., L.M. Abriola, B. Amos, E.J. Suchomel, K.D. Pennell, F.E. Löffler and J.A. Christ. 2013. Microbially enhanced dissolution and reductive dechlorination of PCE by a mixed culture: Model validation and sensitivity analysis. *Journal of Contaminant Hydrology* **151**: 117-130.

Christ, J.A., L.D. Lemke, and L.M. Abriola. 2009. The influence of dimensionality on simulations of mass recovery from nonuniform dense non-aqueous phase liquid (DNAPL) source zones. *Advances in Water Resources* **32**: 401–412.

Christ, J. A., C. A. Ramsburg, K. D. Pennell, and L. M. Abriola. 2010. Predicting DNAPL Mass Discharge from Pool-Dominated Source Zones. *Journal of Contaminant Hydrology* **114**: 18-34.

Christ, J.A., K.D. Pennell, and L.M. Abriola. 2012. Quantification of Experimental Subsurface Fluid Saturations from High-Resolution Source Zone Images. *Water Resour. Res.* doi:10.1029/2011WR010400, in press.

Ervin, R.E., A. Boroumand, L.M. Abriola, and C.A. Ramsburg. 2011. Kinetic Limitations on Tracer Partitioning in Ganglia Dominated Source Zones. *Journal of Contaminant Hydrology* **126**: 195-207.

Huang, J., J.A. Christ, and M.N. Goltz. 2010. Analytical solutions for efficient interpretation of single-well push-pull tracer tests. *Water Resour. Res.* **46**: W08538.

Li, K. and L. M. Abriola. 2009. A multi-stage multi-criteria spatial sampling strategy for estimating contaminant mass discharge and its uncertainty. *Water Resour. Res.* **45**(6): W06407.

Miller, E., L. Abriola, and A. Aghasi. 2012. Hydrological and Geophysical Signal Processing for Environmental Remediation and Restoration, *IEEE Signal Processing Magazine* **29**(4): 16-26.

VI.2.2. B.2. Technical reports

Ervin, R.E. 2012. Assessment of Partitioning Tracers for Estimation of DNAPL Source Zone Architecture. Doctoral Dissertation, Department of Civil and Environmental Engineering, Tufts University.

Boroumand, A. 2013. An assessment of the rate limited liquid-liquid interphase mass transfer in DNAPL source-zones: Modeling techniques and applications in site characterization. Doctoral Dissertation, Department of Civil and Environmental Engineering, Tufts University.

Wang, X. 2013. Dense Nonaqueous Phase Liquid (DNAPL) Source Zone Characterization in Highly Heterogeneous Permeability Fields. Master Thesis, Department of Civil and Environmental Engineering, Tufts University.

VI.2.3. B.3. Conference or symposium proceedings scientifically recognized and referenced

Ahmed, B., I. Mendoza-Sanchez, R. Khardon, L. Abriola, E. Miller. A Mixture of Experts Based Discretization Approach for Characterizing Subsurface Contaminant Source Zones. *IEEE Statistical Signal Processing Workshop, August 5-8, 2012, Ann Arbor, MI.*

Ahmed, B., I. Mendoza-Sanchez, R. Khardon, L. Abriola, E. Miller. A Discriminative-Generative Approach To The Characterization Of Subsurface Contaminant Source Zones. *International Geoscience and Remote Sensing Symposium 2012, July 22-27, 2012, Munich, Germany.*

Ervin, R.E. and C.A. Ramsburg. 2009. Exploring the Potential of Nonlinear and Non-Equilibrium Alcohol Partitioning for Assessment of DNAPL Source Zone Architecture. *In: Proceedings of the World Environmental & Water Resources Congress. 17-21 May 2009, Kansas City, MO.*

Zhang, H., I. Mendoza-Sanchez, L. Abriola, E. Miller. Manifold Regression For Subsurface Contaminant Characterization. *International Geoscience and Remote Sensing Symposium 2012, July 22-27, 2012, Munich, Germany.*

VI.2.4. B.4. Conference or symposium abstracts

Abriola L.M., K. Pennell, C. A. Ramsburg, E. L. Miller, J. Christ, N. L. Capiro, I. Mendoza-Sanchez, A. Boroumand, R. E. Irvin, D. I. Walker, H. Zhang. Characterization of DNAPL Source Zone Architecture and Prediction of Associated Plume Response: Progress and Perspectives. *Abstract H41M-01, Oral presentation at Fall Meeting, AGU, San Francisco, CA, Dec 3-7, 2012.*

Abriola, L.M., K.D. Pennell, C.A. Ramsburg, E.L. Miller, J.A. Christ, N. Cápiro, I. Mendoza-Sanchez, A. Boroumand, R.E. Ervin, D.I. Walker, and H. Zhang. Characterization of DNAPL Source Zone Architecture and Prediction of Associated Plume Response: Progress and Perspectives. *American Geophysical Union Fall Meeting, paper number H11M-01, San Francisco, CA, Dec 3-7, 2012.*

Abriola, L.M., E.L. Miller, K.D. Pennell, C.A. Ramsburg, J.A. Christ, I. Mendoza-Sanchez, N. Cápiro, R.E. Ervin, D. Walker, A. Boroumand, and H. Zhang. Metric Identification and Protocol Development for Characterizing DNAPL Source Zone Architecture and Associated Plume Response. *Battelle Eighth International Conference on Remediation of Chlorinated and Recalcitrant Compounds, Monterey, CA, May 21-24, 2012.*

Abriola, L.M., E.L. Miller, K.D. Pennell, C.A. Ramsburg, J.A. Christ, I. Mendoza-Sanchez, N. Cápiro, R.E. Ervin, D. Walker, A. Boroumand, and H. Zhang. Metric Identification and Protocol Development for Characterizing DNAPL Source Zone Architecture and Associated Plume Response. *Partners in Environmental Technology Technical Symposium & Workshop, Sponsored by SERDP and ESTCP, Washington, D.C., Nov 29-Dec 1, 2011.*

Abriola, L.M., E.L. Miller, K.D. Pennell, C.A. Ramsburg, J.A. Christ, M. Chen, N. L. Cápiro, B. Ahmed, and R.E. Ervin. Metric Identification and Protocol Development for Characterizing DNAPL Source Zone Architecture and Associated Plume Response. *Partners in Environmental*

Technology Technical Symposium & Workshop, Sponsored by SERDP and ESTCP, Washington, D.C. Nov 30- Dec 2, 2010.

Abriola, L.M., E.L. Miller, K.D. Pennell, C.A. Ramsburg, J.A. Christ, M. Chen, N. Cápiro, B. Ahmed, and R.E. Ervin. Predicting Source Zone Characteristics from Down-Gradient Plume Response. *Partners in Environmental Technology Technical Symposium & Workshop, Sponsored by SERDP and ESTCP, Washington, D.C., Dec 1-3, 2009.*

Cápiro, N.L., B.K. Amos, E.K. Granbery, F.E. Löffler, and K.D. Pennell. Bioaugmentation Following Surfactant Flushing for PCE-DNAPL Source Zone Treatment. *Battelle Bioremediation and Sustainable Environmental Technologies Symposium; Reno, NV, June 27-30, 2011. (invited)*

Cápiro, N.L., E.K. Granbery, B.K. Amos, J. Costanza, N. Keita, F.E. Löffler and K.D. Pennell. Coupled Technologies and Bioenhanced Dissolution for Improved DNAPL Source Zone Bioremediation. *Environmental Protection Agency 19th Annual National Association of Remedial Project Managers (NARPM) Training Conference; June 2-5, 2009. (invited)*

Cápiro, N.L., E.K. Granbery, J.A. Christ and K.D. Pennell. Evaluation of Contaminant Plume Response from Mixed DNAPL Source Zones Following Surfactant Flushing. *American Geophysical Union, Fall Meeting; San Francisco, CA, Dec 14-18, 2009.*

Cápiro, N.L., Granbery, E.K., Amos, B.K., Löffler, F.E., Pennell, K.D. Coupling surfactant flushing and bioaugmentation for PCE-DNAPL source zone treatment. *American Geophysical Union Fall Meeting, San Fransisco, CA, Dec 15-19, 2008.*

Ervin, R.E. and C.A. Ramsburg. Assessing Partitioning Kinetics for Tracers used to Quantify DNAPL Source Zone Architecture Metrics. *Seventh International Conference on Remediation of Chlorinated and Recalcitrant Compounds, Monterey, CA, May 24-27, 2010.*

Ervin, R.E. and C.A. Ramsburg. Exploring the Applicability of using Nonlinear and Non-equilibrium Alcohol Partitioning for Assessment of DNAPL Source Zone Architecture. *World Environmental and Water Resources Congress, Kansas City, MO, May 17-21, 2009.*

Ervin, R.E., A. Boroumand, L.M. Abriola, and C.A. Ramsburg. Influence of Mass Transfer Kinetics on Interpretation of Push-Pull Partitioning Tracer Tests. *American Geophysical Union Fall Meeting, paper number H41M-02, San Francisco, CA, Dec 3-7, 2012.*

Granbery, E.K., N.L. Cápiro, J. Christ, and K.D. Pennell. Characterization of DNAPL Source Zone Architecture and Associated Plume Response in 2-D Aquifer Cell Experiments. Remediation Technology Summit, *RemTec, Atlanta, GA, March 3-5, 2009.* Awarded “Best Student Poster Presentation” by the Adventus Group and Pollution Engineering.

Granbery, E.K., N.L. Cápiro, J. Christ, and K.D. Pennell. Characterization of DNAPL Source Zone Architecture and Associated Plume Response in 2-D Aquifer Cell Experiments. *American Geophysical Union, Fall Meeting, San Francisco, CA, Dec 15-19, 2008.*

Pennell, K.D., L.M. Abriola, E.L. Miller, C.A. Ramsburg, J.A. Christ, N. Cápiro, I. Mendoza-Sanchez, A. Boroumand, R.E. Ervin, D. Walker, and H. Zhang. Development of new approaches for characterizing DNAPL source zone architecture and associated plume response. *REMTEC Technology Summit: NAPL Source Zone Characterization and Management, Westminster, CO, March 4-6, 2013.*

Pennell, K.D., L.M. Abriola, F.E. Loffler. 2009. DNAPL research update: Advancing the state-of-the art. U.S. Environmental Protection Agency, *National Association of Remedial Project Managers (NARPM) Annual Training Conference; June 2-5, 2009, Atlanta, GA. (invited)*

Pennell, K.D., L.M. Abriola. 2008. Development of effective groundwater remediation strategies through coupled experimental and mathematical modeling research. *Joint Geological Society of America and Soil Science Society of America Meeting; Oct 5-9, 2008, Houston, TX. (invited)*

Walker, D. I., N.L. Cápiro, and K.D. Pennell. Competitive Solubilization of Trichloroethene and Tetrachloroethene from Non-Aqueous Phase Liquid Mixtures. *Eighth IAHS International Groundwater Quality Conference, Gainesville, FL, April 21-26, 2013.*

Walker, D. I., N.L. Cápiro, E.K. Granbery, and K.D. Pennell. Composition Dependent Evolution in Mass Flux from Binary Trichloroethene/Tetrachloroethene-DNAPL Source Zones. *American Geophysical Union Fall Meeting, San Francisco, CA, Dec 13-17, 2010.*

Walker, D. I., N.L. Cápiro, E.K. Granbery, and K.D. Pennell. Contaminant Micellar Solubilization from Binary Trichloroethylene/Tetrachloroethylene Non-Aqueous Phase Liquids. *Gordon Research Conference, Environmental Sciences: Water, Holderness, NH, June 20-25, 2010.*

Walker, D. I., N.L. Cápiro, E.K. Granbery, and K.D. Pennell. Plume Response Following Aggressive Mass Removal from Heterogeneous Source Zones Containing Trichloroethene and Tetrachloroethene Mixtures. *Eighth International Conference on Remediation of Chlorinated and Recalcitrant Compounds, Monterey, CA, May 20-24, 2012.*

Wallace, K., L.M. Abriola, M. Chen, C.A. Ramsburg, K.D. Pennell, and J.A. Christ. (2009). Investigating the influence of DNAPL spill characteristics on source zone architecture and mass removal in pool-dominated source zones. *American Geophysical Union Fall Meeting, San Francisco, CA, Dec 2009.*

Wallace, K.A., L.M. Abriola, M. Chen, C.A. Ramsburg, K.D. Pennell, and J.A. Christ. Investigating the Influence of DNAPL Spill Characteristics on Source Zone Architecture and Mass Removal in Pool-Dominated Source Zones. *American Geophysical Union Fall Meeting, paper number H13B-0938 San Francisco, CA, Dec 14-18, 2009.*

Zhang, H., I. Mendoza-Sanchez, J. Christ, E. L. Miller, L. M. Abriola. On the Use of Machine Learning Methods for Characterization of Contaminant Source Zone Architecture. *Abstract H43D-1252 Poster, presented at Fall Meeting, AGU, San Francisco, CA, Dec 5-9, 2011.*

VI.2.5. B.5. Text books or book chapters

Abriola, L.M., J.A. Christ, K.D. Pennell, and C.A. Ramsburg. 2012. Chapter 10: Source Zone Remediation Challenges. *In Delivery and Mixing in the Subsurface: Processes and Design*

Principles for *In Situ* Remediation, P.K. Kitanidis and P.L. McCarty (Eds.). SERDP and ESTCP Environmental Remediation Technology Monograph Series, Vol. 4, Springer, pp. 239-266. ISBN: 978-1-4614-2238-9

Cápiro, N. L. and K. D. Pennell. 2011. Source Control and Chemical Remediation of Contaminated Groundwater Sites. In Groundwater Quantity and Quality Management, Mustafa M. Aral and Stewart Taylor (Eds.). American Society of Civil Engineers. Reston, VA. pp. 475-521.

Pennell, K. D., N. L. Cápiro, D. I. Walker. 2013. Chapter 11: Surfactant and Cosolvent Flushing *Chlorinated Solvent Source Zones, Section IV. Remediation Technologies*. C. Herb Ward and Hans Stroo (Eds.) Strategic Environmental Research Development Program. (*in press*).